Technology Demonstration of a High-Pressure Swirl Oxy-Coal Combustor

Final Technical Report
Department of Energy Grant DE-FE0029113

Ahsan Choudhuri, PhD

June 2020

Energy Division
Aerospace Center, The University of Texas at El Paso
500 W. University Ave.
The University of Texas at El Paso
El Paso, TX 79968

Disclaimer

Abstract

This technical report presents the exploration of the design and prototyping of a High-Pressure Swirl Oxy-coal Combustor. Pressurized oxy-coal combustion systems have the potential to improve efficiency along with an increased carbon capture rate. Reduction of flue gas at higher pressure, smaller system size, and capital cost reductions render high-pressure oxy-coal systems particularly attractive as next-generation energy-producing systems.

High-pressure oxy-coal combustion systems are a recent concept, and thus operability issues of combustor designs for such systems are not fully understood. Significant challenges exist to maintain oxy-coal combustion stability at elevated pressure and a high CO_2 diluent environment. Although a body of knowledge exists for high-pressure oxygen combustion in rocket engines (or similar applications), it is yet to be strategized how these fundamental concepts can be translated to low-temperature CO_2 diluent combustion regimes. The realization of the pressurized oxy-coal based systems requires combustor components to be designed and demonstrated for an operating pressure over 10 bar. However, pressurized oxy-coal combustor design information at this pressure range and scale relevant to validate those proposed systems is currently limited. Experimental data from MW_{th} scale oxy-coal combustors are needed to identify the optimal trade-off between net efficiency and systems size.

The proposed effort is aimed at demonstrating a 1 MW_{th} down-fired swirl Oxy-Coal combustor and investigate the interrelation between combustor operating conditions (pressure; flame stability; flue gas recirculation ratio) and conversion efficiencies to minimize oxygen requirements. One of the key challenges is to configure burner design (i.e., swirl number and injector) and operating conditions for high-pressure oxy-coal combustion systems. These experiments differ from current systems partly due to the high theoretical flame temperature and related burner operability issues associated with oxy-combustion.

An ASPEN PLUS® model study for 550 MWe TIPS and ENEL pressurized oxy-coal systems with CO2 recirculation was performed to evaluate system design, subsystems sizing, and operating condition determination. The system analysis effort included TRL and technology gap determination of subsystems and critical components. This information was scaled to develop design requirements (design pressure and flue gas recirculation: $RR_{Flue\ Gas} = \frac{m_{flue}}{m_{total}}$) for the 1 MW_{th} combustor. The effects of a wide range of carbon dioxide recirculation ratios on the thermal efficiency of ENEL and TIPS cycles are studied. The pressure of 10 bar and 80 bar are used for ENEL and TIPS cycles, respectively. The thermal efficiency of ENEL is significantly higher than the efficiency of TIPS at a pressure of less than 10 bar. The insights from system analysis were then used to design a 1 MW_{th} swirl oxy-coal combustor. Flame temperature analysis and material strength analysis was performed to determine the combustor thickness. The structural integrity of the combustor was validated by finite element analysis using Abacus® and Hypermesh®. Feasibility of igniters and secondary burners are investigated in successful high-pressure oxy-methane combustion. The secondary burners are designed in such a way that it can operate between 100 to 500 kW firing input. Three generations of the pintle injector were designed based on swirl numbers (S=0, 0.9, and 1.2). Key pintle injector parameters such as pintle size, pintle orifice size, spray pattern were investigated by cold flow tests. Information from these tests was used to modify injector design for smooth and successful operation. A 5 mm pintle orifice size was decided upon as the optimum size for oxy-coal operation for the combustor. Shadow sizing experiments were performed to identify the atomization rate of each injector. Different coal water slurry mixtures (30 – 50% coal by wt% in the mixture) at various total momentum ratios (TMR) were investigated for this purpose. These experiments provided decisive information to choose the best design of the injector. The injector with 1.2 swirl provided higher atomization in all cases

than other designs. The mean equivalent droplet size of the jet was similar at different TMR and mixture ratios using this injector, thus making it suitable for use in most cases. Therefore, the 1.2 swirl-pintle injector was chosen for the shakedown test. The combustor and other sub-systems, including feed systems and control and data acquisition, have been manufactured, assembled, and integrated. The total system integration and installation began on July 1, 2020. The shake-down tests and initial operational capability demonstration are expected to be completed by September 30, 2020.

Table of Contents

List of Tables

Table of Figures

Executive Summary

High-pressure oxy-coal combustion systems are a new concept that has the potential to improve efficiency by recovering latent heat of the steam in flue gas and achieve nearly 90% CO_2 capture. Additionally, due to the reduction of flue gas at higher pressure, smaller system size and capital cost reductions are also possible. The current effort aims at prototyping a 1 MW_{th} down-fired swirl Oxy-Coal combustor and investigate the interrelation between combustor operating conditions (pressure; flame stability; flue gas recirculation ratio) and conversion efficiencies to minimize oxygen requirements. A major focus of this work is to perform a model analysis of pressurized oxy-coal systems to identify key design and operation parameters. An ASPEN PLUS® model study for 550 MW_e TIPS and ENEL pressurized oxy-coal systems with CO_2 recirculation was performed to evaluate system design, subsystems sizing, and operating condition determination. The system analysis effort included TRL and technology gap determination of subsystems and critical components. This information is then used as the inlet parameters to the 1 MW_{th} combustor for TIPS and ENEL cycles. The effects of a wide range of carbon dioxide recirculation ratios on the thermal efficiency of ENEL and TIPS cycles are studied. The pressure of 10 bar and 80 bar are used for ENEL and TIPS cycles, respectively. The thermal efficiencies of both cycles are validated by the established scientific literature. A separate study has been considered to refine the ENEL and TIPS cycle efficiency. For this, a wide range of conditions for bituminous coal slurry and flue gas recirculation ratios (20 % to 75%) were considered. The combined effect of pressure and recirculation ratios on thermal efficiency was investigated. The study concluded thermal efficiency of ENEL is significantly higher than the efficiency of TIPS at a pressure of less than 10 bar. Finally, Optimized turbomachinery conditions and experimental strategy for High-pressure Oxy-coal power cycles have been established for the current combustor.

A major focus of the current work is presented in Chapter 2; develop the swirl oxy-coal combustor system and validate the design. The combustor is divided into three major parts: Powerhead, Main Body, and Exhaust. Several material strength analysis and flame temperature analysis using NASA CEA is performed to choose combustor fabrication material. An analytical and computational thermal-mechanical analysis is performed to determine the optimum wall thickness of the combustor. Part wise and full combustor structural analysis are performed to validate the structural integrity of the system. Finite element analysis (FEA) using Abacus® and Hypermesh® was done on the full combustor to verify the design. The analysis considered all components, including welds, flanges, and bolts. The FEA yielded a min safety factor of 2.5, thus validating the combustor design. Both conventional and additively manufacturable igniters, secondary burners, and pintle injector designs were explored. Three generations of the pintle injector were designed based on swirl number. An autonomous feed system is designed and built for operating the system. The feed system is capable of remote operation through a control system via LabVIEW. A high-pressure oxy-methane combustion test facility is used to validate igniters and secondary burners operation under high-pressure conditions.

The final section of this report emphasizes on pintle burner (main burner) characterization. The pintle with eight (8) orifices with a diameter of 5 mm each has been considered for pressurized oxy-coal combustion. The current work uses coal-water slurry as working fuel for the main burner. For injection of the slurry, solid coal particles and liquid water are considered as the primary reactants, whereas the gaseous nitrogen (for safety) was acting as the secondary reactant for cold flow tests. Several pintle orifice sizes were tested for identifying optimum orifice size. Shadowgraph is performed using Dantec Dynamic Studio to characterize the injector spray pattern. The secondary reactant entrains into the primary reactant. This causes a breakdown in the jet stream. As the jet moves downstream, it breaks down more and forms many small-scale droplets. The secondary atomization zone is the regime where the maximum atomization takes

place. An image processing tool (ImageJ) is used to measure the spray angle for all test conditions. It is found that as the TMR decreases, so does the spray angle. A shadowgraph tool, namely shadow sizing, is used to characterize the spray droplet. The maximum atomization corresponds to the highest mass flow rate. In addition, the atomization increases with the increase in coal concentration. The size of the droplets is also affected by the increase in coal concentration. The spray droplets atomization mostly fall under mechanism III, only very few falls in mechanism IV in Reynolds-Ohnesorge plot. It is evident that full atomization was not achieved. However, it is concluded pintle orifice of 5 mm shows better atomization of coal slurry jet at a wide range of nitrogen flow conditions. Three different designs of pintle burners are investigated based on swirl number (S =0, 0.9, and 1.2) to achieve a higher atomization rate and compare spray pattern. The jet profiles for S = 0 injector indicates the lowest atomization. S = 1.2 swirl injector provides better jet breakup and creates more small size droplets in the downstream flow. As a result, S = 1.2 swirler provides the best atomization. Thus, this injector is chosen for hot-fire testing of the system. It is anticipated that a higher swirl injector has the potential to enhance the thermal performance of the high-pressure oxy-coal combustion. The total system integration and installation began on July 1, 2020. The shake-down tests and initial operational capability demonstration are expected to be completed by September 30, 2020. The report uses both Metric and English units. To be consistent with scientific literature cycle analyses and injector performance were presented in the Metric unit. However, to ensure maximum compatibility with the U.S. based manufacturers and component suppliers, combustor dimensions and subsystem specifications are kept in the English unit.

Project Information

Project Title:	Technology Demonstration of a High-Pressure Swirl Oxy-Coal Combustor
Grant No:	DE-FE0029113
Agency:	National Energy Technology Laboratory, Department of Energy
DOE Project Manager:	Mark Freeman Project Manager US Department of Energy, NETL Mark.Freeman@NETL.DOE.GOV
Project Period:	10/01/2016 - 03/31/2020
Principal Investigator:	Ahsan Choudhuri, Ph.D. Associate Vice President for Aerospace Center Mr. and Mrs. MacIntosh Murchison Chair II in Engineering The University of Texas at El Paso 500 West University, Room M305C, El Paso, Texas 79968 Tel: (915) 747-6905, E-mail: ahsan@utep.edu
Signature of Submitting Official:	 _____.
Co-Principal Investigator:	Norman Love, Ph.D. Department of Mechanical Engineering The University of Texas at El Paso 500 West University, Suite #110, El Paso, Texas 79968 Tel: (915) 747-8981, E-mail: ndlove@utep.edu
Submitting Institution:	The University of Texas at El Paso
DUNS:	132051285
Submission Date:	06/30/2020

Preface

This is the final technical report on the Department of Energy Grant DE-FE0029113 titled "Technology Demonstration of a High-Pressure Swirl Oxy-Coal Combustor."

Project Overview and Technical Background

Project Objectives

Pressurized oxy-coal combustion-based systems have the potential to improve efficiency by recovering latent heat of the steam in the flue gas and achieve 90% CO_2 capture [1]. Additionally, due to the reduction of flue gas at higher pressure, smaller system size and capital cost reductions are also possible. Although several recent studies [2-4] have delineated the economic feasibilities of pressurized oxy-coal systems, there are some disagreements of the recommended operating pressure to extract maximum benefit from such systems. The two major systems proposed in the literature, i.e., ThermoEnergy Integrated Power System (TIPS) and ENEL System [1,2], recommend an operating pressure between 10 bar to 80 bar to attain maximum net efficiency.

The realization of the pressurized oxy-coal based systems requires combustor components to be designed and demonstrated for an operating pressure over 10 bar. However, pressurized oxy-coal combustor design information at this pressure range and scale relevant to validate those proposed systems is currently limited. Experimental data from MW_{th} scale oxy-coal combustors are needed to identify the optimal trade-off between net efficiency and systems size (capital cost). The overarching goal of the proposed effort to demonstrate a 1 MW_{th} down-fired swirl Oxy-Coal combustor and investigate the interrelation between combustor operating conditions (pressure; flame stability; flue gas recirculation ratio) and conversion efficiencies to minimize oxygen requirements. Swirl burners are widely used in pulverized coal combustion processes and have superior flame holding, higher conversion rates, and low pollutant emission characteristics [5]. However, burner design (i.e., swirl number and injector) and operating conditions need to be carefully evaluated for high-pressure oxy-coal combustion configurations. These experiments differ from current systems partly due to the high theoretical flame temperature and related burner operability issues associated with oxy-combustion.

The project tasks were focused on systems configuration analysis, operating envelop determinations, system design and evaluation, technology readiness level (TRL) and technology gap analyses, design analysis, and modeling of the pressurized oxy-coal combustor, and demonstration and experimental investigations of a 1 MW_{th} scale system.

Objective 1: Systems Configuration Analysis of a 1 MW_{th} Pressurized Oxy-Coal Swirl Combustor [Chapter 1]

ASPEN PLUS® models for 550 MW_e TIPS and ENEL pressurized oxy-coal systems with CO_2 recirculation were used to perform system design, subsystems sizing, and operating condition determination. The system analysis effort included TRL and technology gap determination of subsystems and critical components. The information was then scaled to develop design requirements (design pressure and flue gas recirculation: $RR_{Flue\,Gas} = \frac{m_{flue}}{m_{total}}$) for the 1 MW_{th} combustor. A detailed analysis was performed to understand the scaling aspects of the components and the systems. The overarching aim was to use the combustor operating conditions and performance data generated through the proposed effort to validate net power efficiency analysis of the full-scale TIPS and ENEL pressurized oxy-coal systems.

Objective 2: Design and Construction of a MW_{th} Pressurized Oxy-Coal Swirl Combustor [Chapter 2]

With the requirements synthesized from the system configuration analysis, the design of the 1 MW_{th} pressurized combustor was completed. The design included swirl burner parameters, detailed structural analysis, and flow and combustion optimizations. The structural analysis was done using commercial finite element package Abaqus® and Hypermesh®. The flow optimization

and combustion analysis was performed using ANSYS Fluent® computational fluid dynamics package. The blueprint and CAD model for the combustor was produced in NX® 8.5 computer-aided design package.

Objective 3: Test of the Combustor Performance and Operability [Chapter 3]

The combustor is currently being installed (began on July 1, 2030) and will be tested for a wide range of operating conditions to understand the performance and operational issues. Flame stability analysis and flame temperature and heat flux measurements will be done for a range of pressure, swirl number (ratio of axial flux of the angular momentum to the axial flux of axial momentum), and flue gas recirculation ratio. Flue gas analysis will be performed to produce fundamental combustion information i.e. effects of pressure, swirl number, and stoichiometric ratio on burnout and pollutant emissions.

Key Technology Challenges

High-pressure oxy-coal combustion systems are a recent concept and thus operability issues of combustor designs for such systems are not fully understood. Significant challenges exist to maintain oxy-coal combustion stability at elevated pressure and a high CO_2 diluent environment. Although a body of knowledge exists for high-pressure oxygen combustion in rocket engines (or similar applications), it is yet to be strategized how these fundamental concepts can be translated to low-temperature CO_2 diluent combustion regimes. High pressure and relatively low-temperature environment may result in a negative pressure dependence of mass burning rate [6] and create significant uncertainty in estimating flammability and extinction limits. If the combustion is designed outside of these limits, the incomplete combustion may lead to higher pollutant emissions and lower system efficiency.

Several studies have reported the flame stability issues of pulverized coal combustion in an O_2/CO_2 environment [7-9]. The issues primarily arise from lower flame temperature and burning rates in high CO_2 flame conditions. Additionally, ignition delay may be another major issue. Chen et al., show the narrowing of flammability limit as CO_2 (in comparison to N_2) diluent increases in the mixture[1]. It is important to note that most oxy-coal combustion studies done so far used atmospheric pressure conditions [10]. More studies of high-pressure oxy-coal combustion with dry or wet flue gas recirculation especially on a scale relevant to practical systems are certainly needed to develop design requirements for such combustors.

Chen et al. in their recent review article identifies four key factors critically important for oxy-coal combustion stabilization: (i) flue gas recirculation ratio, (ii) oxygen concentration staging, (iii) mixing, and (iv) reactant preheating [1]. The proposed effort to develop a 1 MW_{th} high-pressure oxy-coal combustor is aimed at investigating these issues as well as demonstrating the technology at a scale relevant to practical operations. As discussed in a later section, a swirl burner with a core pintle injector will be used for the combustor to systematically study and optimize oxygen concentration staging, mixing, and flue gas recirculation ratio to attain high conversion rate while minimizing oxygen requirements.

Chapter 1: Power Cycle Analysis

ASPEN PLUS® models for 550 MW_{th} TIPS and ENEL pressurized oxy-coal systems with CO_2 recirculation are used to perform system design, subsystems sizing, and operating condition determination. The system analysis effort includes TRL and technology gap determination of subsystems and critical components. The information is then be scaled to develop design requirements (design pressure and flue gas recirculation: $RR_{Flue\ Gas} = \frac{m_{flue}}{m_{total}}$) for the 1 MW_{th} combustor. A detailed analysis is performed to understand the scaling aspects of the components and the systems. The overarching aim is to use the combustor operating conditions and performance data generated through the proposed effort to validate net power efficiency analysis of the full-scale TIPS and ENEL pressurized oxy-coal systems. The strategical plans used for system configuration analysis are reported in this section.

During the first year, a strategic plan was developed for power cycle analysis. The cycle analysis of the 550 MW_{th} TIPS and ENEL pressurized oxy-coal systems was performed using the ASPEN PLUS® process simulator. The team has used a pressurized oxy-coal cycle as the benchmark for the ASPEN Plus cycle study. Afterward, the 550 MW_{th} TIPS and ENEL pressurized oxy-coal systems have been modeled. Both TIPS and ENEL system possesses similar upstream configuration. Therefore, at first, the process simulation has been conducted for the upstream. Then the heat exchanger section was added for TIPS and ENEL systems. In the end, the CO_2 capture unit was simulated. These studies have provided the maximum efficient configuration for the TIPS and ENEL system. The information was scaled to develop design requirements for the 1 MW_{th} combustor. Additionally, the system analysis initiative has include TRL and technology gap determination of subsystems and critical components.

1.1. Benchmark Study

The model from Hong et al. [2], shown in Fig.1., was used for this purpose. Using the parameters found in the paper by Hong et al. [2], each portion of the model was input into ASPEN Plus®. The test model after being input into ASPEN Plus is shown in Fig.2. The model that is presented in this report is designed based on a 10 bar pressure.

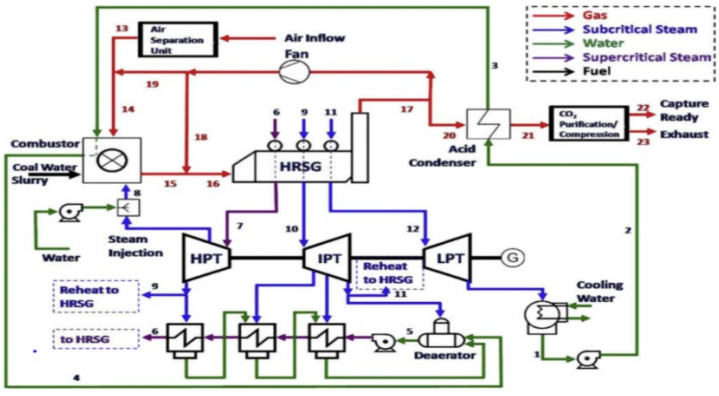

Figure 1. Benchmark cycle [2]

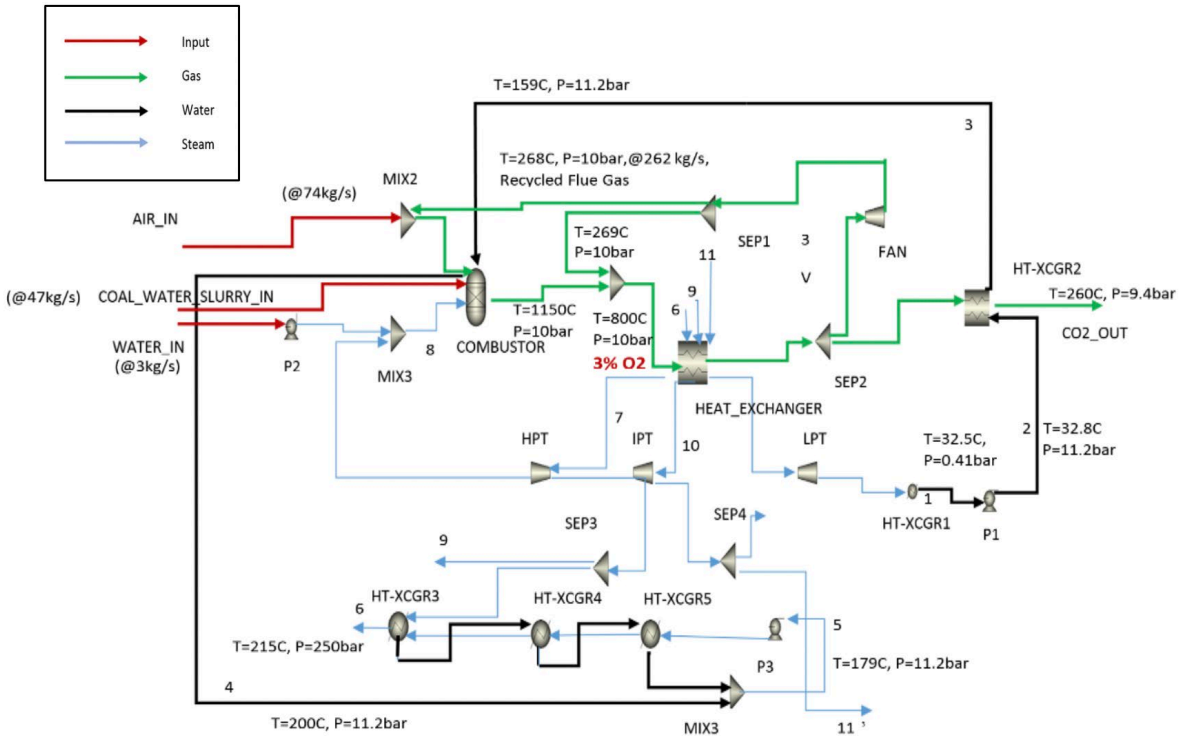

Figure 2.Benchmark cycle as it appears after input into ASPEN Plus

The input materials for the system include a coal water slurry, water, and air, which was then decomposed into O_2 in the Air Separation Unity (ASU). For input materials (Ref. [2]), the values of parameters such as temperature, pressure, flow rates, and mole fractions were input into ASPEN Plus. The flow rates of the water and slurry were 3 kg/s and 46 kg/s, respectively. The air passing from the ASU has a flow rate of 74kg/s at 10bar pressure and 316°C temperature. The ASU delivers an oxygen-rich stream with an O_2 concentration of 95% by volume.

Several mixers and separators were also used in the cycle to combine or bifurcate streams. The primary heat exchanger in the design has been modeled as a boiler, which is kept at a 10-bar pressure. The combustor was represented using the Gibbs model in ASPEN Plus®. This model executes the operation on solids, liquids, and gases, which are all present in the combustor unit.

Coal composition also proves to be an important factor in the composition of flue gas and temperatures resulting from the system. After a brief literature review, a composition of lignite was used for the input coal stream. The composition of the input coal is given in Table 1.

Table 1. Coal composition for model analysis

C	H	O	N	S
73.81%	5.01%	19.91%	0.95%	0.32%

Once the entire cycle was developed, each section was analyzed separately. This was done to simplify the troubleshooting and any discrepancies between the result from ASPEN Plus and those found in Ref. [2]. The first section that was analyzed is the combustor, Fig 3. Data were given as inputs for the incoming streams, and the output data are compared to Ref. [2].

For the test model, a particular stream was chosen as the ideal case. After running the developed model in ASPEN Plus, the exit stream from the combustor yielded 3% molar oxygen. This value was used as a comparison with Ref. [2], which yields the same result. The values of some of the other pressures and temperatures for both Ref. [2] and the developed ASPEN Plus test models are presented in Table 2. The table shows that the maximum percentage of the difference between the two models is 5%. This discrepancy may be due to some slight variations in input pressures and temperatures since Ref. [2] did not specify each input condition. Nevertheless, it is believed that the ASPEN Plus model is validated and could be used to model other complex oxy-coal cycle configurations.

Table 2. Stream parameter comparison between those in the current study using ASPEN Plus [1]

Stream Number (From Fig. 2)	Temperature (°C)			Pressure(bar)		
	Ref. [1]	Test	Percentage of error (%)	Reference	Test	Percentage of error (%)
7	600	600	0	250	247	1.20
16	800	760	5	10	10	0
17	60.51	58.4	3.5	9.351	9	4

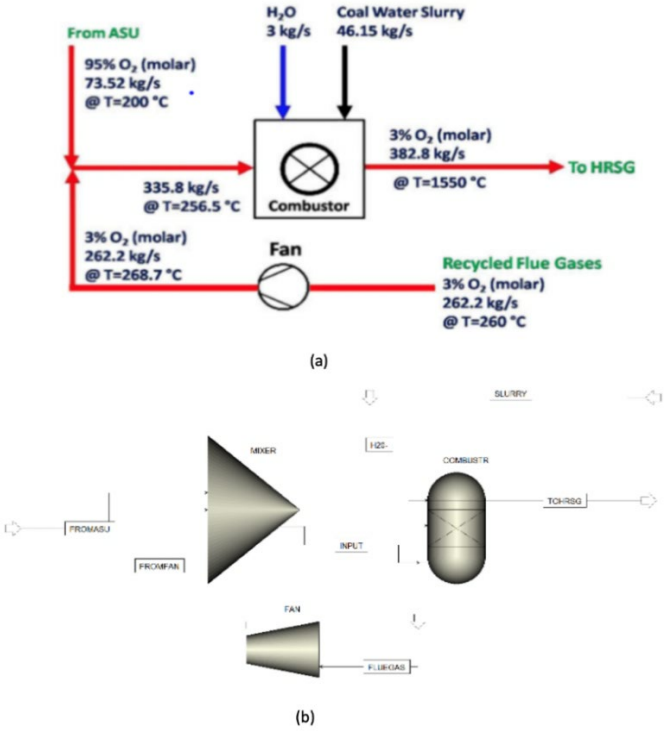

Figure 3. Benchmark cycle upstream configuration (a) from Ref. [2] and (b) after input into ASPEN Plus

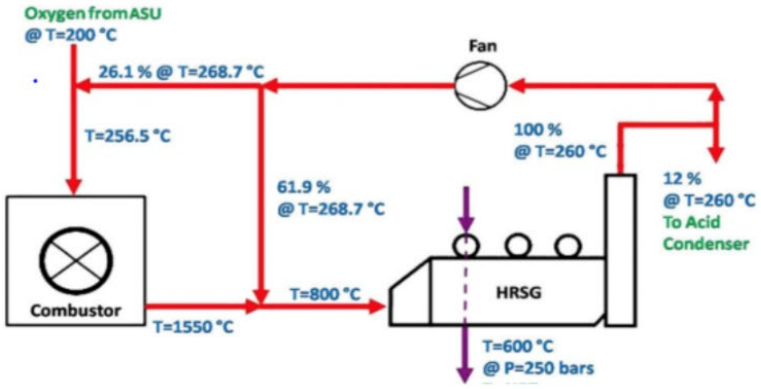

(a)

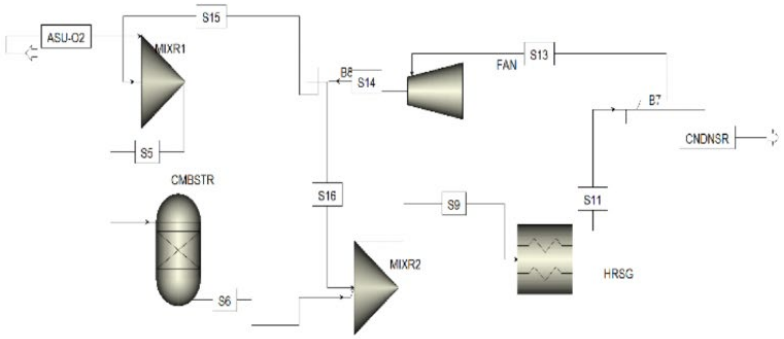

(b)

Figure 4. Cycle configuration after combustor (a) from Ref. [2] and (b) after input into ASPEN Plus

Using the number convention from Fig. 2, the test model has water flowing through streams 1 to 5 and undergoes a phase change to supercritical steam in streams 6 and 7. Streams 9 to 12 are also found to be at the supercritical state. The inlet to the power island is at 247 bar and 600°C, stream 7. The streams 13 to 21 all have gaseous flow with a variation in compositions. By comparing with the corresponding streams of the reference model by Hong et al. [2], the states of the flows are found to match. It can be observed that the stream out from the combustor has a pressure of 20 bar and a temperature of 1600°C. The low temperature is obtained by mixing of oxygen-rich air from ASU with flue gas. The output from the combustor is gaseous and rich in carbon dioxide with a concentration of 3% molar oxygen

1.2. TIPS and ENEL Model Development

With the ASPEN Plus model validated, some changes were incorporated from the reference case to accommodate the cycle parameters for the TIPS and ENEL models. Both cycles were divided into three separate components: upstream, heat exchanger, and carbon capture. Each of these sections is colored in Figs. 5 and 6. Both the TIPS and ENEL cycles have the same upstream configuration; thus, this portion of the cycle was first modeled (Fig. 7). The upstream portion of each cycle has a fan, a mixer, and a combustor. The product from the ASU enters the fan at a rich oxygen percentage. It is seen that ASU supplies up to a 95% stream of pure oxygen. From this portion of the stream, the oxygen is mixed with 9% recycled flue gas. The flue gas is recycled to maintain the temperature [1] and lower the oxygen percentage. Coal slurry, 26% water and 74% coal, is used as the input. The composition of coal is the same as used in Table 1. The pressure of the combustor is maintained at 20bar.

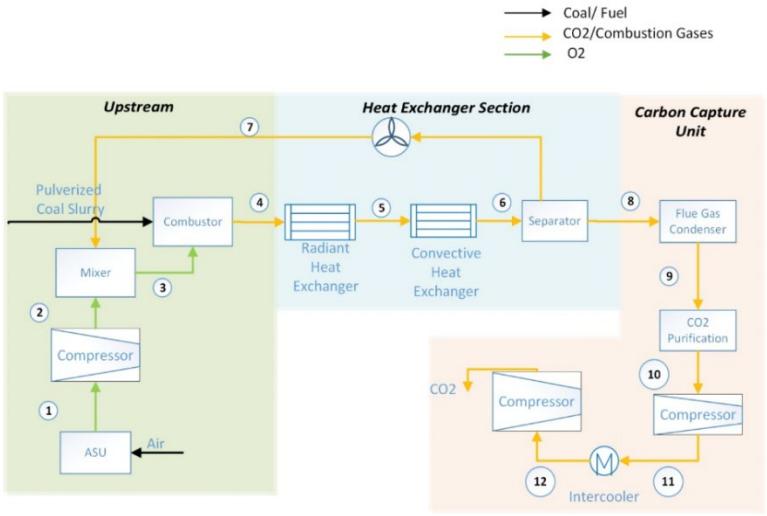

Figure 5. TIPS Cycle

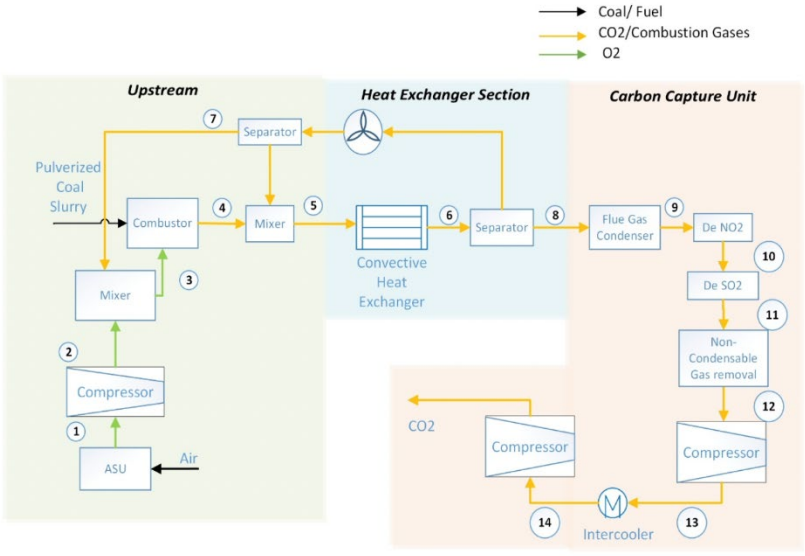

Figure 6. ENEL Cycle

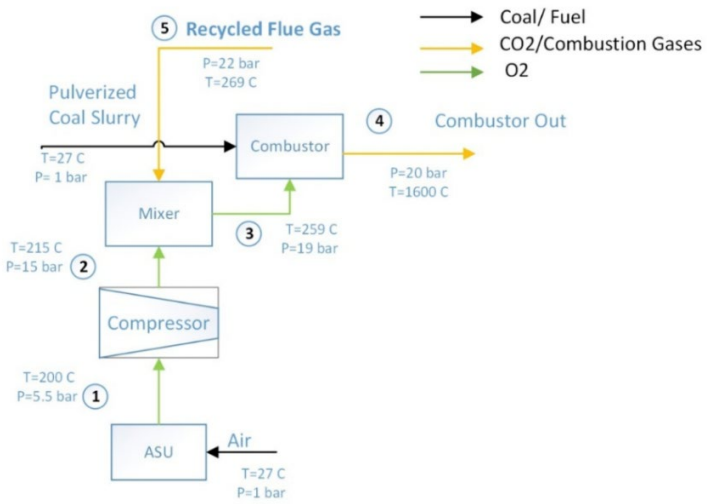

Figure 7. The upstream model used for oxy-coal flow rate analysis

1.3. High-Pressure Oxy-Coal Power Cycle Analysis

ENEL is a prospective cycle configuration for high-pressure oxy-coal power generation [1]. The cycle was originally patented by ITEA [11-13] and investigated by MIT [3,14]. Hong et al. [2] presented a comprehensive layout for ENEL where the combustor operates at a 10-bar pressure. The cycle uses air that is purified and compressed through an Air Separation Unit, yielding as much as 95% molar oxygen. The oxy-coal combustion process yields hot combustion gases, which then pass through a heat recovery steam generation unit (HRSG). The HRSG consists of several heat exchangers. A part of the flue gas is recycled and fed into the combustion chamber to regulate the combustion temperature. The remaining gas goes to the carbon capture unit for sequestration. Meanwhile, a series of water streams pass through the main heat exchanger and pass through the power island consisting of three turbines: high-pressure turbine (HPT), intermediate pressure turbine (IPT), and low-pressure turbine (LPT). Energy is derived from these turbines. The steam passing through a cooling channel is recirculated into the system. The ENEL cycle configuration for the present study is obtained from Hong et al. [2], shown in Figure 8.

The ThermoEnergy Power System (TIPS) developed ThermoEnergy Integrated Power System (TIPS) coal power cycle by putting a combustor operating pressure of 80 bar [2,15]. CANMET [3], Renz [16] are among the very few investigators who investigated the TIPS power cycle. The study conducted by CANMET suggested that in terms of recovering latent heat, the benefit of increasing pressure above 80 bar is relatively small [3]. However, Babcock Power [17] used a different flue gas condenser design and suggested that the recovery mainly can be done from atmospheric pressure to 20.7 bar pressure. Renz [16] provided a layout of the TIPS power cycle. The proposed cycle extracts work in three stages and use the recirculation of flue gas to control the combustion temperature [16]. At each stage, the feed water is heated by the flue gas inside the heat exchangers. Steam enters into the first stage or high-pressure turbine at 285 bar and 600°C and later at medium pressure turbine(MPT) at 60 bar and 620°C. Finally, at the last stage, steam enters into the low-pressure turbine at 5.5 bar and 268°C. The study also used three condensing heat exchangers to heat the feed water by flue gas. The major portion of the feed water is heated up by the first two heat exchangers at 326 bar, 203°C, and 10 bar, 62°C, consecutively. The last heat exchanger is used to produce low-pressure steam of 4 bar at 240°C, which is fed to the low-

pressure turbine. In the present study, the cycle layout used by Renz [16] is presented and the combustor set to operate at an 80-bar pressure, Figure 9.

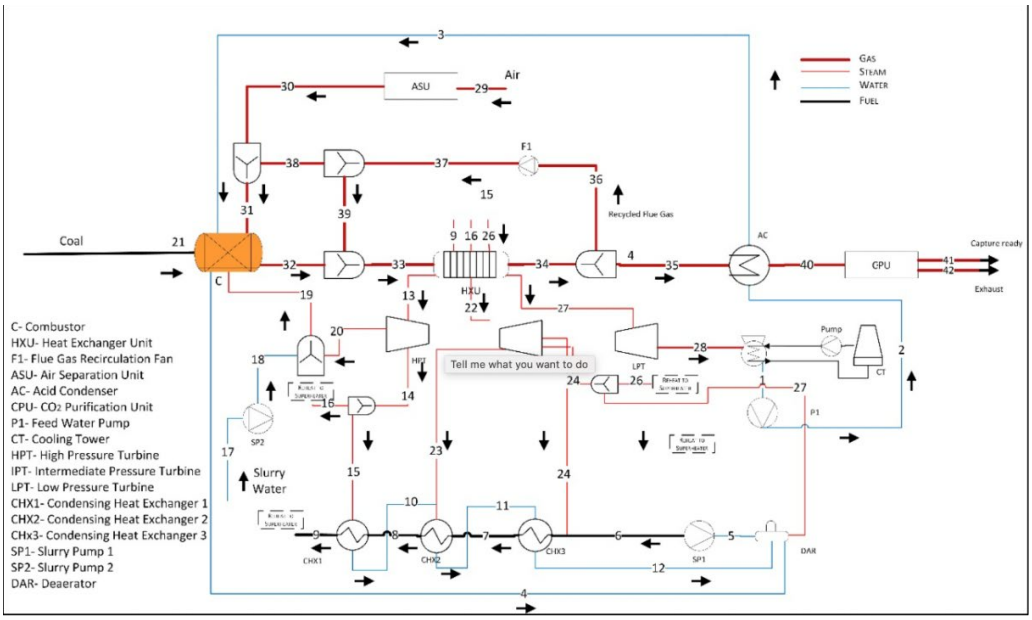

Figure 8. ENEL Coal Power Cycle

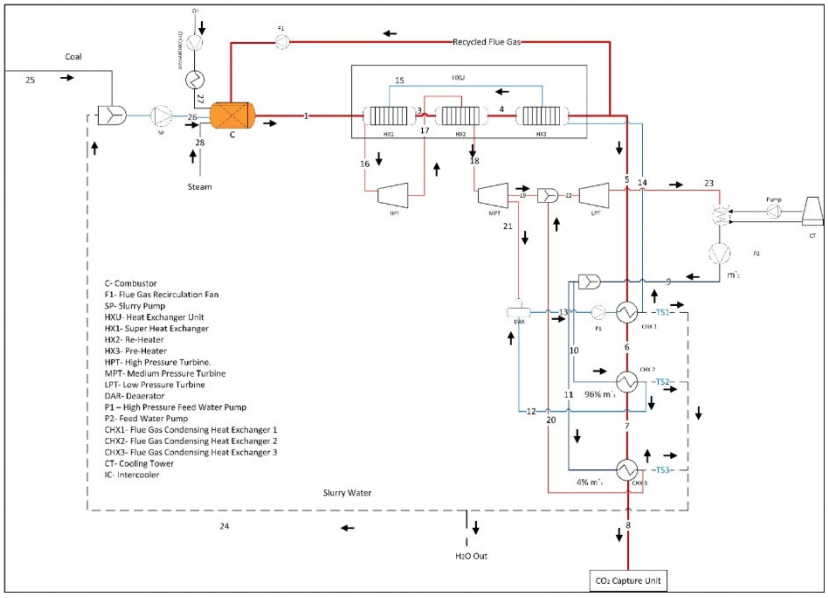

Figure 9. TIPS Coal Power Cycle

The TIPS cycle is studied based on different designs of flue gas condenser and the amount of recoverable latent heat at different pressure levels [1]. Though the recoverable latent heat and net efficiency increase with pressure according to CANMET, after 80 bar, the benefit of increasing pressure does not vary significantly [3]. For this reason, there is a difference in the efficiencies of the TIPS and ENEL cycles. Unlike TIPS, ENEL uses a small temperature difference of 20°C in the flue gas condenser. In the ENEL cycle, most of the latent heat can be recovered at 11 bar

[14]. The maximum efficiencies for both systems correspond to these pressures and are of the same order of magnitude [1].

A coal slurry (coal and water) is mixed with oxygen provided by the Air Separation Unit (ASU) in the combustor. The flow rates of water and coal are 3 kg/s and 18.87 kg/s, respectively. The study was performed using the properties of bituminous coal. The assumed coal composition is shown in Table 3. Air is purified and compressed in the ASU, yielding 95% oxygen by volume. For this research, the ASU unit has not been designed, so oxygen is directly supplied to the system at 200°and 1MPa for ENEL and 8MPa for TIPS. The oxy-coal combustion process yields hot combustion gases, which then pass through the heat recovery steam generation (HRSG) section. The HRSG section consists of several heat exchangers. A part of the flue gas is recycled and fed into the combustion chamber to regulate the combustion temperature. The remaining gas goes to the carbon capture unit for sequestration. Meanwhile, a series of water streams pass through the main heat exchanger and the power island consisting of the high-pressure turbine (HPT), intermediate pressure turbine (IPT), and low-pressure turbine (LPT). The steam passes through a condenser and is recirculated within the system in a closed-loop. For this study, three recirculation ratios are investigated, 25%, 50%, and 75% of the total flue gas. In the ENEL cycle, the recirculation gas stream bifurcates twice. The stream from the heat exchanger section first divides into two parts with one stream directed to the carbon capture unit (CCU), and the other to the combustor. The latter stream splits once more, with a portion diverted to the combustion chamber and the other stream mixing with the combustion products. This is done to regulate the temperature of the streams. Thus, the stream from the heat exchanger section splits with 12% passed to the carbon capture unit. The rest of the flow splits again, with 25% of the flue gas going to the combustor. Here, the flow to the CCU (12%) is kept constant while the flow mixed in the combustor is varied from 25% to 75%. In the TIPS cycle, 100% of the gas is recirculated in the combustion chamber. Thus, the amount of flue gas entering the CCU varies for the three cases investigated.

Table 3. Assumed coal composition for both the ENEL and TIPS models

Proximate (wt%)(dry)	
Moisture	6.4
Ash	7.0
Volatile matter	33.1
Fixed Carbon	53.5
Ultimate (wt%)(dry)	
Carbon	71.1
Hydrogen	4.7
Nitrogen	1.2
Sulfur	0.5
Ash	8.86
Oxygen	1.2
Chlorine	0.014
Fluorine (ppm)	34.6
Heating Value (MJ/kg)	
HHV	29.1
LHV	27.5

The ASPEN model for the ENEL cycle used for this study is shown in Figure 3. For clarity, the cycle has been divided into three sections and is presented in Figures 4 to 9, for both ENEL and TIPS.

The thermodynamic analysis performed by the software for both the cycles are based on the assumptions listed in this section. For the analysis, ideal gas assumptions are implemented for the flue gas. The ideal gas equation is expressed in Eq. (1):

$$\mathrm{Pv} = \mathrm{nRT} \tag{1}$$

Where P is Pressure, v is the specific volume, R is the universal gas constant, T is the temperature, and n is the molar number. The IDEAL method in ASPEN PLUS®, used in this study, assumes the Ideal Gas/Raoult's law/Henry's law to estimate equilibrium phase distribution ratios (K values[19]). Raoult's law assumes that the mole fractions of each of the components in the mixture is constant at constant temperature and pressure. Henry's law states that the amount of gas dissolved in the mixture is proportional to its partial pressure in the gas phase. The model is chosen based on the properties of the participating components. The solid properties are the same for all models. Thus, this model is appropriate as the process involves oxygen, nitrogen, and water vapor at relatively low pressure. For an adiabatic process, which would be seen in an ideal turbine and compressor, the following formula is applicable:

$$\mathrm{C_v dT} = -\mathrm{Pdv} \tag{2}$$

Where $\mathrm{C_v}$ is the specific heat at a constant volume, dT is the small change in temperature, and dv the small change in specific volume. The amount of work that is required for compression of a fluid and the amount of work extracted by the turboexpander can be determined by the change in enthalpy. To calculate these values Eqs. (3) and (4) are used:

$$\mathrm{W} = \mathrm{h\ compressed} - \mathrm{h\ uncompressed} \tag{3}$$

$$\mathrm{W} = \mathrm{h\ combustion\ products} - \mathrm{h\ turboexpander\ exhaust} \tag{4}$$

To calculate the plant efficiency of each cycle, the power production of the system is calculated based on the gross power output and the total power input needed to operate the different components (pump, CCU, ASU, etc.), Eq. (5) .

$$\mathrm{Net\ Plant\ Efficiency} = 1 - \frac{\mathrm{total\ Power\ Input\ Required}}{\mathrm{Gross\ Power\ Output}} \tag{5}$$

Thermal efficiency was also determined in the present study. This parameter is calculated based on the lower heating value, Eq. (6) .

$$\mathrm{Thermal\ Efficiency} = \frac{\mathrm{Gross\ power\ Output}}{\mathrm{Total\ HHV_{fuel}\ Energy\ Input}} \tag{6}$$

The Gibbs free energy of a system is the difference of the enthalpy of the system and the product of temperature and entropy of the system. The magnitude of the change in Gibbs energy indicates

the deviation of the energies of the reactants and products from the equilibrium phase. Gibb's free energy is calculated based on the temperature, entropy and enthalpy of the system, Eq. (7).

$$\text{Gibbs Free Energy} = \text{Enthalpy} - (\text{Temperature} * \text{Entropy}) \quad (7)$$

ASPEN PLUS® facilitates the evaluation of the power produced and predicts the probable products. Error tolerance of 0.0003 and a maximum of 30 iterations are used for convergence. Besides this, the convergence of each block depends on whether the total mass flow rate or energy, in and out, is conserved. The pressure and temperature of the input materials are provided as the inlet parameters in the following section. The combustor is represented by the RGibbs model in ASPEN PLUS®. The RGibbs model operates by minimizing the Gibbs free energy of the system19. RYeild and RStoic blocks were used to prepare the coal slurry for combustion. Since coal is a non-conventional component in ASPEN PLUS®, it is broken down into its constituent elements in the RYeild block. The RStoick block arranges the reactions occurring sequentially. The following reactions were considered:

$$\mathrm{C} + \mathrm{O_2} \rightarrow \mathrm{CO} \quad (8)$$

$$\mathrm{C} + \mathrm{O_2} \rightarrow \mathrm{CO_2} \quad (9)$$

$$\mathrm{Coal - N} + \mathrm{O_2} \rightarrow \mathrm{NO} \quad (10)$$

$$\mathrm{Coal - S} + \mathrm{O_2} \rightarrow \mathrm{SO_2} \quad (11)$$

$$\mathrm{Coal - H} + \mathrm{O_2} \rightarrow \mathrm{H_2O} \quad (12)$$

From the ultimate analysis for the coal used in the study, the stoichiometric chemical reaction is:

$$\mathrm{C_{1.77}H_{1.39}O_{0.17}S_{0.0047}N_{0.26}} + 2.04\,\mathrm{O_2} \rightarrow 1.77\,\mathrm{CO_2} + 0.695\,\mathrm{H_2O} + 0.0047\,\mathrm{SO_2} + 0.0129\,\mathrm{N_2} \quad (13)$$

Two calculator blocks have been used in ASPEN PLUS® to calculate the water in the wet coal and the heat of combustion in the combustor. Ash produced from combustion is also a non-conventional component. It is removed from the stream by using the split block. This can model a splitter where the solid components and fluid components are separated into two individual streams. The solids are removed while the remainder moves onto the rest of the cycle. In the carbon capture section, the RadFrac blocks have been used to model the absorber and the stripper. The heat exchangers, mixers, separators, turbines, compressors, and pumps all operate within the convergence limits to ensure a functional cycle.

Cycle analysis is performed, assuming a 550MW power input (fuel mass flow HHV). The only inputs for the system include flow rates for water and coal for both systems. Coal is supplied at 18.87 kg/s and water at 3 kg/s. The coal is supplied as a slurry with an additional 10% water in the slurry. These components are added at 25°C and 1MPa pressure for ENEL and 8MPa pressure for TIPS. Other parameters are calculated by the software. The ASPEN PLUS® cycle for ENEL is shown in Fig. 10. Similarly, for TIPS the divided sections have been presented in Fig. 11. A basic schematic for the TIPS cycle was analyzed in literature[16]. The figures show the temperature and pressure calculated from the analysis.

The detailed view of the ENEL cycle, presented in Fig. 10, show the temperature and pressure variance for 50% recirculated flue gas. The significance of these figures is that they show the

pressure and temperature at each step of the cycle. For ENEL, the pressure is kept at 1MPa throughout the cycle. The combustion products portray the highest temperature of the cycle and the amount of heat energy produced from burning the fuel. The cycles were simulated without any recirculation gas to check the highest temperature combustion can reach without any cooling. And with no recirculation, ENEL reached 2670°C, while TIPS (Fig.11) reached 2807°C. Figure 3 shows that when 50% of the recirculation gases mix with the combustion products, it results in a 39% decrease in stream temperature when compared to no recirculation case. The temperature is then controlled to reduce the number of heat exchangers required in the HRSG unit. The gas at 225 °C then passes to the CCU and the recirculation lines. It is important to regulate the temperature of the incoming stream of the CCU since the acid gasses like, SOx and NOx have a higher dew temperature at higher operating pressure. In this study, the stream temperature was kept between 200-300°C.

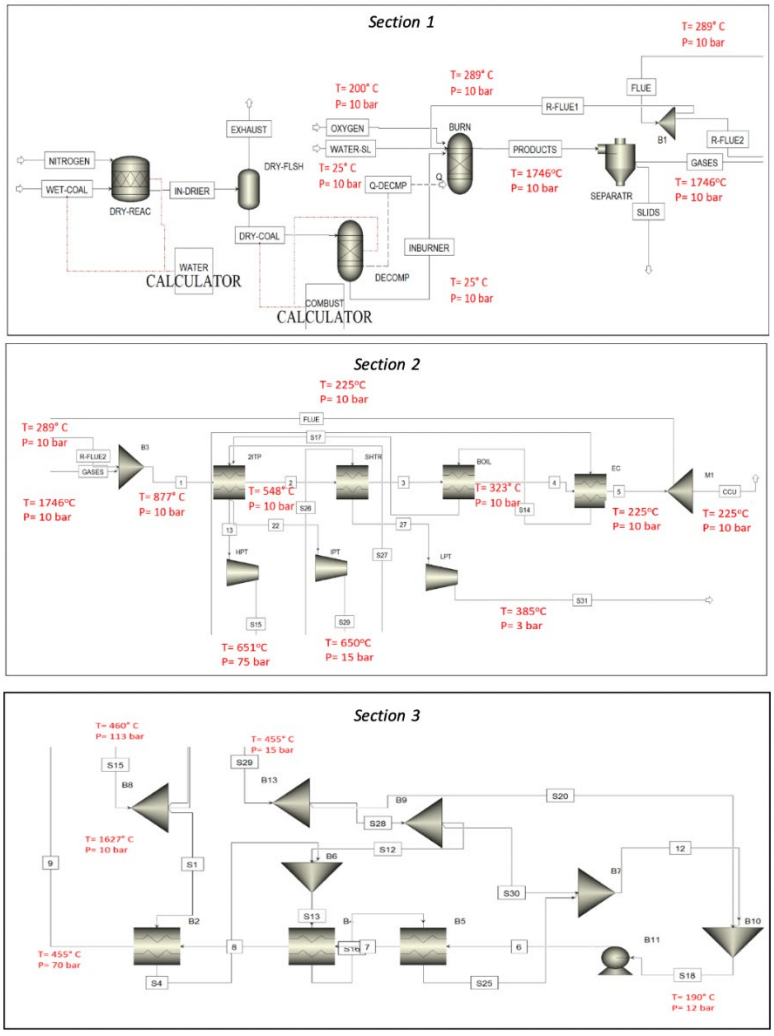

Figure 10. ENEL cycle

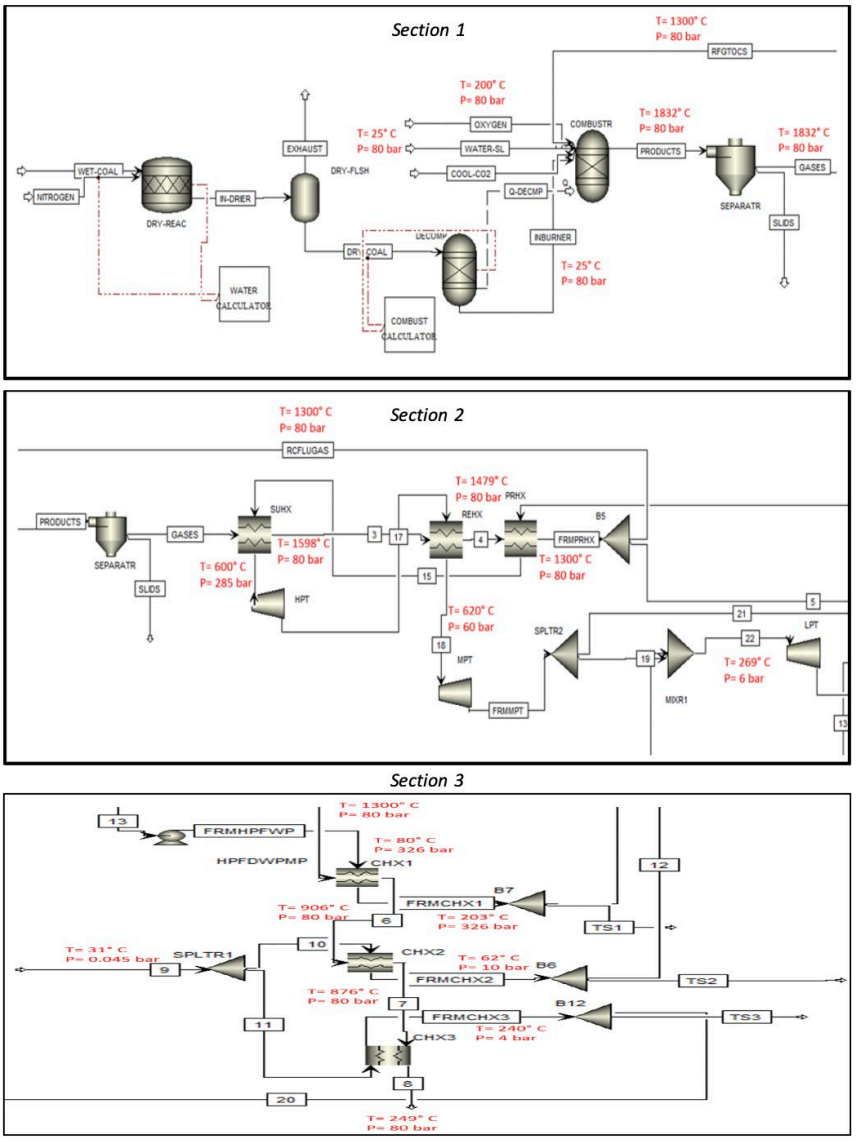

Figure 11. TIPS cycle

1.4. Carbon Capture Unit

For the Carbon Capture Unit (CCU), a basic design has been adopted. In a CCU, the main components are an absorption section and the stripper section. Carbon dioxide removal by absorption and scrubbing by aqueous amine solution is well understood [18]. The basic process, patented in 1930, is one in which CO2 is absorbed from a fuel gas or combustion gas near ambient temperature into an aqueous solution of the amine with low volatility. The amine is regenerated by stripping with water vapor at 100° to 120°C, and the water is condensed from the stripper vapor, leaving pure CO2 that can be compressed to 100 to 150 bar for sequestration. The layout for the CCU used in the present model is given in Figure 12.

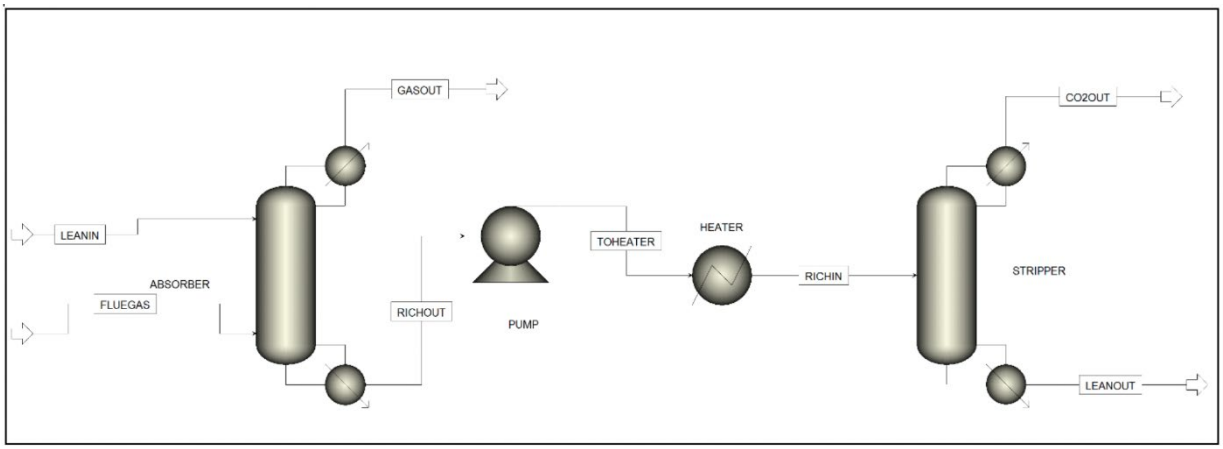

Figure 12. The layout of the general Carbon Capture Unit

In this report, a primary model is presented with calculations made for the TIPS cycle. Forty stages in the absorber are modeled. The pressure of the absorber tower is set to 1 atm. MEA solvent was pushed through the first stage, and the flue gas was delivered through the 40th stage, with stage 1 at the top and 40 at the bottom. Flue gas parameters are the same as those obtained from the combustion model simulation. Although the flue gas pressure is high, absorber pressure is set to be 1 atm. Heat exchangers were used to reducing the temperature of the CO_2 rich solvent stream. This was essential for the efficient operation of the stripper. The number of stages in the stripper was 45. Low-pressure steam was used to strip the CO_2 from the solvent. After stripped CO_2 gas comes out of stage 1 the liquid MEA solvent comes out through stage 45, as shown in Figure 13.

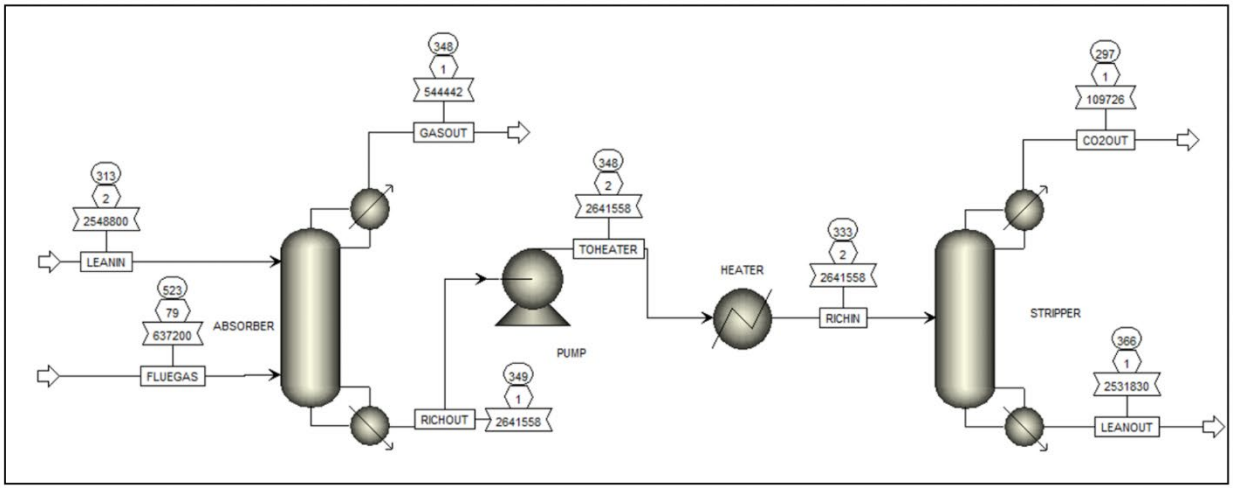

Figure 13. Model used for Carbon Capture Unit, details of settings seen

The products of the process are shown in Table 4. The system achieves a considerable amount of carbon removal. Further study will be done to refine the model and obtain optimum results. Subsequently, the carbon capture unit will be integrated with the entire cycle.

Table 4. Performance and gas composition from the CCU

Total Flow Rate (kg/s)	Flue Gas	Lean In	Rich Out	Gas Out	CO_2 Out	Lean Out
	177	708	734	151	31	703
Mass Fraction						
MEA	0	0.13	0.023	0.0003	2.40E-11	0.14
H_2O	0.14	0.63	0.6	0.18	0.02	0.63
CO_2	0.72	5.00E-08	0.00025	0.66	0.98	1.70E-30
MEAH+	0	0.089	0.14	0	0	0.086
MEACOO-	0	0.14	0.23	0	0	0.139

1.5. TRL Analysis

The main turbomachinery required for the cycle are pumps, fans/compressors, heat exchangers, and turbines. The main heat exchanger or the Heat Recovery Steam Generator (HRGS) can be designed as a single heat exchanger with multi-channels or a series of blocks consisting of economizer, boiler, and superheater. For the present research, a database of available turbomachinery has been presented in the following tables.

1.5.1. Pumps

For the cycle, three pumps will be required for water. A pump will be required to pressurize inlet water to 10bar. Another pump will be required to pressurize recirculating reheat water while the third pump will be needed to pressurize the cooled water coming from the turbine. A slurry pump is also required to pump the coal to the combustor. For ENEL, a wide range of pumps are available operating at 10 bar. However, for TIPS only a few pumps are available. Some of the pumps operating in this range are given in the chart below:

1	**Brand**	**Jet Edge**
	Item	IP36-80DS
	Media:	water
	Operation:	diesel-powered
	Type:	piston
	Flow rate:	6.8 l/min (1.8 us gal/min)
	Pressure:	2700 bar (39160.19 psi), 2500 bar (36259.43 psi)
	Other characteristics:	for water-jet cutting machines
	Available at:	http://www.directindustry.com/prod/jet-edge/product-11866-1734521.html
2	Brand	Sigma
	Item	Sigma/3 (Controltype)
	Media:	water
	Operation:	electric
	Type:	diaphragm
	Flow rate:	Min.: 182 l/h (48.08 us gal/h)
		Max.: 1040 l/h (274.74 us gal/h)
	Pressure:	Min.: 4 bar (58.02 psi)
		Max.: 12 bar (174.05 psi)

	Available at:	http://www.directindustry.com/prod/prominent-gmbh/product-6048-949723.html
3	Brand	Shurflo
	Item	52067
	Media	water
	Operation	electric
	Type	
	Flow	198 (GPH)
	Pressure	Max: 3.4bar (50 (psi)
	Available at:	http://www.northerntool.com/shop/tools/product_200249074_200249074
4	Brand:	Warman
	Item:	438181
	Media:	slurry
	Operation:	electric
	Type:	centrifugal
	Domain:	laboratory
	Other characteristics:	horizontal, replacement, transport
	Flow rate:	Min.: 0 m³/h (0 ft³/h)
		Max.: 10225 m³/h (361092.46 ft³/h)
	Pressure:	Min.: 0 bar (0 psi)
		Max.: 17.25bar (250.19 psi)
	Head:	Min.: 0 m (0' 0")
		Max.: 55 m (180' 5")
	Available at:	http://www.directindustry.com/prod/weir-minerals/product-23306-1804226.html#product-item_438181
5	Brand:	Warman
	Item:	708615
	Media:	slurry
	Type:	centrifugal
	Other characteristics:	horizontal, high-pressure
	Flow rate:	Min.: 0 m³/h (0 ft³/h)
		Max.: 9100 m³/h (321363.46 ft³/h)
	Pressure:	Min.: 0 bar (0 psi)
		Max.: 40 bar (580.15 psi)
	Head:	Min.: 0 m (0' 0")
		Max.: 67 m (219' 10")
	Available at:	http://www.directindustry.com/prod/weir-minerals/product-23306-1804226.html#product-item_708615
6	Brand:	GEHO® DHC
	Item:	438368
	Media:	Slurry
	Type:	Piston

	Other characteristics:	Handles up to 90% solids
	Flow rate:	
	Pressure:	Min.: 1000000 Pa (145.04 psi)
		Max.: 30000000 Pa (4351.13 psi)
	Head:	-
	Available at:	http://www.directindustry.com/prod/weir-minerals/product-23306-1804226.html#product-item_438368

1.5.2. Fan

One fan will be required in the recirculating flue gas line. For ENEL, many fans or compressors are available at 10bar. For ENEL the options are limited. However high-pressure compressors are still available. Some of the fans compatible with the systems include:

1	**SKU**	**B6000/500 FT7.5**
	Part Number	4116020249
	Capacity	20 CFM
	Drive	Belt Drive
	Motor	7.5 HP(5.5 kW)
	Pressure	15 bar(217 Psi)
	Receiver	500 Litres
	Voltage	400 Volts
		Three Phase
	Available at:	https://www.airsupplies.co.uk/abac-pro-15-bar-2-stage-high-pressure-air-compressors-15-bar-7-5-hp
2	SKU	B7000/500 FT10
	Part Number	4116020860
	Capacity	32.6 CFM
	Drive	Belt Drive
	Motor	10 HP(7.5 kW)
	Pressure	15 Bar (217 psi)
	Receiver	500 Liters
	Voltage	400 Volts
		Three Phase

	Available at:	https://www.airsupplies.co.uk/abac-pro-15-bar-2-stage-high-pressure-air-compressors-15-bar-10-hp
3	Type:	air
	Portability:	stationary
	Technology:	piston
	Lubrication:	lubricated
	Other characteristics:	high-pressure, two-stage, skid-mounted
	Applications:	industrial
	Pressure:	Min.: 35 bar (507.63 psi)
		Max.: 345 bar (5003.8 psi)
	Flow:	Min.: 211 l/min (55.74 US gal/min)
		Max.: 1471 l/min (388.6 US gal/min)
	Power:	Min.: 2.2 kW (2.95 hp)
		Max.: 15 kW (20.12 hp)
	Available at:	http://www.directindustry.com/prod/ingersoll-rand/product-5703-445705.html

1.5.3. *Heat Exchangers*

The main heat exchanger is called the heat recovery steam generator (HRSG). It can be designed as a series of heat exchangers, including an economizer, a boiler, and two superheaters. Besides this, the system requires three counter-current heat exchangers in the steam reheating section. These heat exchangers are required to be adaptable to both super and subcritical steam streams. An intercooler with a water-cooled circuit is also required when designing the entire circuit. This intercooler should be able to handle sub-critical steam. Some heat exchangers have been found of different configurations for different fuels using these criteria. Some of the heat exchangers commercially available are:

1	**Company**	**GE**	
	Type	Lignite fired boiler	
	Efficiency	High(44-45% LHV,42-45% HHV)	
	Available at	https://www.gepower.com/steam/products/boilers/tower.html	
		Hard Coal Fired Tower	Lignite Fired Tower
	Fuel	Bituminous	Lignite B

		Sub-bituminous	
		Lignite A	
	Steam Cycle	Ultra-Supercritical	Ultra-supercritical
		Supercritical	Supercritical
		Subcritical	Subcritical
	Size (MW_{th})	Subcritical ≤ 800	Subcritical ≤ 800
		USC/SC ≤ 1350	USC/SC ≤ 1350
	Superheater Outlet Steam Pressure (bar)	≤ 300	≤ 300
	Superheater Steam Temperature (°C)	≤ 605	≤ 605
	Reheater Steam Temperature (°C)	≤ 623	≤ 613
	Design Features	Tangential firing system	Tangential firing system
		Fuel and air staging	Fuel and air staging
		Tilting burners	Spiral wall designs
		Spiral wall designs	Expert firing system for lignite
2	Company	GE	
	Type	Furnace and convective passes, tilting tangential Firing System	
	Available at	https://www.gepower.com/steam/products/boilers/two-pass.html	
		Coal-fired Two Pass	Oil and Gas–fired Two Pass
	Fuel	Bituminous	Oil (Heavy Fuel Oil, No. 2 Oil, No. 6 Oil, Crude Oil etc.)
		Sub-bituminous	Gas (Natural Gas, Coke Oven Gas, Blast Furnace Gas etc.)
		Lignite A	
	Steam Cycle	Ultra-supercritical	Supercritical
		Supercritical	Subcritical

		Subcritical	
	Size (MW_{th})	Subcritical ≤ 800	Subcritical ≤ 800
		USC/SC ≤ 1,350	SC ≤ 1,000
	Superheater Outlet Steam Pressure (bar)	≤ 300	≤ 250
	Superheater Steam Temperature (°C)	≤ 605	≤ 565
	Reheater Steam Temperature (°C)	≤ 623	≤ 565
	Design Features	Tangential firing system	Tangential firing system
		Fuel and air staging	Fuel and air staging
		Tilting burners	Tilting burners
		Vertical and spiral wall designs	Spiral wall designs

3	Company	GE		
	Type	Circulating Fluidized Bed (CFB) Boiler		
	Available at	https://www.gepower.com/steam/products/boilers/tower.html		
		Duel-Grate Arrangement	**Three-Bay Arrangement**	**Advanced Supercritical CFB**
	Fuel	Entire range of fuels, including opportunity fuels such as petroleum coke, biomass, waste coal, oil shale, etc.		
	Steam Cycle	Subcritical	Subcritical	Ultra-Supercritical
				Supercritical
	Size (MW_{th})	350	100-350	660 for lignite B
				Higher for hard coal
	Superheater Outlet Steam Pressure (bar)	≤ 175	≤ 175	≤ 285
	Superheater Steam Temperature (°C)	≤ 565	≤ 565	≤ 605
	Reheater Steam Temperature (°C)	≤ 565	≤ 565	≤ 623
	Design Features	Four cyclones	Up to three cyclones inline	Modular concept

		Double grates	Single grate	Standardized modules
		External beds	In-furnace panels	Up to 8 cyclones
			Steam cooled cyclones	Steam cooled cyclones
				Double fluidizing grates
				External beds
				In-furnace box columns
				In-furnace U-shaped panels
		CFB/NID integrated technology		
		SNCR in-house injection grid		
		JIT limestone feed system		

For validation purposes, a case is selected from literature and then simulated using the newly developed model. After running the model for both layouts, the overall cycle thermal efficiencies have been calculated. The maximum efficiency for ENEL cycle is 34.2%, whereas the efficiency for the TIPS cycle is 33.9%. These values are not significantly different from those presented by Chen et al [1]. Post-combustion gas composition is also obtained from the simulation. From Table 5, 98% of the gases are comprised of those presented. The other percentages are attributable to SO_x and NO_x. A majority of these gases are expected to be removed by absorption in the carbon capture unit.

Table 5 Combustion Gases

	ENEL	**TIPS**
Components	**Mass Fraction**	
CO_2	0.57	0.57
H_2O	0.27	0.27
N_2	0.03	0.029
O_2	0.12	0.11
C	0.01	0.021

The authors studied three different oxygen and carbon dioxide mixture compositions [19]. Similar cases are studied during the cycle analysis. The coal composition and combustion temperature for the cycle analysis are also obtained from the study by Croiset et al. [19]. The mixture compositions and corresponding flame temperatures are provided in Table 6. For this type of

combustion, products are expected to contain almost 8% of ash. In this study, the mass of ash was neglected during the cycle analysis.

Table 6 Case study parameters based on [19]

Cases	O_2 (%) by volume	CO_2 (%)by volume	CO_2 Flowrate (kg/s)	Flame Temperature (°C)
Case 1	28%	72%	169	1400
Case 2	35%	65%	123	1495
Case 3	42%	58%	91	1650

Hu et al. [18] analyzed the combustion product composition for a similar coal burning. The oxy-coal combustion product composition for this study is initially obtained from Hu et al. [18] and evaluated for the cycle operating parameters.

1.6. Effect of Carbon Dioxide Recirculation on Thermal Efficiency

For the present report, three carbon dioxide recirculation percentages have been considered, including 72%, 65%, and 58% carbon dioxide in the flue gas. The three cases result in three different flame temperatures. For the ENEL cycle, the combustion temperature is 1421°C and with a total flow rate of 234.2 kg/s of which 214.5 kg/s is recycled from the flue gas. The thermal efficiency for this case is calculated to be 33%. For the second case, the combustion temperature is 1495°C, and the total mass flow rate is 187.8 kg/s, including 172 kg/s from the flue gas recirculation. The thermal efficiency for case 2 is 30%. Figure 14 presents a graph of the different efficiencies tested, and it is evident that at higher temperatures, the efficiency decreases. However, in these cases, the dominant factor is not temperature but rather the total mass flow rate of the flue gas, due to the higher mass flow rate and dependence on the convective properties of the flue gas in the heat exchanger the efficiency increases. From ASPEN, it is seen that for higher flowrates, the enthalpy of the flue gas stream is highest. For Case 3, although the temperature is highest, the mass flow and mass enthalpy are lowest which neutralizes the benefit of increased temperature. Table 7 shows the unit mass enthalpy and the total mass flow rate for three cases.

Table 7 Mass Enthalpy and Temperature Comparison for difference cases run

Cases	Mass Enthalpy (MJ/kg)	Mass flow rate (kg/s)	Temperature (°C)
Case-1	7.394	214.54	1421
Case-2	7.28	172.04	1495
Case-3	7.0742	142.69	1600

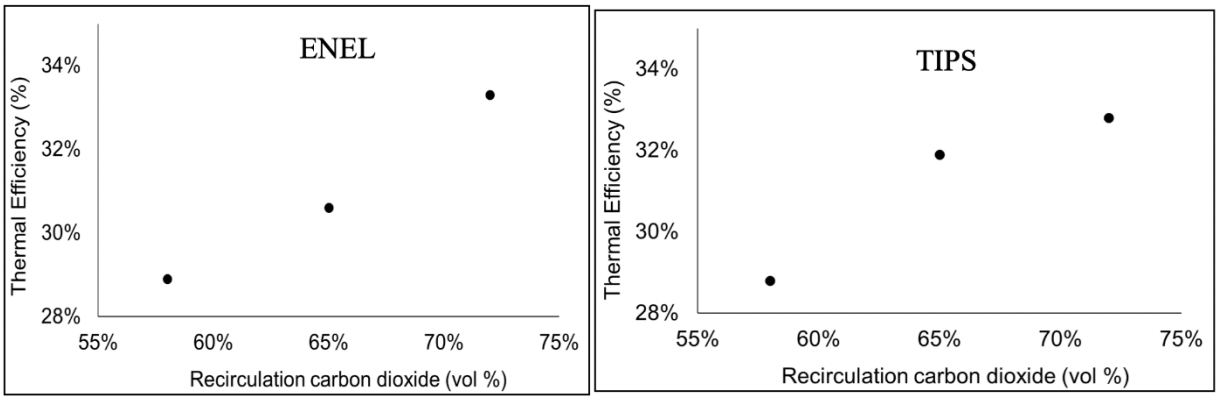

Figure 14 Thermal efficiency versus CO2 diluent composition from the recirculation

The heat transfer behavior between the flue gas was also investigated. From the analysis, It is seen that the temperature of the flue gas increases; however, the mass flow rate decreases. From Figure 15, it can also be seen that both cycles exhibit similar efficiency ranges at the 10-bar pressure for ENEL and an 80bar pressure for TIPS, this was also observed by a cycle analysis study performed by Chen et al. [1].

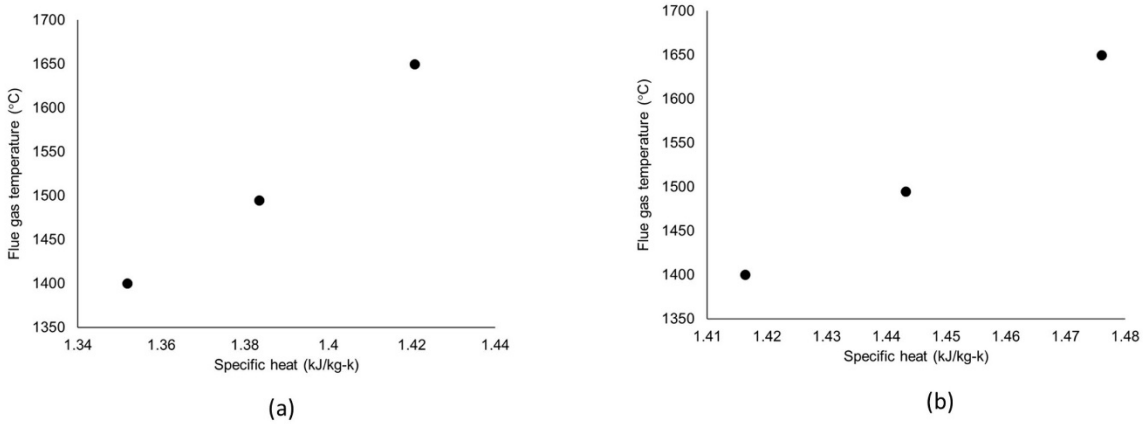

Figure 15 Specific heat at different flue gas temperature (a) ENEL (b) TIPS

The flue gas recirculation percentage affects the combustor temperature and thermal efficiency. The thermal efficiency for the different recirculation ratios is presented in Fig. 16 for both cycles. Different recirculation ratios result in different flame temperature. In Table 8, some important results are presented for three different cases picked from all the recirculation ratios. For ENEL, the combustion temperature for Case 1 is 2307 °C with an amount of 28 kg/s recycled flue gas. The thermal efficiency for this case is calculated to be 35.18%. For the second case, the combustion temperature is calculated to be 1746°C, and the total mass flow rate is 84 kg/s of flue gas recirculation. The thermal efficiency of Case 2 is 35.88%. For Case 3 an efficiency of 35.98% is calculated with a corresponding 251 kg/s of recycled flue gas. Fig 5 presents a graph of the different efficiencies tested, and it is evident that at higher temperatures, the efficiency decreases.

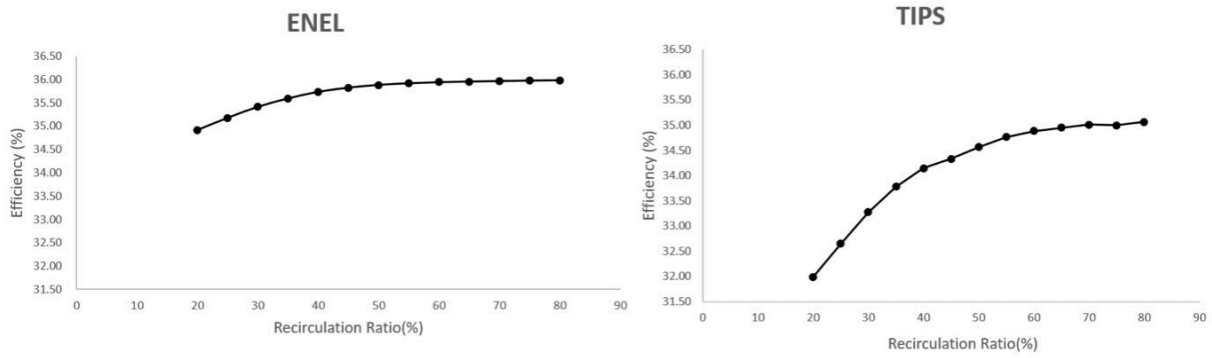

Figure 16 Thermal efficiency plotted against flue gas recirculation

Table 8 Cases for flue gas recirculation

Case Number	Flue Gas Recirculation Ratio (%)	FGR Mass Flow Rate (kg/s)	Combustion Temperature (°C)		Volume Flow Rate (L/s)		Flue Gas Enthalpy (kJ/kg)	
			ENEL	TIPS	ENEL	TIPS	ENEL	TIPS
1	25	28	2307	2494	83478	11226	4728	4475
2	50	84	1746	2059	96890	14046	5896	5469
3	75	251	1049	1538	118659	21872	7071	6448

Thus, it can be said that surprisingly that in these cases, the dominant factor is not temperature but instead the total mass flow rate of the flue gas. Due to the higher mass flow rate and convective properties of the flue gas in the heat exchanger, the efficiency increases. From ASPEN PLUS® it is seen that for higher flowrates, the enthalpy of the flue gas stream is highest. For Case 3, although the recirculation ratio is the highest, the efficiency increased by only 0.2%, whereas, for Case 2 the thermal efficiency increases by 2%. The small increase of efficiency of the cycle for Case 3 is due to the flue gas amount exceeding the optimal quantity, which exceeds the amount that allows for the heat that can be recovered from the system. This is also compounded by the fact that the recirculation flow has to be cooled before transferring to the CCU. This cool flue gas when it enters the combustor in large amounts, and the effects of the lower combustion temperature are evident. It is evident from Table 2 that for the same recirculation ratio ENEL has lower combustion temperature than TIPS. The reason for that is to be believed in the lower pressure environment of ENEL comparing to TIPS. As ENEL runs at a lower pressure, the water vapor present in the ENEL cycle can absorb more heat from the combustion than the water vapor present in the high-pressure TIPS cycle. It results in a lower temperature for the combustion and a higher volume flow rate for ENEL. This high-volume flow rate enables the flue gas of ENEL to have higher enthalpy, which ultimately results in higher efficiency for ENEL.

For TIPS an identical trend is seen. Recirculation rates of 25%, 50% and 75% flue gas in the TIPS cycle yields 33%, 34%, and 34.32% efficiencies. For the cases tested, efficiencies are lower than for ENEL and 50% recirculation should be used for best performance.

1.7. Energy Budget for the ENEL and TIPS Cycles

The detailed study of the power consumption of the different components for a 50% recirculation rate of carbon dioxide can be seen in Fig. 17 and are also summarized in Table 9.

For a rate of 50% of recirculating flue gas, ENEL produces a gross power out of 122 MW while the TIPS cycle produces 115 MW. For both cycles, 15% of the energy is consumed by the ASU. The ENEL cycle utilizes 30.5%, while the TIPS cycle uses 33.6% of the total input power to separate the carbon dioxide in the carbon capture unit. The CCU has been designed so that 4% of the CO2 entering the CCU is captured with an input power of 32.9 MW. The performance of the CCU can be enhanced at the cost of depleting the net energy and could be optimized in another study. The net power produced for the ENEL cycle is 36%, while for TIPS, it is 34%. The difference in the energy scenarios is due to the difference in the operating pressure and the basic layout of the system.

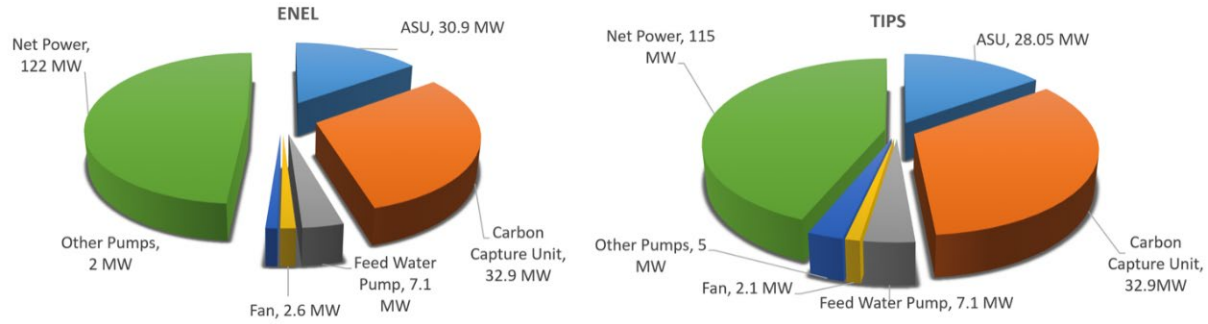

Figure 17 Energy budget for the ENEL and TIPS cycles

Table 9 Energy budget of both ENEL and TIPS cycles

	ENEL	TIPS
Thermal Energy input(MW)		
HHV	550	550
LHV	523	523
Gross power Output(MW)	197.5	187.4
Net Power Output(MW)	122	132.5
Gross efficiency (%)		
HHV	36	34

LHV	38	35.8
Net efficiency (%)		
HHV	22.2	24.9
LHV	23	26.1
Fuel Demand (kg/s)	18.87	18.87
Water demand(kg/s)	3	3
Recirculation ratio	50	50

For the two cycles, the net efficiency differs by 4%. However, both systems are not optimized in this study, and most parameters are kept constant for both cases. With this in mind, the results obtained show that ENEL performs better this energy input.

1.8. Convergence Parameters used in ASPEN PLUS Model

ASPEN PLUS® facilitates the evaluation of the power produced and predicts the probable products. Error tolerance of 0.0003 and a maximum of 30 iterations are used for convergence for this study. Besides this, the convergence of each block depends on whether the total mass flow rate or energy, in and out, is conserved. The pressure and temperature properties are used as the inlet parameters to ASPEN PLUS. These properties are listed in Tables 10 and 11.

Table 10 Combustor inlet parameters

Parameters	**TIPS**	**ENEL**
Coal-Slurry mass flow rate (kg/s)	35.02	35.02
Coal-Slurry temperature (°C)	132	132
Oxygen mass flow rate (kg/s)	50	50
Oxygen temperature(°C)	200	200
Nitrogen mass flow rate (kg/s)	6.3	6.3
Feed water for steam cycle (kg/s)	130	130
Feed water temperature(°C)	31	31
Pressure range (bar)	1-12	10-80
Recirculation gas ratio (%)	20-75	20-75

Table 11 Case conditions

	Recirculation Ratio (%)	Pressure (bar)	
		ENEL	TIPS
Case-1	20	1	10
Case-2	35	3	20
Case-3	50	5	50
Case-4	65	10	70
Case-5	75	12	80

The primary focus of the study presented in this report is to change the recirculation ratio and investigate its effect on combustion. The efficiency of the pressurized oxy-coal power cycle was defined as:

$$\eta_{th} = \frac{\sum W_T}{\sum Q_{Th}} \tag{14}$$

$\sum W_T$ is the sum of the power generated by the turbines from the steam cycle and $\sum Q_{Th}$ is the thermal power input into the combustor. Although the feedwater pumps were modeled using ASPEN, they were not included in the efficiency calculations.

The minimum internal temperature approach (MITA) constraint between the cold and hot stream was maintained for the heat exchangers since the approach temperature will stay the same for a particular heat exchanger with the change of inlet process and service fluid temperature. Also, the mechanical and thermal efficiencies for the turbomachinery were kept the same for comparison purposes. Feedwater and bleeds from the turbines were mixed to maintain a saturated liquid stream at the pump inlet to make sure no vapor enters the pumps. Different parameters used for different components are presented in Table 12.

Table 12 Block constraints used in the current model

Component	Constraints	TIPS	ENEL
Heat Recovery Section	MITA-HRSG	150°C	30°C
High-Pressure Turbine	Isentropic Efficiency	90%	90%
	Inlet Pressure	285 bar	250 bar
Intermediate Pressure Turbine	Isentropic Efficiency	93%	90%
	Inlet Pressure	60 bar	70 bar
Low-Pressure Turbine	Isentropic Efficiency	89%	90%
	Inlet Pressure	5.5 bar	21 bar
Pumps	Inlet Stream	Saturated Liquid	Saturated Liquid

Both ENEL and TIPS power cycle models are run for 5 recirculation ratios from 20% to 75% to find out which cycle and what condition produced the highest efficiency. The main purpose of recirculating gases into the combustion chamber is to control combustion temperature. It was seen from the results that both with the increase of pressure and recirculation ratio, the efficiency increases. The highest efficiency achieved for ENEL and TIPS is comparable. However, ENEL achieves the same efficiency at a pressure of 10 bar compared to 80 for the TIPS cycle.

1.9. Combined Effects of Pressures and Recirculation Ratios on Thermal Efficiency

In Figure 18, the change of combustion temperature for ENEL with different recirculation ratios and pressure is presented. Figure 19 presents the change in the combustion temperature of the TIPS cycle at different recirculation ratios and pressures. From Figure 19, it can be seen that with the increase of recirculation gas (RG) amount in the combustor chamber, the combustion temperature decreases for both TIPS and ENEL. Since the recirculation gas extraction point is after the heat exchangers, it has a significantly lower amount of temperature than the product gas. Thus, the increasing mass of this low-temperature gas entering the combustion chamber decreases the combustion temperature.

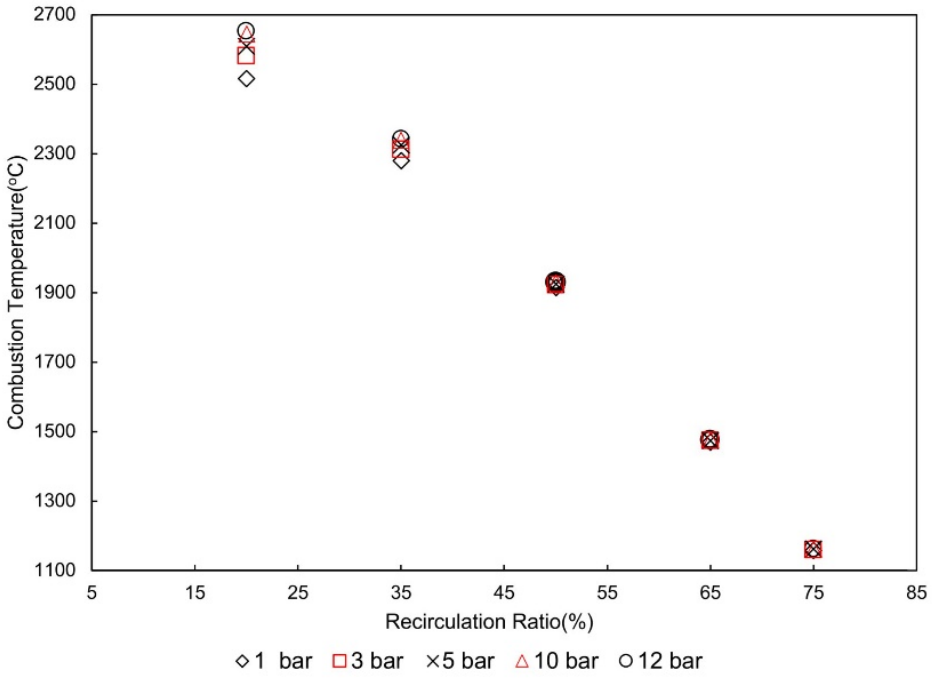

Figure 18 Combustion temperature for the ENEL cycle at different recirculation ratios

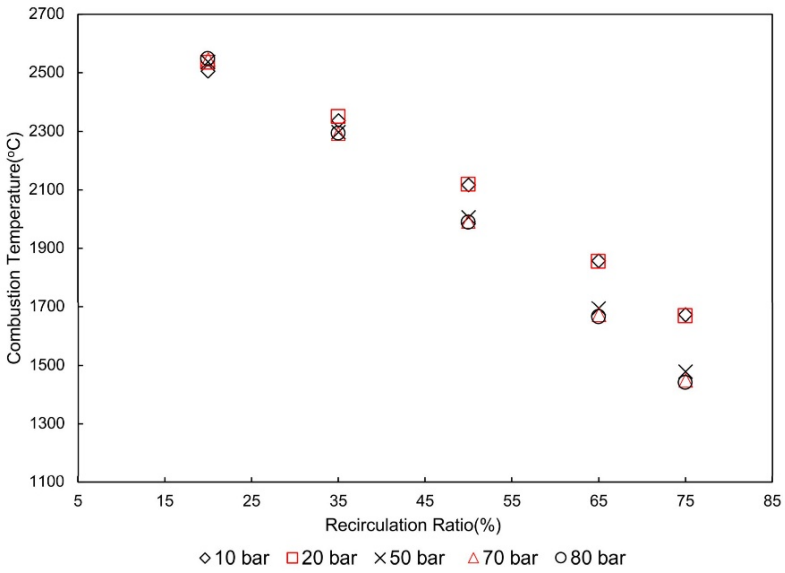

Figure 19 Combustion temperature for the TIPS cycle at different recirculation ratios

Figure 20 and Figure 21 show the change of efficiency with the change of recirculation ratio consecutively for ENEL and TIPS. From these figures, it can be seen that although the product gas temperature decreases with increased recirculation ratio, the efficiency of the whole cycle increases. A lower temperature in the product gas is associated with lower temperature differences in the heat exchangers. This high recirculation ratio will increase the total mass of carbon dioxide and decrease the mass of oxygen in the product gas, which results in lower heat capacity. However, increasing the recirculation ratio increases total mass in the product gas, which plays an important role in the total heat transfer in the heat exchanger. Since convection heat transfer is a function of temperature difference, heat capacity, and mass flow rate, all have an impact on the total heat transfer between the product gas and steam for power generation. In this case, the effect of mass flow surpasses the effect of the temperature difference and heat capacity causing high heat transfer with the high mass flow.

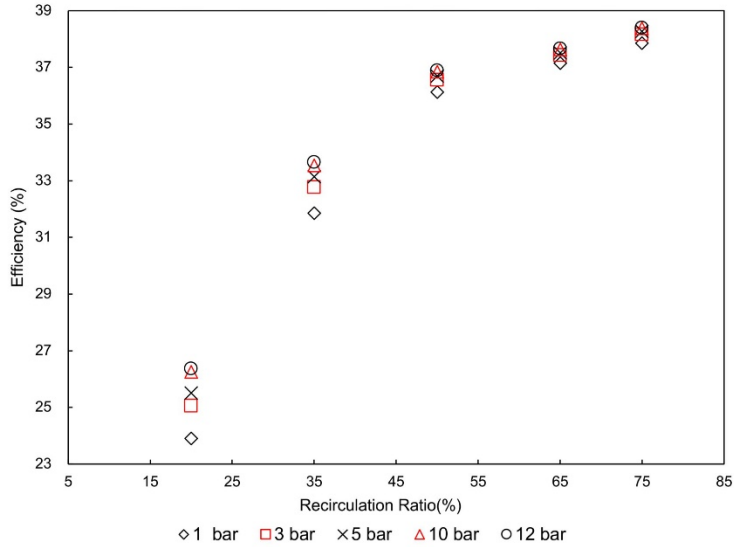

Figure 20 Efficiency for the ENEL cycle at different recirculation ratios.

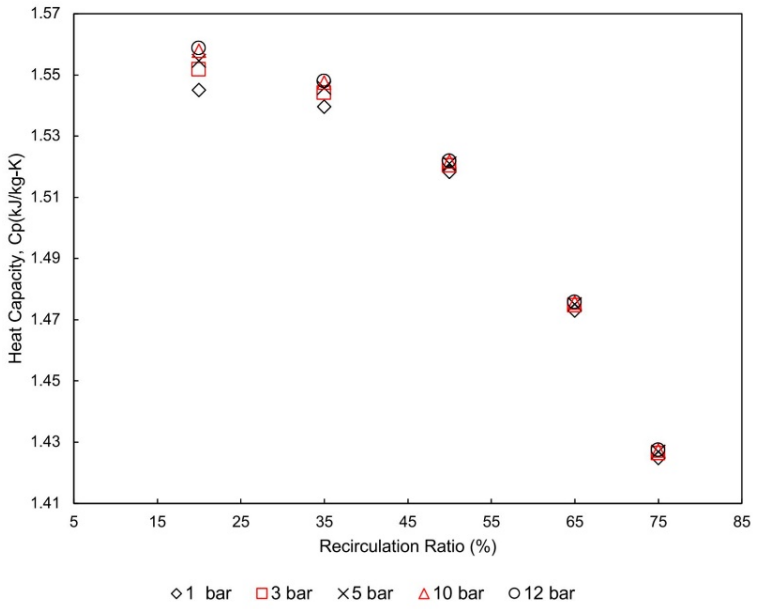

Figure 21 Heat capacity of the combustor exit products for the ENEL cycle at different recirculation ratios

Figure 21 and Figure 23 depict the change of heat capacity of the stream exiting the combustor at different recirculation ratios. It can be seen from these figures that with increased recirculation ratio, heat capacity for the exhaust for both ENEL and TIPS goes down. It can be seen for both the cycles that as the recirculation ratio increases, the mass flow rate coming out of the combustor increases, the same trend as the efficiency change with the recirculation ratio.

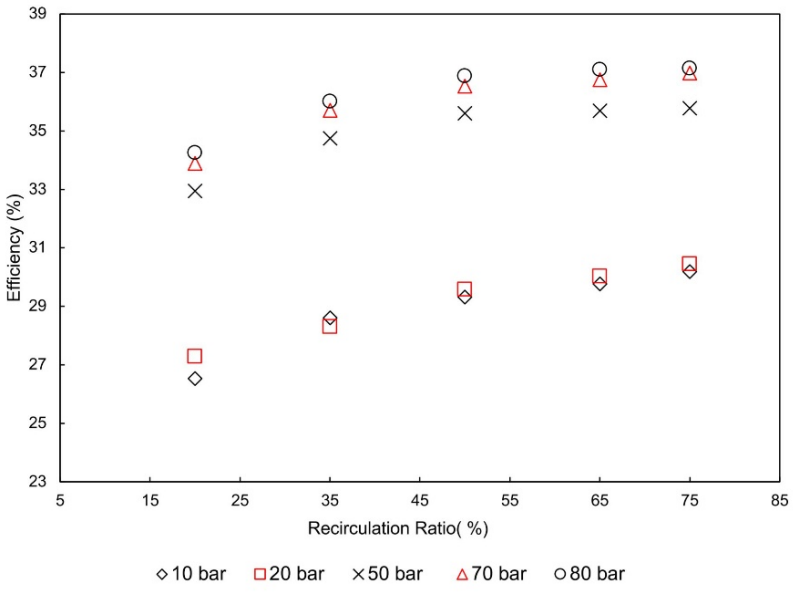

Figure 22 Efficiency for the TIPS cycle at different recirculation ratios

From Figure 9, it can be seen that for the TIPS cycle, the exhaust exiting the combustor goes into the heat exchanger with an unchanged mass flow rate. For increasing the recirculation ratio, the

total mass flow rate of hot gas passing through the heat exchanger increases. On the other hand, from Figure 8, it can be seen that the ENEL cycle splits the recirculation gases twice. Product gas first splits into a stream to the carbon capture unit and a recirculation stream. However, although the total mass flow rate is the same for all the cases, with increasing recirculation ratio, the mass flow rate of the hot exhaust stream coming out of the combustor increases and the mass flow rate of the comparatively cold stream decreases. Hence, it can be concluded that the mass flow rate of the exhaust gas of the combustor is the dominant factor in these cases for producing higher efficiencies. For the same pressure, ENEL has higher efficiency with the increase of recirculation gas compared to the TIPS cycle.

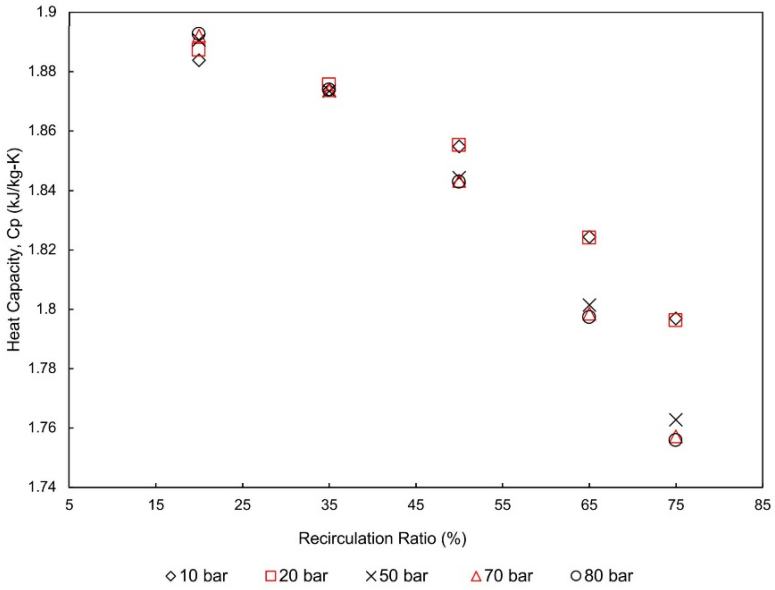

Figure 23 Heat capacity for the TIPS cycle at different recirculation ratios

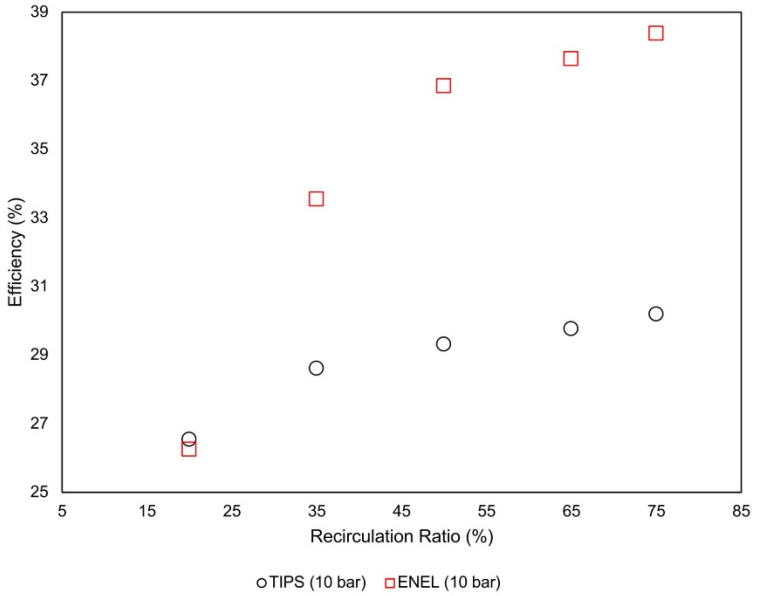

Figure 24 Efficiency for the ENEL and TIPS cycles at 10 bar and different recirculation ratios

Figure 24 presents the efficiencies for both ENEL and TIPS cycles with different recirculation ratios at 10 bar. The difference between the two cycles can be explained by the exhaust mass flow difference from the combustor between TIPS and ENEL. For example, at a 50% recirculation ratio, the efficiency for the ENEL cycle is 36.85%, and the efficiency for the TIPS cycle is 29.31%. The ENEL and TIPS combustor temperatures are 1929°C and 2117°C, respectively. Despite the high temperature of the TIPS cycle, ENEL has higher mass flow coming out of the combustor resulting in higher efficiency. At a 50% recirculation ratio, ENEL uses 191.7 kg/s of exhaust gas, and TIPS uses 167 kg/s as recycled flue gas. The mass flow rate results in increased heat transfer, which eventually leads to higher efficiency for ENEL. Figure 24 shows that with increasing recirculation ratio, the mass difference for the exhaust stream between TIPS and ENEL increases with efficiency.

2. Chapter 2: System Design and Analysis

With the requirements synthesized from the system configuration analysis, the design of the 1 MW_{th} pressurized combustor was completed. This chapter describes the design and analysis of a High-Pressure Swirl Oxy-Coal Combustor, and it's components. In addition, the design of the pilot burner facility is included in this chapter. The fuel oxidizer delivery system and control and data acquisition systems for the combustor is also discussed. Although all combuster operating conditions are presented in the report are in Metric unit the combustor dimensions are kept in English units to ensure maximum compatibility with the U.S. based manufacturers and component suppliers.

2.1. High-Pressure Swirl Oxy-Coal Combustor Design

The design of the high-pressure swirl oxy-coal combustor was divided into three major parts.

i. Powerhead
ii. Combustor body
iii. Exhaust

The powerhead houses the igniters, the pilot burners, and the pintle injector. The combustor body houses all the analyzing components such as flame scanners, heat flux sensors, thermocouples, etc. The exhaust system collects ashes and cools the exhaust gases before directing to the environment.

2.1.1. Powerhead Design

The powerhead houses a pintle injector, two secondary burners, and two igniters. The secondary burner and the igniter are tested in the High-Pressure Combustion system. The powerhead is designed as a tapered cap that will hold the burners at a 45° angle, and this position would minimize the collision of the flame tips of the secondary burners.

The material of the powerhead is stainless steel 410 with a thickness of 3.5 in. These parameters are to be kept the same for the combustor body to avoid thermal mismatch. The outer and inner diameter of the powerhead is 18 in and 11 in respectively. The component that supports the injector, ignites, and burners were designed with a conical shape with a 45-degree slope. This provides enough real estate to support the components and provides an optimal configuration for the ignition of the burners and the pintle injector.

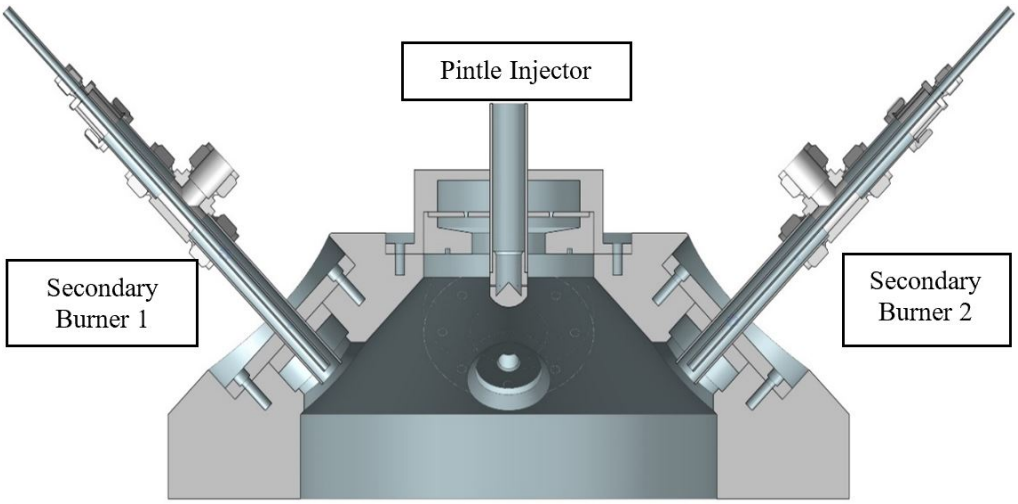

Figure 25: Cross-section of Powerhead through secondary burners

The pintle injector will be positioned on the top of the truncated cone on the face with the smallest diameter. The four other components will be along the sides of the powerhead. Each of these will fit into orifices having 2 in diameter orifices. These orifices can be replaced with a blind cover; which will allow for the system to be interchangeable in need to change firing inputs or replace hardware. Figure 25 and Figure 26 show the cross-sectional view of the powerhead through the secondary burners and through the igniters, respectively.

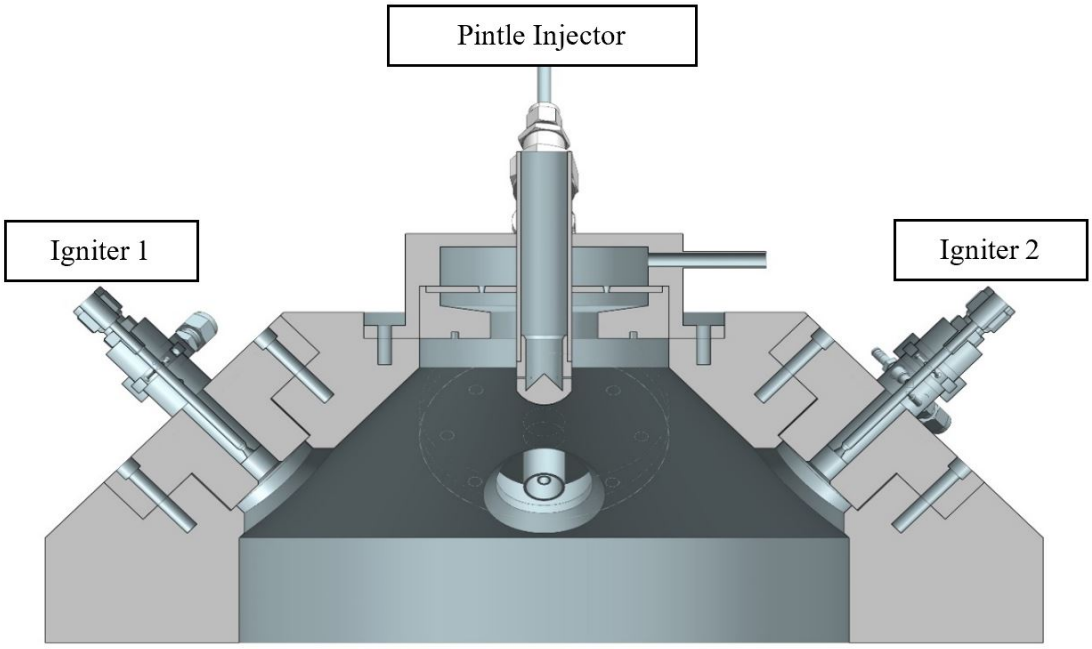

Figure 26 Cross-section of Powerhead through igniters

Figure 27 Procured Powerhead

2.1.1.1. Igniter Design

The secondary burner is ignited using an igniter. The igniter inlets are situated at two opposite sides of the powerhead. The igniter design is opted from [20]. The igniter is designed to operate using oxygen and methane. The ignition system uses an internal swirl injection where the mixing of the working fluids is directed by the momentum of interacting streams. The oxidizer flows through an axial inlet and is interfaced with four tangential fuel inlets that create a swirl that mixes the gases prior to ignition. The oxygen gas is injected through the center of the igniter, whereas the methane gas mixes vertically. The inlet connections for the fuel and oxidizer inlets are 1/4-inches and 3/8-inches tubing, respectively. The inlet pressures of the fuel and oxidizer have been tested from 8 to 13 bar inlet pressures. The unit is fitted with D Series Cryogen Solenoid valves connected with 1/4-inch tubing. These valves have a maximum operating pressure of 25 bar. The igniter is designed to be installed onto a 0.532-inch diameter hole so that the flame exit is flush with the combustion device inner wall. A circular boss is fabricated with a matching thickness to install the 1.5-inches long tube of the igniter into the combustion device. It is necessary to close the igniter inlet valves when the combustor chamber pressure exceeds the inlet pressure to the igniter valve to prevent backflow into the igniter. The igniter operational burn time is 3 to 5s. The operating conditions for the igniter can be found in Table 13. The igniter can be seen in Fig. 28.

Table 13 Igniter Operating Conditions

Inlet Igniter Port Pressures (bar)	8 – 13
Combustion Chamber Pressure (bar)	5- 10
Mixture Ratio	1-3
Maximum burn time (seconds)	5
Igniter Body Temperature (K)	150 - 800

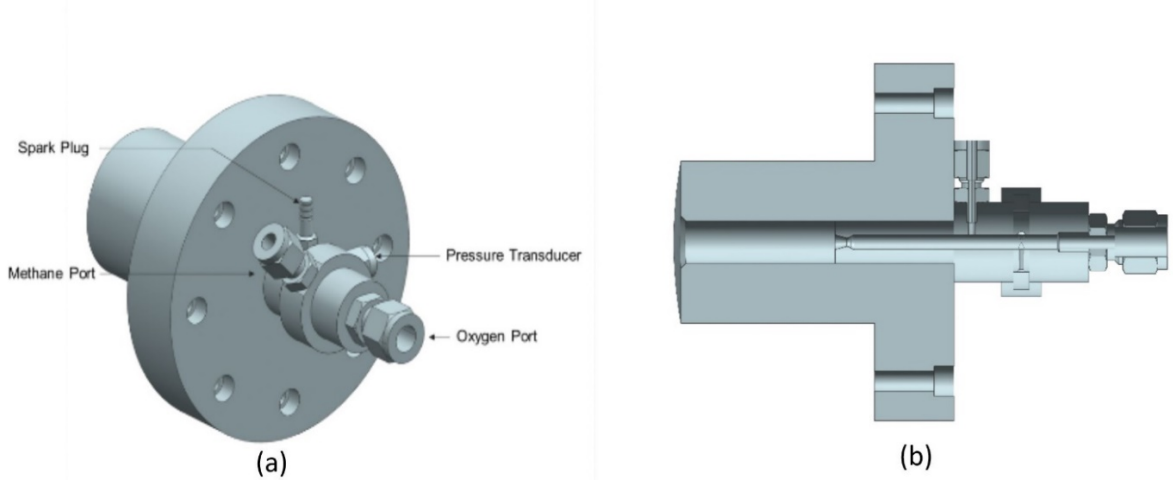

Figure 28 (a) Igniter manifold (b) cross-section view of the igniter manifold

A standard 1/4-32 spark plug (PART #: EVOG10350) serves as the ignition source for the torch igniter, Figure 29. The ignition source is a standard 1/4–32 spark plug connected to a 12 W power source with a signal generation of 150 Hz. The produced excitation voltage is 12 kV.

Figure 29 Spark plug (Model: EVOG10350, ¼ 32)

2.1.1.2. Secondary Burner Design

A shear co-axial injector is designed to operate at a firing input of up to 200 kW and 20 bar pressures. Methane is used as the fuel along with pure oxygen as the oxidizer. The oxygen port is designed in such a way that carbon dioxide can be added as a diluent if required. The mass flowrate for the methane and oxygen is calculated from the power input using Eqs (15) and (16) at stoichiometric conditions. The lower heating value (LHV) characterizes the heat of combustion of the fuel. The lower heating value of methane is 50,000 kJ/kg. At stoichiometric conditions the $^{O}/_{F}$ ratio is 4.

$$\dot{m}_{\text{methane}} = \frac{\text{Firing Input}}{\text{LHV}} \tag{15}$$

$$\dot{m}_{oxygen} = \dot{m}_{\text{methane}} \times \left(^{O}/_{F}\right)_{st} \tag{16}$$

When designing the shear-coaxial injector, two non-dimensional parameters, including velocity ratio (VR) and momentum flux ratio (J) are thoroughly observed. The formula for velocity ratio and momentum flux ratio is shown Eqs (17) and (18)[1]

$$VR = \frac{v_{methane}}{v_{oxygen}} \tag{17}$$

$$J = \frac{(\rho . v^2)_{methane}}{(\rho . v^2)_{oxygen}} \tag{18}$$

For this particular case, the burner and velocity ratios are varied between 4.85 to 7 momentum flux ratios are varied between 12 to 20. Lux et al. use similar ranges of velocity ratios and momentum flux ratios to design high-pressure liquid oxygen/methane coaxial injector [21]. The image of the burner can be seen in Fig. 30. The design conditions for the burner can be found in Table 14.

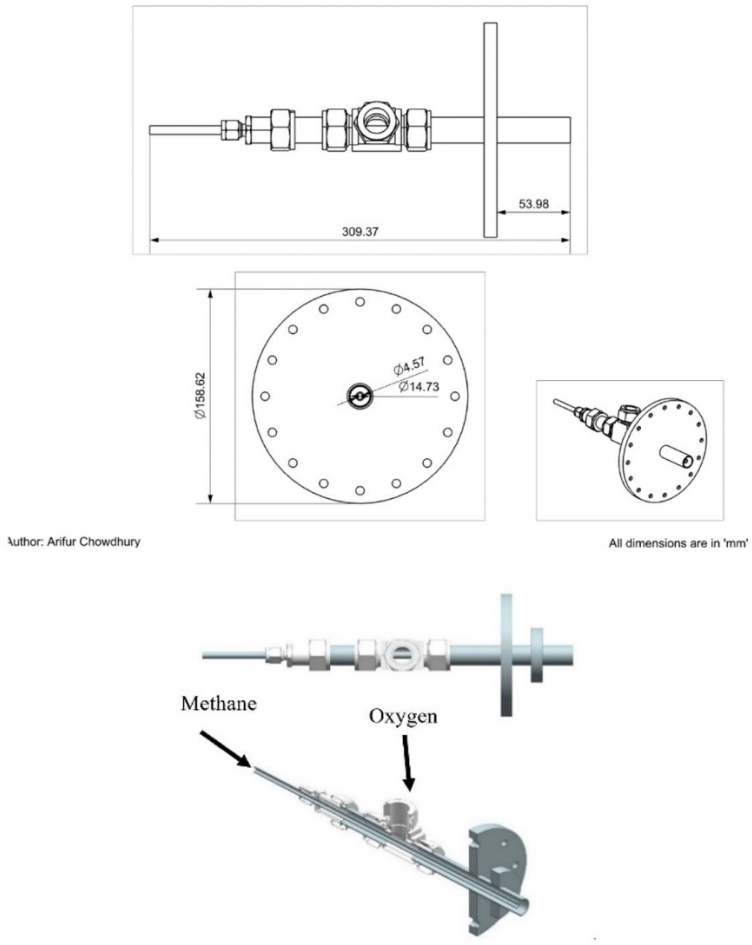

Figure 30 Secondary burner

The methane-oxygen shear-coaxial burner is designed to operate up to 200 kW power input and 20 bar pressure. The shear-coaxial injector utilizes the shear forces between the fuel and oxidizer to mix[21]. The shear forces are driven by the momentum flux difference between two streams. The burner is designed in such a way that it can be operated at different firing inputs up to 200 kW. The operating conditions for the burner can be found in Table 15.

Table 14 Secondary Burner Design Conditions

Power Input (kW)	200
Operating Pressure (bar)	20
Operating Temperature (K)	1500
Momentum flux ratio	12-20

Table 15 Burner Operating Condition

Secondary Burner	
Power Input (kW)	50 - 200
CH_4 mass flowrate (kg/s)	0.004
O_2 mass flowrate (kg/s)	0.016
CH_4 velocity (m/s)	18.20
O_2 velocity (m/s)	3.75
Momentum flux ratio	≈12

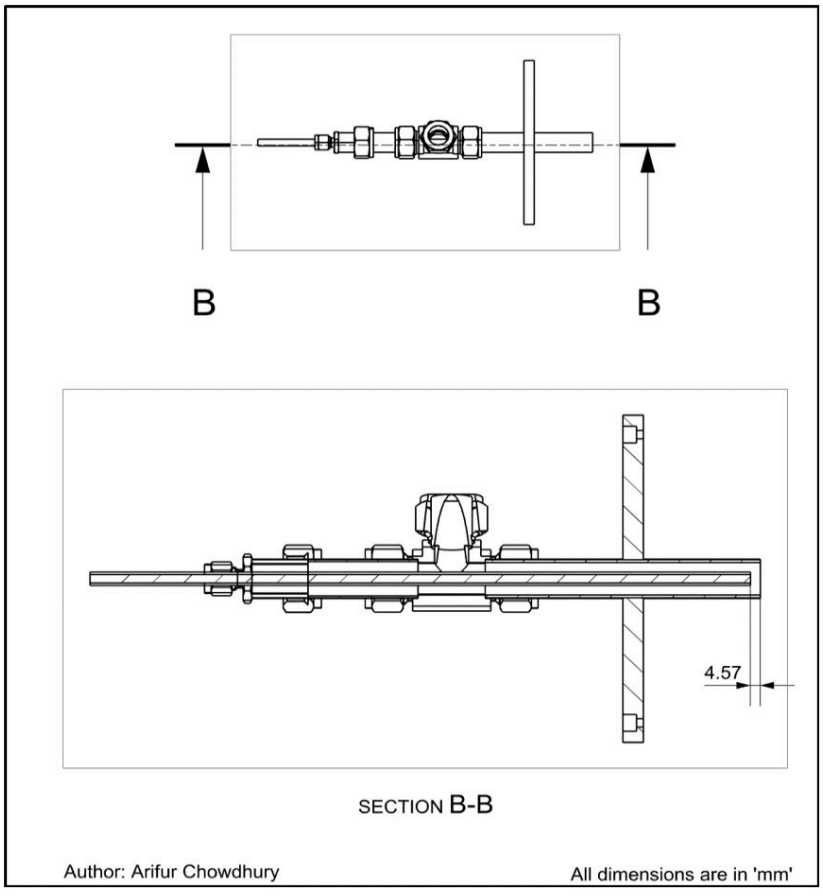

Figure 31 Main burner methane port recess length

It is found from the literature that recessing the high-velocity jet port with respect to the injection plane may enhance the combustion performance [21]. Kendrick et al. found that a recess of 1di

(where 'di' represents high-velocity jet diameter) in LOx/H2 combustion increases the flame expansion rate and width of the flame volume [22]. Tripathi et al investigated that the increment of momentum flux ratio or recess length enhances the jet breakup [23]. The authors also have found that the effect of recess length is higher when the momentum flux ratio is small. However, it is demonstrated that increasing the recess length above 1.5di does not further improve the combustion performance [23]. Although Wheeler and Kirby have found that a recess length close to 1.3di in LOx/CH4 combustion still demonstrates a further enhancement in terms of combustion efficiency [24]. For the proposed injector, the recess length of 1di is used, Fig. 31.

2.1.1.3. Pintle Injector Design

The basic configuration of a bipropellant pintle injector is shown in Figure 32. One propellant is fed through outer injector flow passages into a circumferential annulus and exits the injector as an axially flowing annular sheet that arrives at the impingement point with a uniform velocity profile. The other propellant enters the injector body via a separate centrally located passage and flows axially through a central pintle sleeve toward the injector, where it is turned to uniform radial flow by the pintle tip's internal contoured surface. On the manufacturing side, the simplicity of the pintle design makes it preferable when compared with injectors of other configurations. It can be designed to integrate the possibility for quick changes on the critical injection elements while keeping the main body unaffected. However, special efforts are still needed to guarantee the metering orifices dimensions accuracy or the correct size of the annular gap controlling the axial flow.

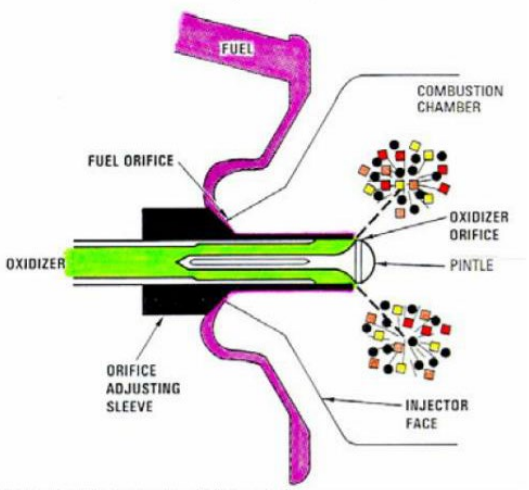

Dressler, G. A., "Summary of Deep Throttling Rocket Engines with Emphasis on Apollo LMDE," AIAA Paper 2006-5220

Figure 32 Sketch of Pintle Injector

For design purposes, the coal is used in a slurry with water in a $75{:}25\%$ by mass ratio, respectively. The maximum powder size is $200\ \mu m$. Since the slurry consists of solid particles suspended in a liquid, the properties of the slurry mixture depend on the constituents. The density of the slurry ρ_{sl} can be calculated from Eq. (19):

$$\rho_{sl} = \frac{100}{\left(\frac{C_w}{\rho_{co}}\right) + \left(\frac{1 - C_w}{\rho_w}\right)} \tag{19}$$

Where the c_w is the percentage of solids concentration by weight, and ρ_{co} and ρ_w are the density of coal and water, respectively. The oxygen properties were taken at 11 bar pressure, expected injection pressure, and room temperature $25\ C^0$.

The momentum ratio is an important parameter to achieve a specific spray angle where the mixture or the jet does not impinge on the combustor wall. Based on the firing input and lower heating value of coal, the mass flowrate could be calculated, Eq. (20). The oxygen flow rate is calculated from the assumed O/F ratio and methane flowrate in Eq. (21).

$$\dot{m} = \frac{Firing\ Input}{LHV} \tag{20}$$

$$\dot{m}_o = \dot{m} \left(\frac{O}{F}\right)_{st} \tag{21}$$

The coal slurry mass flow rate is calculated using Eq. (22).

$$\dot{m}_{sl} = \frac{100 * \dot{m}}{C_w} \tag{22}$$

After defining the properties and mass flowrates for the oxygen and slurry, the dimensions of the pintle are calculated. The total area of the slurry ports is calculated using Eq (23).

$$A_{sl} = N\frac{\pi}{4} D_o^2 \tag{23}$$

From the area and the mass flow rate, the velocity of the slurry is calculated, Eq (24).

$$v_{sl} = \frac{\dot{m}_{sl}}{A_{sl}\,\rho_{sl}} \tag{24}$$

The total momentum ratio (TMR) between the oxygen and the slurry is estimated using Eq. (25).

$$TMR = \tan\alpha \tag{25}$$

Where α is the angle formed from the centerline to the edge of the slurry spray, also known as the spray cone angle. From the total momentum ratio, the mass flowrates of oxygen and slurry, and slurry velocity, the oxygen velocity can be calculated, Eq (26).

$$v_o = \frac{TMR\ \dot{m}_{sl}\ v_{sl}}{\dot{m}_o} \tag{26}$$

After the velocity is calculated, the area for the oxygen port is determined from the mass flowrate velocity and density of oxygen.

$$A_o = \frac{\dot{m}_o}{v_o \rho_o} \tag{2}$$

Then the outer diameter of the annulus is calculated from the required area of oxygen, inner diameter and wall thickness of the pintle. The diameter of the pintle (D_p) is estimated assumed to be 1 inch standard tubing, t is the wall thickness of the tube and D_a is the outer diameter of the annulus.

$$D_a = \sqrt{\frac{4A_O}{\pi} + (D_p + 2t)^2} \tag{28}$$

By subtracting the outer diameter of the pintle from the outer diameter of the annulus, the oxygen gap size is determined.

$$Gap = \frac{D_a - (D_p + 2t)}{2} \tag{29}$$

The total power input for the oxy-coal combustor is $1.05\ MW$ which is divided into 2 natural gas, and 1 coal slurry burners. Each slurry injector is designed for a power rating of $750\ kW$. Also, the operating pressure for the project is $10\ bar$.

Table 16 Pintle injector design parameters

Name	Value	Unit
Firing input for each slurry burner	250	kW
Lower Heating Value of Coal	27.5	MJ/kg
O/F ratio by mass	2.56	-

Table 17 Pintle Injector propellent parameters at 11 bar pressure

Propellent Properties			Propellent Mass flow rate		
Name	**Value**	**Unit**	**Name**	**Value**	**Unit**
Density of oxygen	14.3	kg/m^3	**Coal mass flowrate**	0.027	kg/s
Density of Coal	1500	kg/m^3	**Oxygen mass flowrate**	0.070	kg/s
Density of Water	998.6	kg/m^3	**Slurry mass flowrate**	0.068	kg/s
Density of Slurry	1200	kg/m^3	**Total mass flowrate**	0.0354	kg/s

From Eqs (22)-(29) the variation of orifice diameter on the pintle post (D_p) for the coal slurry causes a change in the dimensions of the annulus or gap. These two-length scale dimensions have a direct effect on the velocity expected in the combustor and, therefore on the total momentum ratio resulting in variation of the spray angle. Figure 33 shows the velocity and the relationship to the oxygen gap. Increasing the ratio between the two parameters results in decreasing in the velocity for the slurry and oxygen.

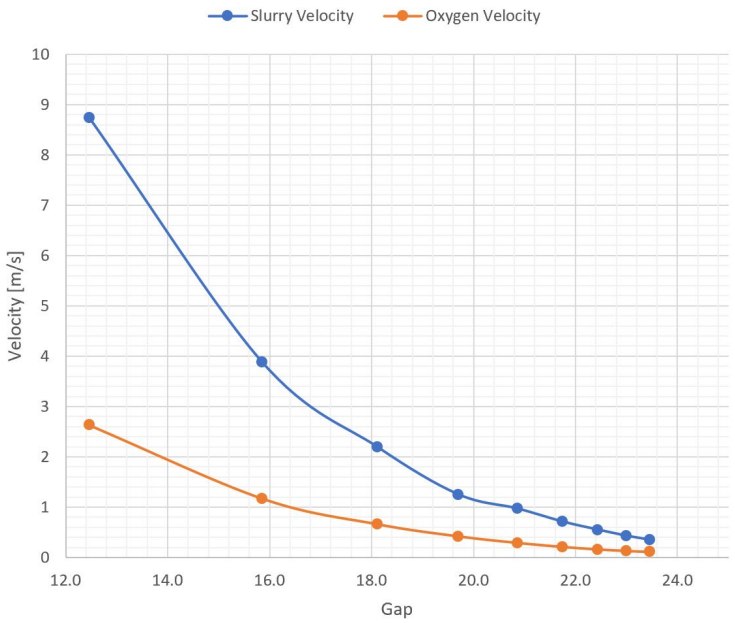

Figure 33 Plot of Gap size with velocity from ports

The Gap size is chosen to be 15.9mm, resulting in slurry velocity of $3.88\ \mathrm{m/s}$ and oxygen velocity of $1.17\ \mathrm{m/s}$ considering the manufacturability and velocity. By fixing the $\mathrm{D_p}$ and varying the Gap, the spray angle can be manipulated to achieve minimal contact between spray with the combustor walls. In Figure 34 the relationship between the spray angle and Gap is presented. The larger angle corresponds to a smaller Gap size. To minimize contact of the spray with the combustor wall, a spray angle of $30^0$is selected.

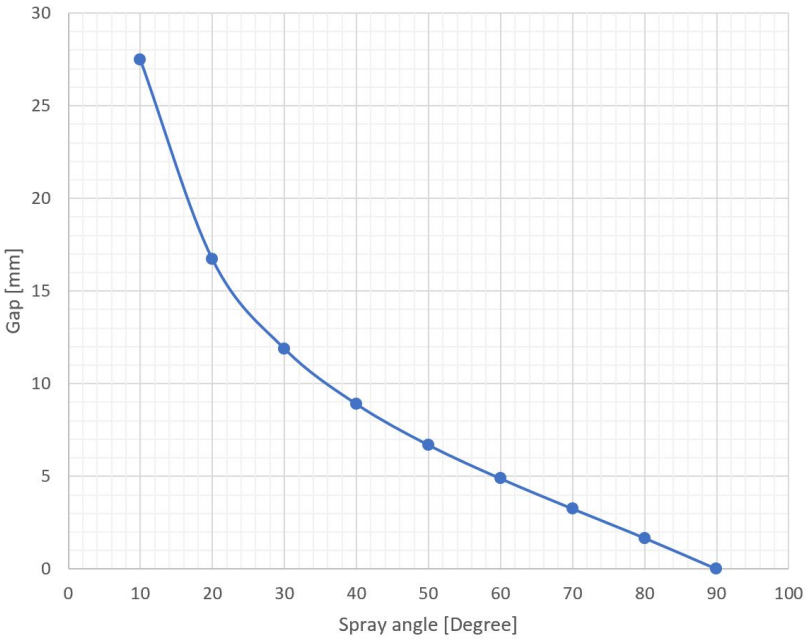

Figure 34 Spray Angle and Gap Sizing

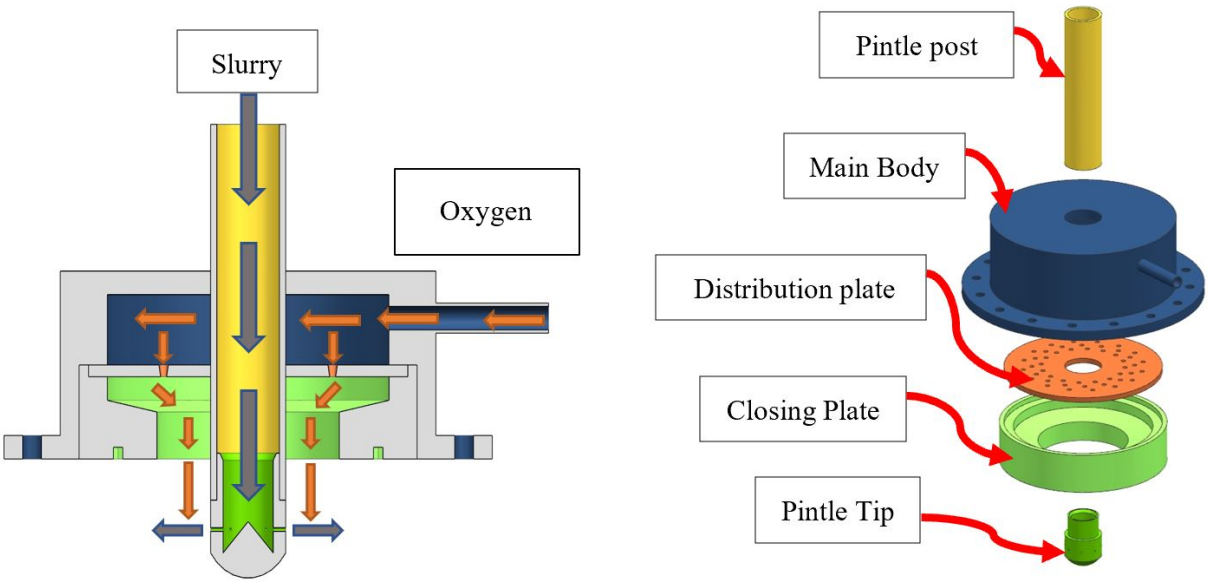

Figure 35 Pintle injector schematic drawing

Figure 35 shows the pintle injector design and the 5 primary components. These components are the main body, pintle post, pintle tip, distribution plate, and closing plate. The main body and pintle post are welded together. The distribution plate will be supported by the closing plate and attached to the pintle post. The closing plate is threaded and screwed into the main body. The pintle tip and closing plate are interchangeable, and the rest of the components are fixed. The advantage of having this modular design is flexibility during the operation of the device.

2.1.1.4. 1st Generation Swirl-Pintle Injector Design (S= 0.9)

In order to improve atomization, a swirler is implemented in the pintle injector design. The swirler will allow for tailored oxy-fuel mixture in to the chamber. In addition, they will help to stabilize the flame. The introduction of CO_2 in the main oxy-fuel flow will increase the chance of flame extinction. Moreover, it will decrease the flame temperature. Thereby increasing the chance of flame detachment and flame extinction. The swirler design will incorporate necessary oxy-fuel mixing during these conditions by inducing a swirling motion to the flow. It will also help to anchor the flame and reduce flame extinction possibilities. The designed swirler will provide clockwise turning momentum to the oxygen flow and will rotate the flow in the clockwise direction.

The swirler is designed based on Swirl number. A swirl number is chosen and the swirler parameters are calculated from the swirl number. For proper mixing criteria, we chose a swirl number of 0.9. The following equation is used to calculate the flow turning angle or blade angle to achieve the aforementioned swirl,

$$S = \frac{2}{3} tan\varphi \tag{30}$$

Where, φ is the blade turning angle or flow turning angle.

The flow turning angle is calculated to be 53°.

A set of airfoil-shaped vanes are considered to design the swirler. The design of the airfoil vane is such that they turn the flow at 53° at the exit of the swirler. The swirler consists of eight identical airfoil vanes, as shown in Figure 36. A NACA airfoil plotter is used to design the airfoil according to the aforementioned swirler criteria. The design parameters for a single airfoil vane is provided below-

- Nominal NACA 2430 airfoil
- Chord width – 0.63 inches
- Camber radius – 0.522 inches
- The angle of attack 0° to the flow path

The airfoil vanes are made of Stainless Steel 410. The vanes are attached to the closing plate using laser weld. For this case, it is assumed that the difference between the inner and outer radii of the closing plate and the injector post is negligible, i.e., a hub-less swirler.

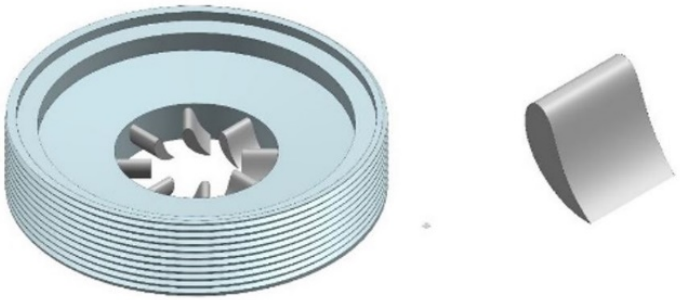

Figure 36 Swirler with detailed view of vane (right)

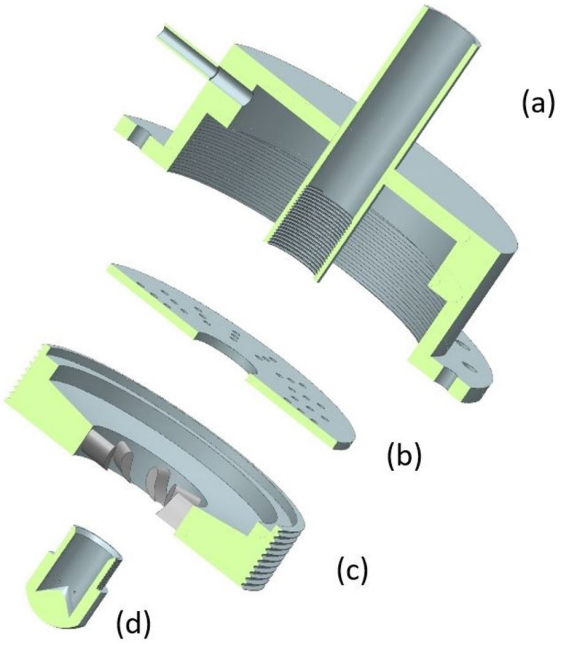

Figure 37 Cut section view of Injector Assembly consisting of (a) main body (b)distribution plate (c) swirler & (d) nozzle

Figure 37 shows the assembly of the injector. The assembly consists of the main injector body with the pintle post welded to it. The pintle post passes through the center of the assembly. The distribution plate is placed after it, and the nozzle is attached with the pintle post. The swirler is screwed in the main body of the injector.

2.1.1.5. 2nd Generation Swirl-Pintlle Injector Design (S=1.2)

The second-generation swirl-pintle design involved increasing swirl number to 1.2. The goal was to further enhance atomization. Tests inferred that increasing swirl resulted in increased atomization. An increase in swirl number enhances the chances of better atomization and flame stability [25,26]. The change of the swirl number has a significant effect of the flame dynamics [27]. During the hot fire test, the swirler will promote the increased mixing of the hot gases and will help the flame to anchor.

Similar to the 1st generation design, a set of 8 airfoil-shaped vanes are considered to design the swirler. The blade angle was calculated similarly to the previous design. The design of the airfoil vane is such that they turn the flow at 60.9° at the exit of the swirler, resulting in Swirl no. S = 1.2. A NACA airfoil plotter is used to design the airfoil according to the aforementioned swirler criteria. The design parameters for a single airfoil vane is provided below-

- Nominal NACA 2430 airfoil
- Chord width – 0.63 inches
- Camber radius – 0.522 inches
- The angle of attack 0° to the flow path

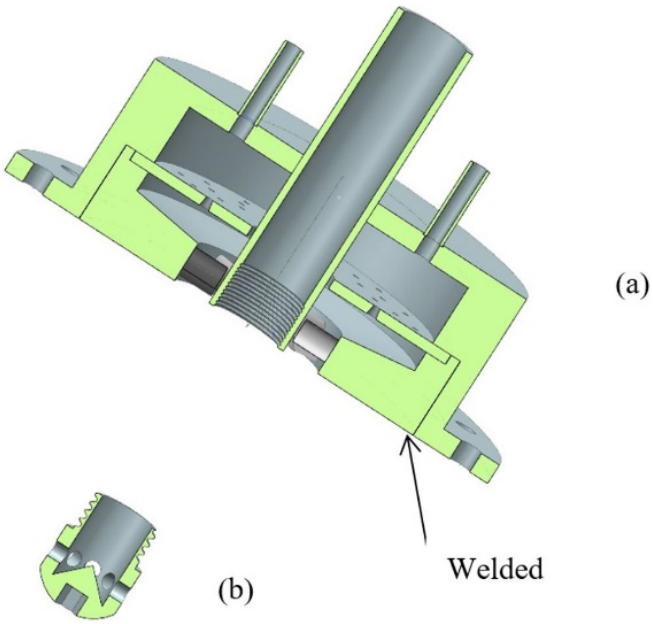

Figure 38 Cut section view of second-generation Injector Assembly consisting of (a) main body, distribution plate, and closing plate with swirler (b) nozzle tip. Only the nozzle tip is modular

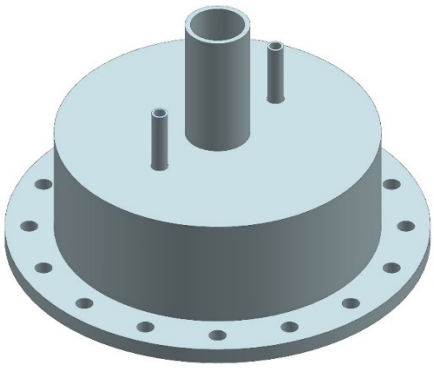

Figure 39 Injector main body casing

Figures 38 and 39 show the second generation swirl-pintle injector. In the second-generation model, contrary to the first one, the closing plate is welded to the main body. This makes the entire unit leak proof. The only detachable part is the pintle tip, screwed onto the pintle post. In addition, the oxidizer port has been shifted from the side of the main body to the top, as shown in Figure 39. After analysis, it has been found that ports at the top will fill the oxygen rapidly into the main body of the injector. The normal injection will impinge on the distribution plate and direct the oxygen to the swirler. The number of oxidizer port has also been increased to 2 from 1. It was noticed that the atomization was not perfectly mirrored on the two sides of the injector in some cases. The injection from one side might have caused the flow to be skewed. Two ports at the top of the injector have been added To have an even distribution on either side.

The threads of the pintle tip and the inner threads of the pintle post have been made into tapered ½" NPT threads. The change was driven due to the innumerable leaks encountered during testing. These new threads, when lined with Teflon tapes, should seal the tip and prevent leaking. A hole to fit tools has been added to the tip to easily unscrew the tip in case of clogs, as shown in Figure 40.

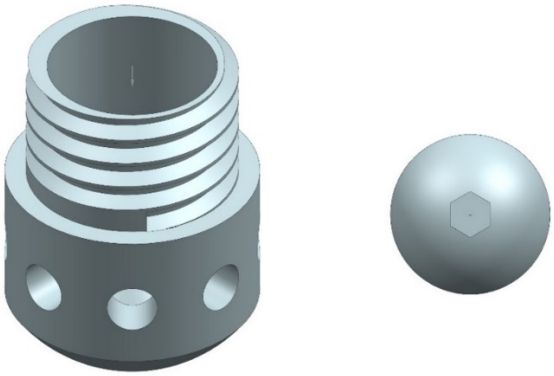

Figure 40 Pintle tip 5mm NPT with the bottom view (right)

2.1.2. Combustor Main Body Design

The combustor design currently consists of two combustion chambers united by flanges, the flanges are rated for 300 psi. The overall design shows the powerhead, ports, and exhaust. The combustor will be suspended in a vertical position using eyebolt hooks. Figure 41 presents the

complete design showing in an exploded view. The combustor main body has an 18-inch outer diameter and 16-inch inner diameter. A refractory liner with 2.5 inch wall thickness is implemented inside the combustor. The module with the refractory will be attached right after the power head as shown in Figure 42. The refractory material will protect the wall of the combustor from the excessive heat during combustion. The liner will slide through the top of the combustor body. A ledge built with the combustor will support the liner.

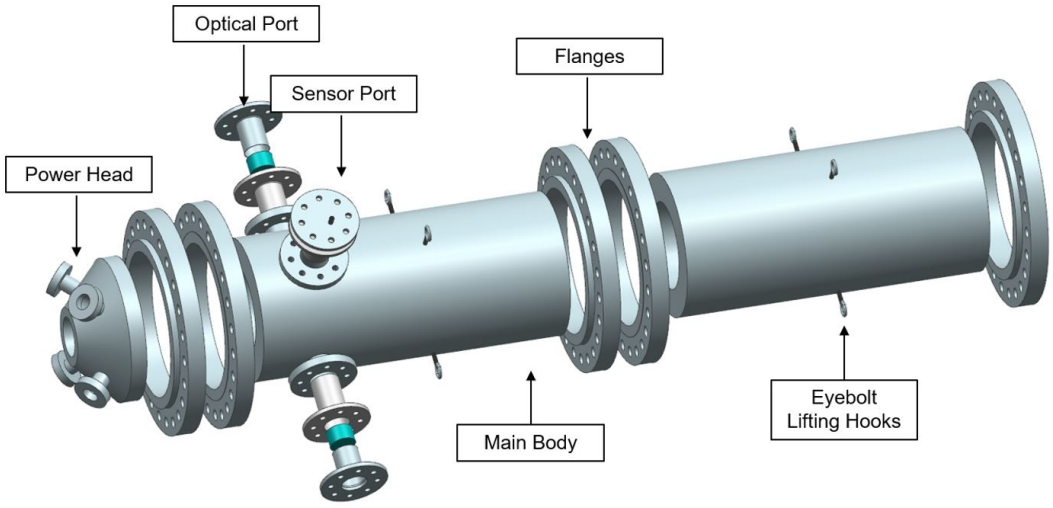

Figure 41 Exploded view assembly of the current design for the oxy-coal combustor

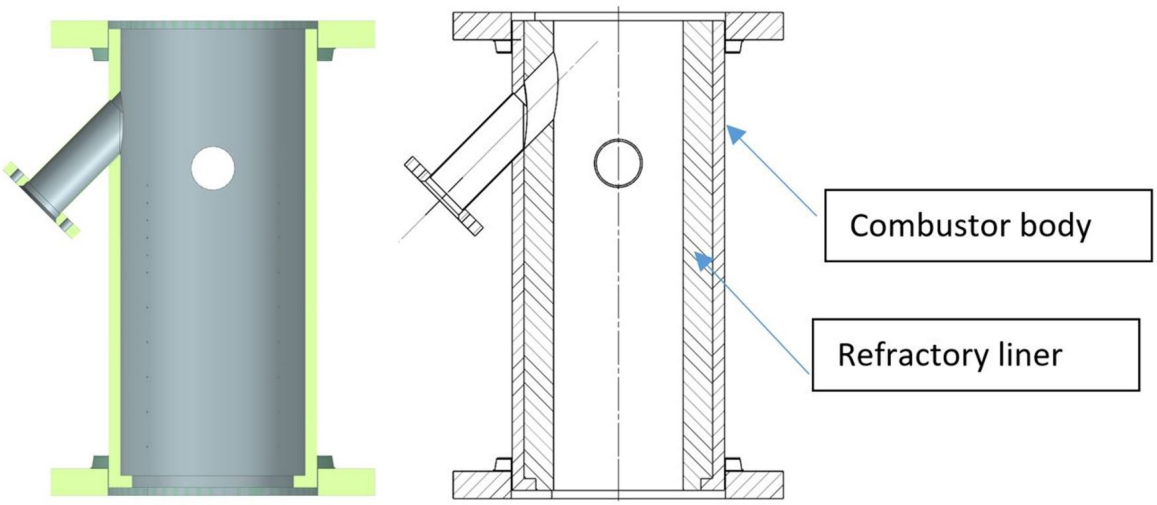

Figure 42 Combustor body of 1inch thickness (left) and assembly of combustor body with refractory liner (right)

2.1.2.1. Flame Temperature Analysis

The flame temperature must be known in order to validate the combustor design. The adiabatic flame temperature has been calculated using NASA CEA. Since coal is not found as a compound in the CEA database the coal was simulated using the percentage of each of the constituent

elements of coal. In order to validate the process, the flame temperature reported by Zheng et al.[28] have been calculated. The graphs in Figure 43 and Figure 44 show that the obtained temperatures are close to the temperatures reported by Zheng et al, shown in Figure 43.

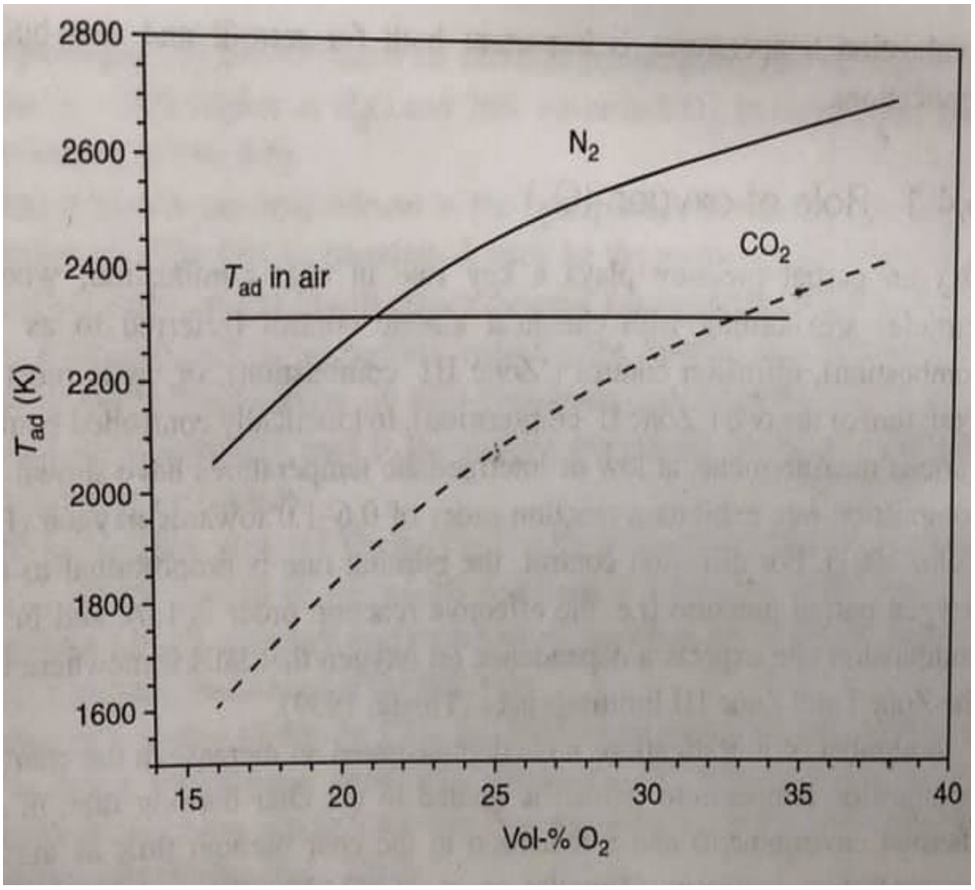

Figure 43 Adiabatic flame temperature as reported by Zheng et al. [28]

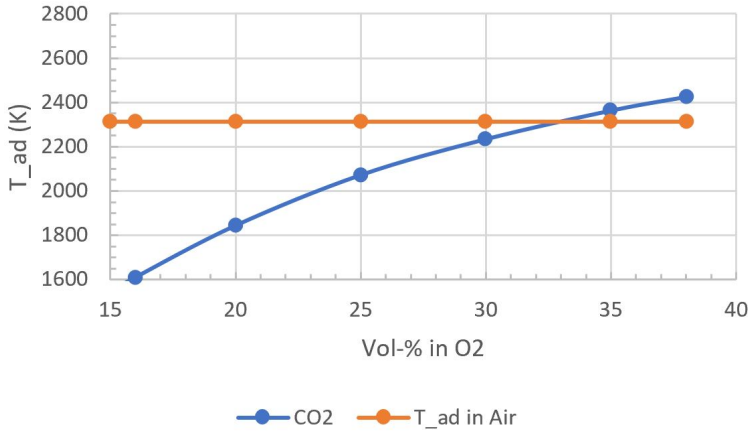

Figure 44 Adiabatic flame temperature obtained to validate calculation method to validate Zheng et al. [28]

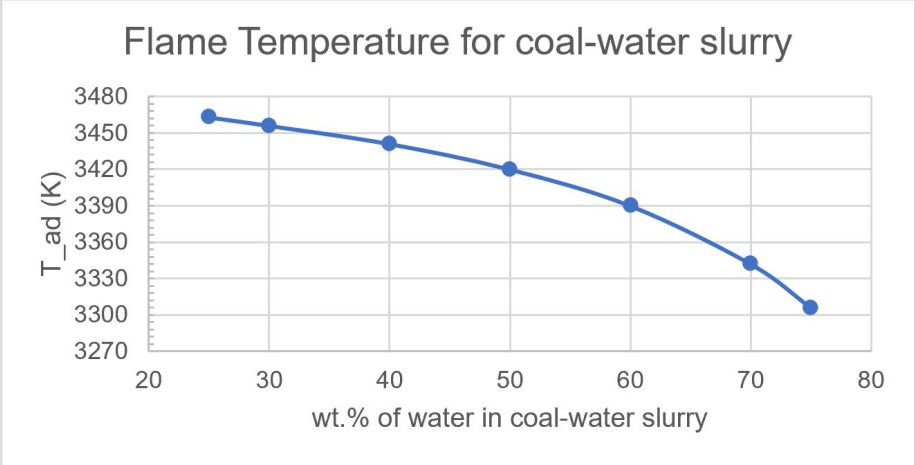

Figure 45 Adiabatic flame temperature for different coal-water slurry ratio

After validation of the method, the adiabatic flame temperature of bituminous coal for this project has been calculated. The stoichiometric mixture at 298K has been used for the combustion simulation in NASA CEA. The adiabatic flame temperature has been found to be 3465K. This corresponds to the temperature range predicted by Hong et al. [2] for the oxy-coal combustion of bituminous coal.

Adiabatic temperature for different coal-water slurry mixture with different water ratio was also calculated. Figure 45 shows the change of adiabatic flame temperature with the change of the coal-water slurry ratio.

Steps to calculate the adiabatic flame temperature in NASA CEA are stated below:

- Coal Chemical formula was calculated. Ultimate analysis:
- Wt.% of each component was calculated and ash was ignored
- Each component was inserted with wt.% as fuel in NASA CEA
- According to the formula mass of oxygen for stoichiometry = 68.48 g
- Mass of water for the different coal-slurry ratio was calculated
- Mass of CO2 for each percentage CO_2-O_2 mixture was calculated
- That water mass is used in oxidizer mixer for NASA CEA
    - $(Wt.\%\ of\ O_2\ in\ oxidizer) = \frac{Mass\ of\ O_2}{(Total\ mass\ of\ O_2 + Water\ mass\ from\ Coal\ slurry)}$
- For each slurry ratio calculated water mass was inserted into the above formula to get wt.% of O_2

2.1.2.2. Material Selection

In order to find the material of the combustor, yield strength of different materials with temperature were compared to each other. The search was constricted to steel because this kind of material is widely available, inexpensive, and easy to manufacture compared to other materials. The research group had an already built combustor with a methane burner made with Stainless Steel 410 previously used at 232 kW and 16 bars where the wall reached 325°C.

A comparison between steel of 300-series, carbon steel and Stainless Steel 410 was made to decide upon a material. The study is shown in Figure 46. The difference in yield strengths between SS 410 and other materials is clearly visible. So, it was clear that SS 410 is the material with the highest temperature endurance than the other options. For this reason, it was decided that SS 410 would be the material that would be used for the combustor body, flanges (to avoid any mismatch referring to thermal expansion), powerhead, and exhaust.

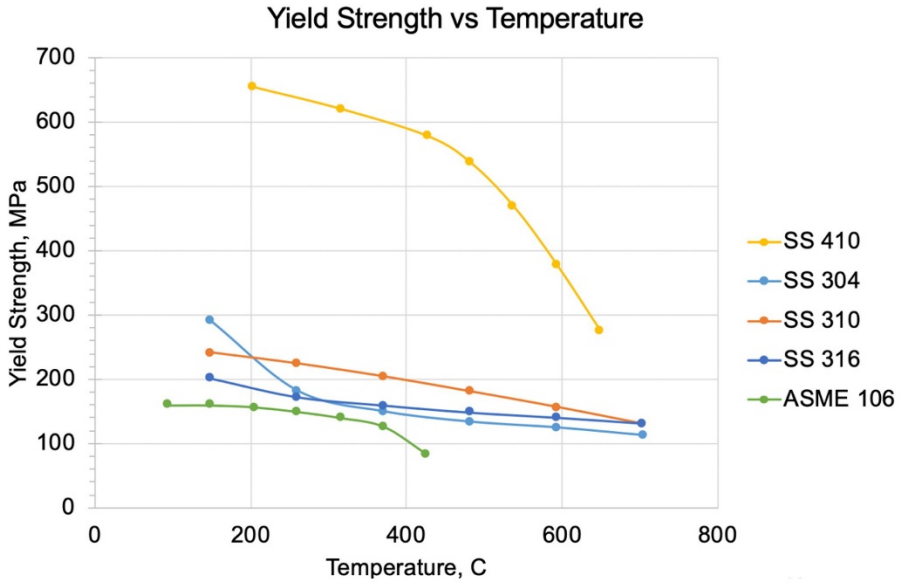

Figure 46 Yield Strength comparison with increasing temperature for different materials

Figure 46 clearly shows 410 has higher yield strength even at 400°C. The drop in yield strength of SS 410 starts above 325°C, which is the higher operating end of our system. As SS 410 has the highest temperature endurance, it is selected as the manufacturing material.

2.1.2.3. Thickness Analysis

A simple thermal and mechanical analysis was done to decide upon the wall thickness of the combustor. The analysis considered both thin wall and thick wall cylindrical vessel approach. The following equations were used for this analysis.

Thick wall Combustor- Hoop Stress ($\frac{r_i}{t}$ >10):

$$\sigma_c = \frac{r_i^2 P_i - r_o^2 P_o}{(r_o^2 - r_i^2)} + \frac{(P_i - P_o) r_i^2 r_o^2}{(r_o^2 - r_i^2) r_i^2} \tag{31}$$

Thin wall Combustor- Hoop Stress ($\frac{r_i}{t}$ <10):

$$\sigma_c = \frac{P_i * r_i}{t} \tag{32}$$

Thermal Stress:

$$\sigma_{Th} = \frac{\mathrm{E} * \alpha * (T_{in} - T_{air})}{2 * (1 - \nu)} \tag{33}$$

Where,

σ_c= Circumferential stress or Hoop stress

r_i= Inner radius

r_o= Outer radius

t = thickness

P_i= Inner Pressure

P_o= Outer Pressure = Atmospheric pressure

α= Coefficient of thermal expansion

ν= Poisson's ratio

Total Stress = Factor of safety*(Hoop Stress + Thermal Stress)

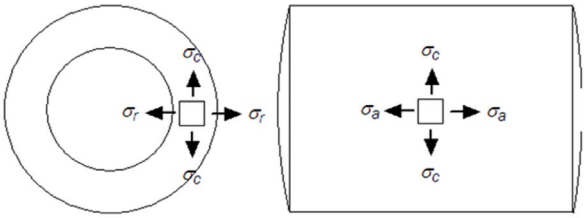

Figure 47 Control volume showing thick wall stress analysis

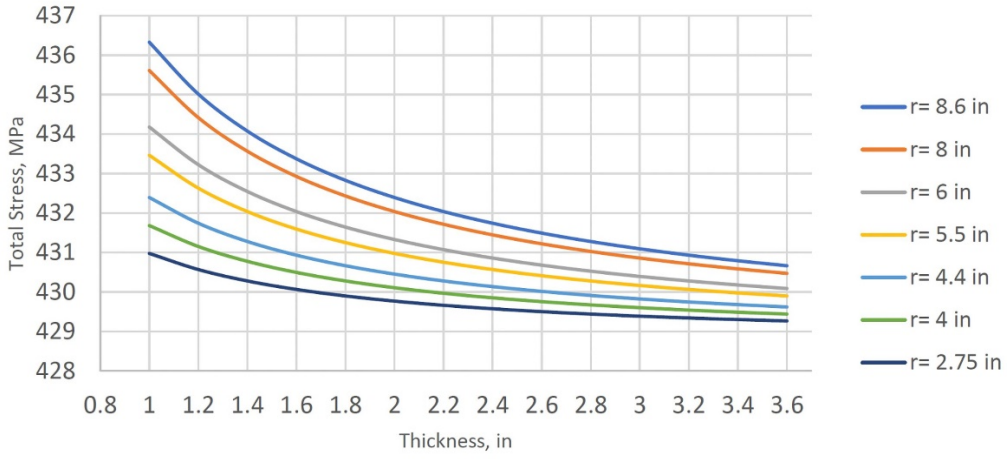

Figure 48 Total stress on combustor body at different wall thickness

Figure 48 shows stress at the combustor for different wall thicknesses and different inner radius. All of the conditions shown above satisfy the safety factor criteria. Since the radius and the thickness of the previously experimented combustor also satisfied the requirement, it was decided to keep that one to run the present project. That combustor has a radius of 5.5 inches and a thickness of 3.5 inches. This decision was also supported by Figure 49, which showed that stress with increasing temperature doesn't vary much if the thickness is varied. Selecting the thickness of the previously used combustor can also provide the option of lowering the safety factor for higher temperature operation and slowing down the heat transfer from the wall chamber to the outside wall, which was attractive to the investigation.

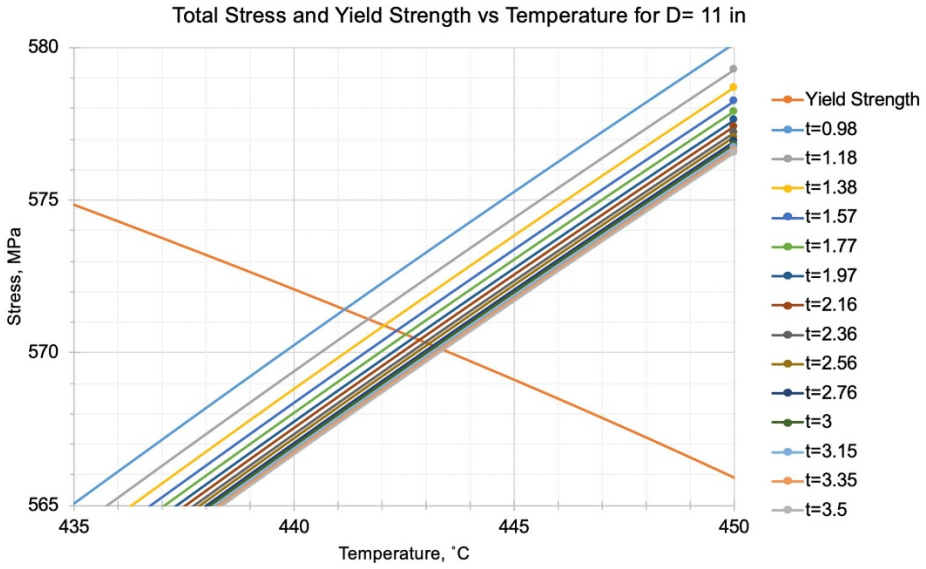

Figure 49 Comparison of combustor strength for different thickness

2.1.2.4. Thermocouple Port Analysis

Finite element analysis (FEA) was done to check the stresses on the combustor body. ANSYS FEA software tool was used for this purpose. One-third of the whole combustor was modeled with ten (10) thermocouple ports; the current combustor design will have 30 thermocouples. The allowable depth for those thermocouple holes was assessed. A hand calculation was used considering maximum allowable wall temperature and working pressure to compare with the model results. Thick and thin wall pressure vessel equations were used to find out those stresses. Figure 50 represents the maximum stress experienced on the hole for different wall thicknesses as a function of temperature. In Figure 50, the orange line represents the change in yield strength for 410 SS, which decreases as temperature increases. As thickness between the interior wall and the bottom of the thermocouple port is increased, the change in stress becomes smaller. The team has set that the maximum allowable wall temperature is 400oC, based on Figure 13, having a wall thickness of 3mm (0.12 inch) for holes of 0.375 mm (0.125 inch) is best. This parameter will be used to proceed with an FEA.

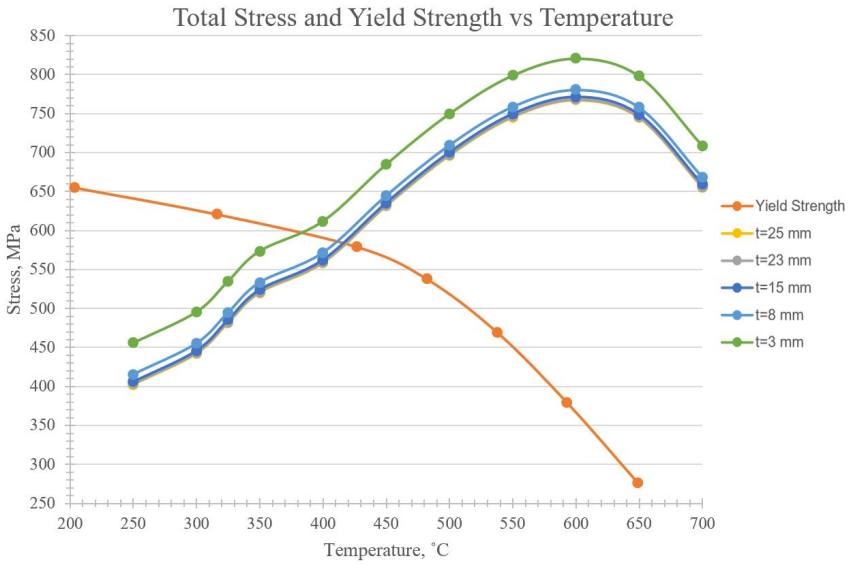

Figure 50 Stress vs. Temperature curve

A mesh of 216,773 elements was made for the model, as shown in Figure 51(a). Due to the limit of 500,000 elements and computational time, the number of elements was not increased. Mesh in the regions surrounding the holes, were refined as these are the crucial parts of the model. However, due to the wide variation of element sizes, the average aspect ratio was 9.6. The minimum value was 1.2, which indicates a reasonable value of aspect ratio. The mesh was implemented in order to have smaller elements and higher quality near the orifices and increase in size as they get further from the area of interest. Figure 51(a) shows the mesh generated and Figure 51(b) shows the thermal boundary conditions applied. Convection boundary conditions were applied on the inner and outer walls of the combustor section. The adiabatic flame temperature for a steady-state process, as found using NASA CEA software, is 1800 ˚C. This has been used as the temperature of the convective gases inside the combustor. On the outer surface of the combustor, as indicated by "A" in Figure 51(b), an air of ambient temperature has been assumed to remove heat convectively. The model has been made for one-third of the combustor. Frictionless supports have been applied on the cross-sections of the combustor walls to pose symmetrical conditions.

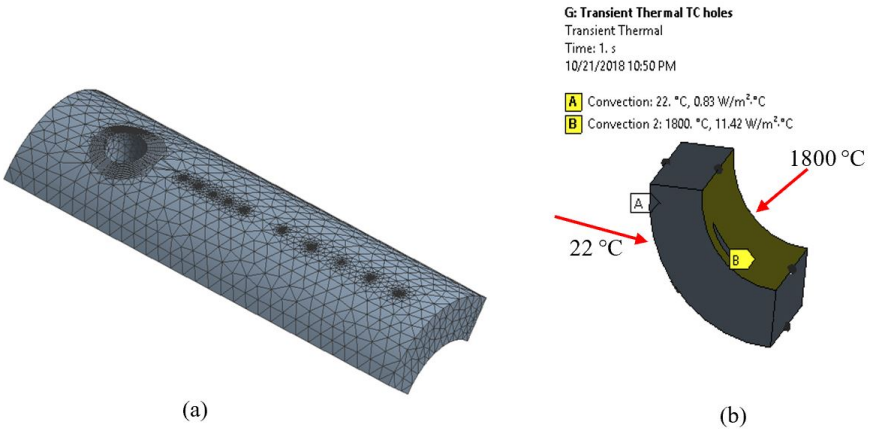

Figure 51 - (a) Mesh for the model (b) boundary conditions as applied on the section

A transient thermal analysis was done, and then it was coupled with transient structural analysis. Figure 52 shows the result of temperature after running the simulation for 30s. From the simulation, it was visible that increasing runtime temperature was increasing. The maximum temperature the combustor reaches is 43.2°C after running it for 30s. And as expected, the inside wall has the maximum temperature. Figure 53 shows the change of temperature for the inside wall with time.

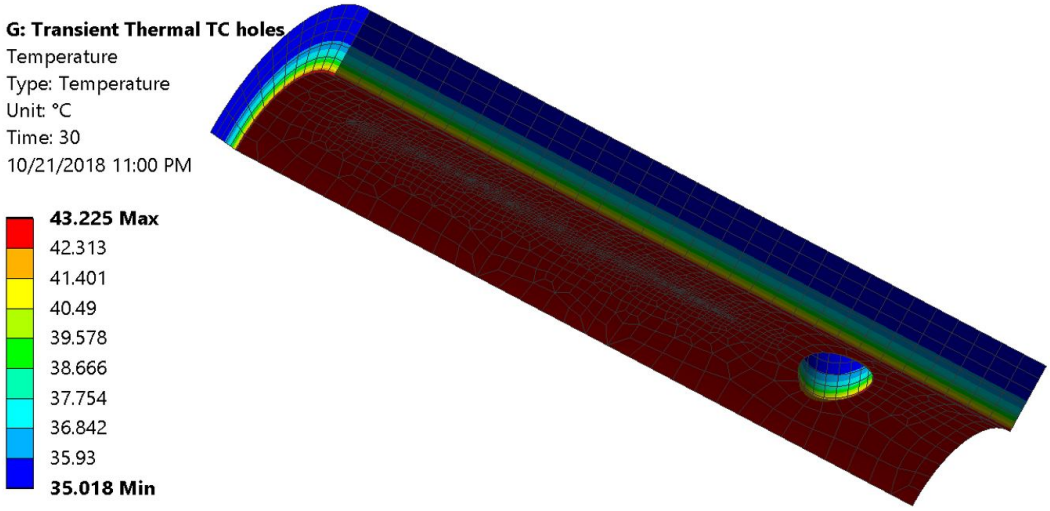

Figure 52 Transient Thermal Analysis

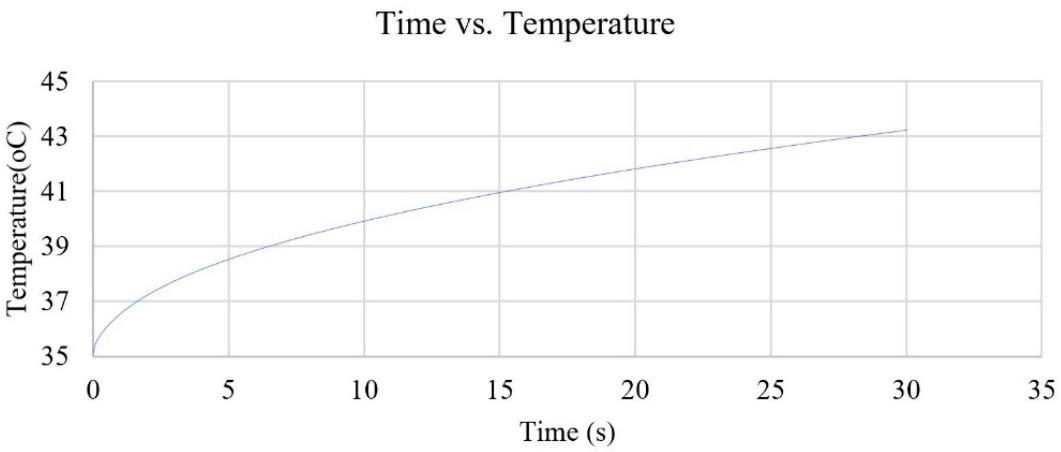

Figure 53 Time vs. Temperature for inside wall

The results found from the transient thermal analysis were inputted into the transient structural analysis; to extract the total stress and deformation. The simulation runs for 10 seconds of operation. Figure 54 represents the deformation with the selected operating conditions at the tenth second. The maximum deformation the walls reach is 0.055 mm. Figure 55 represents the von Mises stresses on the combustor wall. It can be seen that there is a stress concentration around the holes, but the maximum stress was 5 MPa (50 bar); below the yield strength. Based on the results of the FEA, the structural design is acceptable to run for 10 seconds without active cooling.

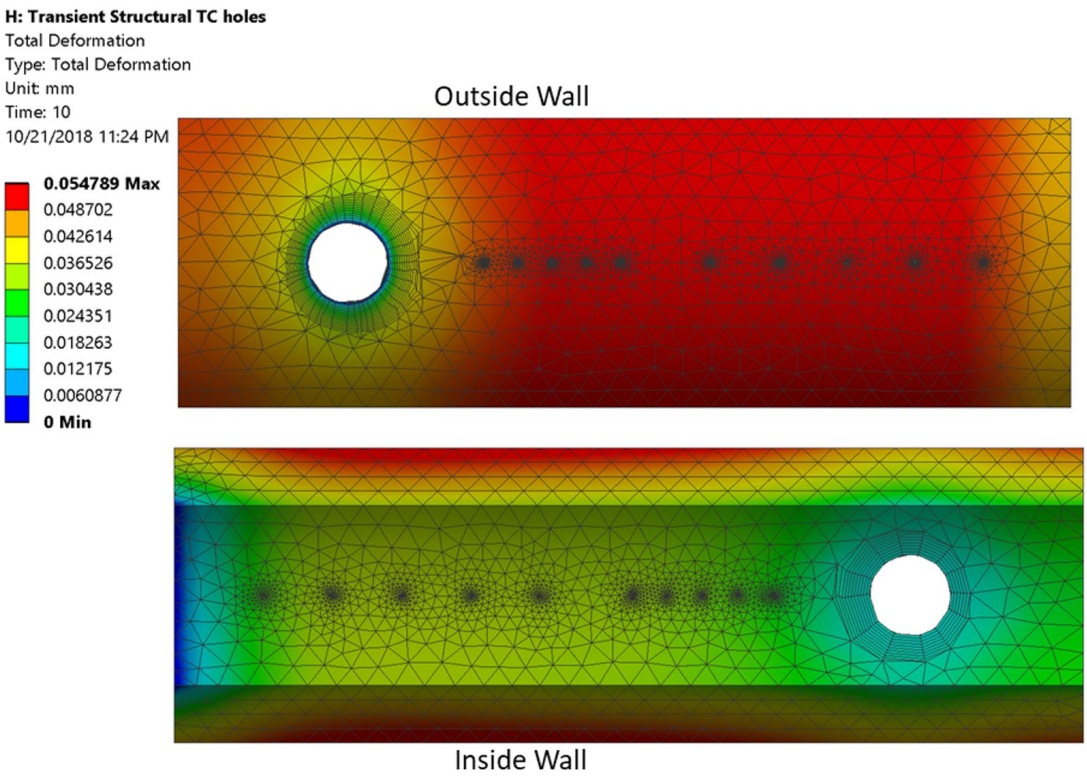

Figure 54 Deformation of combustor wall.

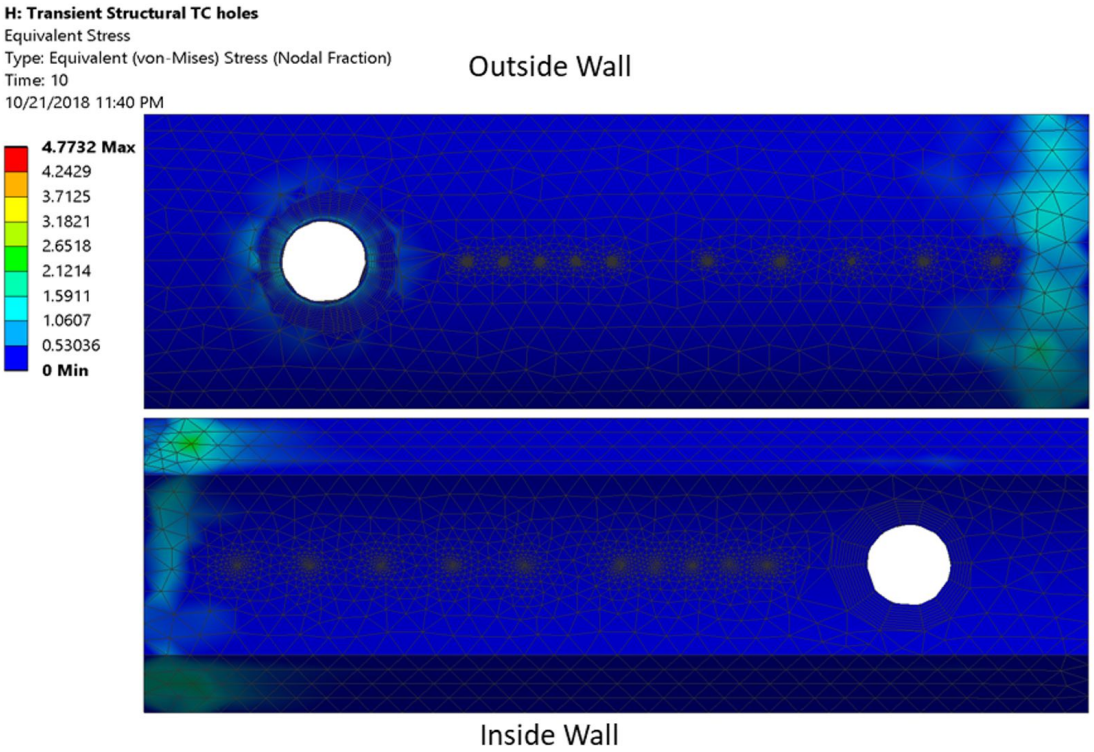

Figure 55 Stresses on combustor walls

2.1.2.5. FEA of Combustor Body

To validate the combustor body, an FEA is an essential part of the design and manufacture of such components. For this FEA, the use of NX 11, and Hypermesh 13, are the main software's used through the analysis.

The procedure taken for this analysis is as follows:

I. Import combustor components into Hypermesh 13 as IGS files from NX 11
II. Develop a 3D mesh as a solid map with one volume for mappable solids
III. Develop a 3D tetramesh with volume tetra for non-mappable solids
IV. Define Boundary Conditions and Material Properties
V. Run three main analyses for the combustor
    a. Heat Transfer
    b. Thermal Stress
    c. Thermal and Mechanical Stress
VI. Analyze results
VII. Validate design

A total of 30 components list is prepared for FEA analysis. A list of such components can be seen in Table 18.

Table 18 List of FEA components

Component Number	Component Name	Component Number	Component Name
1	Main Combustor	16	Flange Combustor5
2	Simple Combustor	17	Weld Flange Combustor0
3	Exhaust Conical	18	Weld Flange Combustor1
4	Exhaust Cylinder Flange1	19	Weld Flange Combustor2
5	Exhaust Cylinder Flange2	20	Weld Flange Combustor3
6	Exhaust Cylinder Flange3	21	Weld Flange Combustor4
7	Exhaust Tube	22	Weld Flange Combustor5
8	Exhaust 6in Flange	23	Weld Exhaust Port Bottom1
9	Power Head	24	Weld Exhaust Port Bottom2
10	Exhaust Conical Extension	25	Weld Exhaust Port Bottom3
11	Flange Combustor0	26	Weld Exhaust Port Top1
12	Flange Combustor1	27	Weld Exhaust Port Top2
13	Flange Combustor2	28	Weld Exhaust Port Top3
14	Flange Combustor3	29	Weld Exhaust Tube
15	Flange Combustor4	30	Weld Exhaust Extension

2.1.2.5.1. Mesh

As the components were imported into Hypermesh 13, the "solid edit" feature was used to separate most of the components into mappable solids for a 3D Solid Map mesh. The size of the mesh was varied until a 0.25in mesh size 1st order element quads was decided upon.

Figure 56 shows a zoomed-in section of component #14 as the mesh was created by 3D Solid Map mesh.

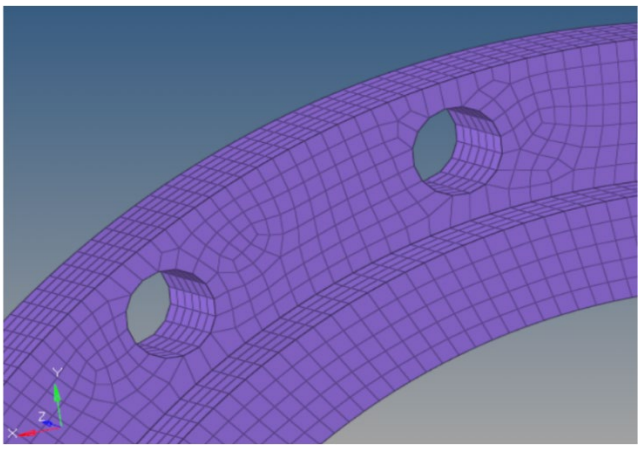

Figure 56 Combustor flange zoomed-in section

As mentioned previously, mappable solids were meshed using the 3D Solid Map mesh. The non-mappable solids were meshed using the 3D tetramesh feature with the volume tetra using curvature and a mesh size of 0.25in. In Figure 57, component #1 was meshed using both features described above. The main combustor cylinder was separated into three components, meshed, and then brought together as one solid component. As there were a total of 30 different components, the use of Rigid Body Elements (RBEs) and weld elements was needed to connect the whole assembly.

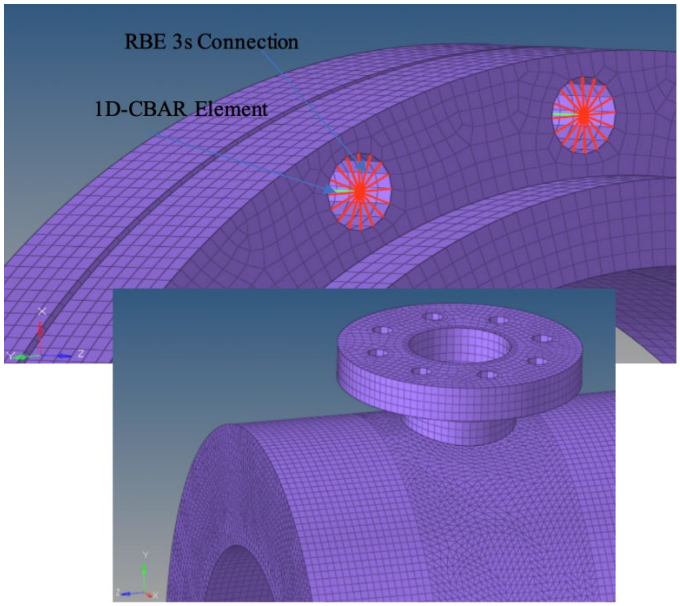

Figure 57 Mesh of componet#1

The bolt connections in the combustor flanges were represented by the use of RBE 3's for connection to the flange and 1D element CBAR for the bolts. In Figure 58, the connection of the RBE 3's and bolts are shown. In Figure 58, the red "spider web" is the RBE3s connections to the nodes in the flanges. At the center of the "spider web" the connection of the 1D-CBAR element is made. In this model, the use of a 1.25in bolt was decided based on previous mathematical calculations.

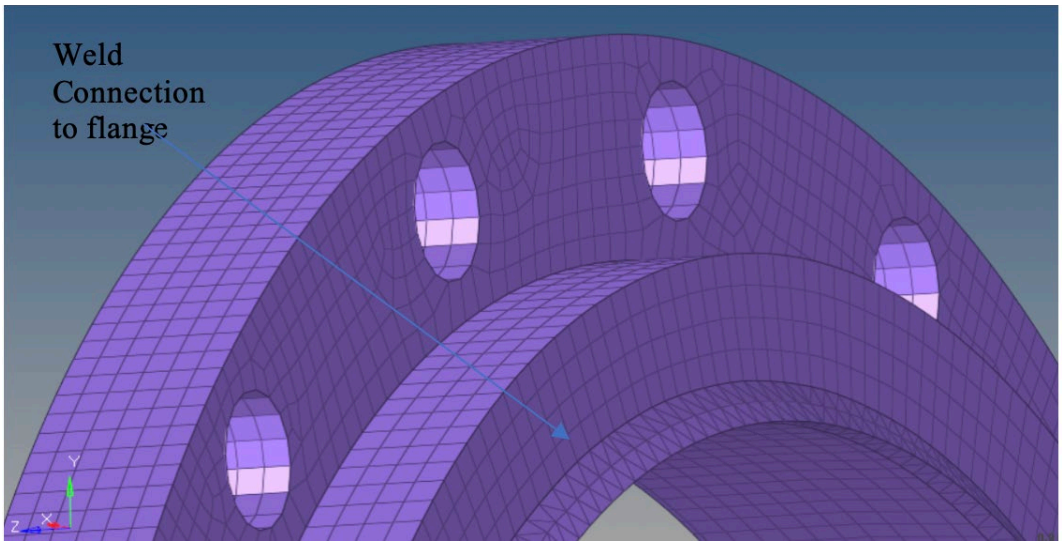

Figure 58 Weld on the flange

Once the bolt connections were completed, the connection of the flanges to the main combustor was done. The first approach of this connection was to use RBE2s which is a stiffer connection than RBE3s to simulate a weld connection. This was later discussed, and the CAD model of the weld connection was decided upon to better visualize the stress concentrations that the weld might see.

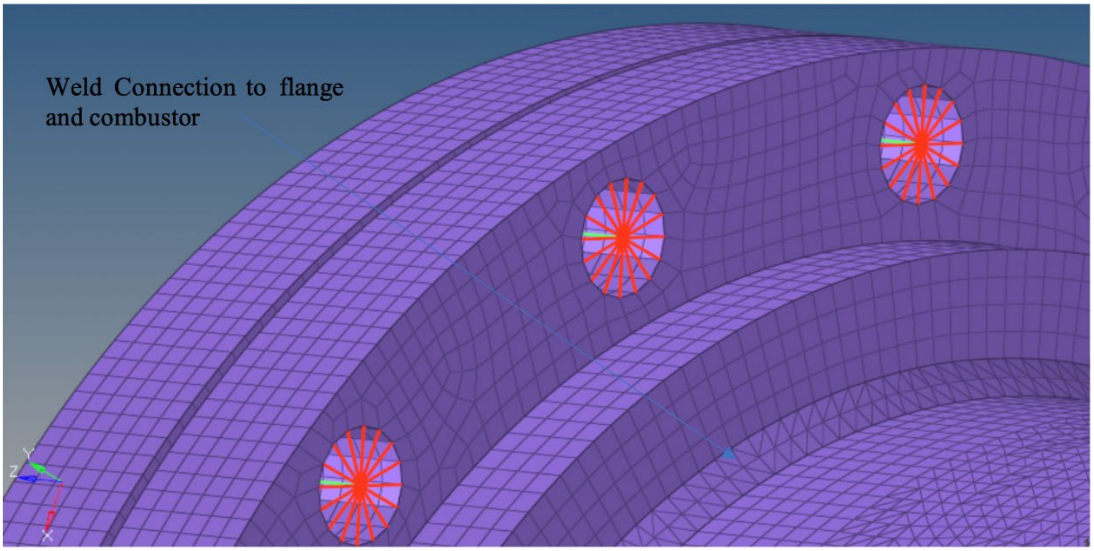

Figure 59 Weld connection to the flange and the combustor

The weld connection for this scenario will be a fillet weld with a 0.25in height seen in Figure 59 based on previous calculations. Additionally, in Figure 59, the weld connection can be seen in both the flange and the combustor. The connection of the weld elements to the flange and the combustor was done by the "face equivalence" feature. The connection of the weld component was given a tolerance of 0.09in to the closest nodes to have a complete connection of the weld to the flange and combustor.

This process was repeated for all the components that will be using a fillet weld connection. For components #3, #8, and #10, the use of face equivalence was done without the weld component as a butt weld will be used for these components. As all the components were meshed and connected, the total number of elements and nodes are as presented in Table 19.

Table 19 Mesh Characteristics

Number of elements	2.25E+06
Number of nodes	1.38E+06

2.1.2.5.2. Boundary Conditions and Materials

The materials presented in Table 20 were decided upon for the combustor, welds, and bolts. These materials were chosen based on their material properties that fitted the needs of this combustor and based on previous mathematical calculations.

Table 20 Material Properties of different parts of the combustor

Material Properties						
Components	Material	Density [slinches/in^3]	Young's Modulus [PSI]	Poisson's Ratio	Thermal Conductivity [lbf/s °F]	Thermal Expansion [°F]
Combustor	410 Stainless Steel	7.25E-04	2.90E+07	0.285	3.1162	5.50E-06
Bolts	Black-Oxide Steel Grade 5	7.35E-04	2.76E+07	0.27	6.48	6.39E-06
Welds	410 Stainless Steel	7.25E-04	2.90E+07	0.285	3.1162	5.50E-06

In this FEA, the validation of the main combustor design was the main focus and priority. For this reason, there are only two main boundary conditions that will allow us to validate the design at this stage. The first boundary condition is the inner wall temperature of the main combustor to be set at 588 °Kelvin (1060 °Rankine). This value was chosen as the worst-case scenario of the temperature inside the wall of the combustor. If the combustor reaches a higher value than the one given, the material properties will begin to fail and, by consequence, the combustor. The second boundary condition is an inner wall constant pressure of 10 bar (145 PSI) throughout the whole combustor. The final set of boundary conditions that were used were the convection heat transfer coefficient of air as 0.04 [lbf/in s °R] at room temperature of 25 °C (536 °Rankine) at all the outer walls of the main combustor and the constraints of the combustor.

The constraints chosen for this case are as if the combustor is being held horizontally. This horizontal constrain allows for any expansion or contraction of the combustor. In Figure 60, the main combustor can be seen isolated from the rest of the components with all of the boundary conditions mentioned previously.

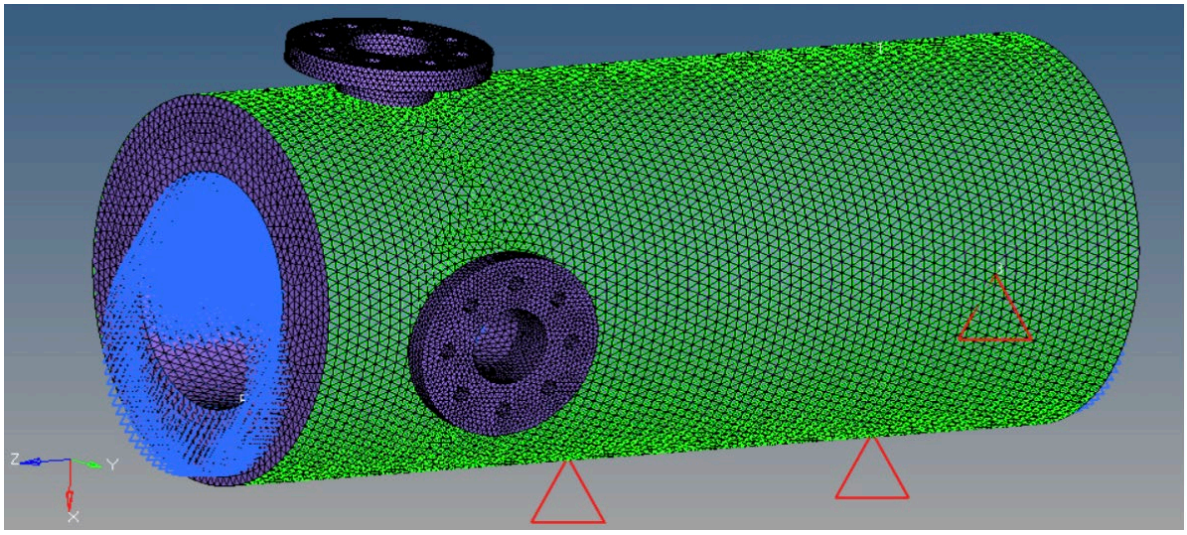

Figure 60 Combustor with boundary conditions

2.1.2.5.3. Combustor Main Body Heat Transfer Analysis

The model was run using only the pressure and temperature described in the boundary conditions to obtain heat transfer to the wall. As seen in Figure 61, the combustor wall has a uniform heat transfer conduction within the combustor wall. The inner wall, as it was stated before, has a temperature of 1060 °Rankine (589°K). As the heat transfer analysis ran, it calculated that the outside wall by conduction and convection at room temperature is 1031 °Rankine (572°K) at its lowest point.

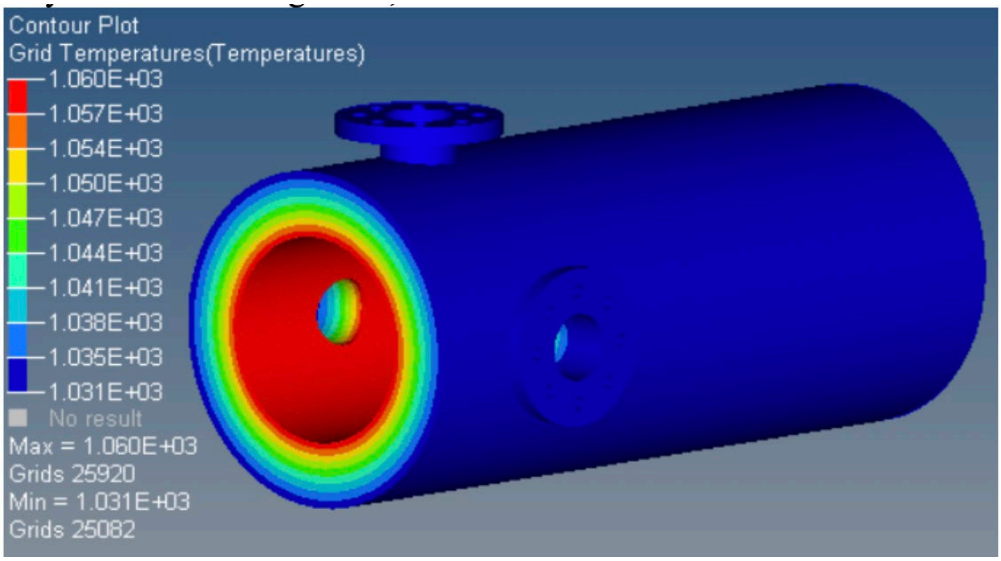

Figure 61 Temperature contour of the combustor

2.1.2.5.4. Thermal Stress Analysis

In the thermal stress analysis seen in Figure 62, the simulation is taking into consideration the position of the combustor by setting constraints. This means that both the heat transfer and constraints are creating stress along the combustor as its being held horizontally. The maximum stress that the combustor is undertaking is seen at the portholes along the combustor. It can be seen that at the portholes have stress concentrations with a maximum stress of 5.327E+03 PSI. The lowest stress can be seen at the portholes since they see the least amount of temperature from the combustor, and there is no load or constrains acting on them.

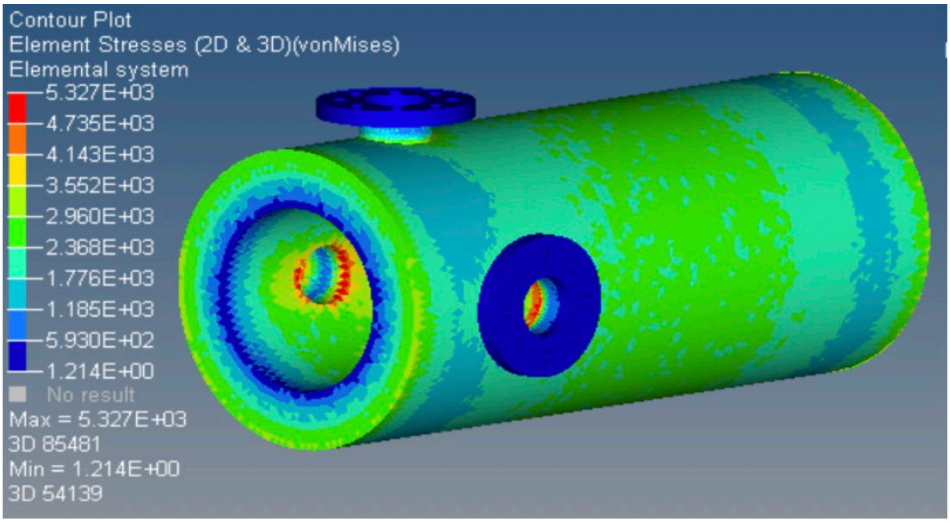

Figure 62 Thermal analysis on the combustor

2.1.2.5.5. Thermal and Mechanical Stress

In the thermal and mechanical stress, the analysis is taking into consideration all of the boundary conditions given. It is taking the thermal gradient, the inner wall pressure, and the constrains that hold the combustor horizontally.

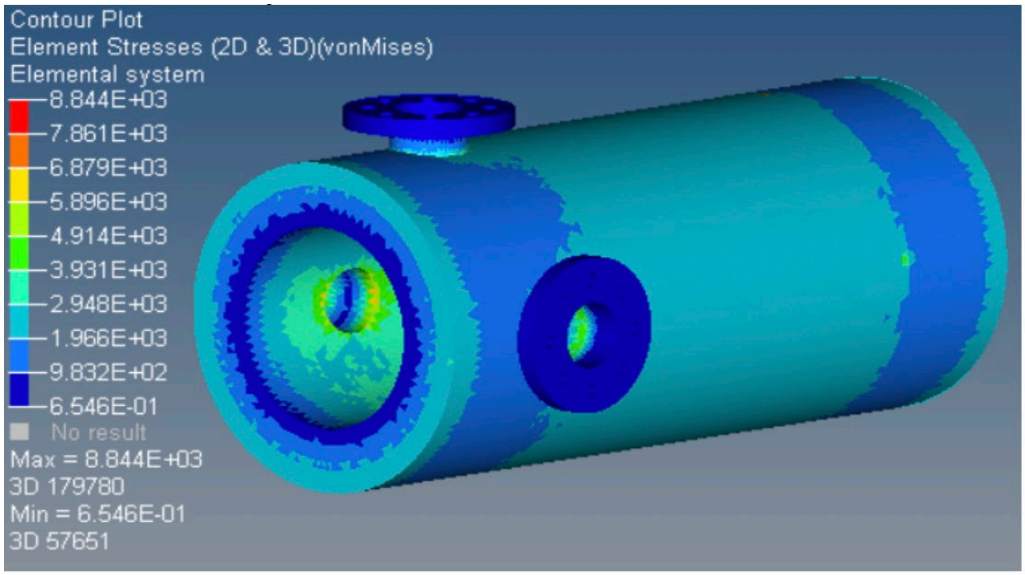

Figure 63 Thermal and Mechanical analysis of the combustor

As seen in Figure 63, thermal and mechanical stress results are shown. In this case, as mentioned previously, the inner pressure of 10 bar (145 PSIA) is considered as well as the heat transfer gradient and the constraints. All these boundary conditions give out maximum stress along the combustor of 8.844E+03 PSI, which, compared to the thermal stress, there is a 3.517E+06 PSI stress difference. This serves as a mathematical check as the inner pressure should increase the stress seen through the combustor.

The validation of the design of the combustor can be made by looking at all the results from the analysis described above taking in consideration all these results. In the heat transfer analysis, the outer temperature of the combustor and the inner wall temperature are 1060 and 1030 °Rankine respectively. By having stainless steel 410, the melting point of such material is 3155 ° Rankine giving it a 2.9 safety factor. In the thermal and mechanical analysis, its shown that the combustor being held horizontal with a 1060 °Rankine inner wall temperature and a 10 bar (145 PSIA), the maximum stress is 8.844E+03 which compared to the yield strength of stainless steel 410 (60E+03 PSI) it gives out a 6.7 safety factor.

2.1.3. Exhaust System

The exhaust products from the combustion process will contain hot gaseous products and ashes. The goal is to analyze the composition products of the exhaust before it is released to the atmosphere. We will use an emission analyzer that requires exhaust gasses to be cooled and be free of any ash. In order to achieve this, it is proposed to incorporate a cooling water system at the bottom of the system; this will inject water droplets that will allow to cool the hot exhaust and help trap the ash. A water reservoir will be used for the water supply, and a water pump will be used to transport the water from the reservoir inside the combustor chamber. An exhaust manifold will be attached at the end of the combustor length to collect the excess water and the soaked ashes. The ashes and the water will collect at the bottom of the exhaust manifold. This portion of the system is designed to be modular, which allows them to be modified for different test durations and to allow for waste extraction. The selected diameter for the water pipe diameter is 6 inches; wide enough to accommodate a cleaning device to remove any ash that impinges onto the wall.

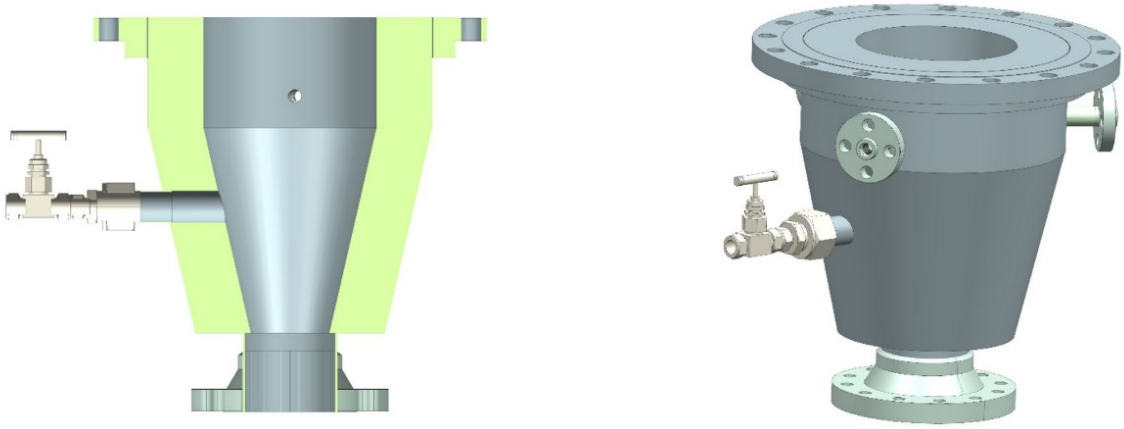

Figure 64 Exhaust System

Hot gasses will exit through the exhaust port as indicated by the white components in Figure 64. This section will have the smallest cross-sectional area of the entire system post-combustion; this portion will likely experience the highest temperatures. A 2-inch exhaust port and tube were

selected, then the diameter would decrease with a reducer and finally reach a needle valve, choking the flow to mitigate excessive heating in one localized area.

Quantity of water required to cool down the hot gasses was estimated, which help set requirements for the water sprinkler system. Convection heat transfer equation was applied, taking the assumption that the hot gas temperature will be 1800°C, and the mass flow rate will be 0.048 kg/s. The total mass flow rate for water was found to be 1.15 kg/s (18 GPM). It is found that a minimum of three water sprinklers is needed to deliver the water onto the system. Each sprinkler will have a spray angle of 120°, which would be enough span to cover the interior of the system.

2.1.4. Flange Selection

Flanges were used as the connecting medium between the main components of the combustor. In order to identify flange requirements, the stresses on the flanges and the pressure rating was reviewed. Following equations were used for this case:

- Operating Forces on flange, $F_{operating}$= Fl + GFHD + GFs
- Seating force on flange, $F_{seating}$= Gfseat
- Fl = (P*Aflange + weight)
- Hydrostatic forces on GFHD= P*Geff-flange
- Gasket sealing forces, GFs= Maintenance factor* P*Geff-flange
- Bolt material: Stainless steel with tensile strength of 70,000 psi (4830 bar)

The highest force the flanges will have to carry is found to be 1570 kN, and the required bolt area is 5 in^2. The 410 SS 300 class flange was selected to meet the requirements. It will have the same material as the combustor, which prevents thermal mismatch. Additionally, working pressure for 410 SS at 400°C is 28.4 bar.

2.1.5. Weld Thickness Calculation

Welding is required to attach the combustor cylinder with the flange. The height and material of the weld should be chosen carefully. They must able to withstand the stress due to the operating pressure and weight of the whole combustor. Since, in this case, the combustor cylinder and the flange are two metal bodies whose central axis is perpendicular to each other, the transverse fillet joint will the best choice, as shown in Figure 65.

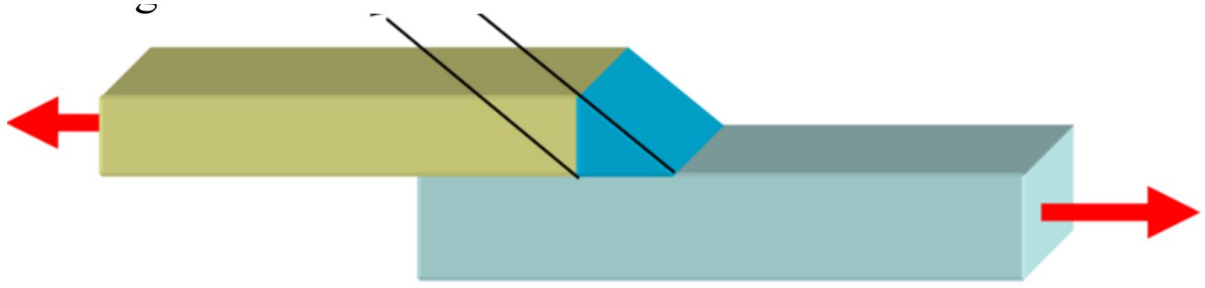

Figure 65 Traverse Fillet Weld

The middle plane of the welding cross-section has the minimum area; that section is most susceptible to failure. The height of that area is called weld throat. Hand calculation was done to check to find out what was the minimum weld height to withstand total stress on the weld.

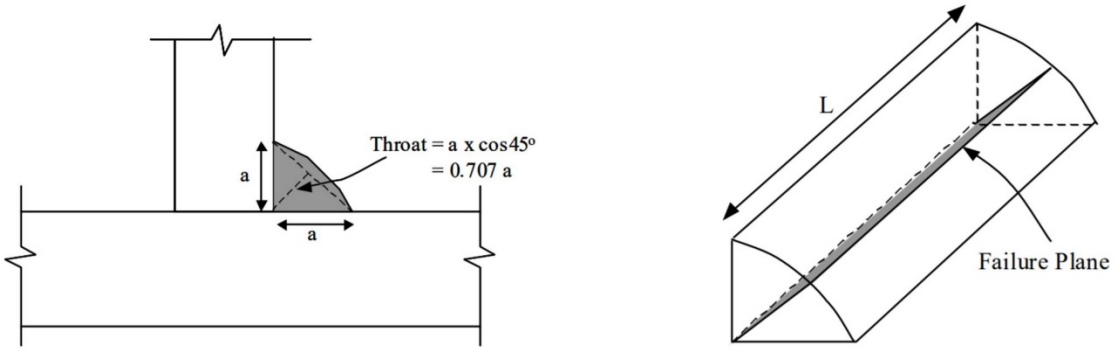

Figure 66 Cross-section of a transverse fillet weld

Total allowable stress on the weld is,

$$Allowable\ stress = \phi R_{\mathrm{n}} = 0.75 * f_w * 0.707a * L$$

Where,

$$\mathrm{f_w} = Ultimate\ Shear\ Strength = 0.6 * Tensile\ Strength$$

And the operating conditions are,

- Operating pressure = 10 bar =145 psi
- Mass = 2.5 ton = 5000 lbm
- Weight = 5,000 lbm × 32 ft/s^2 = 160,870 lbf
- Operating stress = Weight + Operating pressure = 57,042 psi = 57 ksi

Material for the weld was chosen to be 410 SS, the same as the body material, in order to minimize thermal mismatch. Weld of 410 SS has a tensile strength of 80,000 psi. According to the equation stated above, for a weld height of 0.05 in (a=0.05 in), allowable stress is 79,160 psi, which is far above the operating stress of 57,042 psi. Therefore, considering the total operating stress and material strength, it can be concluded that 0.05-inch weld height is to be welded between the flanges and the combustor body.

2.1.6. Full Combustor Assembly FEA

In this section, the Finite Element Analysis (FEA) of the complete assembly is described. A fully coupled thermal-mechanical analysis of the full assembly was performed at steady-state combustion conditions. This model explicitly considers the bolt preload and the flange loading through contact. The steady-state heat flux is assumed. While the welds were modeled, the weld calculations were performed analytically. A component list of the complete assembly is provided in Table 21. These components are subjected to FEA.

Table 21 Complete Combustor Assembly

Component Number	Component Name
1	Power Head
2	Bolt Flange Connection
3	Vertical Stand Plate
4	Bolt Stand Connection
5	Main Combustor
6	Simple Combustor
7	Exhaust Assembly

Analysis Approach:

- A 45° symmetry was considered using NX, shown in Figure 67
- The model was meshed in Altair Hypermesh and solved using a coupled temperature-displacement implicit solver in Abaqus 6.14
- The bolted connections were modeled using bolt preload and full contact to capture the coupling of the thermal strains with the bolt preload and strain energy flow due to the joint stiffness
- The combustor was modeled in the proposed “hanging” configuration
- The internal pressure of 290 psi (20 bar) was considered
- Free convection was considered for all exterior surfaces
- The heat flux due to combustion was estimated, as discussed in section d.
- Forced convection was considered for the remainder of the interior surface w
- Weld calculation by hand was performed as per Shigley’s[1]
- Bolt load calculation by hand was performed as per Shigley’s

The sections to follow will go into detail of the model approach described above.

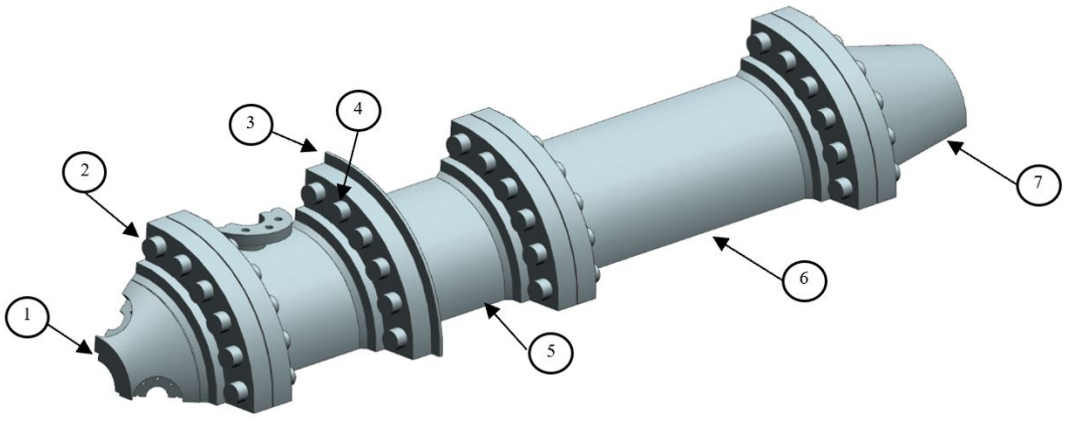

Figure 67 45° Assembly symmetry of combustor showing all components for FEA

2.1.6.1. Analysis Acceptance Criteria

The design parameters for the final design are presented below.

- The components presented have to have a minimum safety factor of 2.0 with respect to the Von Misses Stress.

- All bolted connections must have a minimum proof load factor and joint separation factor above 2.0
- All welds must have a safety of factor of 2.0 with respect to the shear stress

2.1.6.2. Mesh

Once the 45° symmetry cut was done, the model was then imported to Hypermesh 17.2 to develop a mesh of the model. Using the "solid edit" feature, the assembly of the combustor was separated into mappable solids which allows for a 3D Multi-Solid Map Mesh. In Figure 68 and 69, the solid edit feature is shown of the main combustor body, weld components, and flanges.

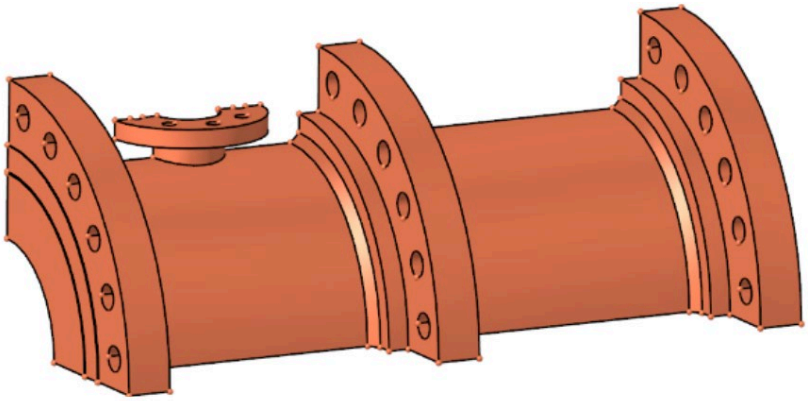

Figure 68 Import Model of Main Combustor Body

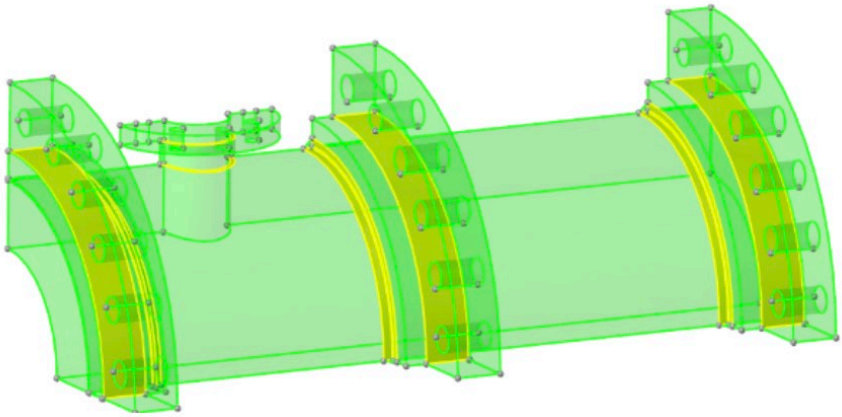

Figure 69 Mappable Solids using Solid Edit feature

The size of the mesh was varied until a 0.25 in mesh size 1st order element quads was decided upon for the main combustor body, flanges, and the bolts. For the powerhead component, a tetrahedral 0.25 in mesh was used with curvature to complete the mesh. Figures 70 and 71 show the completed mesh and detailed sections of the model.

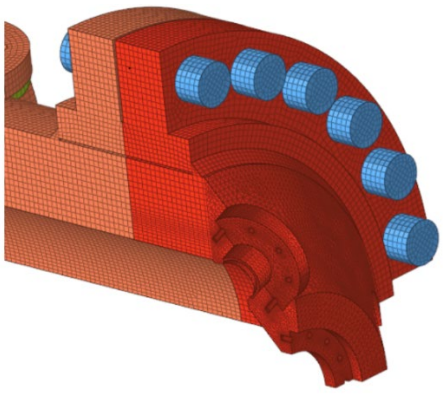

Figure 70 Zoom-in section of the powerhead mesh

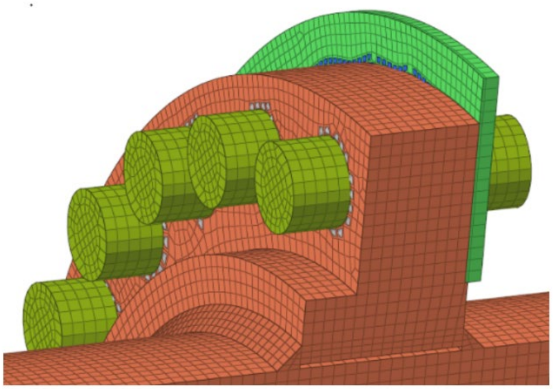

Figure 71 Zoom-in section of the flange, weld, and bolt mesh

2.1.6.3. Boundary Conditions and Materials

Once the mesh and contact interactions were created, the model was imported to Abaqus 2016 with the export solver deck feature used in Hypermesh 17. All of the contact interactions were imported as well as the contact property, which will be defined depending on the type of analysis.

Using Abaqus 2016, a total of 8 boundary conditions were defined in the model.

1. Inner Wall Heat flux
    a. $68.73 \frac{lb_f}{sec^2\, in^{2\circ} F} = 260 \frac{kW}{m^2}$
2. Gravity Load
    a. $386.1 \frac{in}{s^2} = 9.81 \frac{m}{s^2}$
3. Inner Wall Pressure
    a. 290 psi = 20 bar
4. Bolt Load
    a. 80,000 psi
5. Free Convection
    a. 530 Rankine = 25 °C
6. Thermal Contact Property

a. Thermal Conductance (Conduction)

7. Mechanical Contact Property
   a. Normal Behavior (Contact between surfaces)
   b. Tangential Behavior (Friction between surfaces)
8. Constraint at Vertical Stand Plate
   a. 6 DOF constraint

The boundary conditions are shown in Figure 72. Material properties used in the analysis are presented in Table 22.

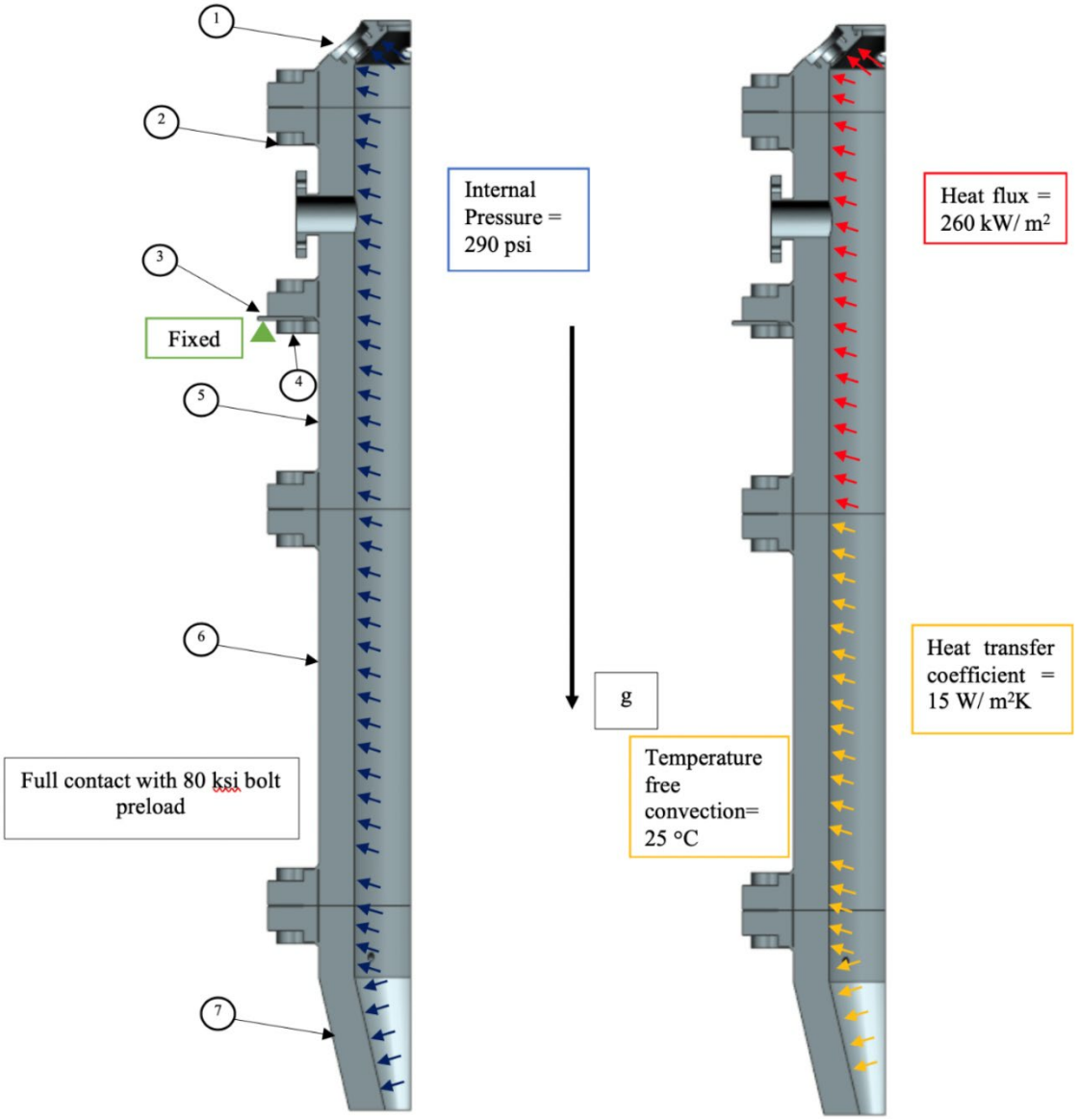

Figure 72 Boundary Conditions

Table 22 Material Properties for FEA

Material Properties						
Components	**Material**	**Density [sinches/in^3]**	**Young's Modulus [PSI]**	**Poisson's Ratio**	**Thermal Conductivity [lbf/s °F]**	**Thermal Expansion [°F]**
Combustor	410 Stainless Steel	7.25E-04	2.90E+07	0.285	3.1162	5.50E-06
Bolts	Black-Oxide Steel Grade 8	7.35E-04	2.76E+07	0.27	6.48	6.39E-06
Welds	410 Stainless Steel	7.25E-04	2.90E+07	0.285	3.1162	5.50E-06

2.1.6.4. Weld Design

Table 23 depicts the results from the analytical calculation for the welds and the criteria that was considered and met. Each section has considered the weight load and the operational load applied on the welds

Table 23 Weld Parameters

Part	**Type**	**Thickness**	**Total Load [PSI]**	**Allowable Stress [PSI]**	**Factor of Safety**	**Criteria Met**
Power Head	SS 410 Transverse fillet	0.5 in	6.00+03	1.2E+04	2.47	Yes
Main Combustor Wall	SS 410 Transverse fillet	0.5 in	6.00+03	1.2E+04	2.47	Yes
Vertical Stand	SS 410 Transverse fillet	0.5 in	6.00+03	1.2E+04	2.47	Yes
Secondary Combustor Wall	SS 410 Transverse fillet	0.5 in	3.00+03	1.2E+04	2.47	Yes
Exhaust Wall	SS 410 Transverse fillet	0.5 in	2.00+03	1.2E+04	2.47	Yes

2.1.6.5. Bolt Load

Table 24 depicts the results from the analytical calculation for the bolt load and the criteria that were considered and met. The sections are broken down by the intersection of the joints. Most of the load is driven by the preload, and the effect of the operational force is lesser.

Table 24 Bolt Load

Part	Preload [PSI]	Proof Load factor	Joint Separation Load Factor	Proof Strength [PSI]	Bolt Stress [PSI]	Criteria Met
Power Head/Main Combustor Wall	80,000	29.5	51.65	1.70E+05	8.10E+04	Yes
Vertical Stand	80,000	29.5	51.65	1.70E+05	8.10E+04	Yes
Main Combustor Wall/ Secondary Combustor Wall	80,000	31	54.20	1.70E+05	8.10E+04	Yes
Secondary Combustor Wall/ Exhaust Wall	80,000	31.4	54.86	1.70E+05	8.10E+04	Yes

2.1.6.6. Thermal Mechanical Analysis

For the thermal-mechanical analysis, the mesh type was a 3D-Stress mesh with reduced integration, and the step module a Static-General. The boundary conditions used in this analysis can be looked at in detail at a previous section of this report. Figures 73 illustrate the boundary conditions inputs into the model using Abaqus 2016

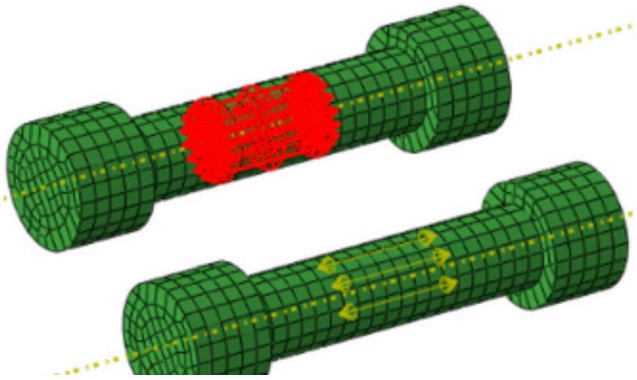

Figure 73 Bolt Load of 80,000 psi at the center of the bolt

A total of 24 bolts are included in the 45° symmetry cut of the combustor. Each bolt load was done, creating a datum plane at the center of the bolts and selecting the cross-section of each bolt for the force to act upon. The force of 80,000 psi was calculated on previous sections of this report of how much force each bolt would be subjected to.

Table 25 Thermal Mechanical Results

Part	Max Effective Stress [PSI]	Allowable Stress [PSI]	Factor of Safety	Criteria Met
Power Head	3.88E+04	9.42E+04	2.43	Yes
Main Combustor Wall	3.01E+04	9.42E+04	3.13	Yes
Secondary Combustor Wall	3.43E+04	9.42E+04	2.75	Yes
Exhaust Wall	3.45E+04	9.42E+04	2.73	Yes
Flanges	8.03E+04	9.42E+04	4.66*	Yes

In the thermal mechanical analysis results, the highest and lowest stresses that Abaqus calculates are 1.205e+05 and 2.282e+01 psi respectively. There are localized stresses under the bolt head that are less the minimum acceptable factor safety, but these are deemed to be limited by localized plasticity and will not propagate or cause significant failure

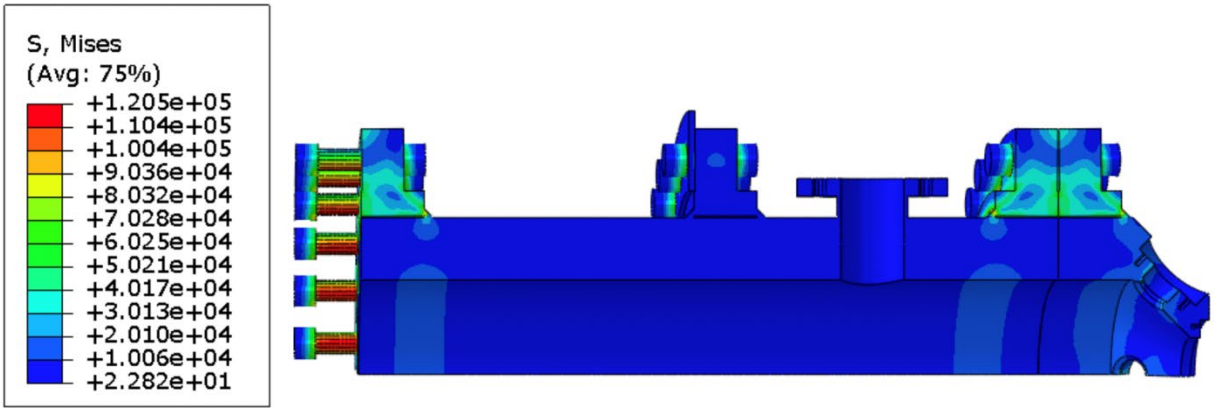

Figure 74Thermal Mechanical Stress Distribution (psi)

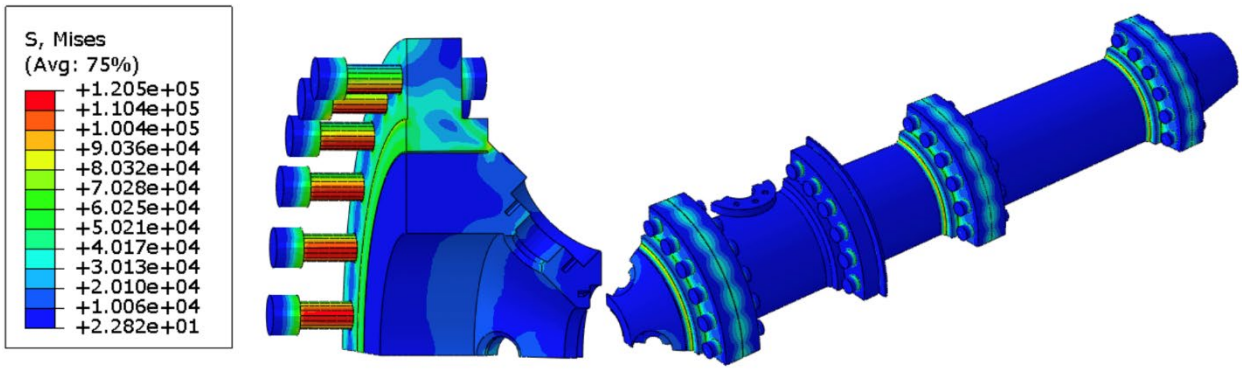

Figure 75 Thermal Mechanical Stress Distribution at the outer surfaces and zoomed- in the section of powerhead (psi)

In Figure 75, the zoomed-in section of the flange, powerhead, and bolt components gives a better visual representation of the stress distribution along with such components. The weld connection between these components can also be seen as it distributes the stress to the powerhead and flange components.

The engineering analysis confirms that the final combustor design will meet the engineering design requirements. The future will include the accusation of the combustor, inspection and assembly, preliminary qualifications, and then the shake-down test milestone.

2.2. Oxy-Coal Feed System Design

A highly autonomous delivery system was designed to operate the 1MW_{th} system. Figure 76 shows the piping and instrumentation diagram for the fuel, oxidizer, and diluent delivery system. Other subsystems included are secondary burner lines, pilot igniters, and water sprinklers. Figure 77 includes the piping and instrumentation diagram for the exhaust system and the main body.

The feed system consists of 9 lines of stainless steel seamless tubing: igniter oxidizer, igniter fuel, three cooling gas, secondary burner oxidizer, secondary burner fuel, Pintle injector oxidizer, pintle injector fuel. The gases will be remotely controlled, so that the moment the gas source is open, no human is required to be present in the test area to operate the system. For testing, oxygen and methane will be used, which will be delivered in both the secondary burner and igniter lines; the cooling gas to be used is carbon dioxide. The pintle injector will be operated with oxygen and coal slurry. In the following section, the breakdown for the gas source sheds, and the test cell will be discussed, and an explanation for each component will be provided.

The lines start with a gas tank, which would be followed by a pressure regulator. The tank will be set at a pressure that adds the chamber pressure and the pressure drop. The next component is a check valve to stop any backflow into the tanks. The following component is the pressure relief valve, which is set to be 450 psig (31 bar), and is placed next to the regulator to prevent overpressure in the line should the regulator fail. Afterward is the solenoid valve, normally closed, an electronic component that would permit the user remotely to control the valve; when is energized it would open, which would enable us to operate at a safe distance. It has a pressure transducer to read the pressure that is leaving the test cell. Afterward, the flowmeters are used to monitor the volumetric flow to confirm a steady flow of the gases. All lines are interconnected with

the carbon dioxide line, with solenoids that would be closed during operation, so that it would facilitate the purging of the lines. The solenoids previous to the intersection would be closed off to prevent the mixing of any propellant and would be opened so the entirety of the lines can be purged at the same time. The dotted line is the building break. This whole section is repeated throughout all gaseous lines, with a little variance in the carbon dioxide line.

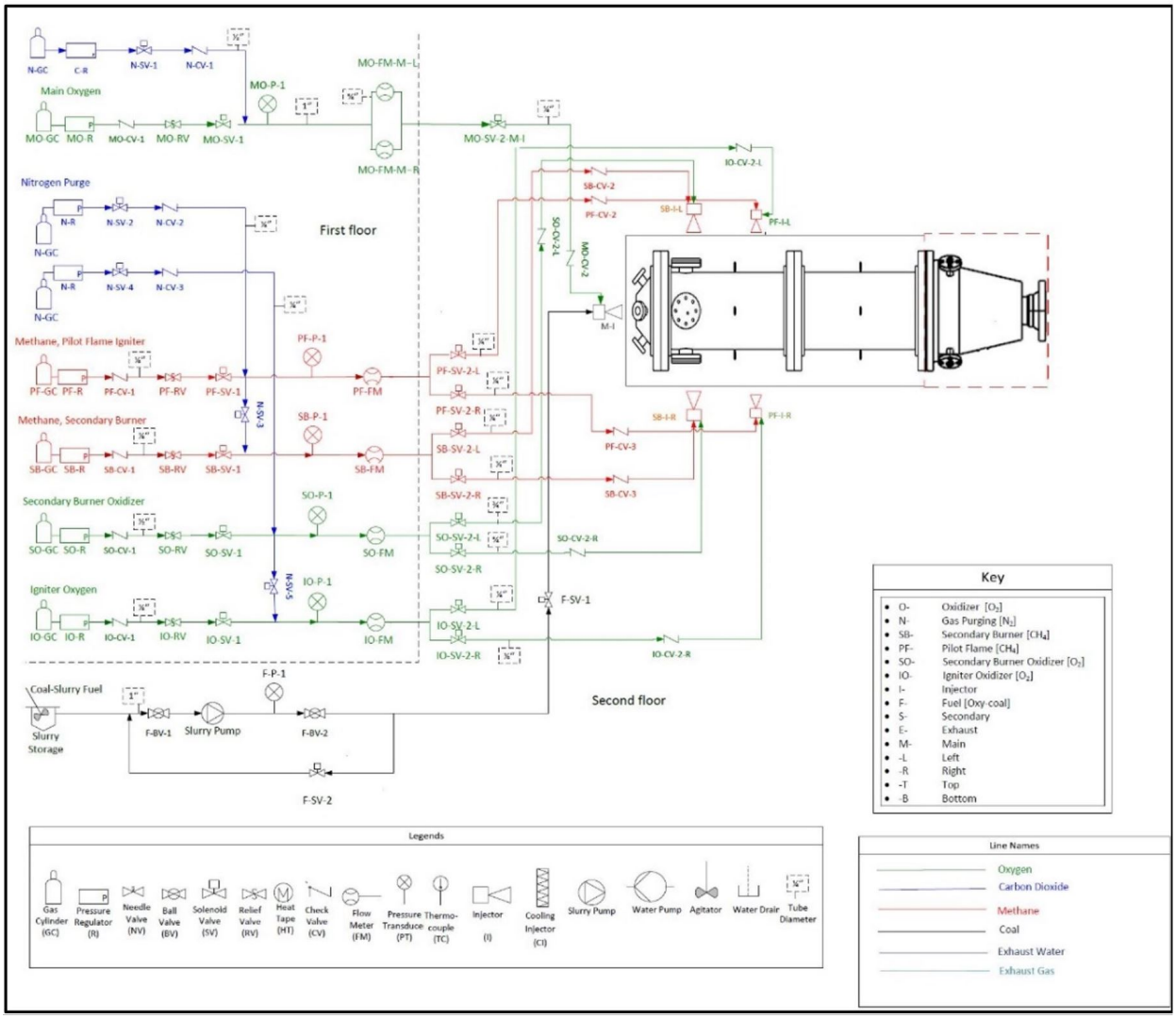

Figure 76 Piping and Instrumentation Diagram for Fuel, Oxidizer and Diluent Delivery

The coal slurry line starts at the slurry delivery tank. A manual ball valve is to introduce slurry in the feed line. A slurry pump is used to feed the flow to the pintle injector. Two solenoid ball valves are used to introduce slurry in the injector remotely. A bypass line is added. In the case of solenoid valve failure, the bypass line will prevent the slurry pump from damage.

Figure 78 shows the developed gaseous delivery system ready to be mounted at the vertical test stand.

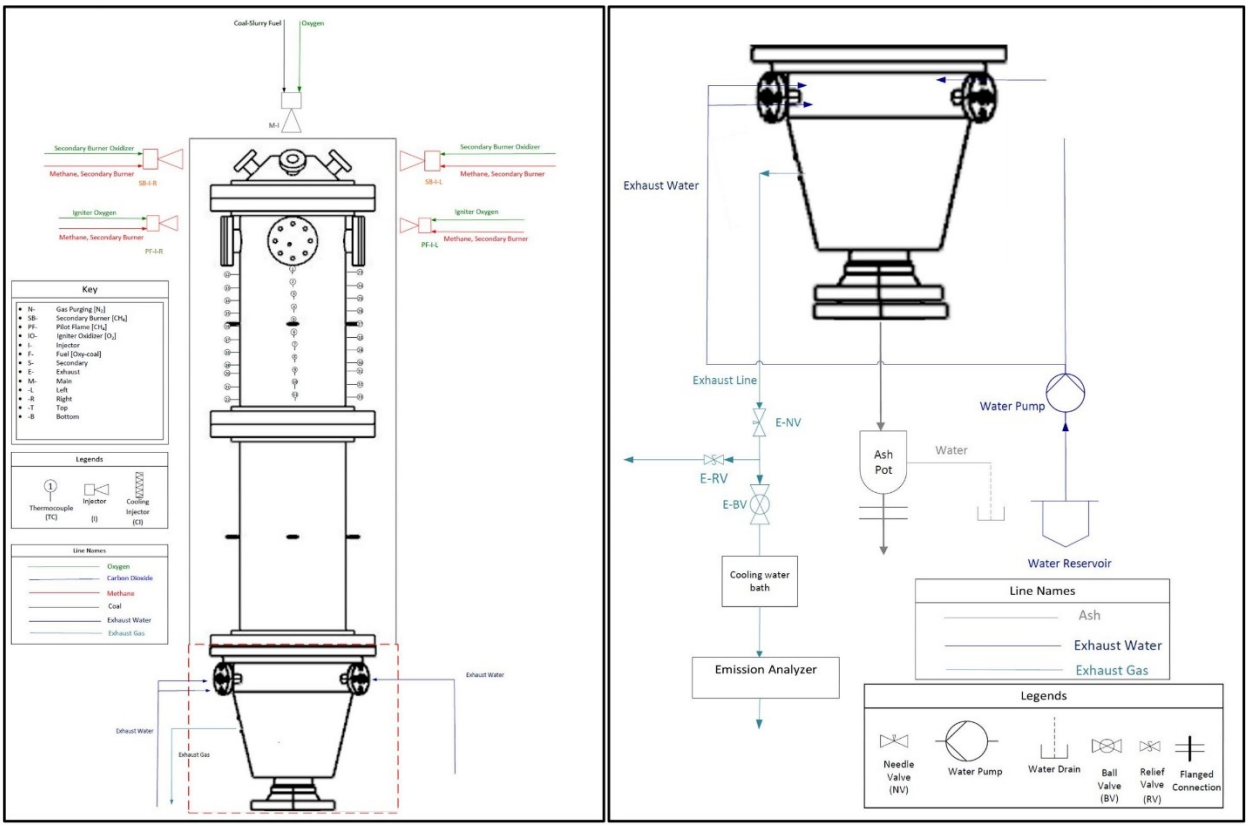

Figure 77 Piping and Instrumentation diagram combustor body (left) and exhaust system (right)

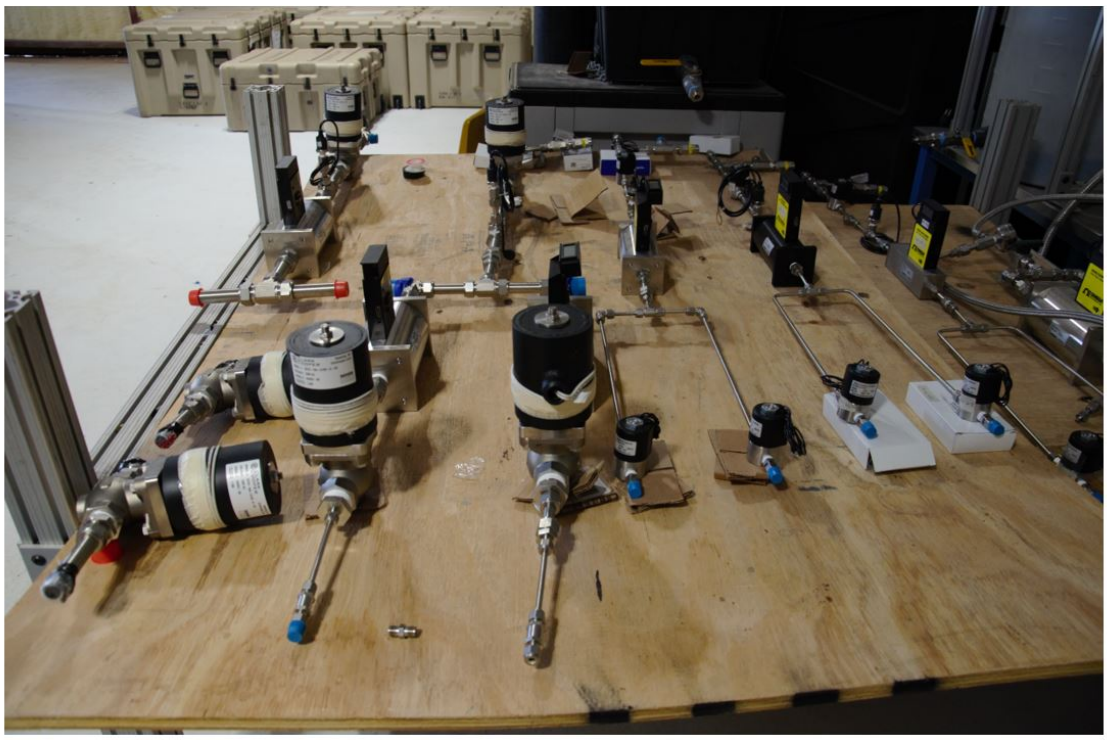

Figure 78 Developed gas delivery System

2.3. Control Station

The Control station provides supervisory, control, and data acquisition signals for both direct and alternating current devices on the burner test and the burner test feed system. The test station houses an Ethernet network allowing DAQ systems to communicate to a remote computer or data center via the fiber-optic link. The Test station provides power the test station and all HPC instrumentation via a three-phase 120 VAC/60Hz, grounded power source. The test station has the capacity of controlling up to 64 solenoids and recording data from 32 pressure transducers, 32 flowmeters, and 60 thermocouples.

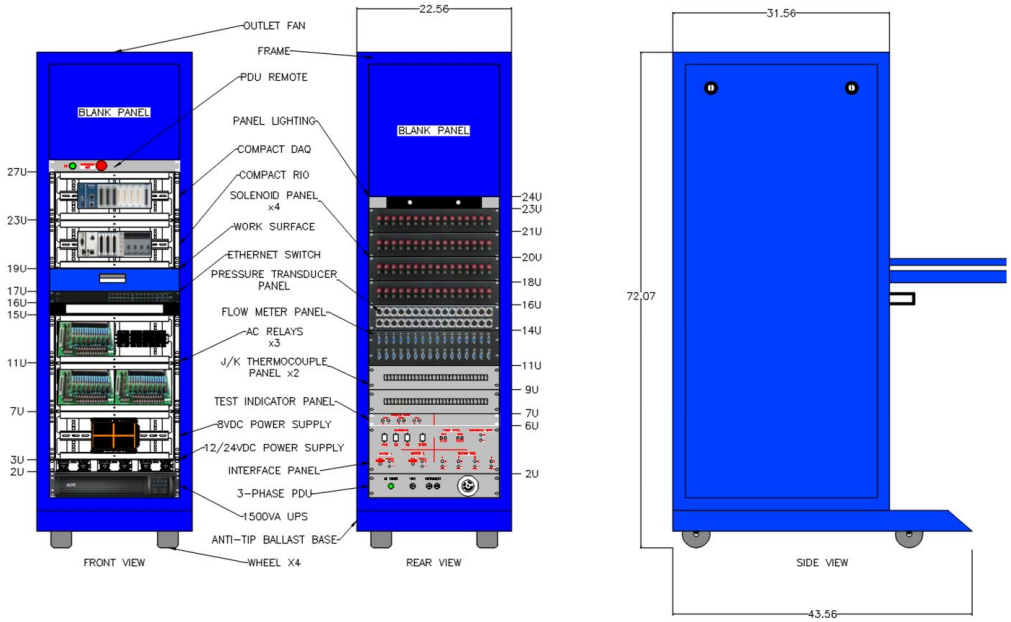

Figure 79 Control System CAD

The Emissions station houses three emissions analyzers and a required vacuum pump. Power to the analyzers is provided through a single 120 VAC/60Hz, grounded power source. The Station and each analyzer may be used as a stand-alone unit or may be connected to the Test Station network for measurement transmission to the Data Center.

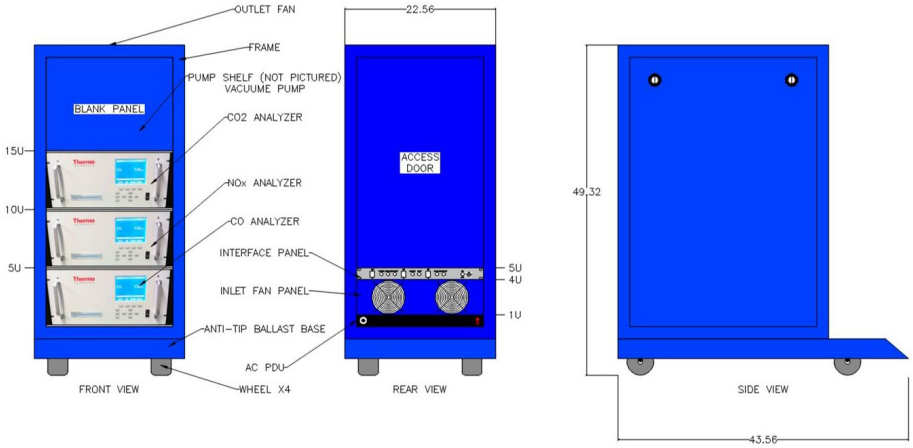

Figure 80 Emission Analyzer

Figure 81 LabView Interface

The LabView control interface can be found in Figure 81. The LabView window provides real-time information about the line pressure, line temperature, flowrates, combustor pressure, and combustor temperature. During the test, in the beginning, the lines are pressurized by manually opening the solenoid valves. The combustor is equipped with two different igniters. Two of these igniters have separate spark plugs. The spark plugs can be operated using the program. The LabView is programmed in such a way that the test can be conducted using a pre-programmed auto sequence. It also allows to record the necessary data during the test. It is also equipped with '**EMERGENCY STOP'**. The '**EMERGENCY STOP'** can be initiated due to any malfunctioning during the test. The 'EMERGENCY STOP' will also be automatically initiated if the combustor wall temperature reaches above 600K or feed line pressure exceeds 25 bar.

The electrical components interface and wiring were designed. Details instrumentation diagram of the wiring and components were made. A few examples are provided in the following figures.

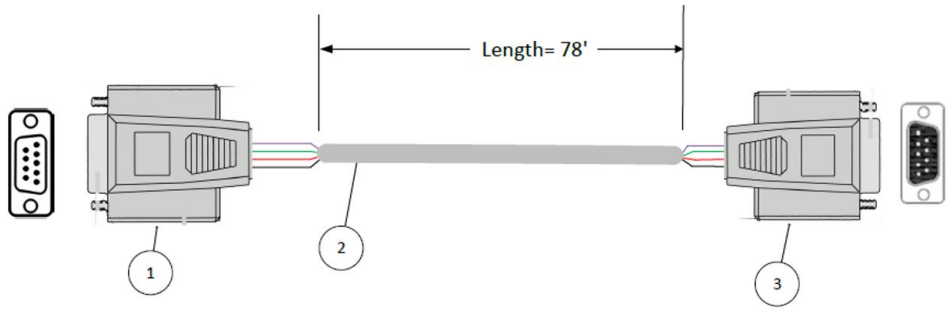

Wiring Schematic

Pin Description	
1	Not Connected
2	0- 5 VDC Output Indication
3	0- 5 VDC Output Common
4	Power Supply, Positive
5	Power Supply, Common
6	Not Connected
7	Not Connected
8	Not Connected
9	Not Connected

Component Description	
	0-5 VDC Output Indication
	0-5 VDC Output Common
	Power Supply, Common
	Power Supply, Positive

Component Description	
1	DB9 Connector Female
2	Cable: 20 AWG, 4 wires, shielded, brown outer PVC insulation
3	DB9 Connector Male

Figure 82 Instrument and wiring diagram of a Flowmeter

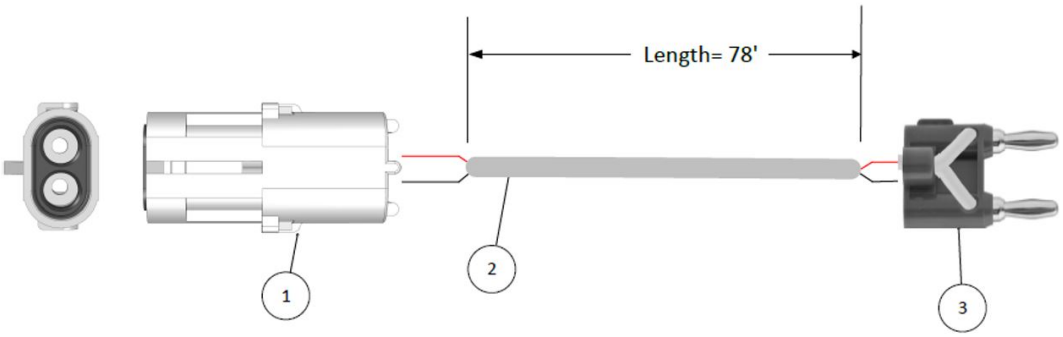

Wiring Schematic

Component Description	
———	Power Supply, Positive
———	Power Supply, Common

	Pin Description
1	Power Supply, Positive
2	Power Supply, Common

Component Description	
1	2 Pole DC Connector Female
2	Cable: 18 AWG, 2 wires, unshielded, Orange outer PVC insulation
3	2 Pole DC Connector Male

Figure 83 Instrument and wiring diagram of a Solenoid valve

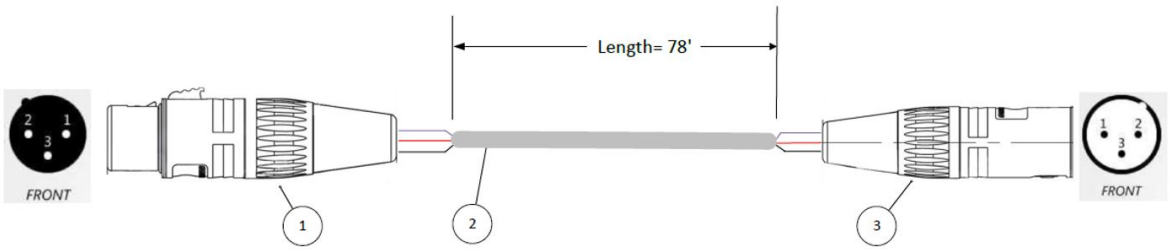

Wiring Schematic

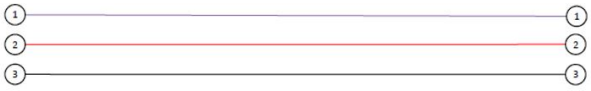

Pin Description	
1	0-5 VDC Output Indication
2	Power Supply, Positive
3	Power Supply, Common

Component Description	
	0-5 VDC Output Indication
	Power Supply, Positive
	Power Supply, Common

Component Description	
1	XLR Connector Female
2	Cable: 18 AWG, 3 wires, shielded, White outer PTFE insulation
3	XLR Connector Male

Figure 84 Instrument and wiring diagram of a Pressure Transducer

2.4. Secondary Burner and Igniter Test Facility

A 500 kW_{th} capacity high-pressure combustion system is used to test the secondary burners. The secondary burner test facility consisted of a high-pressure combustor, feed system, and control system. Figure 85 shows the high-pressure combustor used for testing secondary burners and igniters.

The high-pressure combustor is capable of testing two igniters and one secondary burner simultaneously. In addition, the combustor facilitates both atmospheric and pressurized testing. The combustor has a similar outer and inner diameter as the oxy-coal combustor. The construction material of the combustor is SS 410. The combustor is also optically accessible from the top enabling flame studies at high pressure. The operating pressure is 20 bar.

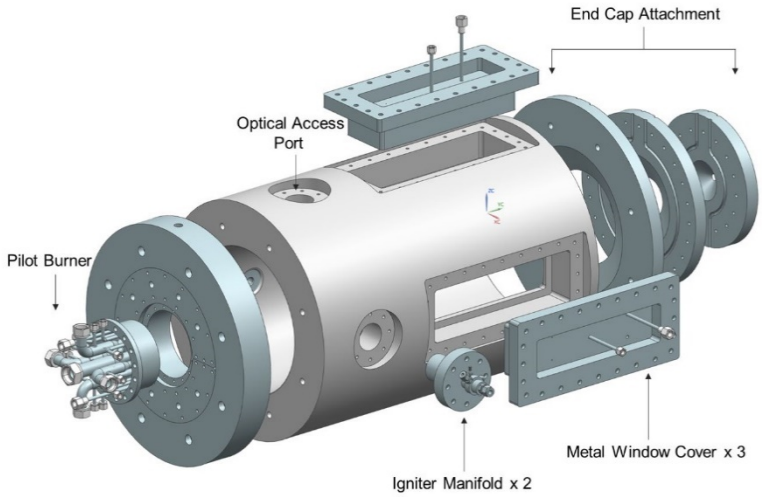

Figure 85 High-Pressure Combustor

The combustor has an exit inner diameter of 11 inch. However, to pressurize the combustor up to 20 bar, the exit area must be reduced. The combustor is pressurized by manipulating the exit area. For this purpose, the exit of the combustor is restricted using a converging nozzle. At ideal condition, the critical pressure ratio for hot combustion gas products is 0.54 [29]. The critical pressure ratio can be calculated from Eq. (34):

$$\text{Critical Pressure Ratio} = \frac{P^*}{P_0} \tag{34}$$

Where, P* is the exit pressure and P_o is the chamber pressure. During the test, the combustion products are released to the atmosphere (1 bar) [29]. Therefore, if the chamber pressure raises above 1.85 bar the flow at the exhaust will be choked. For our case, the maximum critical pressure ratio is 20. Thus, the exhaust is chocked at the exit. At choked condition, the velocity of exhaust is Mach 1 [29]. The throat area is calculated using Eq. (35)

$$\dot{m} = \frac{A\,P_t}{\sqrt{T_t}}\sqrt{\frac{\gamma}{R}\left(\frac{\gamma+1}{2}\right)^{\frac{-\gamma+1}{2(\gamma-1)}}} \tag{35}$$

The combustor end cap is designed such a way that the desired exit area can be achieved. The combustor end cap consists of three flanges. The first flange is attached with the combustor main body and the second flange is bolted onto the first flange. The diameter reduction from the first and second flanges are 7 inches and 3 inches, respectively. The third flange is attached with the second flange. The third flange is equipped to attach a small exit diameter adapter to pressurize the combustor, Figure 86.

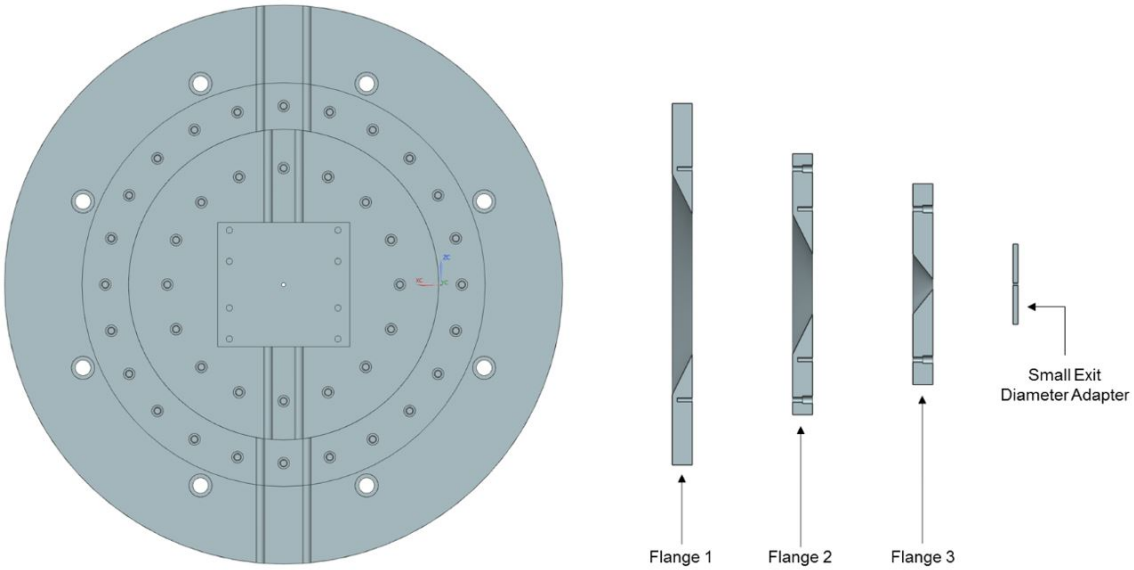

Figure 86 Combustor end cap

The feed system consists of 5 lines of stainless steel seamless tubing: Secondary burner oxidizer, secondary burner fuel, cooling gas, igniter oxidizer, igniter fuel. The gases will be remotely controlled, so that the moment the gas source is open, no human is required to be present in the test area to operate the system. For testing, oxygen and methane will be used, which will be delivered in both the injector and igniter lines; the cooling gas to be used is carbon dioxide. In the following section, the breakdown for the gas source sheds, and the test cell will be discussed and an explanation for each component will be provided.

The feed system consists of a bank of gas tanks fitted with tank regulators, needle valves, solenoid valves, manual ball valves, thermocouples, pressure transducers, and flowmeters. The fuel, oxidizer, and diluents are delivered from K-bottles. The K-bottles are situated in two different locations. The K-bottles for the main burner is located 15 m away from the combustor. On the other hand, the K-bottles for the igniters is located adjacent to the combustor. The detailed view of the feed system can be found in Figure 87. The area bounded by the red rectangle is located 15 m away from the main test side. This is where the main burner gas tanks are situated. The gas tank regulators are selected based on the test conditions. The maximum operating pressure during the test is 20 bar. Therefore, the tank regulators are selected to provide up to 35-bar delivery pressure. The needle valves are positioned right after the regulators. This facilitates controlling the gas flow during the test if necessary. During the test, carbon dioxide is used as the diluent. A thermocouple is placed in the diluents line. The carbon dioxide possesses the threat of condensation during the expansion process. The thermocouple measures the gas temperature in the line. The normally closed solenoid valves are put in the line to remotely control the flow. The solenoid valves have a response time of 0.5 s for opening the valves. The manual ball valves are placed to control the gas flow and isolate different system sections. The abundance of manual ball valves and solenoid valves enhance system compartmentalization and safety. These valves also provide enhanced control during the operation of the system.

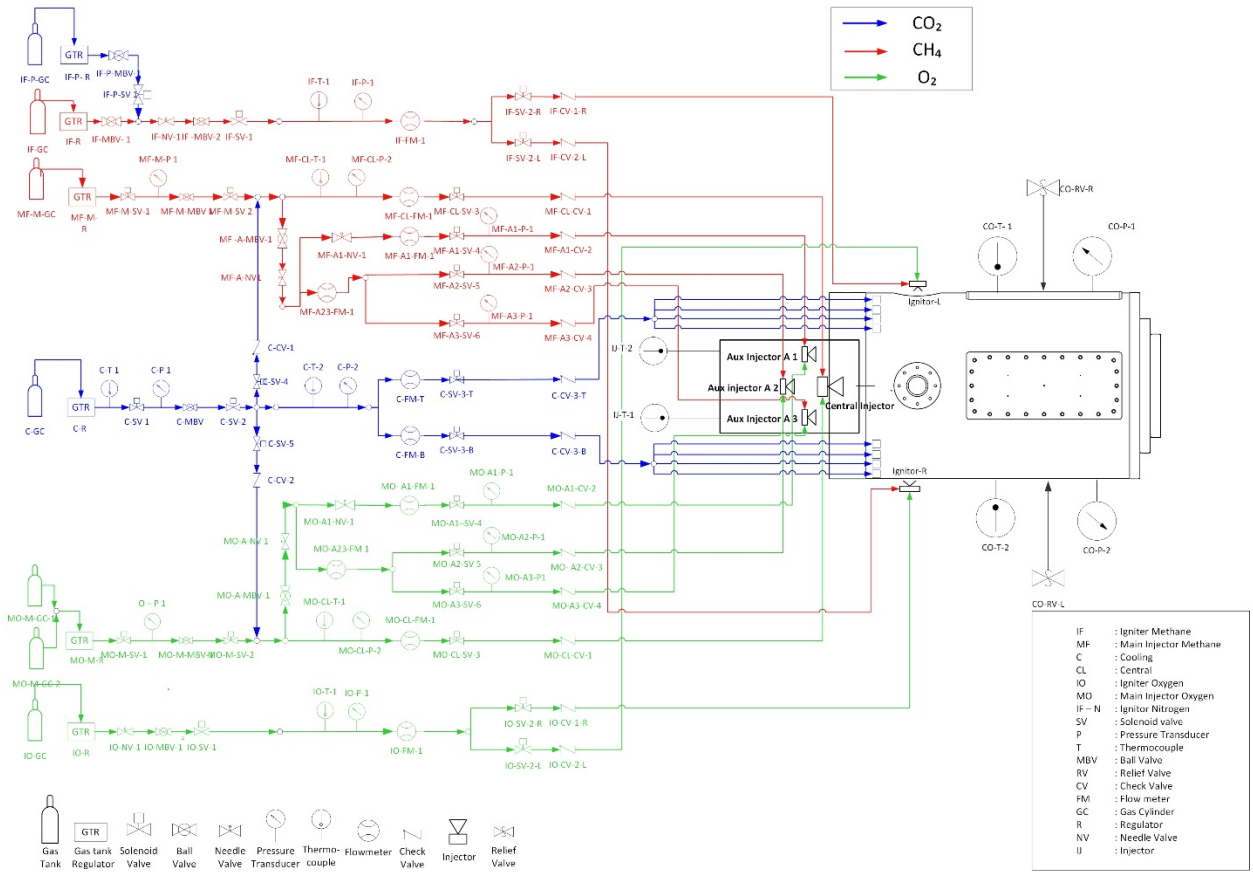

Figure 87 High Pressure combustor piping and instrumentation diagram

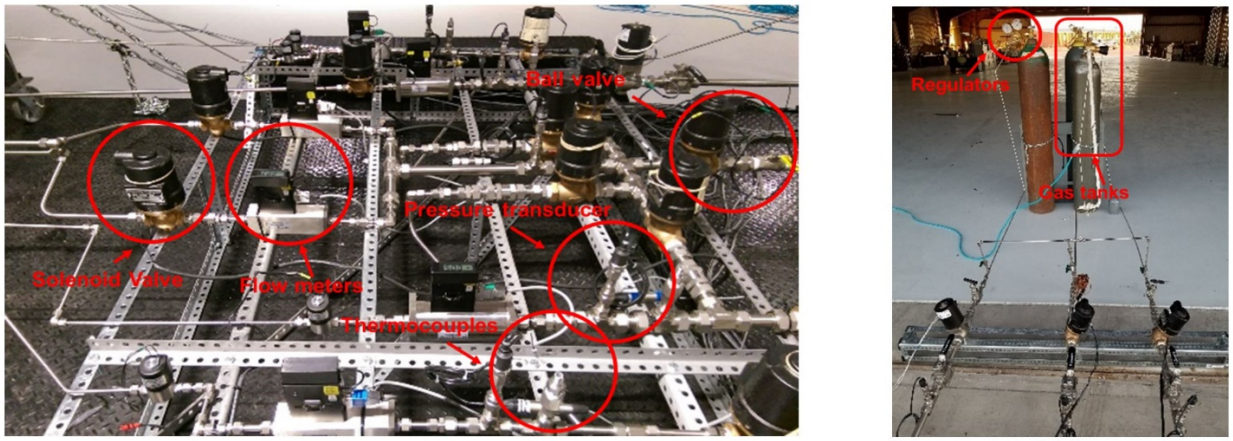

(a) (b)

Figure 88 (a) Valve train (b) Valve train close to the main burner gas tank facility

The methane and oxygen tank regulators have 1/4” (6.35mm) compression outlet connections. The carbon dioxide tank regulator has 1/2” (12.7mm) compression outlet connections. The 15m tubing between the main burner methane, oxygen, carbon dioxide gas tanks and the trailer valve train are 1” (25.4mm) tubing. An adapter is used to convert the 1/4” (6.35mm) and 1/2” (12.7mm)

tubing to 1” (25.4mm) tubing. Afterward, different sizes of adapters are used to feed fuel, oxidizer, and diluents into the combustor. The inlet connections for the main burner fuel is 1/4” (6.35mm) and oxidizer connection is 3/4” (19.05mm) tubing. The inlet connections for the igniter and burner fuel and oxidizer ports is 1/4” (6.35mm) and 3/8” (9.53mm) tubing, respectively. The cooling manifold has eight inlets. The inlet connections for the cooling system manifolds are 1/2" (12.7 mm). The feed lines are leak checked using nitrogen gas. The detailed images of the feed system can be seen in Figure 88.

A control system with a similar capacity is used for this system. The control system allows the remote operation of the system using optical fiber transmission. A LabView interface is used for operating the system. The test facility layout is seen in Figure 89.

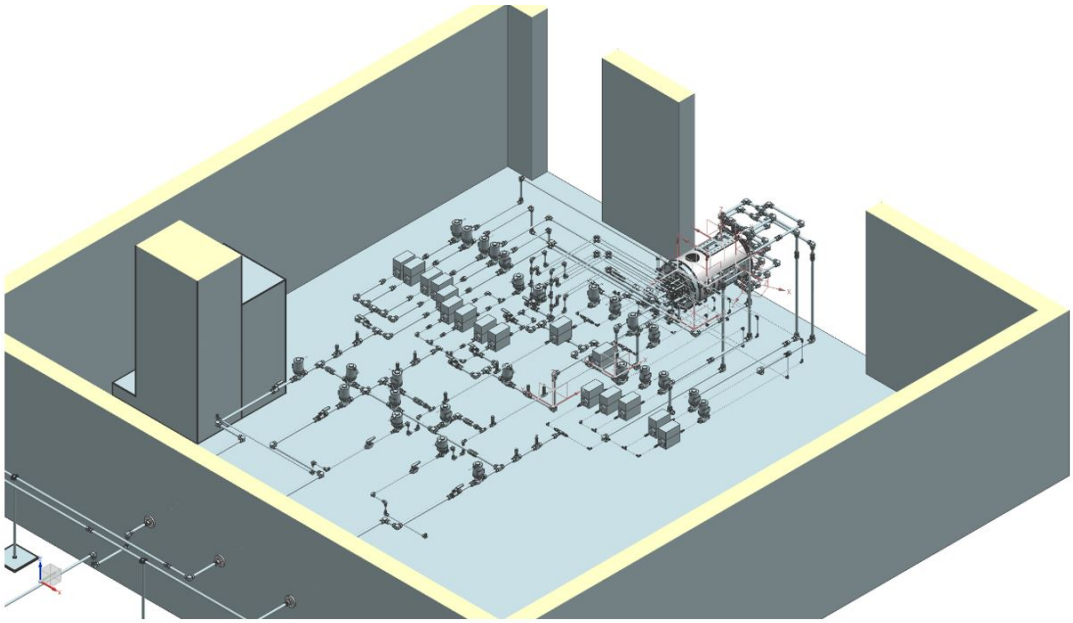

Figure 89 Test facility schematic

2.4.1. Additively Manufacturable Burner Test Capacity

The current high-pressure combustion facility also enables testing of additively manufacture smart secondary burners with integrated temperature sensing capabilities. A shear coaxial burner was designed for using with oxy-coal system. The methane-oxygen shear-coaxial burner is able to operate up to 500 kW power input and 20 bar pressure. The shear-coaxial injector utilizes the shear forces between the fuel and oxidizer to mix [21]. The shear forces are driven by the momentum flux difference between two streams. The injector was manufactured using the Electron Beam Melting (EBM), a metal 3D Printing technique. The burner can be seen in Figure 90.

The total power is divided among one primary and three secondary injectors. The center injector is the primary injector where the circumferential injectors are the secondary injectors. Each of the injectors is designed in such a way that the center port delivers methane and oxygen. The step-down geometry of the injectors is made to create a pressure drop across the line. Although the fuel and oxidizer doesn’t mix before it reaches into the combustion chamber, the pressure drop across the line helps in preventing the flame from propagating inside the line in case of any emergency. The primary injector is designed to carry between 40 to 275 kW and each secondary injector 15 to 75 kW. The velocity ratio and momentum flux ratio are kept similar for both primary

and secondary injectors. The detailed breakdown of power inputs, mass flow rate, velocity flowrates, and momentum flux ratios are shown in Table 26. The actual burner is shown in Figure 91.

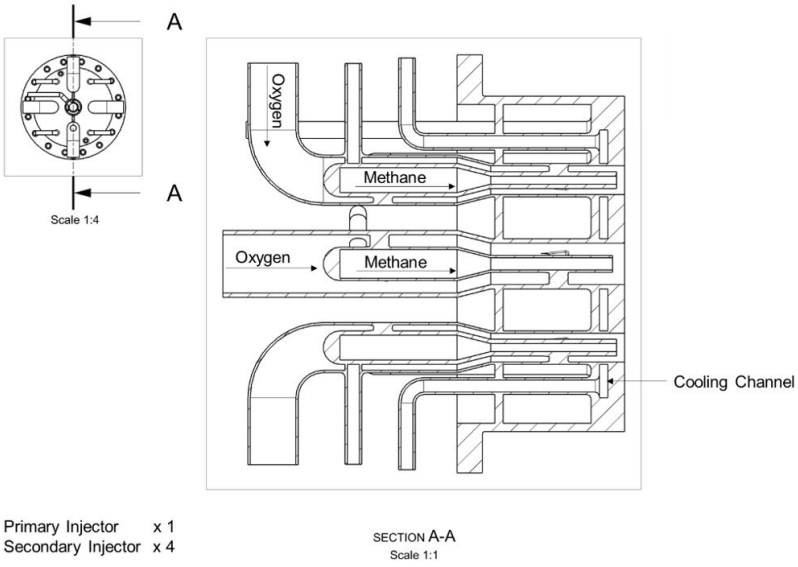

Figure 90 Burner cross-sectional view

Table 26 Burner Parameters

	Primary Injector	Secondary Injector (Each)
Power Input (kW)	40 - 275	15 - 75
CH_4 mass flowrate (kg/s)	0.0008 - 0.004	0.0003 - 0.0015
O_2 mass flowrate (kg/s)	0.0032 - 0.016	0.0012 - 0.006
CH_4 velocity (m/s)	3.5 - 18	3.5 - 17
O_2 velocity (m/s)	0.75 – 3.5	0.75 – 3.5
Momentum flux ratio	≈12	≈12

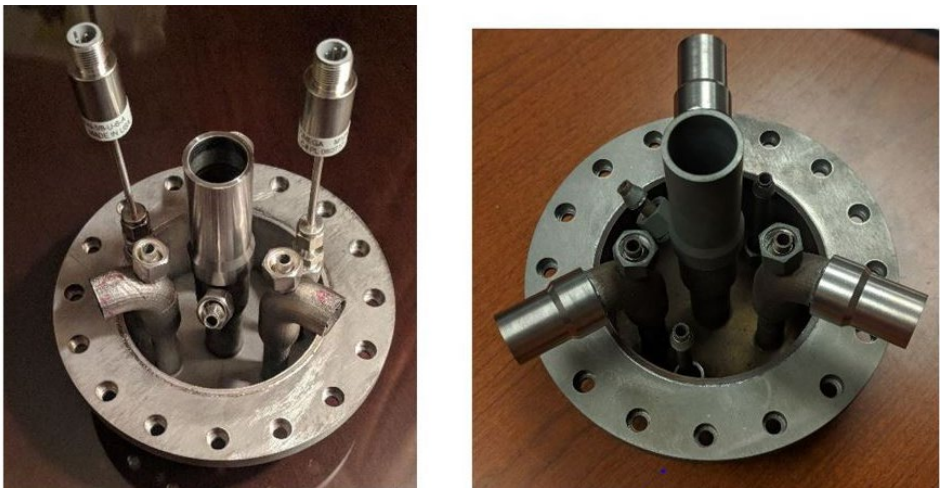

Figure 91 Additively Manufactured Secondary Burners with integrated thermocouple

2.5. Test Stand

A vertical test stand is built for carrying out this experiment. The test stand will be used to vertically mount the combustor. The combustor will be chained to the stand using eye bolts welded on the combustor wall. The powerhead will be on the top side along with the piping. The exhaust system of the combustor will be placed downwards to collect ash and other by-products. A tube leading to the ground will be attached to the end of the exhaust will aid in deposing the wastes. The test stand is presented in Figure 92 and Figure 93

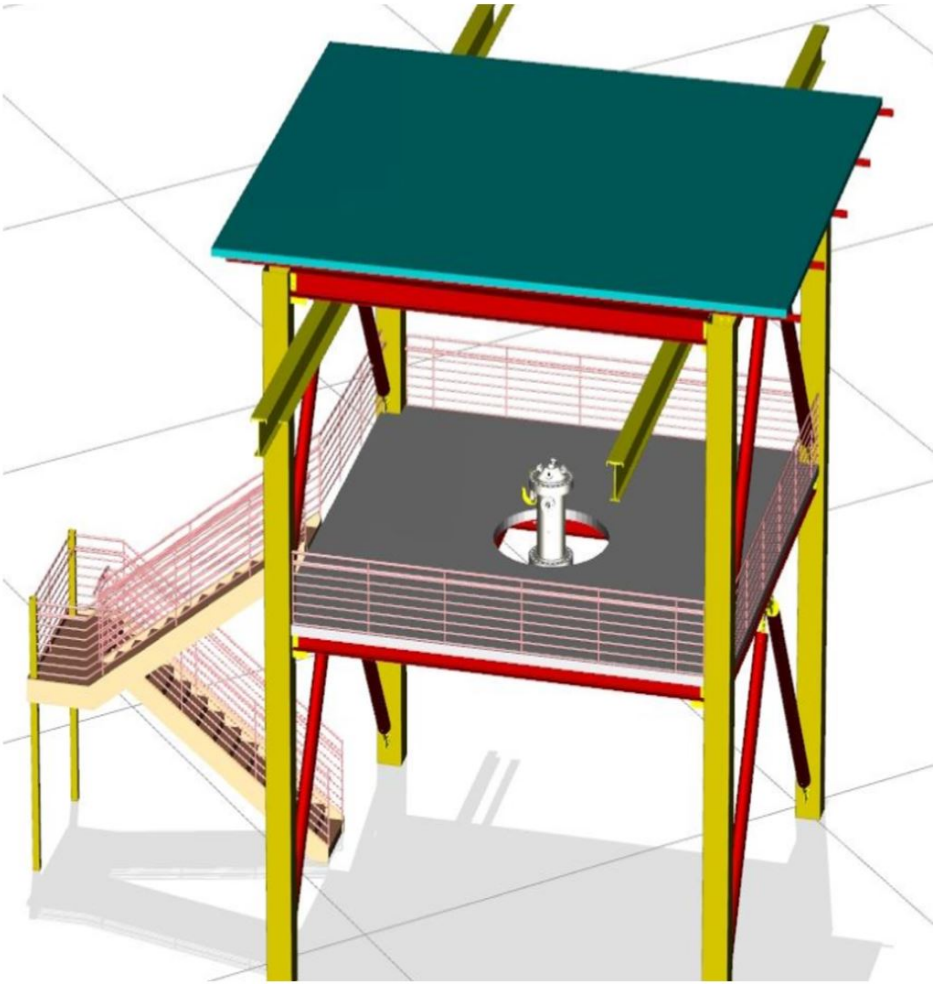

Figure 92 Test stand CAD

Figure 93 Vertical Test Stand

2.6. Combustor Assembly

The high-pressure swirl oxy-coal combustor is in the process of being assembled inside a Vertical Test Stand. This will be accomplished by connecting each section of the combustor through bolting flanges. Each flange is a 300-class flange of 28 in of OD and 18.18 in of ID. To secure the combustor into the Vertical Test Stand, supporting plates will be placed around the opening were the combustor will fit. Additionally, extensions around the Powerhead flange (denominated as "ears") will be included, to support the weight of the combustor at that point. A complete assembly of the combustor is presented in Figure 94 with the supporting plates via powerhead flange ear connections. Figure 95 presents a CAD model of the combustor assembly in the test stand.

A detailed assembly plan is presented in **Appendix B.**

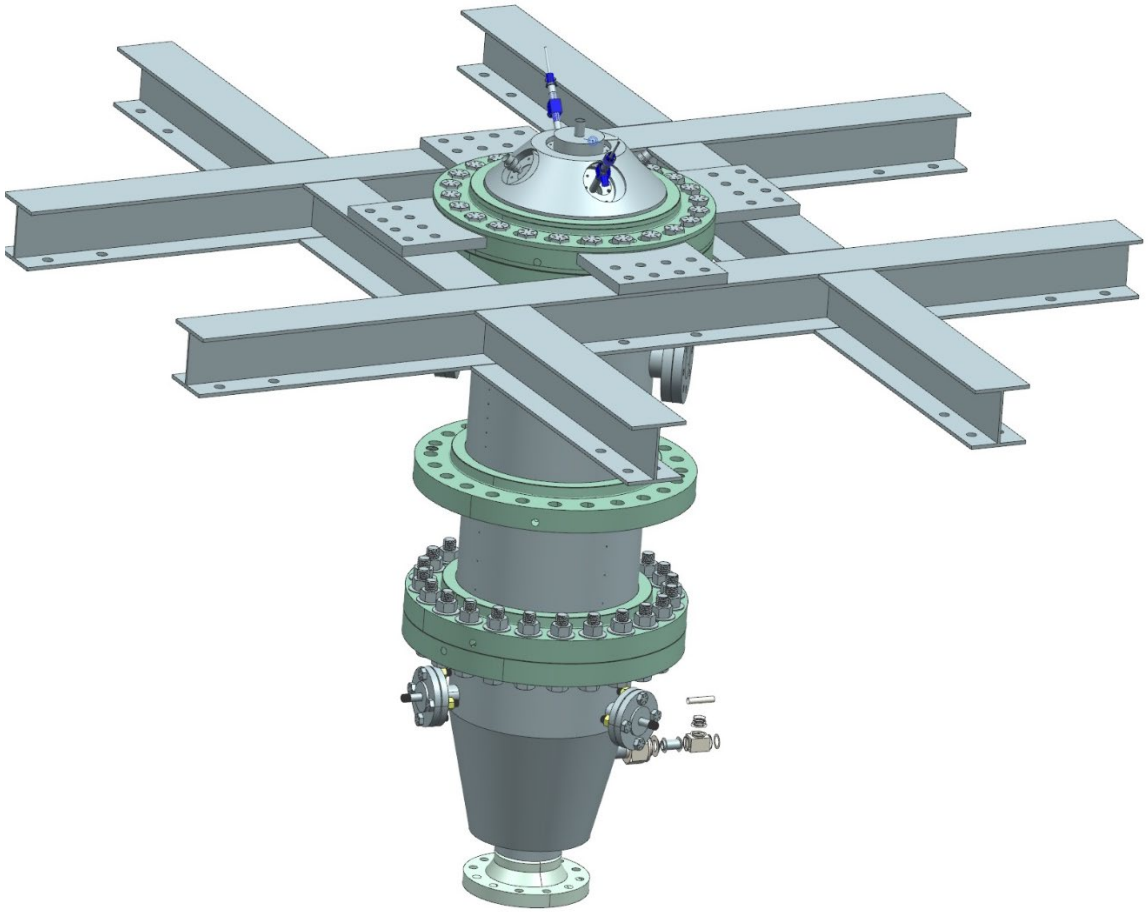

Figure 94 Combustor assembly connected to the supporting plates using the powerhead flange welded ears

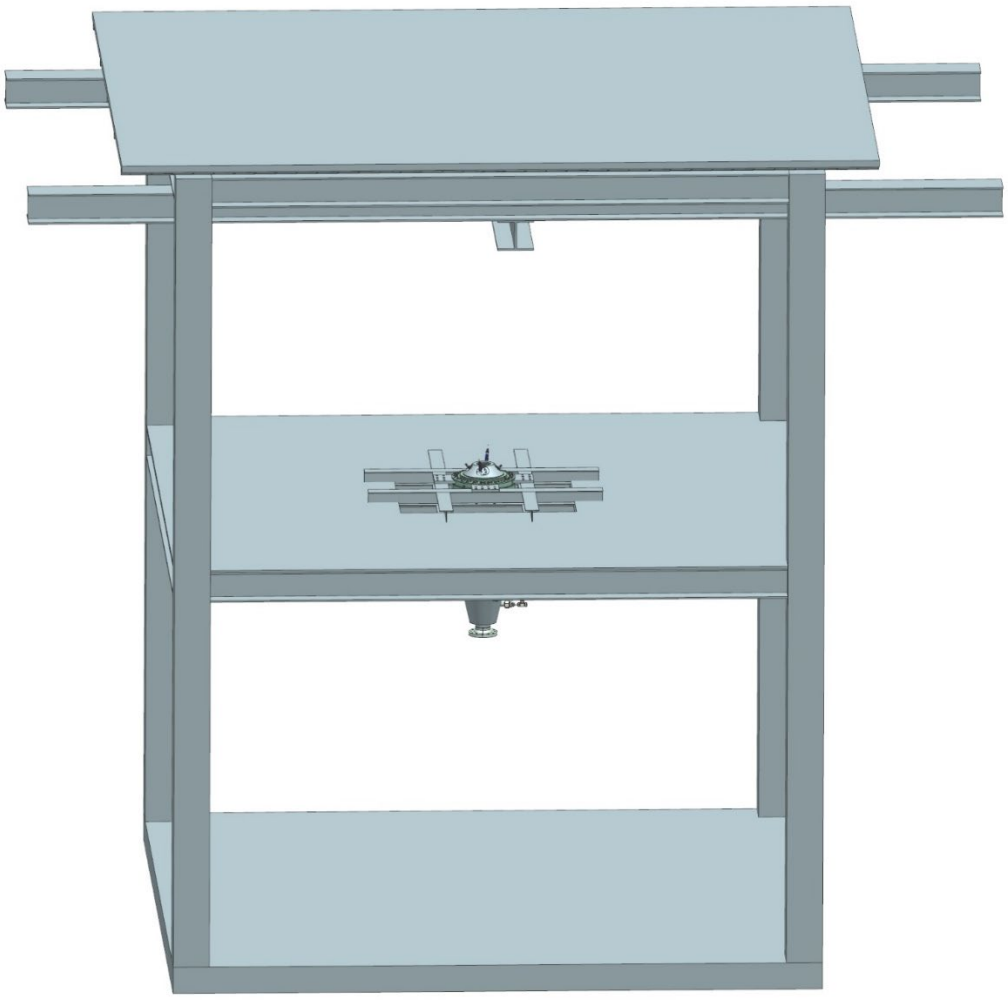

Figure 95 CAD of Combustor Assembly in the test stand

3. Chapter 3: Experimental Analysis

3.1. Pilot Burner Hot Fire Test

A high-pressure combustion system mentioned in the previous chapter is used to validate the operationality of the igniters and secondary burners. The igniters are tested below 3 bar chamber pressure to validate successful ignitions. The secondary burners are tested up to 20 bar chamber pressure to confirm operability.

3.1.1. Atmospheric Test

Before conducting the pilot burner test, the ignition system was tested extensively to ensure igniter reliability. Ignition system test conditions can be found in Table 27.

Table 27 Ignition system test parameters

Case	Test Duration (seconds)	Oxygen Inlet Pressure (psig)	Methane Inlet Pressure (psig)	Oxygen Mass Flowrate (kg/s)	Methane Mass Flowrate (kg/s)	
Case 1	2s	150±5	150±5	0.004±.0005	0.002±.0005	Igniter 1
Case 2	5s	150±5	150±5	0.004±.0005	0.002±.0005	Igniter 1
Case 3	2s	150±5	150±5	0.004±.0005	0.002±.0005	Igniter 2
Case 4	5s	150±5	150±5	0.004±.0005	0.002±.0005	Igniter 2

Once the ignition system operation was established, a 10s test was conducted with the burner power input of 30kW. The igniter inlet pressure remained at 150 psi. The test was conducted at the atmospheric condition inside of the combustor. At first, the feed lines were manually primed. Afterward, the auto sequence was initiated to perform the actual 10s test. The igniter is kept ON for 3s. During this time, the pilot burner fuel-oxidizer mixer was injected and ignited. The detailed test sequence and burner operating conditions can be found in Table 28 Table 29 respectively. Figure 96 shows the flame ignition, propagation, and stabilization at different time steps during the test.

Table 28 Test Sequence

			Status	**Time Step**	**Run Time**
Priming Sequence (Manual)					
Step	1	_____Open IO-SV-2			5s
Step	2	_____Close IO-SV-2			
Step	3	_____Open PF-SV-2			5s
Step	4	_____Close PF-SV-2			

Step	5	_____Open F-SV-1			5s
Step	6	_____Open F-SV-2			5s
Step	7	_____Close F-SV-2			
Step	8	_____Open O-SV-1			5s
Step	9	_____Open O-SV-2			5s
Step	10	_____Close O-SV-2			
Step	11	_____Open C-SV-1			5s
Step	12	_____Open C-SV-2			
Step	13	_____Close C-SV-2			
Test Sequence (Auto)				(0s-9s)	
Step	14	All Close (Sparker ON)		0s	
Step	16	OPEN IO-SV-2, PF-SV-2, F-SV-2, O-SV-2, C-SV-2		1s	
Step	17	OPEN IO-SV-3-R, IO-SV-3-L		2s	
Step	18	OPEN PF-SV-3-R, PF-SV-3-L	Ignition Flame ON	3s	
Step	19	OPEN O-SV-3, F-SV-3 (Burner Flame ON)	Ignition Flame ON, Burner Flame ON	4s	
Step	20	OPEN C-SV-3	Ignition Flame ON, Burner Flame ON	5s	
Step	21	CLOSE (PF-SV-3-R, PF-SV-3-L, O-SV-3, F-SV-3, IO-SV-2, PF-SV-2,)	Burner Flame ON	6s	
Step	22		Burner Flame ON	7s	
Step	23		Burner Flame ON	8s	
Step	24	CLOSE (O-SV-3, F-SV-3, C-SV-3, O-SV-2, F-SV-2, C-SV-2)	Test End	9s	

Table 29 Burner Operating Conditions

Case	Test Duration (seconds)	Oxygen Inlet Pressure (psig)	Methane Inlet Pressure (psig)	Oxygen Mass Flowrate (kg/s)	Methane Mass Flowrate (kg/s)

Case 1	10s-20s	25±5	15±5	0.0006±.0001	0.0024±.0001

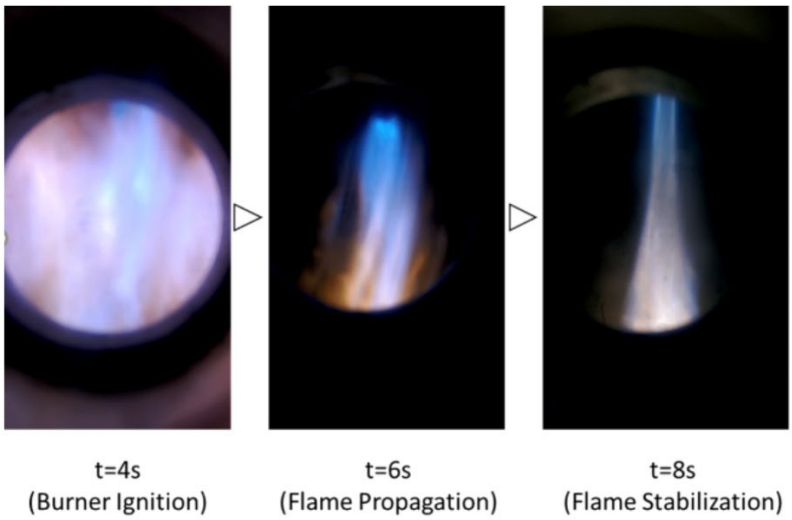

Figure 96 Flame structure captured from igniters at t=4s and then burner at t=8s

3.1.2. Pressurized Test

During the experiment, the main burner is ignited using the pilot flame. The igniter is run for 4s. During the last 2s of the igniter operation, the main burner fuel and oxidizer line are opened and the main burner is ignited. The main burner is operated for 20s. Figure 97 shows the main burner flame. It can be seen that the flame is yellow in color, characteristic of a fuel-rich environment. Figure 98 demonstrates the ignition of the gases in the combustor. Figure 99 shows the flame during the primary burner test. The O/F ratio during the main burner operation is 3.3. During operation, the flame is yellow, signifying a methane-rich flame. It can also be observed that the flame is highly turbulent and has the initiation of a wrinkled flame front. The volumetric flow rates for the igniter methane, igniter oxygen, main burner methane, and main burner oxygen is shown in Figure 100(a). The O/F ratio during the igniter operation is close to 2, which is fuel-rich. The corresponding pressure curve for the experiment is seen in Figure 100(b). Figure 100(b) shows that the chamber pressure initially rises up to 2 bar as the igniter is initiated. The flow through the main burner is then initiated after 2s of igniter operation. Thus, there are 2s of overlapping operations between the main burner and the igniter. The oxygen volumetric flowrate initially spikes up to 1100 standard liters per minute (SLPM) and gradually decreases to 500 SLPM, Figure 8(b). The chamber pressure during the operation raises up to 7 bar Figure 100(b).

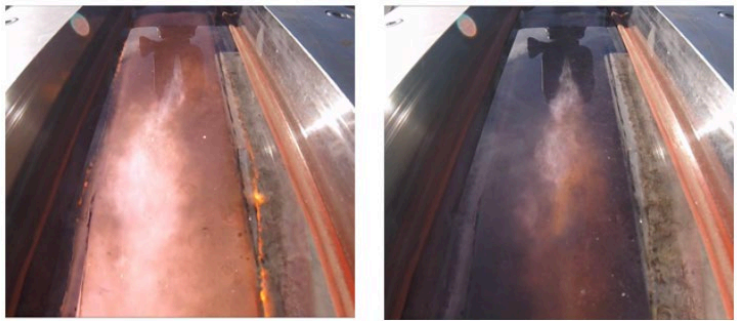

Figure 97 Main burner flame initiation

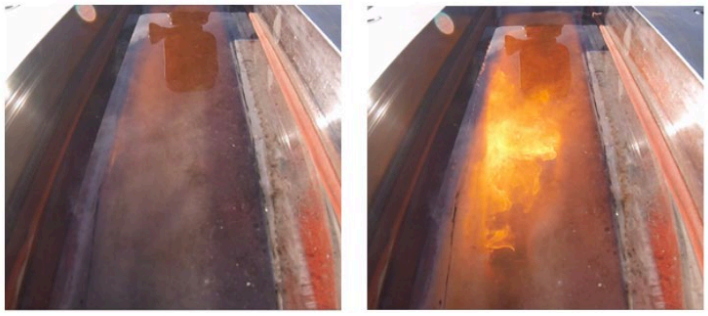

Figure 98 Igniter flame initiation

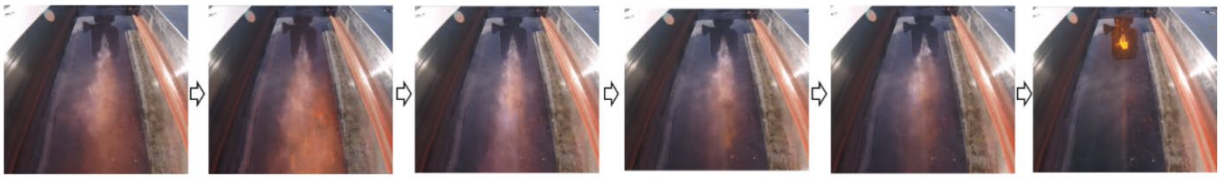

Figure 99 160 kW and 7 bar flame images during the test

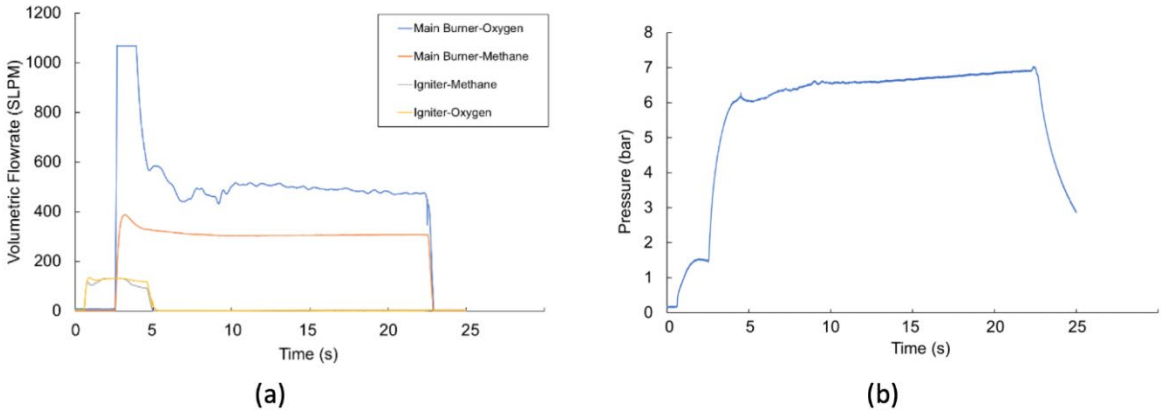

Figure 100 Volumetric flowrate and (b) Pressure vs. time during an experiment

3.2. Cold Flow Test

The purpose of the experimental study of the pintle injector is to observe and record the spray pattern and cone angle from the burner. The cone angle is the distance from the centerline of the injector to the edge of the spray cone measured using optical methods described later in this section. The fluids that are initially being used are water and nitrogen injected through the ports of the pintle injector with a steady, constant flow. Water flow is delivered from a pump at 10 bar, and nitrogen is delivered from K-bottles at the same pressure.

- Injector Pressure: **1 to 10 bars (145 PSI)**
- Duration of Test: **1 to 5 minutes**
- Temperature: **25˚ to 40˚C**
- Fluids Used: **Water and Nitrogen**

3.2.1. Test Facility

The test apparatus includes water container, gas tanks, fluid delivery systems, and pintle injector. The piping and instrumentation diagram and photograph for the fluid delivery system can be found in Figure 101 and Figure 102, respectively. A instrumentation list can be found on Table 30. The injector data is presented in the metric unit.

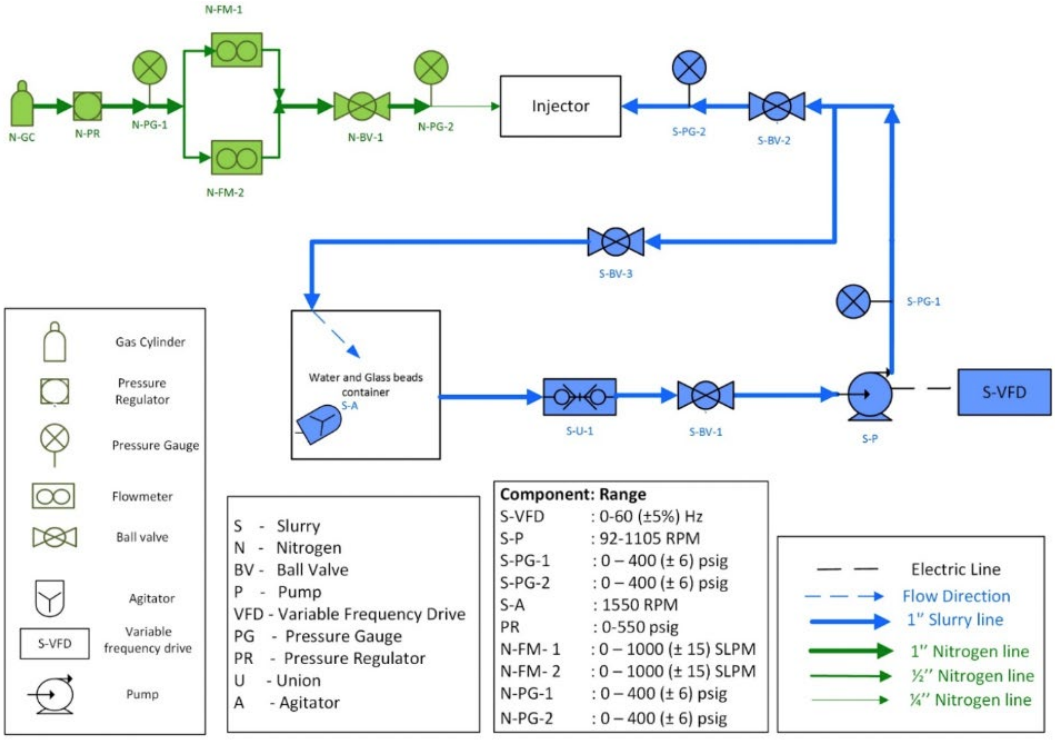

Figure 101 Piping and Instrumentation Diagram for cold flow test of the pintle injector

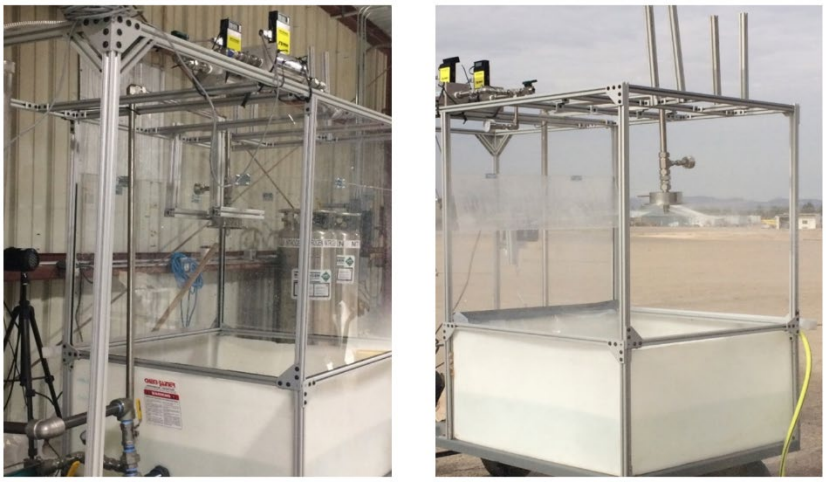

Figure 102 Photograph of actual water test system being used with pintle injector

Table 30 Instrumentation list corresponding to Figure 101

SLURRY LINE		
Schematic Notation	**Part Type**	**Range**
S-MV-1	Manual Valve	-
S-MV-2	Manual Valve	-
S-MV-3	Manual Valve	-
S-FC	Frequency (Pump) Controller	0-60 (±5%) Hz
S-P	Pump	92-1105 RMP
S-DT	Drain Tank	-
S-PG-1	Pressure Gauge	0 – 200 (± 6) psig
S-PG-2	Pressure Gauge	0 – 200 (± 6) psig

NITROGEN LINE		
Schematic Notation	**Part Type**	**Range**
N-GC	Gas Cylinder	-
N-PR	Pressure Regulators	0-550 psig
N-MV-1	Manual Valve	-
N-FM	Flowmeter	0 – 1000 (± 15) SLPM
N-PG-1	Pressure Gauge	0 – 450 (± 6) psig
N-PG-2	Pressure Gauge	0 – 450 (± 6) psig

3.2.2. Shadowgraph system

Visualization of the spray is being done in order to determine patterns and cone angles from the injector. Images from the injector are being captured using a shadow sizing imaging setup. The technique uses the refraction of light to create a shadow that is captured by a high-speed camera connected to a computer. A FlowSense camera from Dantec Dynamics is used which records with a speed of 5000 fps with 29 megapixel resolution, interframe time of 200 ns, and pixel size of 5.5 µm. A glass diffuser plate is placed between a light source and the test setup which creates shadows of the streams and droplets and are analyzed using the computer software. Figure 103 shows the schematic of the shadowgraph system. Results from the testing are expected to be presented in the upcoming quarterly report.

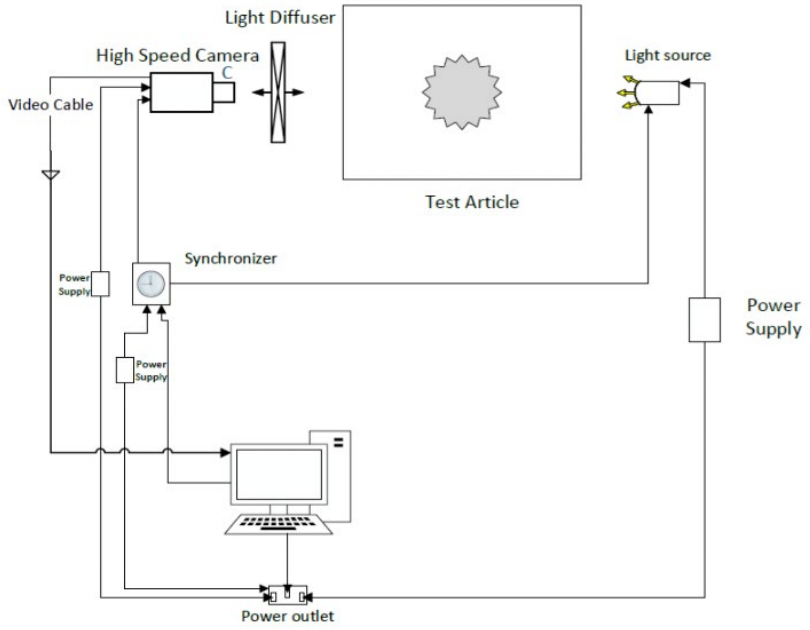

Figure 103 Shadow sizing experimental setup to characterize injector performance

3.2.3. Glass Beads-Water Slurry Tests

Initially, water-glass beads slurry was used to characterize the spray pattern of the injector. Glass beads with 20 µm mean diameter was mixed with water to create the slurry. Test operations produced shadowgraph photos of the injector spray. The initial test is geared to generate a baseline. Subsequent tests will ultimately be evolved into analyzing spray characteristics of a working fluid that will have similar characteristics to the coal-water slurry mixture. In addition, these tests also enable the characterizing effect of pintle hole sizes.

3.2.3.1. Operating Conditions

The following tables detail the test conditions that were assessed. Table 31 presents pintle tip designs that were tested with different orifice sizes and inside shapes. Figure 104 shows different orifice sizes and internal shapes that were used in the experiment. Table 32 presents the total momentum ratios (TMR) tested and lists the different angle sprays achieved. TMRs were varied by fluctuating the mass flow rate on the fluids. Water was used to take the role of the slurry flow. Table 33 is presented in which the mass flow of the slurry and the nitrogen are varied to obtain different Total Momentum Ratios (TMR) and, therefore, different angle sprays. The mixture of the slurry was also varied, ranging from 25% to 65% of glass beads.

Table 31 Pintle Tip parameters for 0.75 mm & 1 mm

Diameter Orifice on Pintle Tip (mm)	Shape of Plate Orifice	Cone/Flat
0.75	Curved	Cone
1.0	Curved	Flat
1 mm	Curved	Cone
2 mm	Curved	Cone
3 mm	Curved	Cone
5 mm	Curved	Cone

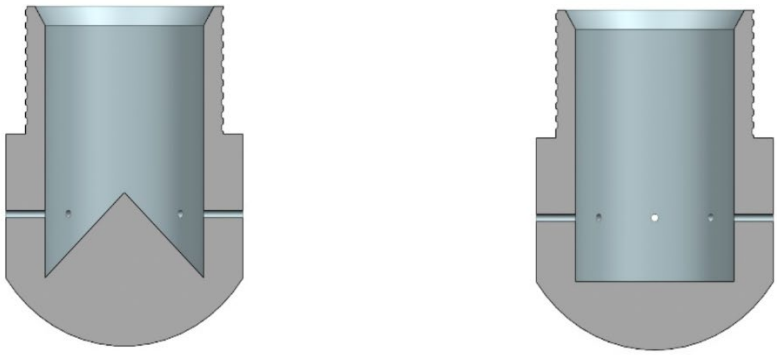

Figure 104 Cone shape (left) and flat shape (right) tips

Table 32 Test Matrix for Orifice Diameters of 0.75 mm and 1.0 mm.

WATER		NITROGEN		
P (psi)	Mass Flowrate (kg/s)	P (psi)	Mass Flowrate (kg/s)	Total Momentum Ratio
60±5	0.0276	0	0	N/A
60±5	0.0276	100±5	0.0033	48.74
60±5	0.0276	200±5	0.0057	28.29
60±5	0.0276	300±5	0.0085	21.29
60±5	0.0276	400±5	0.0111	17.85
60±5	0.0276	500±5	0.0131	11.57
60±5	0.0376	0	0	N/A
60±5	0.0376	100±5	0.0033	99.92
60±5	0.0376	200±5	0.0057	64.84
60±5	0.0376	300±5	0.0085	43.75
60±5	0.0376	400±5	0.0111	33.42
60±5	0.0376	500±5	0.0131	31.32

Table 33 Test Matrix for Orifice Diameters of 1 mm, 2 mm, 3 mm and 5 mm.

WATER		**NITROGEN**	
P (psi)	Mass Flowrate (kg/s)	P (psi)	Mass Flowrate (kg/s)
60±5	0.0276	0	0
60±5	0.0276	100±5	0.0033
60±5	0.0276	200±5	0.0057
60±5	0.0276	300±5	0.0085
60±5	0.0276	400±5	0.0111
60±5	0.0276	500±5	0.0131

3.2.3.2. Shadowgraph Analysis

In the following section, the shadowgraph photos for the test listed in Table 31. Images include the TMR resulted from each test. In the case of no nitrogen flow, the spray angle is 90˚ resulting in no TMR available. As can be seen in Figure 105, the increase in spray angle as a function of TMR decreases once the angle approaches 90 degrees, which resulted in a reduced experimental spray angle. Figure 106 shows an oscillation is present in the spray after the TMR exceeds 30.

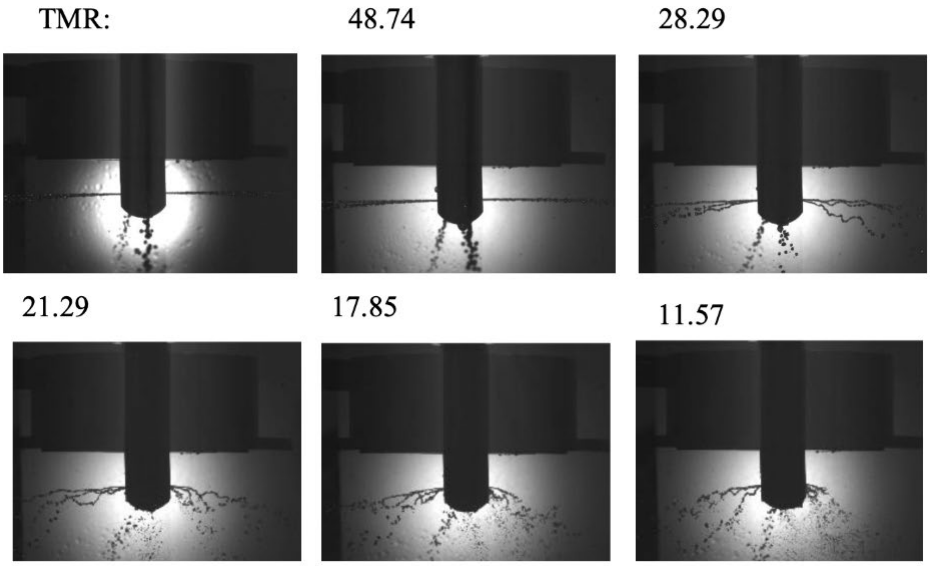

Figure 105 Jet Atomization for 1 mm Pintle Orifice at 0.0276 kg/s water

For the tip with a 0.75 mm orifice, the TMR tested produced higher angles. This is because the orifice has a higher velocity at the exit. Similar to the previous test, the rate at which the spray angles change decreases with an increase of TMR. However, the same phenomena happen where the spray angle decreases as the TMR increases. Also, it was observed that at lower TMR values, there is a higher deviation as they decrease between the experimental and theoretical

angles as shown in Figure 108. Finally, with this tip configuration in Figure 107 it was observed that oscillation of the spray starts after the 65 TMR mark.

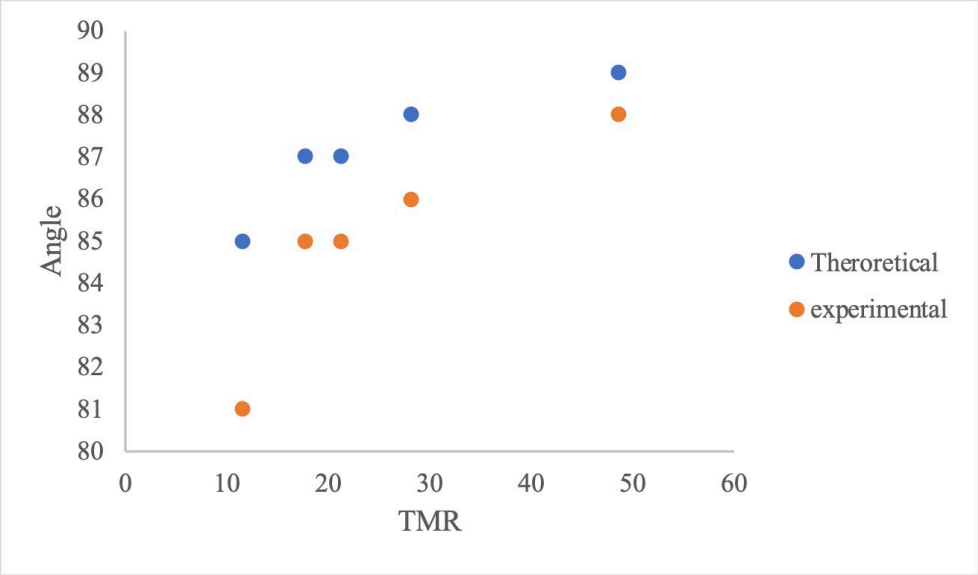

Figure 106 Flow Turning Angle at Different TMR

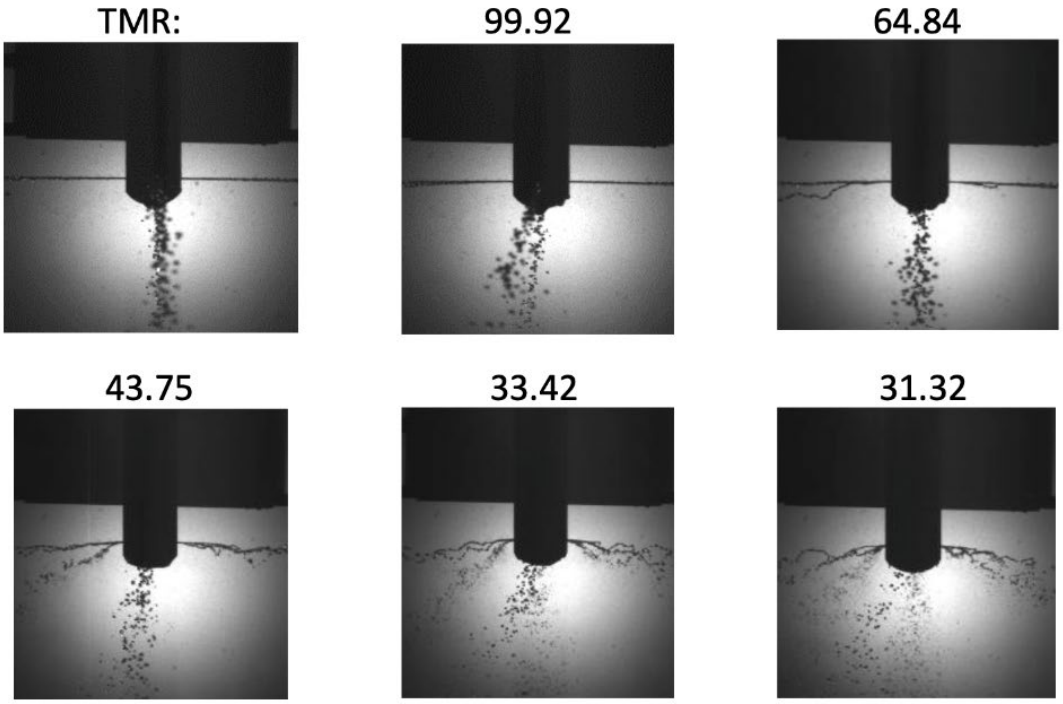

Figure 107 Jet Atomization for 0.75 mm Pintle Orifice at 0.0276 kg/s water

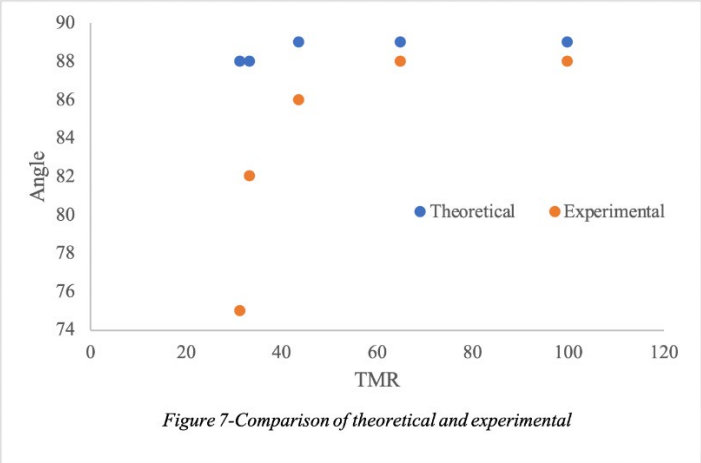

Figure 108 Flow Turning Angle at Different TMR

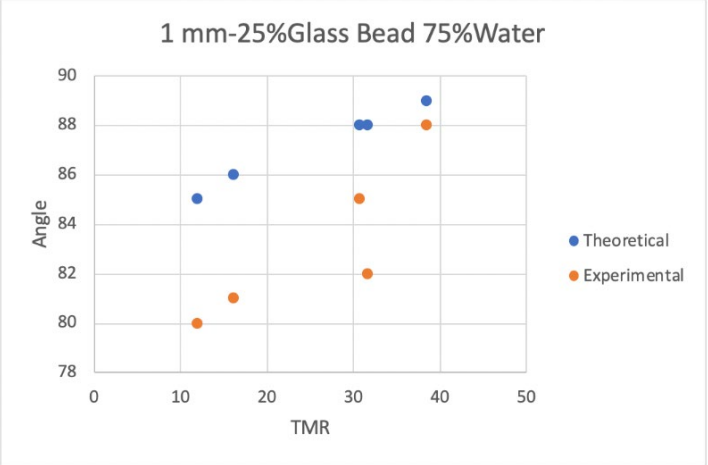

Figure 109 Flow Turning Angle at Different TMR (1 mm Pintle Orifice and 25% Glass Beads)

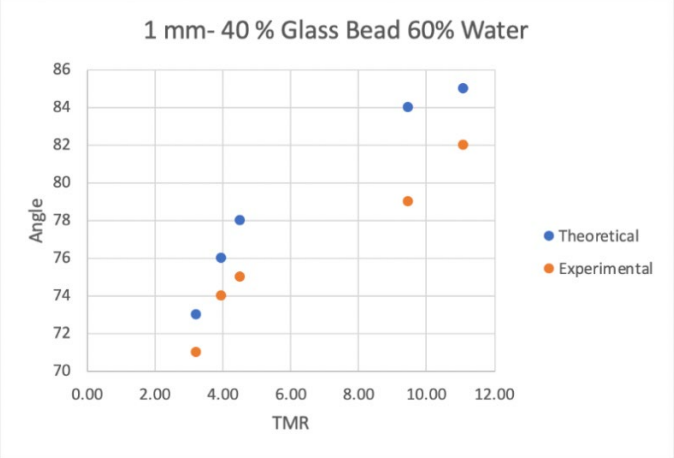

Figure 110 Flow Turning Angle at Different TMR (1 mm Pintle Orifice and 40% Glass Beads)

Data for 1 mm and 5 mm tip were performed in the earlier stages of the test. However, for the 1 mm tip, the atomization that was desired was not presented, and the angle was wide enough to impinge the combustor wall, as seen in Figures 109 & 110. Therefore, this tip was discarded for the last two mixtures. On the other hand, the 5 mm tip could not form a satisfactory spray. The injection was more of a stream, and droplets were lost on the stream.

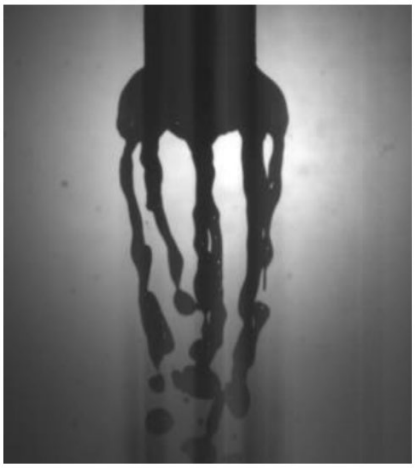

Figure 111 Flow Turning Angle at Different TMR (5 mm Pintle Orifice and 50% Glass Beads without nitrogen flow)

The results that gave a satisfactory spray were the tips for 2 and 3 mm. The following figures depict the comparison between the mixture and the tips.

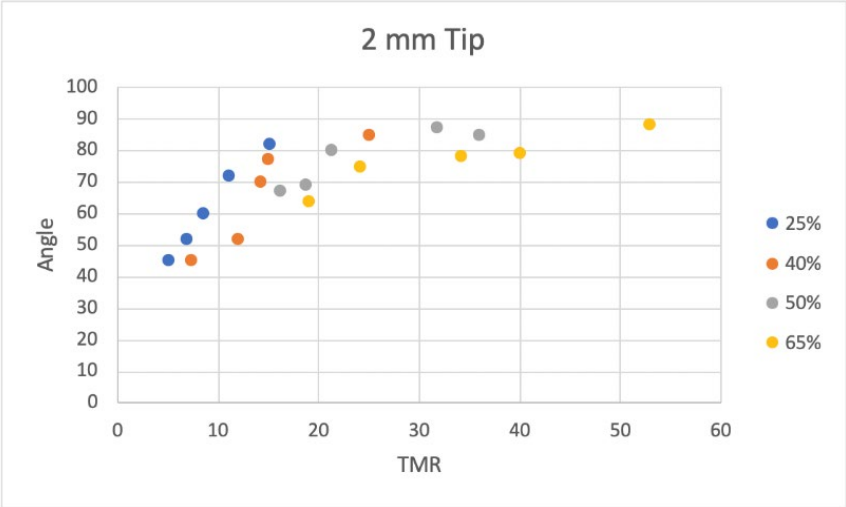

Figure 112 Flow Turning Angle at Different TMR and Glass Beads Concentrations (2 mm Pintle Orifice)

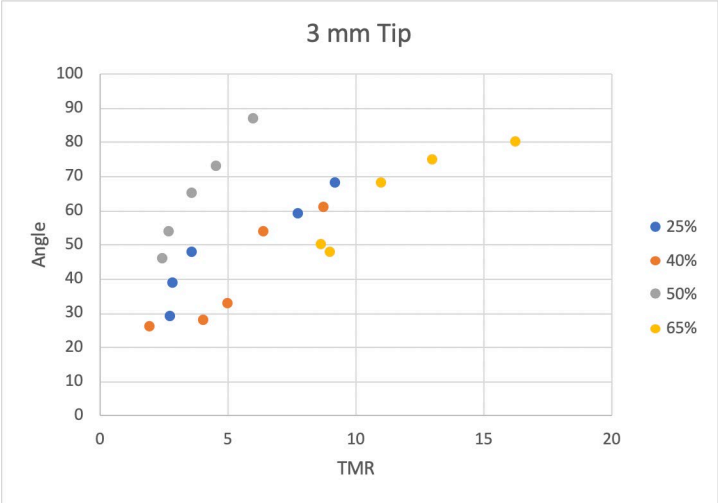

Figure 113 Flow Turning Angle at Different TMR and Glass Beads Concentrations (3 mm Pintle Orifice)

Figure 112 shows, as the glass bead content in the slurry increases, it can be observed that the TMR covers a wider range. For example, the 65 % glass bead slurry for the 2 mm tip goes from TMR of 52 to 19, whereas the 25 % goes from 16 to 8. Additionally, at the lower range of the TMR, both tips have presented atomization and a uniform cone.

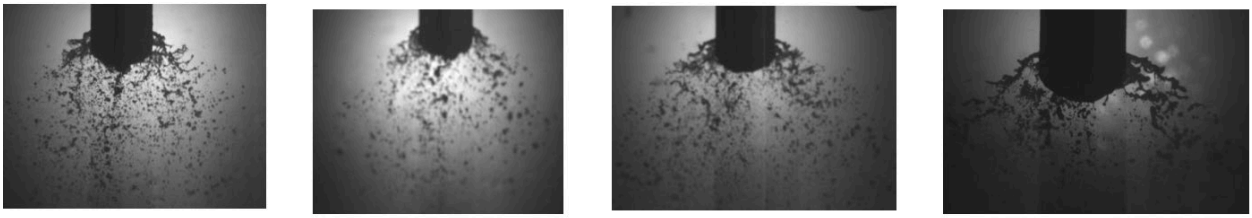

Figure 114 Jet Atomization for 2 mm tip at 25%, 40%, 50% and 65%.

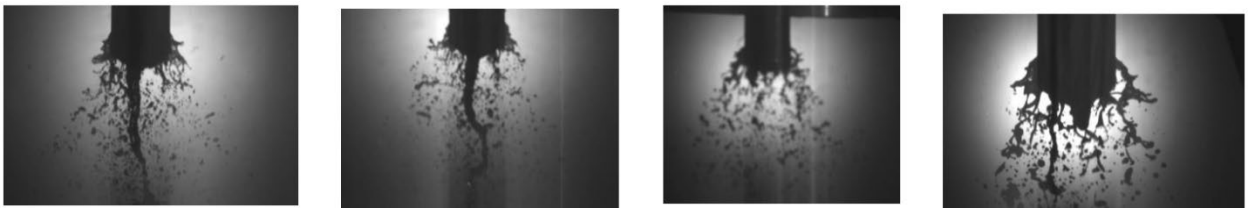

Figure 115 Jet Atomization for 3 mm tip at 25%, 40%, 50% and 65%

From the plots in Fig. 112 and Fig. 113, it can be concluded that at a higher mixture, the 3 mm tip gives a lower angle. However, when the shadowgraph pictures are compared, is evident that higher atomization is presented in the 2 mm tip.

There is a large deviance between the theoretical and experimental angles as the TMR decreases was observed. This indicates that to operate the injector, additional experimental tests have to be done to be sure that the spray does not impinge on the powerhead and combustor wall. It is expected that the same trend TMD vs Spray angle will be also seen once a mixture of Glass

beads and water become the operating fluid for the experiment. This is predicted because the density of the glass beads will have a great impact on the experiment. In addition, it was observed during testing operations that the current design of the injector doesn't provide an even distribution of the gaseous fluid prior to its exit at the port, as evidenced in Figure 117, where the spray angle is shorter in one side than the other. Some options have been explored, such as adding a secondary port. Some fluid simulations will be done to choose the correct solution.

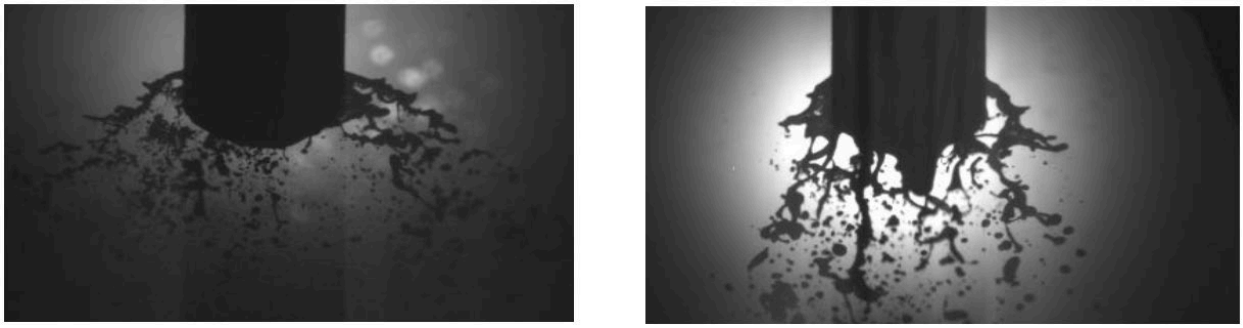

Figure 116 Jet Atomization for 2 mm and 3mm tip (65 % Glass Beads)

Figure 117 Typical Jet Atomization (No even distribution of gaseous flow is seen)

Overall, there was no impact on the flow due to the shape inside the tip. Additionally, it can be observed that the smaller orifice tip gave the smallest angle spray but had the biggest hysteresis. The size of the orifice can present a problem for the system, causing a clogging on the piping itself.

For the cold coal test comparison between tips 1mm, 2mm, 3mm & 5mm, the 2 mm tip will be selected to perform the tests, due to the atomization presented throughout the tests. Some concerns that have been observed in the presence of foreign objects that clog the tip that is not

glass beads. Therefore, it is recommended that an inline filter is placed on the system. Another observation is the settlement of the slurry when it stops flowing through the pipe. Water continues to flow towards the exit, and glass beads are settled on the pipes. It is recommended the inclusion of clean water or inert gas line near the injector is placed to purge the glass beads on the piping before testing.

3.2.4. Coal-Water Slurry Tests

Glass beads-water slurry tests provided significant insight to spray pattern. Additionally, effect of the pintle orifice size on the operationality of the system was obtained. Previous tests provided conclusive evidence to decide upon an optimum pintle orifice size. The next step is to characterize the spray pattern using the operating working fluid; coal-water slurry.

3.2.4.1. Coal Composition

Coal has been procured from Asbury Coals; it is a coarse variety of C3 bituminous coal. The calculations for fine pulverized coal were completed. However, due to unavailability of the exact coal, the current C3 bituminous coal will be used for experiments. The size distribution of the coal is presented in Table 34. As seen from the distribution, there is a minor percentage of coal particle of larger than 600microns. A mesh will be added to the feed line to eliminate particles larger than 600microns. Thus, the calculations relating to the coal particle size will remain valid for the coal procured. The typical analysis of C3 Bituminous coal is given in Table 6.

Table 34 Different material content in coal by wt%

Element	Percentage (%)
Ash	8
Volatile	34.6
Moisture	3.5
Sulfur	0.71
Carbon (Fixed)	57

Table 35 Size distribution of C3 Bituminous Coal

Size	Percentage (%)
+20 Mesh (850 Microns)	2.5
+30 Mesh (600 Microns)	10
+40 Mesh (425 Microns)	15
+100 Mesh (150 Microns)	37
+200 Mesh (75 Microns)	18
-200 Mesh (75 Microns)	17

3.2.4.2. No swirl Pintle Injector (S = 0) Analysis

coal water tests were first performed using no swirl injector. The test was conducted by varying the water and coal proportions in the slurry mixture. The Coal/Water mixing proportion is varied from 30/70 % to 50/50 %. The test matrix was designed to evaluate the performance of the pintle injector at different mixture conditions. Tip with an orifice size of 5mm was tested for this work. Different nitrogen flows were tested to compare Total Momentum Ratios. This yielded different spray angles, diameters, and overall atomization. The following tables summarize the different test cases for this study. Table 36 provides a test matrix and results from different test conditions.

Table 36 Test Matrix and Results for S = 0 Injector

Sets	Test Points	Tip (mm)	Mixture	Slurry Mass Flow (kg/s)	Nitrogen Mass Flow (kg/s)	TMR	Experimental Spray Angle	Theoretical Spray Angle
Set1	1	5	30% Coal-70% Water	0.0823	0.0067	6.1	57	81
	2	5	30% Coal-70% Water	0.0823	0.0091	3.5	45	74
	3	5	30% Coal-70% Water	0.081	0.0241	2.4	45	67
Set2	4	5	40% Coal-60% Water	0.0821	0.0068	5.1	53	79
	5	5	40% Coal-60% Water	0.0821	0.0093	3.3	42	73
	6	5	40% Coal-60% Water	0.0821	0.0243	2.4	42	67
Set3	7	5	50% Water-50% Coal	0.0833	0.0071	4.4	45	77
	8	5	50% Water-	0.0833	0.0093	3.3	40	73

Sets	Test Points	Tip (mm)	Mixture	Slurry Mass Flow (kg/s)	Nitrogen Mass Flow (kg/s)	TMR	Experimental Spray Angle	Theoretical Spray Angle
			50% Coal					
	9	5	50% Water-50% Coal	0.0833	0.0237	2.6	30	69

Figure 118 represents the test with 30% of coal by weight. The progression of the pictures follows the increase in the mass flow of nitrogen. The breakup in the jet can be observed as the spray travels downstream. It is noted in Table 32 that TMR and spray angle decreases in a couple. Atomization is clearly more present at the highest nitrogen mass flow from the figure. A higher count of particles was found at the lowest TMR conditions (or high nitrogen flow conditions). Spray with continuous-wave and droplet generation is observed from the firsts 2 tests due to high TMR and low nitrogen flow. The first 2 tests also show less atomization.

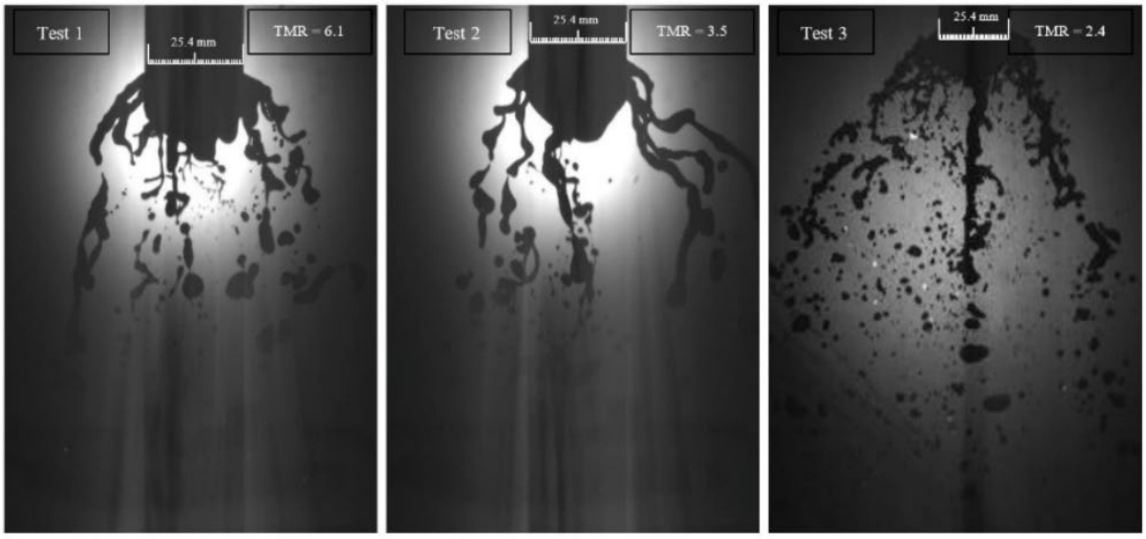

Figure 118 Jet Atomization at Different TMR (30% coal and 70 % water mixing condition)

Figure 119 and 120 provides results from TMR tests at a coal concentration of 40% and 50% by weight, respectively. In Figures 119 and 120, as the concentration by weight of coal is increased, the individual streams start to blur and provide more atomization. An increase in atomization is evident in both high nitrogen flowrate conditions shown in Test 6 and Test 9. A higher number of particle size are also found in Test 6 and Test 9. Thus, atomization is highest at the lowest TMR. It is obvious that particle detection and jet breakup analysis are focused on Test 3, Test 6, and Test 9 In addition, increasing coal concentration create less atomization in low flowrate of nitrogen shown by Test 7 and 8. It is also observed that increasing coal concentration decreases spray angle. This results in a more focused oxy-fuel induction to the chamber.

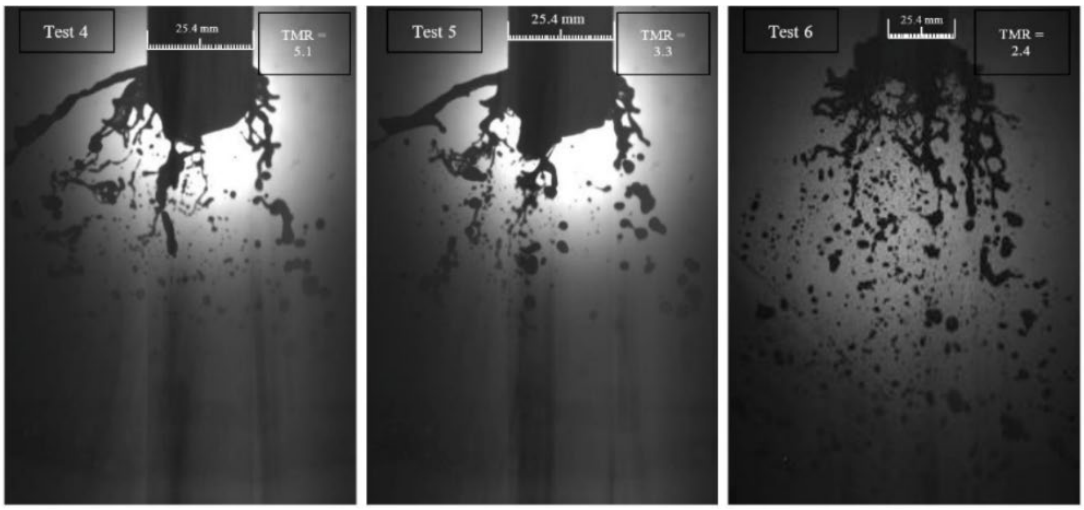

Figure 119 Jet Atomization at Different TMR (40% coal and 60 % water mixing condition)

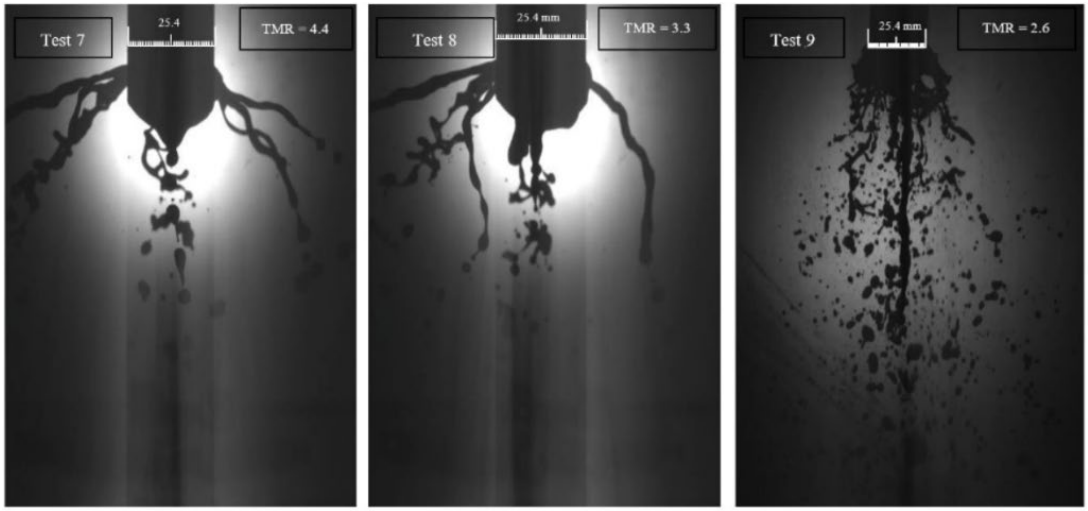

Figure 120 Jet Atomization at Different TMR (50% coal and 50 % water mixing condition)

Figure 121 shows different zones seen in the liquid jet spray from a typical pintle injector. There are three main zones as the liquid jet breaks up; breakup is classified by zones as follows:

i. Near the field of the nozzle, the difference between velocity creates instability, and stripping of filaments appears. This is called the primary atomization zone. In here the largest ligaments and droplets are produced

ii. Further downstream, the gas velocity decreases due to mixing with the external atmosphere, and the instabilities grow. This is called the jet breakup zone.

iii. In here the ligaments and droplets from the other zones break up further into smaller and more stable droplets, depending on the local Weber Number; called secondary atomization zone.

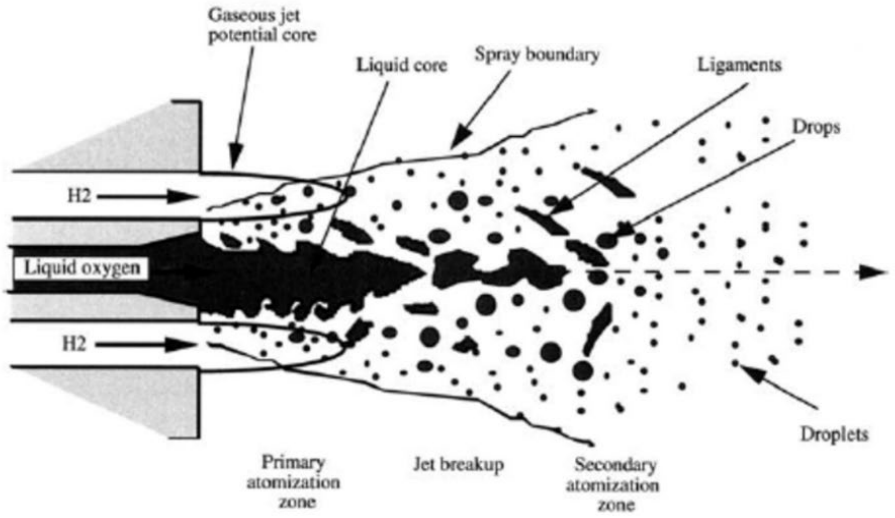

Figure 121 Depiction of jet breakup

For current tests with the highest atomization, the zones are obtained by taking measurement of spray. Each zone explained and the approximation of its length in Figures 122 through 124.

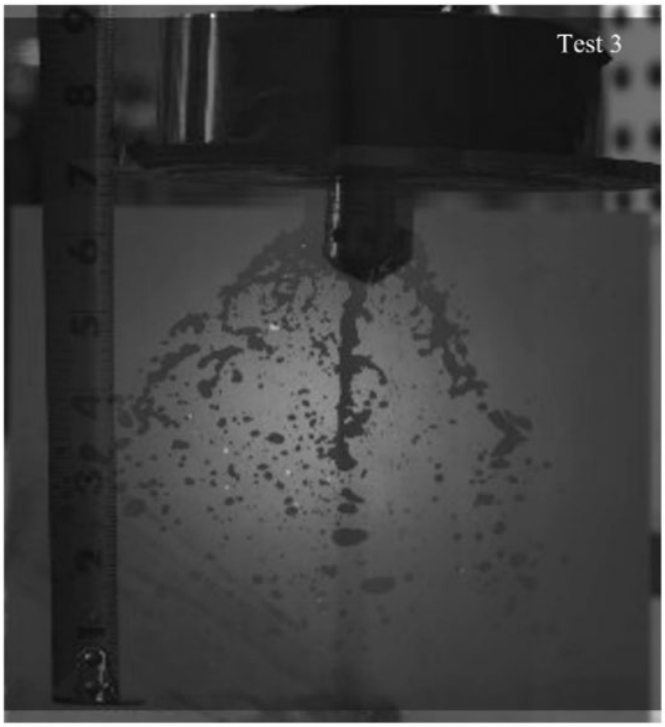

Figure 122 Jet break up at high nitrogen flow condition (for 30% coal and 70% water)

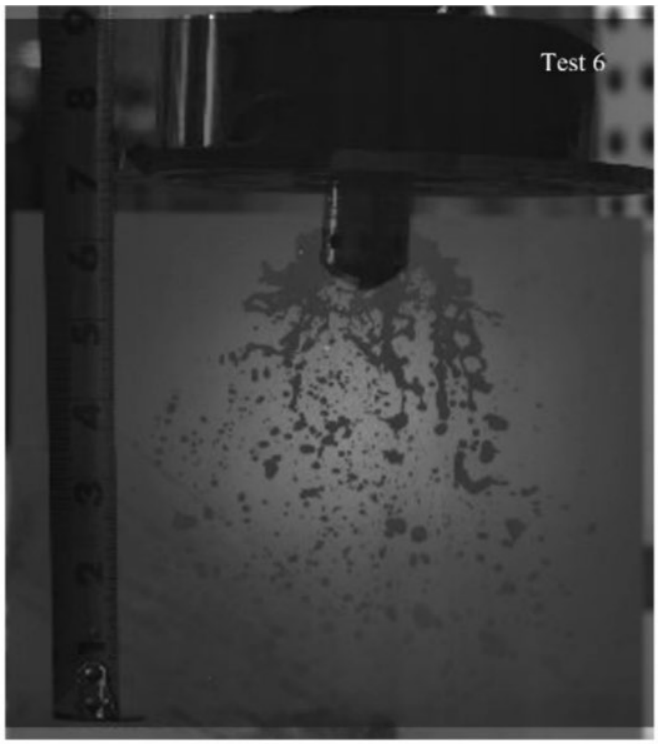

Figure 123 Jet break up at high nitrogen flow condition (for 40% coal and 60% water)

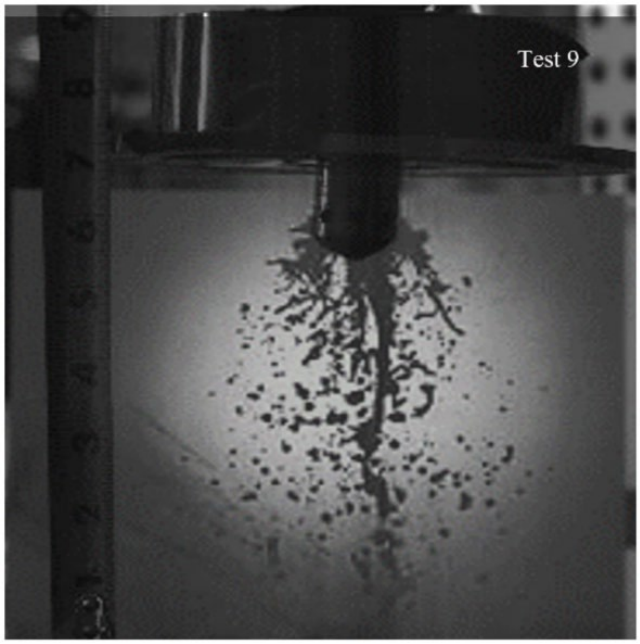

Figure 124 Jet break up at high nitrogen flow condition (for 50% coal and 50% water)

Figure 125 shows contours and equivalent diameter of detected particles in the highest atomization conditions. Dantec Dynamic Studio software was used to process the contours. A shadowgraph command, namely shadow sizing, is used. Shadow sizing detects and subtracts the data to obtain the contours. Reynolds and Weber numbers were obtained by velocity analysis

performed using dynamic studio. Table 37 summarizes the findings in the equivalent diameter for each of the tests with highest atomization

Table 37 Results obtained at highest atomization conditions

Test Number	No. of Particles	Mean Equiv. Diameter (mm)	Maximum Equiv. Diameter (mm)	Minimum Equiv. Diameter (mm)	Avg. Reynolds	Avg. Weber
3	428	12.57	89.18	3.9	5659	38.91
6	608	10.92	53.19	3.57	4913	11.47
9	776	11.57	50.88	3.90	5209	38.69

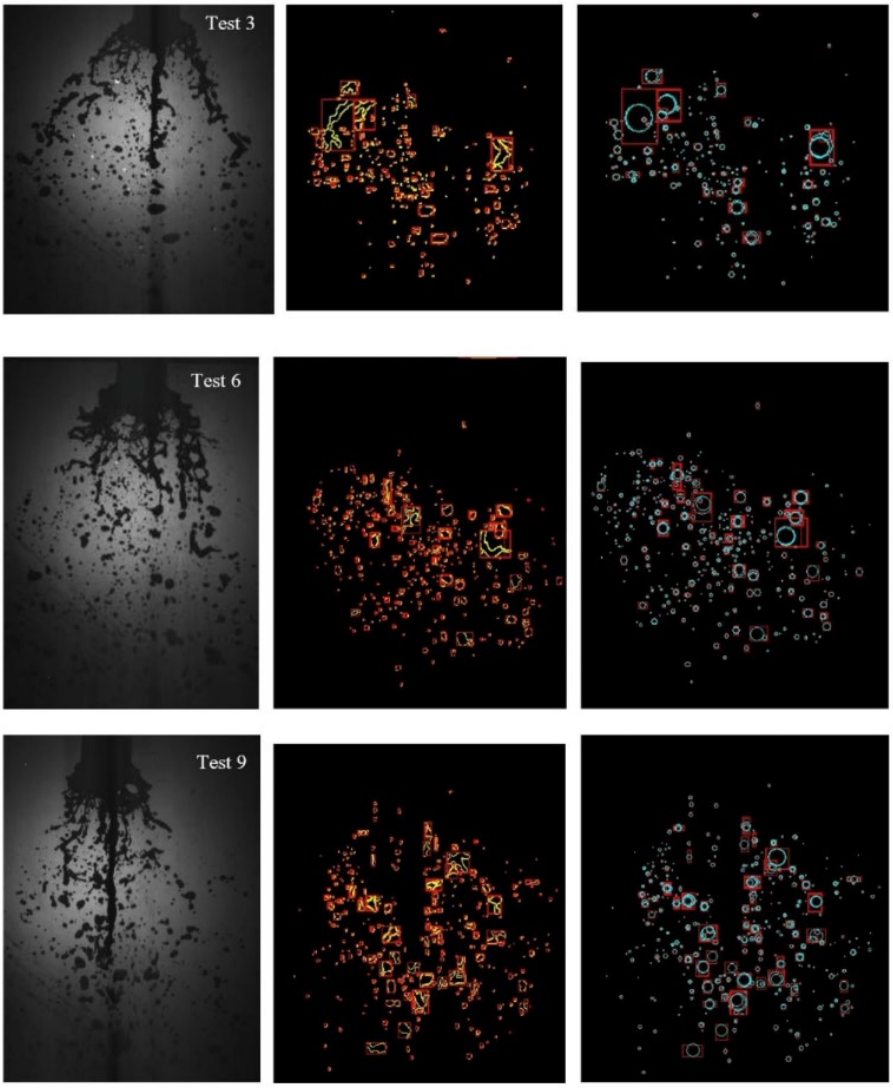

Figure 125 Jet Particles Contours at highest atomization condition

Table 37 compares the mean diameter for all of the tests. As a general trend for all tests, at the downstream of the spray, more droplets break out from the main jet. As the jet is being ejected through the nozzle, N_2 strikes the ligament of the slurry jet. Those upstream ligaments break down to relatively smaller ligaments. They further breakdown into smaller droplets as the flow moves downwards. Air entrainment from the ambient also plays a role in the atomization of the jet as it progresses downstream. Therefore, the highest atomization is observed at the downstream of the tests with the highest N_2 mass flow rate. Thus, further analysis is placed on these tests.

The next step was to characterize the properties of the stream at the onset of liquid-gas interaction. The goal is to increase the liquid surface area to enhance vaporization, mixing and burning. To achieve this, an unstable liquid jet stream that breaks up and forms droplets in interaction with gas is essential. This results in an interaction among inertial, viscous, and surface tension forces [30].

Liquid viscosity has a damping effect on the growth of disturbances on the surface, and surface tension will keep the liquid together; on the other hand, aerodynamic forces encourage it. Pressure oscillations and turbulence in the injected fluids, along with the surrounding gases, are part of the dynamics of atomization. The following nondimensional parameters can characterize this: Reynolds, Weber, and Ohnesorge numbers; listed respectively below.

$$\mathrm{Re} = \frac{U_l d}{\vartheta_l} \quad | \quad \mathrm{We} = \frac{\rho_l U_l^2 d}{\sigma} \quad | \quad \mathrm{Oh} = \frac{\mu_l}{\sqrt{\rho_l \sigma d}}$$

Reynolds measures the ratio of viscous to aerodynamic forces. Weber relates aerodynamic forces to surface tension. Ohnesorge is a combination of Weber and Reynolds and depends on both the liquid properties and the nozzle diameter. Comparison between the Ohnesorge number and Reynolds number determines what mechanism the droplets follow. This determines the intensity of the jet breakup and spray is atomization level. Figure 126 shows a different mechanism of jet break up.

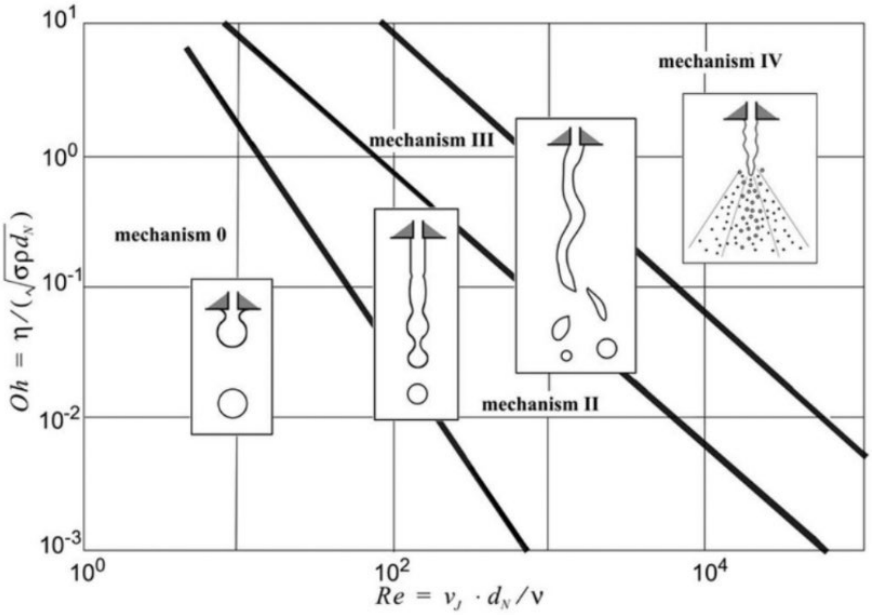

Figure 126 Jet Mechanism Diagram [31]

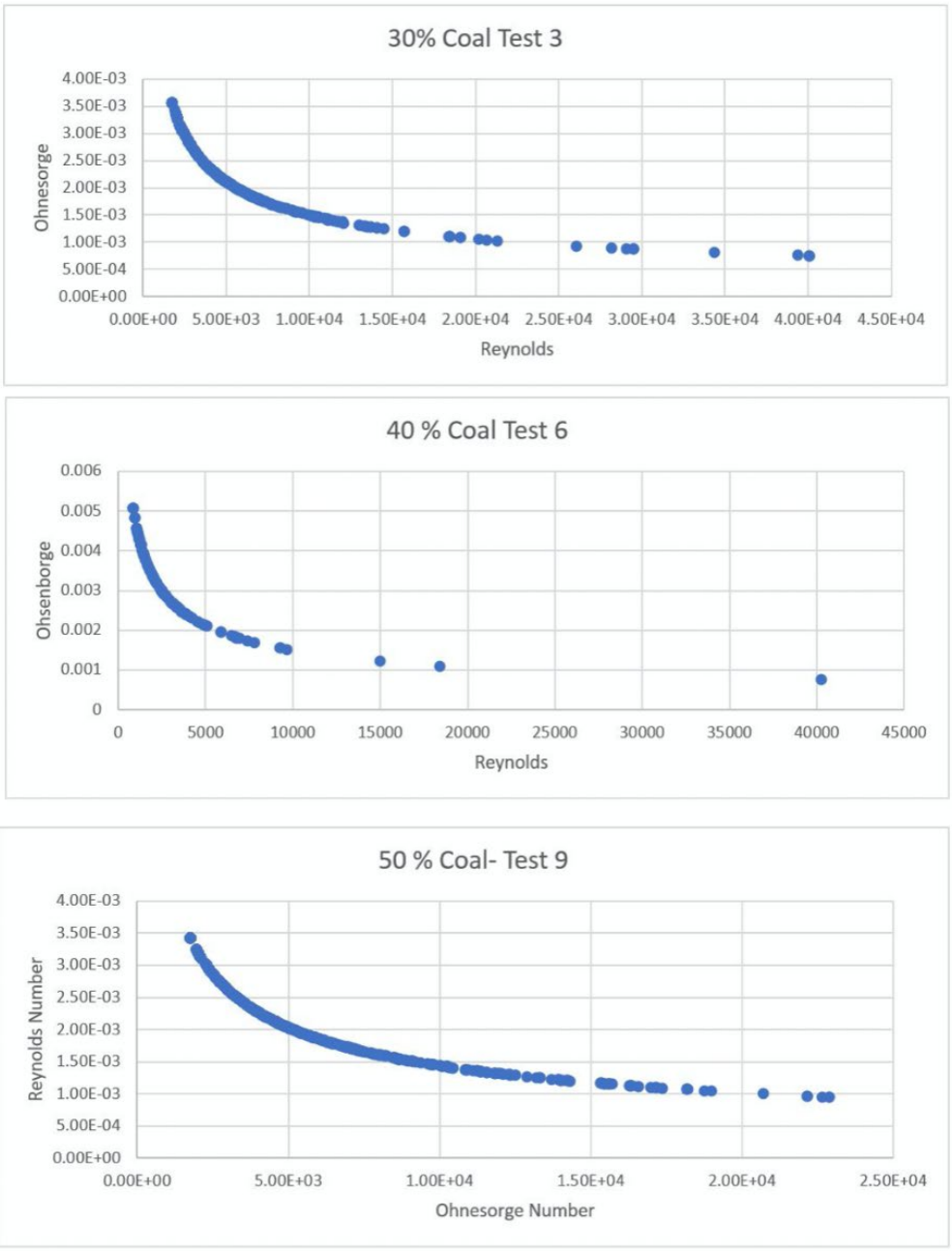

Figure 127 Ohnesorge vs Reynolds for Tests 3, 6, and 9 corresponding to Table 36

Figure 127 shows plots for Re vs. Oh, for all the highest atomization conditions. The plots show that most of the sprays fall in mechanism 3, known as wave and droplet. It infers that a higher Reynolds number is required to drive the sprays to the atomization mechanism, which is labeled as mechanism 4 in Fig. 126. This can be obtained by increasing the mass flow of the nitrogen which in turn decreases the TMR and the droplet size of the spray. Future testing will decrease TMR to obtain a spray on the atomization zone of the graph. In addition, swirlers will be incorporated to observe their effect on atomization.

3.2.4.3. 1st Generation Swirl-Pintle Injector (S = 0.9) Analysis

coal water test for the 1st generation Swirler injector was carried out. The design was presented in the previous chapters. Theoretically, implementing swirler will increases atomization. This section will analyze and compare swirler effecton atomization. The tests were conducted similarly to previous coal-water conditions. Pintle tip with an orifice size of 5mm was tested for this work. Different nitrogen flows were tested to compare Total Momentum Ratios. This yielded different spray angles, diameters, and overall atomization. Table 38 presents the testing conditions and results for the injector with swirlers.

Table 38 Text Matrix and Test Results for S = 0.9 Injector

Sets	Test Points	Tip (mm)	Mixture	Slurry Mass Flow (kg/s)	Nitrogen Mass Flow (kg/s)	TMR	Experimental Spray Angle	Theoretical Spray Angle
Set 1	10	5	30% Coal-70% Water	0.0823	0.0067	2.7	48	69
	11	5	30% Coal-70% Water	0.0823	0.0091	1.98	52	63
	12	5	30% Coal-70% Water	0.081	0.0241	1.4	40	54
Set 2	13	5	40% Coal-60% Water	0.0821	0.0068	2.8	43	70
	14	5	40% Coal-60% Water	0.0821	0.0093	1.7	37	59
	15	5	40% Coal-60% Water	0.0821	0.0243	1.3	42	52
Set 3	16	5	50% Water-50% Coal	0.0833	0.0071	1.9	47	62
	17	5	50% Water-50% Coal	0.0833	0.0093	1.5	45	56
	18	5	50% Water-50% Coal	0.0833	0.0237	1.2	30	50

The Jet profiles show that the atomization is not sound under zero swirl injector, as listed in Figure 118 to 120. On the other hand, S = 0.9 injector shows better atomization, as shown in Figure 128 to 130. From figures 128 – 130, at Tests 3, 6, and 9, a higher number of droplets are observed compared to other tests. Test 3, 6, and 9 have the highest mass flow rate of N_2, where atomization is clearly more present. This is attributed to the entrainment of the nitrogen with the slurry after being ejected. The momentum of N_2 helps to break down the kinetic energy of the jet stream. In other words, the force due to the momentum of the nitrogen stream in these three cases is strong enough to overcome the shear of the slurry stream. Hence, these three cases atomization is predominant. Additionally, comparing these results to the swirler injector data, it can be observed that atomization is increased in all cases. The trend where at the highest mass flow of N_2, Test 12, 15, and 18, can be observed the highest atomization, is present in these tests.

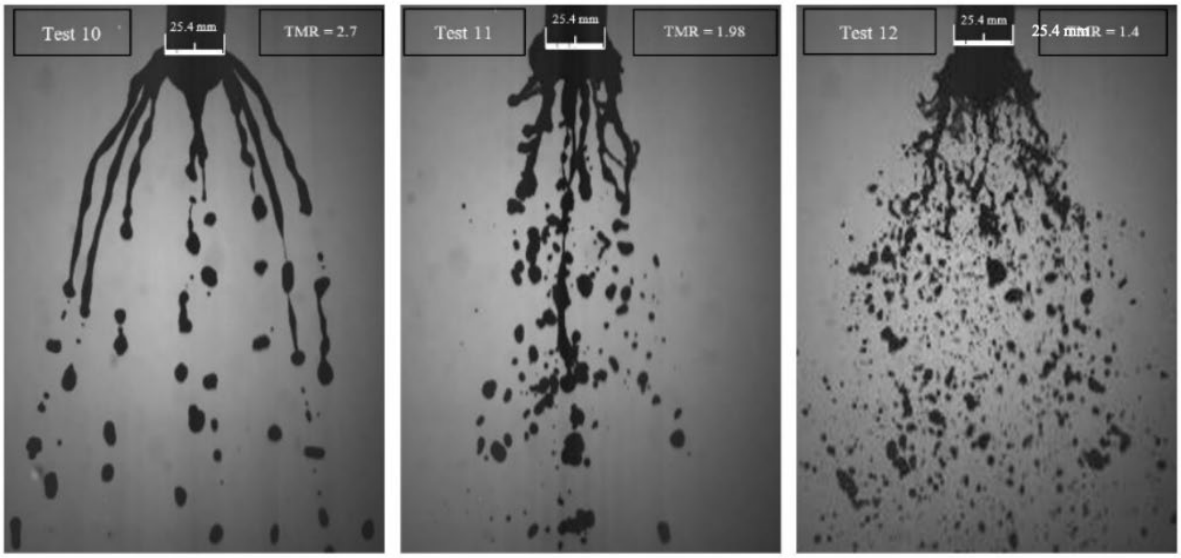

Figure 128 Jet Atomization at Different TMR (30% coal and 70 % water, S = 0.9)

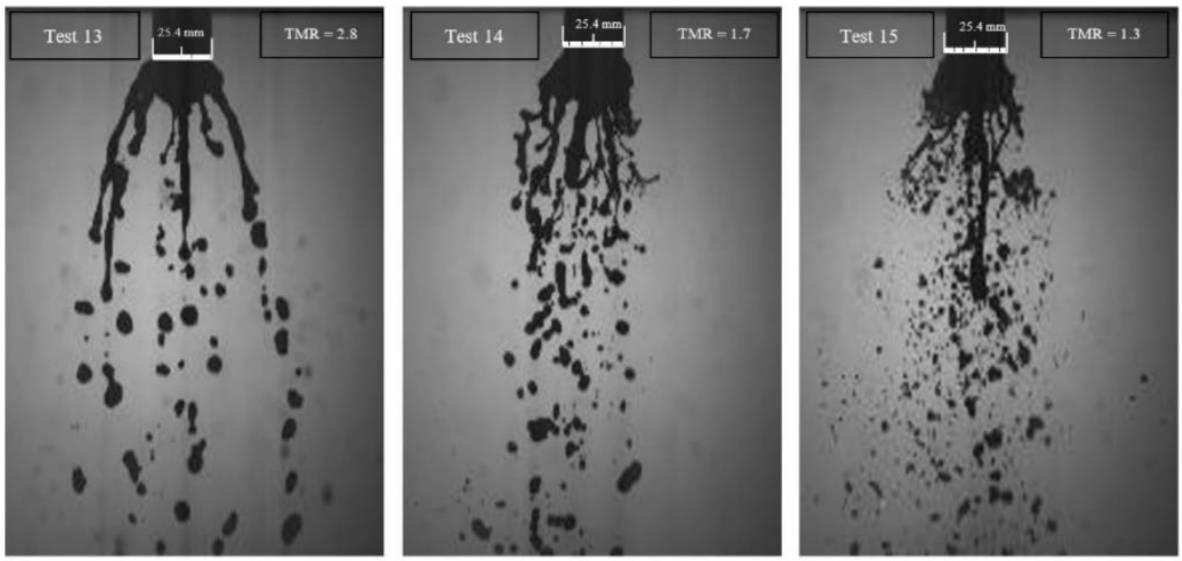

Figure 129 Jet Atomization at Different TMR (40% coal and 60 % water, S = 0.9)

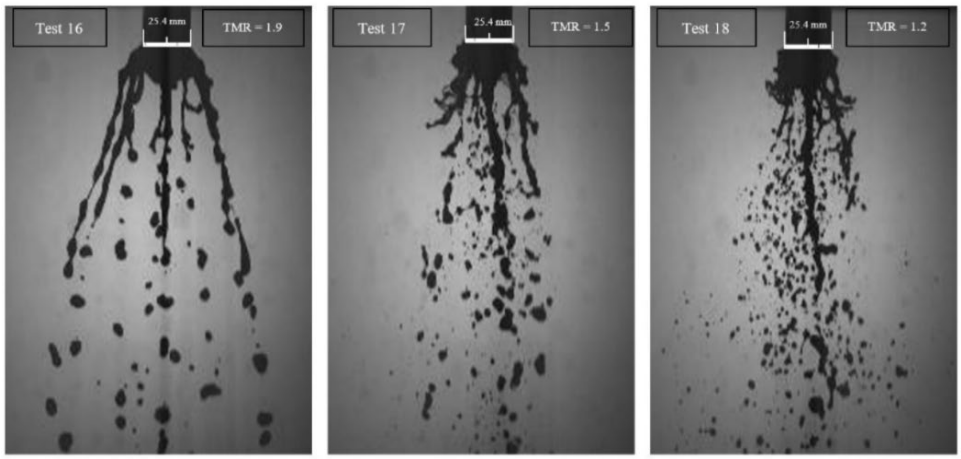

Figure 130 Jet Atomization at Different TMR (50% coal and 50 % water, S = 0.9)

The detection and the characteristics of the droplets were measured using in the Dynamic studio. In Dynamic studio, the shadow sizing method under the particle characterization has been implemented. In shadow sizing, an initial threshold level is set based on a droplet used as a base reference. The program then detects the droplets of similar gray levels. This process was repeated at a different gray level to detect as many droplets as possible from the image.

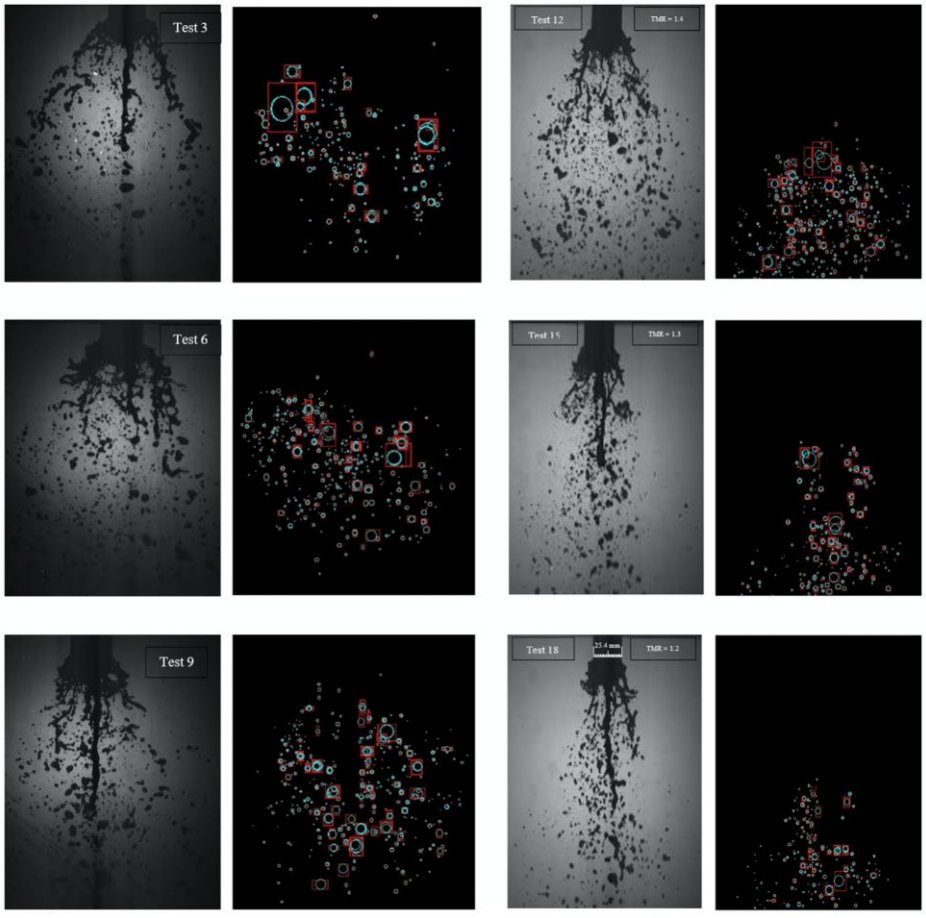

Figure 131 Spray Droplets Detected Through Shadow Sizing (S =0.9)

At the start of each test, the camera was calibrated and synchronized with the system. The shadow sizing method measures the contour of the droplet first. Afterward, it generates the equivalent diameter of the droplet. The processes of detecting and generating the equivalent diameters are shown in Figure 131. The Reynolds and Weber numbers were then calculated. The Reynolds number is generated to determine if the spray is turbulent. It is found that the flow is turbulent at test 3 and 9. The flow under test 6 is just below the critical Reynolds number. The characteristics of the droplets are listed in Table 39.

Table 39 Spray droplet size analysis for 1st generation swirler injector

Test Number	Number of Particles	Mean Equiv. Diameter (mm)	Avg. Reynolds
3	428	12.57	5659
6	608	10.92	4913
9	776	11.57	5209
12	505	2.50	5730
15	472	1.82	4182
18	208	2.48	5830

It can be observed from Table 39 that the atomization increases as the total mass flow rate of the slurry increases. It means with the increase in flow momentum, and the jet breaks up more. It could also be seen from Table 39 that the number of droplets increases with the coal concentrations. This could be an effect of reducing surface tension due to lowering the water concentration. Finest droplets were found at test 6 and 15, whereas the other tests have higher mean equivalence diameter. However, Swirler injector yields the highest atomization with droplets mean diameter reaching 2.50 mm. It is expected that test 15 would lead to better combustion since the jet breaks up and forms fine particles at the secondary atomization zone. At test 3 and 6, and test 12 and 15, the Reynolds numbers decreased as the concentration of the coal increased. The total density of the slurry decreases as the concentration of the water decreases. Therefore, the Reynold number drops in test 6 and 15 compared to test 3 and test 12. On the other hand, test 9 and 18 exhibits a higher Reynolds number since the slurry mass flow rate was relatively higher.

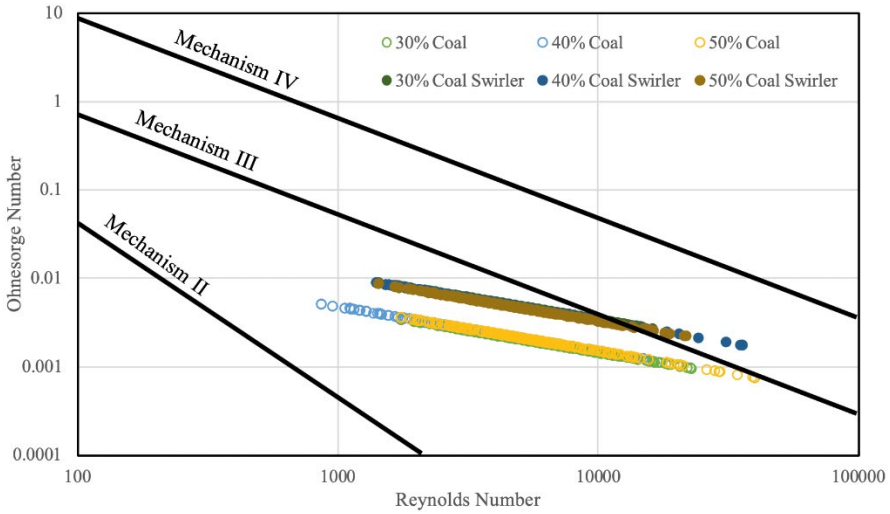

Figure 132 The change of Ohnesorge Number with Reynolds Number (S =0.9)

Figure 132 shows that the swirler injector falls under in mechanism IV, the atomization zone. However, most of them fall under mechanism III. Therefore, the spray is not fully atomized. It could be because the mass flow rate of gas was not sufficient to break up the jet stream. For the swirler, it presents the atomization due to fact that the closing plate with the swirlers could accelerate the entrainment of the gas into the jet stream. This would lead to better atomization. By increasing the mass flow of the oxidizer, full spray atomization will be obtained.

3.2.4.4. 2nd Generation Swirl-Pintle Injector (S = 1.2) Analysis

A higher swirl is implemented in the 2nd generation swirl pintle injector to achieve more atomization. Cold-water tests were performed for this injector to verify the increase in atomization. The Coal/Water mixing proportion is kept similar to previous test conditions. Pintle tip orifice was kept at the optimum 5 mm size. Total Momentum Ratios were varied by varying nitrogen flowrate. This yielded different spray angles, diameters, and overall atomization. The following tables summarize the different test runs for this study. Table 40 presents the conditions for the tests and results for the injector with swirl number 1.2

Table 40 Test Matrix and results for Swirl Number 1.2

Test Run	Tip (mm)	Mixture	Slurry Mass Flow (kg/s)	Nitrogen Mass Flow (kg/s)	TMR
19	5	30% Coal-70% Water	0.065	0.0215	0.42
20	5	30% Coal-70% Water	0.065	0.0342	0.31
21	5	30% Coal-70% Water	0.065	0.0305	0.21
22	5	30% Coal-70% Water	0.065	0.0489	0.16

23	5	40% Coal-60% Water	0.067	0.0226	0.39
24	5	40% Coal-60% Water	0.067	0.0278	0.32
25	5	40% Coal-60% Water	0.067	0.0325	0.28
26	5	40% Coal-60% Water	0.069	0.0512	0.14
27	5	50% Water- 50% Coal	0.061	0.0195	0.43
28	5	50% Water-50% Coal	0.061	0.0264	0.29
29	5	50% Water-50% Coal	0.061	0.0305	0.25
30	5	50% Water-50% Coal	0.065	0.0513	0.12

Figure 133 to 135 show at tests 21, 24, and 27, a higher number of droplets are observed compared to other tests. Test 21, 24, and 27 have the highest mass flow rate of N_2, where atomization is clearly more present. This is attributed to the entrainment of the nitrogen with the slurry after being ejected. The momentum of N_2 helps to break down the kinetic energy of the jet stream. In other words, the force due to the momentum of the nitrogen stream in these three cases is strong enough to overcome the shear of the slurry stream. Hence, these cases atomization is predominant. However, it can be observed that small droplets, and a decrease of the core jet are present in tests 20, 23, and 26.

The previous testing concluded an increase in nitrogen mass flowrate results in TMR decrease. This progression is also evident in current cases, shown in figures 133 to 135. In these figures from left to right, it demonstrates the increase of the mass flow of nitrogen. The major difference is in the change in the exit area of the oxygen due to the blockage of the swirlers and the position of the swirlers. Due to the reduction of area, velocity increases. Due to the swirlers, momentum is increased. In consequence, the spray angle is decreased even further. This is observed both on the images and by the TMR. Since all the calculated TMR is lower than 1, this shows that the spray angle is lower than 45˚ and no impingement on the combustor wall will happen. As the spray goes further down, the breakup is also noticed.

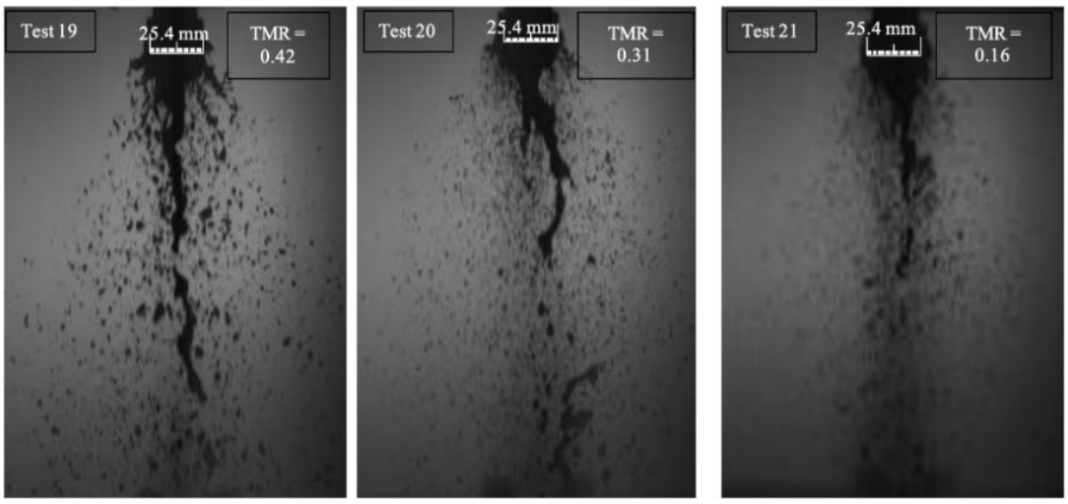

Figure 133 Jet Atomization at Different TMR (30% coal and 70 % water, S =1.2)

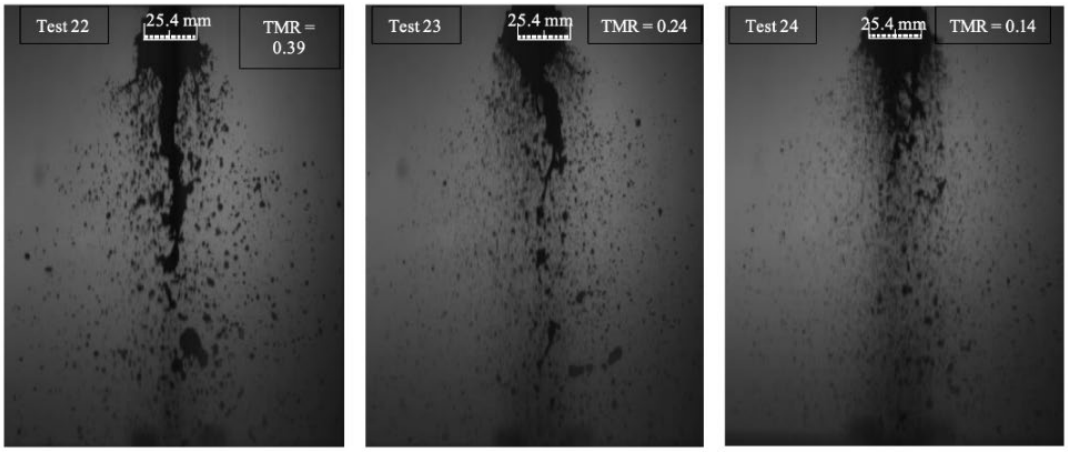

Figure 134 Jet Atomization at Different TMR (40% coal and 60 % water, S =1.2)

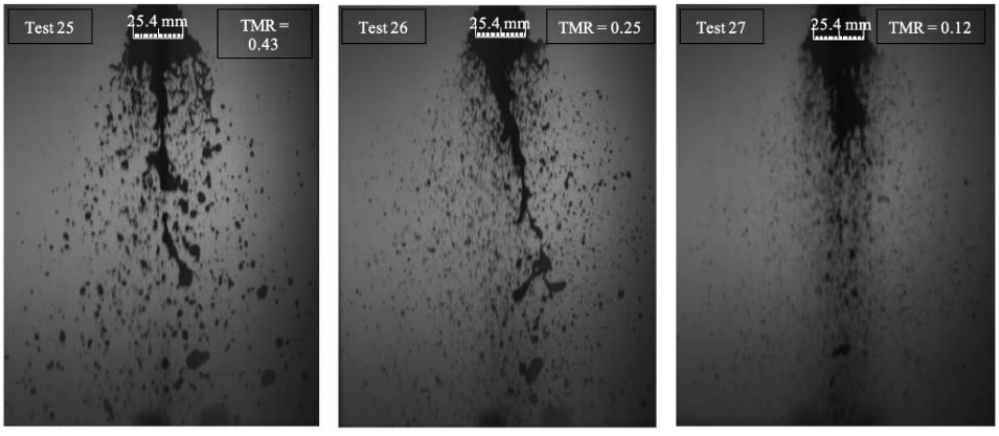

Figure 135 Jet Atomization at Different TMR (50% coal and 50 % water, S =1.2)

Shadowgraph results show that in most cases, the mean diameter decreased to approximately 1.5 mm. Finest droplets are at tests with 40%. However, the highest number of droplets are found in tests, with 50% of Coal that can be found in Figure 136. Complete mean equivalent diameter

for the cases Table 40 is listed in Table 41. It is clearly evident that the 2nd generation swirl-pintle injector dominates over the other design in terms of atomization.

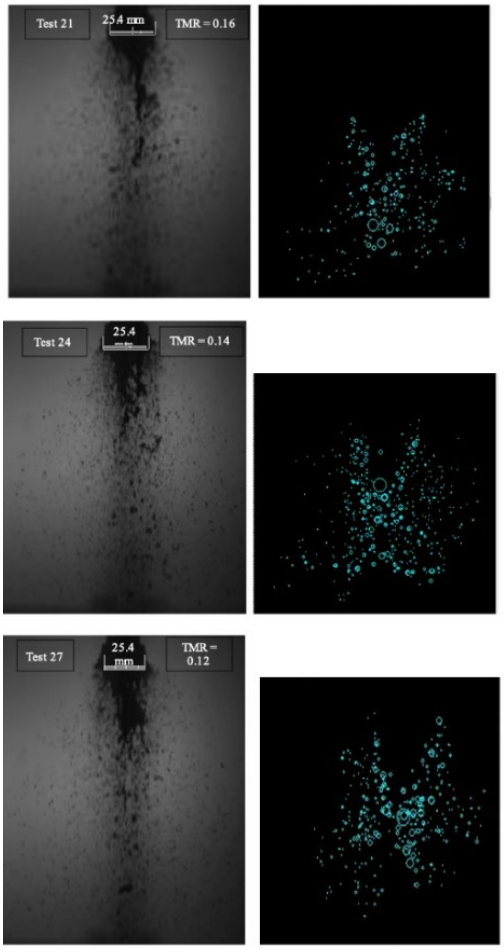

Figure 136 Spray Droplets Detected through Shadow Sizing (S = 1.2)

Table 41 Observed Mean Equivalence Diameter per Test

Test Number	Mean Equv. Diameter (mm)
19	1.79
20	1.27
21	1.20
22	1.33
23	1.21
24	1.15
25	2.06
26	1.31

27	1.23

3.2.5. Combustor Shakedown Test

The cold flow tests provided significant insight into injector characteristics. It was evident that a higher swirl is required for better atomization. Therefore, the 2nd generation swirl-pintle injector with S = 1.2 was chosen for hot fire operations. The test procedure, test matrix, and LabVIEW operation sequence are prepared. The shakedown test is soon to be conducted.

The proposed test matrix and test sequences are provided in the following subsections.

3.2.5.1. Combustor Shakedown Test Matrix

Table 42 Proposed Test Matrix based on varying coal concentration

	Test Points	Tip (mm)	Mixture	Slurry Mass Flow (kg/s)	Oxygen Mass Flow (kg/s)	Theoretical Spray Angle	Tank Pressure	Firing Input
Set 1	1	5	30% Coal-70% Water	0.0823	0.0067	83		
	2	5	30% Coal-70% Water	0.0823	0.0091	81		
	3	5	30% Coal-70% Water	0.081	0.0241	69		
Set 2	4	5	40% Coal-60% Water	0.0821	0.0068	83		
	5	5	40% Coal-60% Water	0.0821	0.0093	81		
	6	5	40% Coal-60% Water	0.0821	0.0243	69		
Set 3	7	5	50% Water-50% Coal	0.0833	0.0071	83		
	8	5	50% Water-50% Coal	0.0833	0.0093	82		
	9	5	50% Water-50% Coal	0.0833	0.0237	69		

Table 43 Proposed Test Matrix at varying Firing Input for 40% Coal Slurry Concentration

	Total Power (kW)	Power Inputs (kW)		Flowrate (kg/s)			
		Main Injector	Secondary Burner	Main Injector Slurry	Secondary Burner CH4	Main Injector O_2	Secondary Burner O2
Case 1	100	75	25	0.0068	0.0005	0.007	0.002
Case 2	200	150	50	0.0136	0.0010	0.014	0.004
Case 3	300	225	75	0.0205	0.0015	0.021	0.006
Case 4	400	300	100	0.0273	0.0020	0.028	0.008
Case 5	500	375	125	0.0341	0.0025	0.035	0.010

Case 6	600	450	150	0.0409	0.0030	0.042	0.012
Case 7	700	525	175	0.0477	0.0035	0.049	0.014
Case 8	800	600	200	0.0545	0.0040	0.056	0.016
Case 9	900	675	225	0.0614	0.0045	0.063	0.018
Case 10	1000	750	250	0.0682	0.0050	0.070	0.020

3.2.5.2. Test Sequence

The following tables provide the proposed operation sequence for the shakedown test of the combustor.

Table 44 Feed line priming at the start of the test

Priming Sequence		**Run Time**
Step 1	Open IO-SV-1	5 s
Step 2	Close IO-SV-1	
Step 3	Open IF-SV-2	5 s
Step 4	Close IF-SV-2	
Step 5	Open SB-SV-1	5s
Step 6	Close SB-SV-1	
Step 7	Open SO-SV-1	5s
Step 8	Close SO-SV-1	
Step 9	Open MO-M-SV-1	
Step 10	Open MO-SV-2-M-I	5s
Step 11	Close MO-SV-2-M-I	
Step 12	Turn ON F-SV-1	30s

Step 13	Turn ON F-SV-2	
Step 14	Turn Off F-SV-1	

Table 45 Igniter operation sequence following successful priming

Test Sequence (Auto)		**Status**	**Time Step**
Step 1	All valve Close Sparker on		0 s
Step 2	OPEN: • IO-SV-1 • PF-SV-1		1 s
Step 3	Turn on Spark Plug		3s
Step 4	OPEN: • IO-SV-2-R OR • IO-SV-2-L		2 s
Step 5	OPEN: • PF-SV-2-R OR • PF-SV-2-L	Ignition Flame ON	3-5 s
Step 6	Turn off Spark Plug		
Step 7	CLOSE: • PF-SV-2-R • IO-SV-2-R OR • PF-SV-2-L • IO-SV-2-L	Ignition Flame OFF	6 s
Step 8	CLOSE:	Test End	7-10 s

	All		

Table 46 Secondary Burner operation sequence following successful ignition

Test Sequence (Auto)		**Status**	**Time Step**
Step 1	All valve Close Sparker ON		0 s
Step 2	OPEN: • IO-SV-2 • PF-SV-2 • SB-SV-2 • SO-SV-2		1 s
Step 3	OPEN: • IO-SV-2-R OR: • IO-SV-2-L		2 s
Step 4	OPEN: • PF-SV-2-R OR: • PF-SV-2-L	Ignition Flame ON	3-4 s
Step 5	OPEN: • SO-SV-2-R OR: • SO-SV-2-L		5-6 s
Step 6	OPEN: • SB-SV-2-R OR: • SB-SV-2-L	Ignition Flame ON Secondary Burner Flame ON	5-6 s
Step 7	CLOSE: • PF-SV-2-R	Ignition Flame OFF Secondary Burner Flame ON	5-15 s

	• IO-SV-3-R OR: • PF-SV-3-L • IO-SV-3-L		
Step 8	CLOSE: • SB-SV-2-R • SO-SV-3-R OR: • SB-SV-3-L • SO-SV-3-L	Secondary Burner Flame OFF	16 s
Step 9	CLOSE: • All	Test End	17-25 s

Table 47 Pintle Injector operation sequence following successful secondary burner flame detection in the chamber

Test Sequence (Auto)		**Status**	**Time Step**
Step 1	All valve Close Sparker ON		0 s
Step 2	OPEN: • IO-SV-2 • PF-SV-2 • SB-SV-2 • SO-SV-2		1 s
Step 3	OPEN: • IO-SV-2-R OR: • IO-SV-2-L		2 s
Step 4	OPEN: • PF-SV-2-R OR:	Ignition Flame ON	3-4 s

	• PF-SV-2-L		
	OPEN: • SO-SV-2-R OR: • SO-SV-2-L		
Step 5	OPEN: • SB-SV-2-R OR: • SB-SV-2-L	Ignition Flame ON Secondary Burner Flame ON	5-6 s
	OPEN: • MO-SV-2-R OR: • MO-SV-2-L		
	OPEN: • F-SV-1 CLOSE: • F-SV-2	Ignition Flame ON Secondary Burner Flame ON Main Coal Slurry Flame ON	
Step 6	CLOSE: • PF-SV-3-R • IO-SV-3-R OR: • PF-SV-3-L • IO-SV-3-L	Ignition Flame OFF Secondary Burner Flame ON Main Coal Slurry Flame ON	5-60 s
Step 7	CLOSE: • SB-SV-2-R • SO-SV-3-R OR: • SB-SV-3-L • SO-SV-3-L	Secondary Burner Flame OFF Main Coal Slurry Flame ON	36 s

	OPEN: • F-SV-2 CLOSE: • F-SV-1 • MO-SV-2-R OR: • F-SV-1 • MO-SV-2-L	Main Coal Slurry Flame OFF	60 s
Step 8	CLOSE: • All	Test End	60-75 s

4. Concluding Remarks

The project report presents the exploration of the design and prototyping of a High-Pressure Swirl Oxy-coal Combustor. High-pressure oxy-coal combustion systems have the potential to improve efficiency along with an increased carbon capture rate. Reduction of flue gas at higher pressure, smaller system size, and capital cost reductions render high-pressure oxy-coal systems particularly attractive as next-generation energy-producing systems.

The first objective of this effort was focused on the model analysis of pressurized oxy-coal systems to identify essential design and operating parameters. An ASPEN PLUS® model study for 550 MWe TIPS and ENEL pressurized oxy-coal systems with CO_2 recirculation was performed to evaluate system design, subsystems sizing, and operating condition determination. The effects of a wide range of carbon dioxide recirculation ratios on the thermal efficiency of ENEL and TIPS cycles were studied. The combined effect of pressure and recirculation ratios on thermal efficiency was investigated. The study concluded thermal efficiency of ENEL is significantly higher than the efficiency of TIPS at a pressure of less than 10 bar. The system analysis effort included TRL and technology gap determination of subsystems and critical components. This information was then scaled to determine the requirements for the 1 MW_{th} combustor.

Based on the cycle analysis, the design of a 1 MWth swirl oxy-coal combustor was completed. The unique combustor configuration was designed to have three modular sections: Powerhead, Main Body, and Exhaust. A full combustor FEA analysis was performed to validate the design. The analysis considered all components, including welds, flanges, and bolts. Additionally, Igniters, secondary burners, and cold-slurry injectors were designed and tested. All subsystems, including feed system and control and data acquisition systems, were designed, integrated, and tested. The combustor was manufactured, and various sub-systems were integrated. The total system integration and installation began on July 1, 2020. The shake-down tests and initial operational capability demonstration are expected to be completed by September 30, 2020.

Appendix A

Assembly Procedure

The assembly procedure has been developed to assemble the different parts of the combustor on the vertical test stand. The different sections of the procedure are as follows:

OBJECTIVE

The purpose of this document is to set a series of rules and procedures to ensure the correct and safe way to assemble the Oxy-Coal Combustor. The combustor is a device where the combustion of oxygen, methane, and coal slurry will take place. Additionally, the combustion will be pressurized at 10 bars (145 psi). The combustor consists of three parts, which are considered industrial size:

Powerhead – 800 lbs.

Main Body – 2600 lbs.

Exhaust – 1600 lbs.

Each component has to be securely attached to each other and to the vertical test stand. Components will be secured through bolting through the flanges with a Sealing Gasket at the interface. Each part must be securely accommodated into the vertical test stand that is found at the Fabens facility. After the assembly of the combustor, the feed system assembly will take place.

INTRODUCTION

Participants and Roles

At least 4 people should be participating in this assembly. The list below shows the role of each participant, and their contact information is listed in Table 1.

Table 1 Test Personnel

Name	Role	Description	Email
Person 1	Technician 1	Ensure hardware installation is completed and it meets all installation requirements	TBD
Person 2	Technician 2	Assists during hardware installation is completed, and it meets all installation requirements	TBD
Person 3	Lift Operator	Operates heavy on-site machinery	TBD
Person 4	Operation Conductor	Ensure the procedure is followed, and all test and safety requirements are met	TBD

Safety Considerations

This procedure poses a series of hazards to personnel and equipment. Refer to the Hazards presented in this section for a list of hazards associated with the operation of this setup. Use extreme caution when operating and having any of the components lifted.

Use approved personal protective equipment (PPE):

Eyes

Safety glasses shall be worn at all times. Safety glasses may be found at the entrance of the research facility. Must comply with the CSA Standard of Z94.3

Figure 137 Safety glass

Hard Hats:

Hard hats shall be used to protect the head from collision impact, debris, among other hazards. They are proven to save lives in the workplace. These may be found at the entrance of the research facility. Must comply with ANSI/ISEA Z89.1-2009.

Figure 138 Hard hat

Feet:

Steel-toe boots must be worn at all times while inside the research facilities to protect the feet. Must meet ASTM F2413. Must be non-slip.

Figure 139 Steel toe shoe

Visibility Vest

A high-visibility vest allows employees to be seen in a low-light environment and reduce the risk of injury significantly by being easily spotted. This vest has to be bright and attention-grabbing, with strips of reflective material. Since most of the work will be during daylight, bright colors such as fluorescent yellow-green shall be used. Must comply with ANSI/ISEA 107-2015.

Hazards

	System	Hazard	Severity	Likelihood	Mitigation
1	All	Collision	3-High	2 - Infrequent	Device has to be moved at a slow rate; a spotter will be used during operation.
2	Device	Drop	4-Critical	2 - Infrequent	All cranes, hooks, fork lifts have to be rated for the weight, ensure hooks and sling are properly secured, ensure bolts are secured
3	Lift Heavy Machinery	Load Operation Error	3-High	2 - Infrequent	Hiring a professional operator
4	Personnel	Personnel Fall	4-Critical	3-Frequent	Use of fall protection gear and non-slip shoes

Requirements for Assembly

- Weather conditions shall permit workers to operate without interference: Clear visibility, no snowfall.
- Lighting has to be appropriate, whether on a clear day or with halogen lights.
- Heavy Machinery rated for a minimum of 5000 pounds

Location:

Technology and Innovation Acceleration Park

1611 N Fabens Rd

Fabens, TX 79838

Test Article Description

A high-pressure combustor will be assembled inside a Vertical Test Stand. This will be accomplished by connecting each section of the combustor through bolting flanges. Each flange is a 300-class flange of 28 in of OD and 18.18 in of ID. To secure the combustor into the Vertical Test Stand, supporting plates will be placed around the opening were the combustor would fit. Additionally, extensions around the Powerhead flange (denominated as “ears”) will be included, to support the weight of the combustor at that point.

Drawings of Assembly

Vertical Test Stand

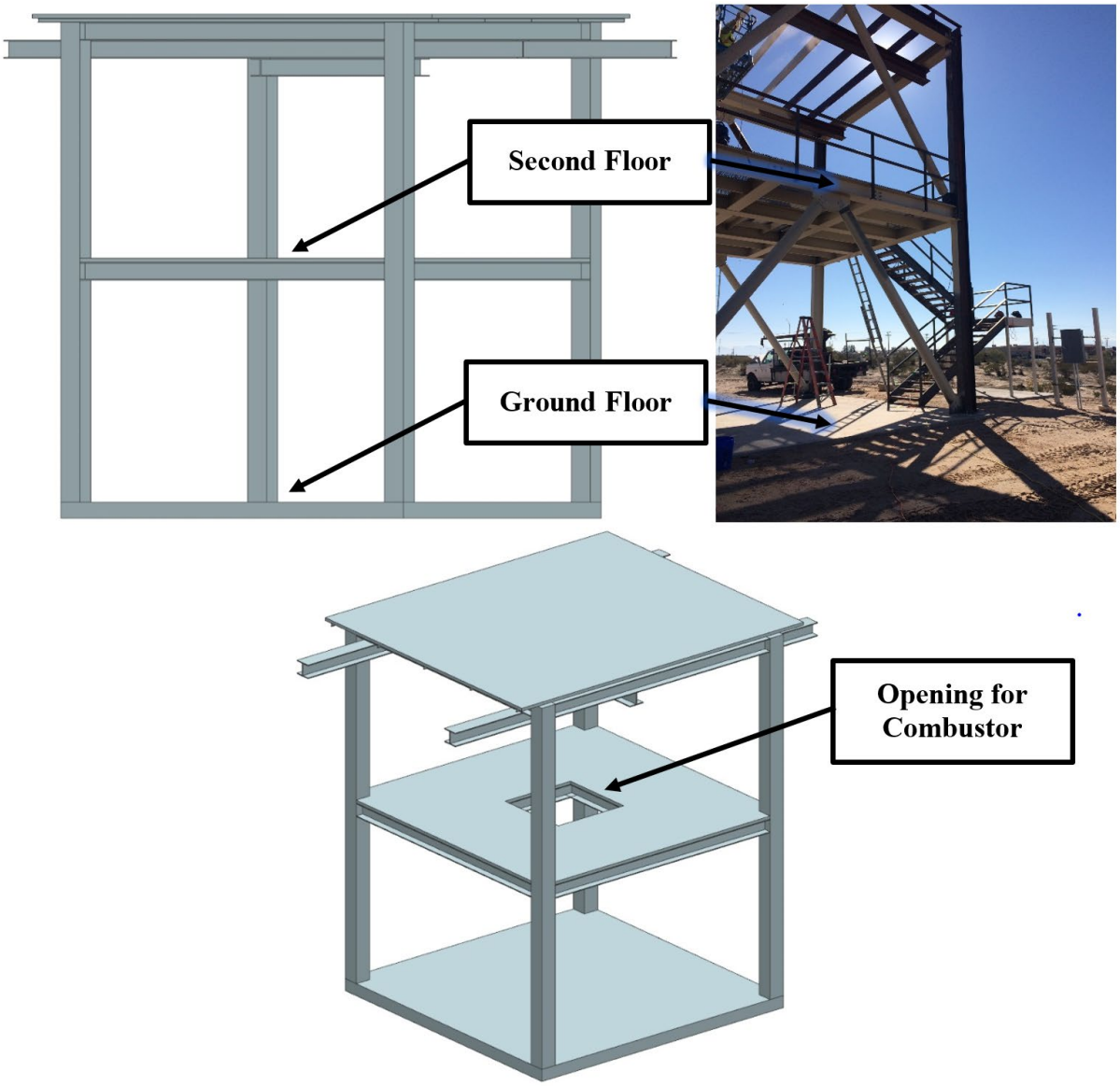

Figure 141 Vertical Test stand

Combustor Assembly

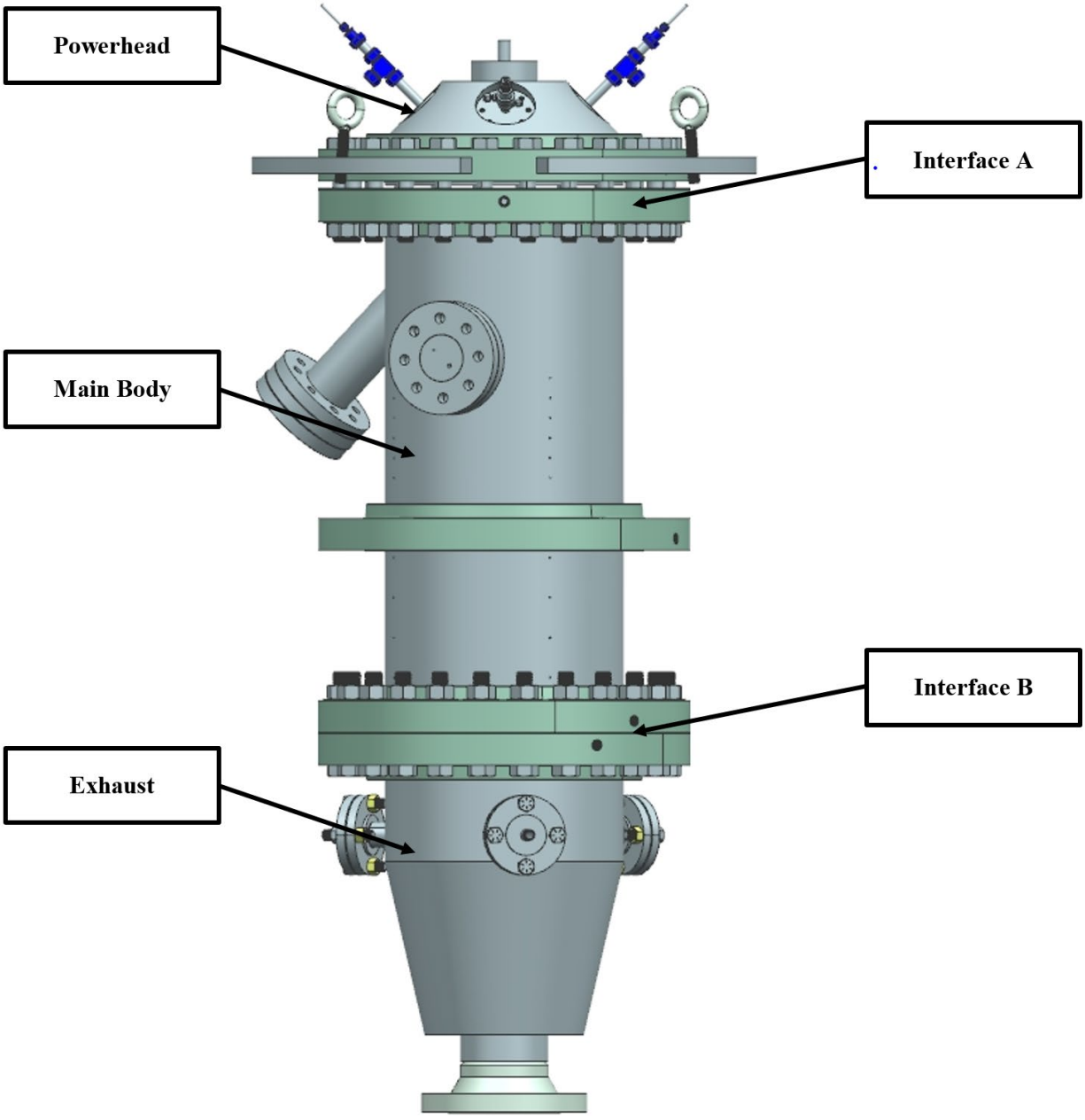

Figure 142 Oxy-coal combustor

Powerhead

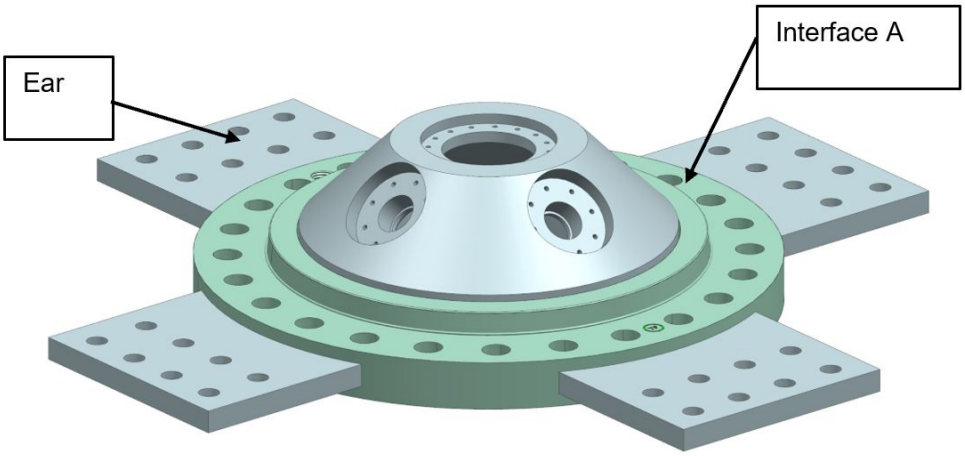

Figure 143 Powerhead

Main body

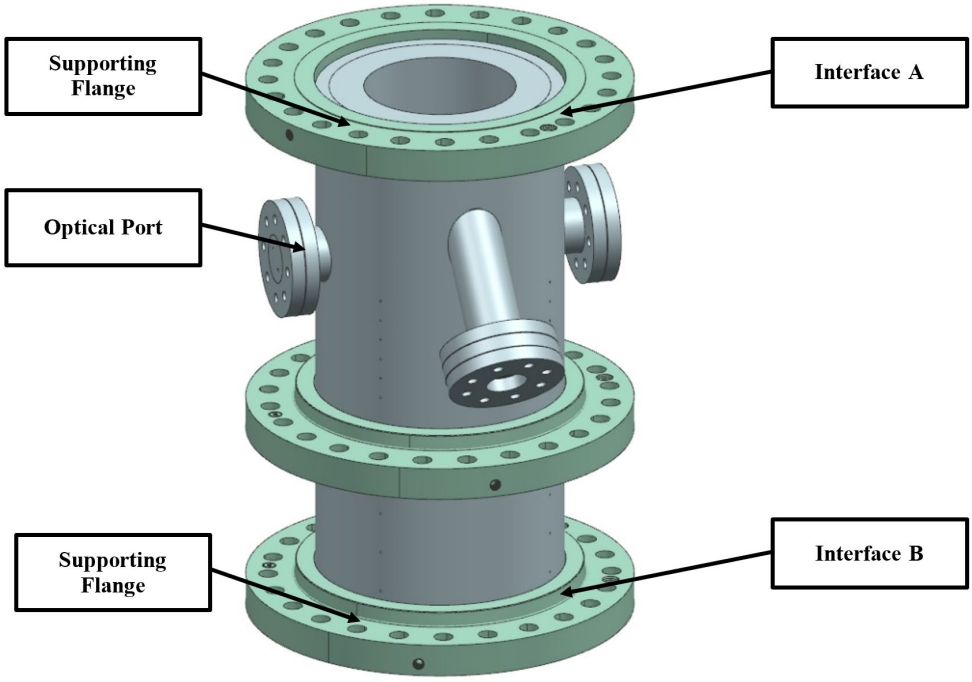

Figure 144 Main Body

Exhaust

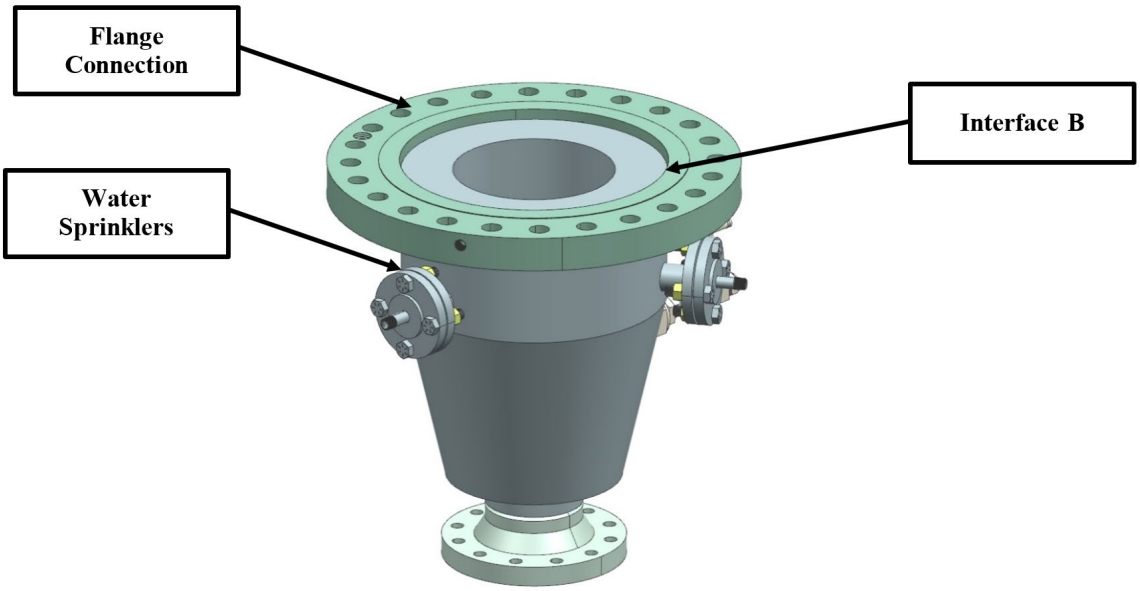

Figure 145 Exhaust

Sealing, Bolts and Nuts

Sealing

The sealing gasket will be used in-between flanges. All gaskets are custom made matching the flanges.

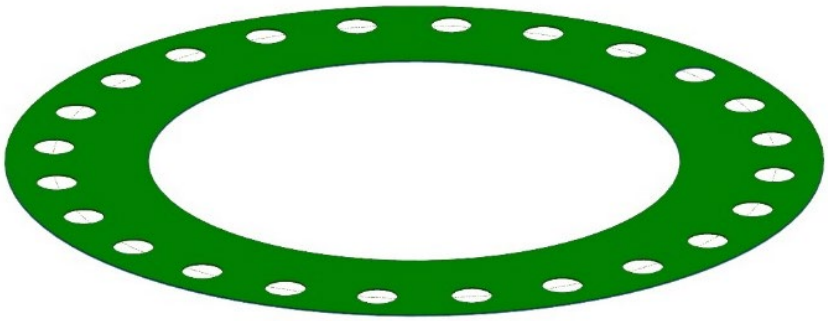

Figure 146 Sealing Gasket

Bolts, Nuts and Washers

The bolts and nuts are to be of SAE Grade 8. Bolts are 1 ¼- 7 UNC. Nuts and washers are corresponding to the bolts.

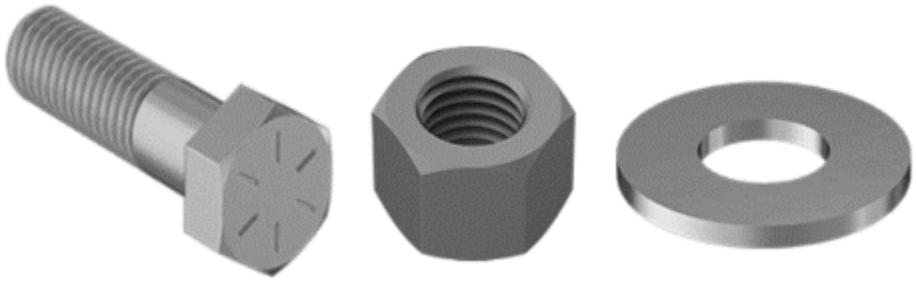

Figure 147 Bolts, Nut and washer

Pre-Procedure

- Ask all personnel that will not be part of the team to leave the assembly area during operation
- Verify all personnel is wearing appropriate PPE as specified in the Safety Section
- Inspect all equipment used for assembly for damage that may cause malfunction.

Assembly Procedure

Powerhead

- Put 4 eyebolt hooks through the bolt holes of the plate in the figure below
- Hook the lifting chains on the eyebolt hooks

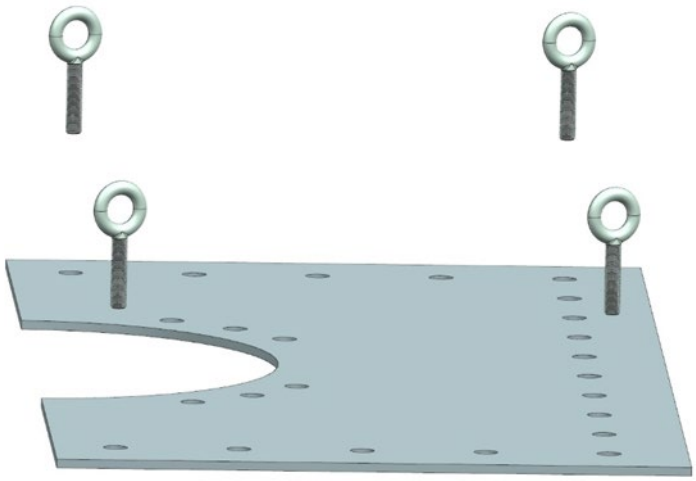

Figure 148 Stand plate to hold powerhead

- Hook the lifting chains to the crane
- Lift the Plates until it reaches the second floor of the Vertical Test Stand
- Move the vehicle, until the Plates are inside of the Vertical Test Stand
- Place the Plates into position, align, and finally drop
- Technician 2 should be on the lower half the second floor of the Vertical Test Stand, lifted and able to move arms freely

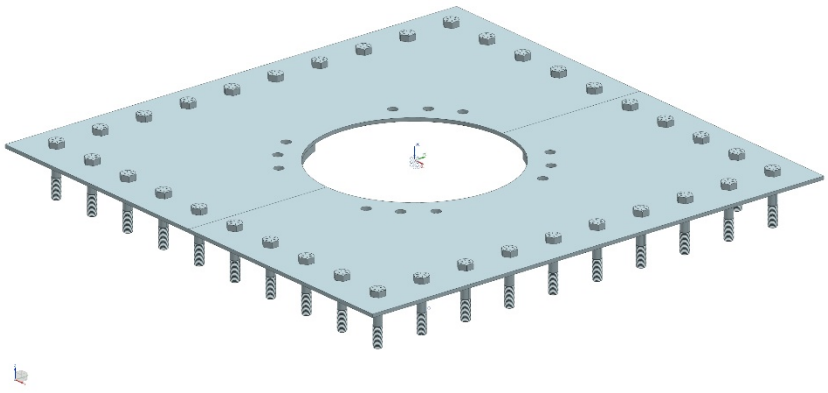

Figure 149 Assemble supporting stand plate for powerhead

- Technician 1 will place bolts from the upper half of the second floor and Technician 2 will place the washers and nuts

- Technician 2 will take the torque wrench and increase the torque the bolts to a third of the total torque; do two-thirds next and then the final third of torque; verify torque on all bolts is adequate. Use designated bolt pattern

Assembly of Powerhead into Vertical Test Stand

- With a Forklift, have the arms go through the base of the pallet where the Powerhead is resting and drive the Fork Lift to the Vertical Test Stand
- Place the pallet on the ground, next to the Vertical Test Stand.
- Put hooks through the lifting eyebolt hooks to lift the Powerhead

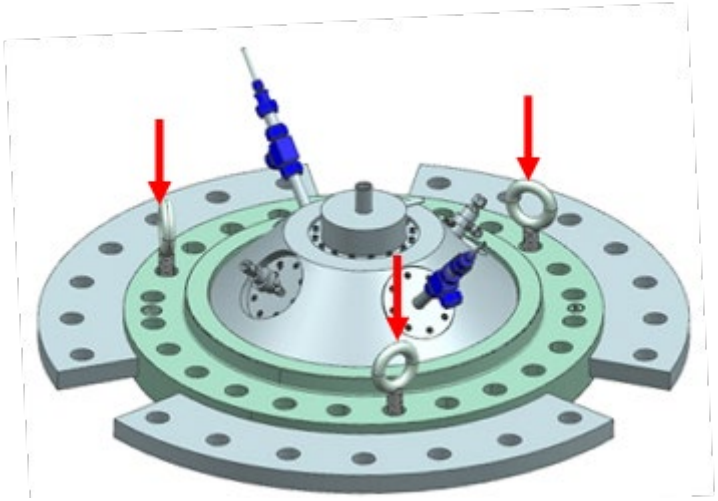

Figure 150 Lifting points for the powerhead

- The Crane should have the Chains Slings from Figure 15.

Figure 151 Chain slings

- Use the Crane to lift the Powerhead to the second floor of the Vertical Test Stand.
- Extend the Jib, until the Component is inside of the Vertical Test Stand

- Place Powerhead, making sure that the Ears are aligned to the Plates, following the next figure

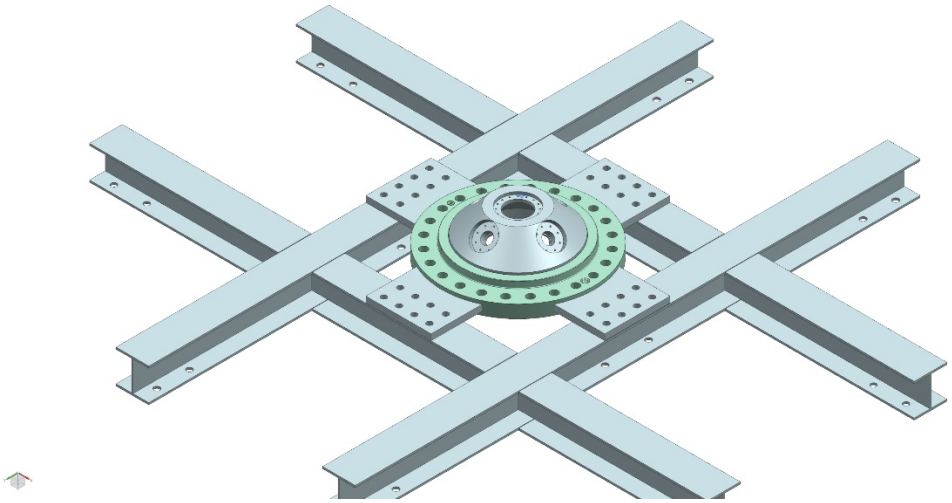

Figure 152 Powerhead Assembly in Vertical Test Stand

- Take off the eyebolt hooks
- Place the Bolts for the Powerhead
- Technician 2, lifted to reach the bottom of the second floor, from below will place the washers and nuts
- Use the torque wrench and increase the torque of the bolts to a third of the total torque; two-thirds and final torque; verify torque on all bolts. Use designated bolt pattern, shown in Figure 17.

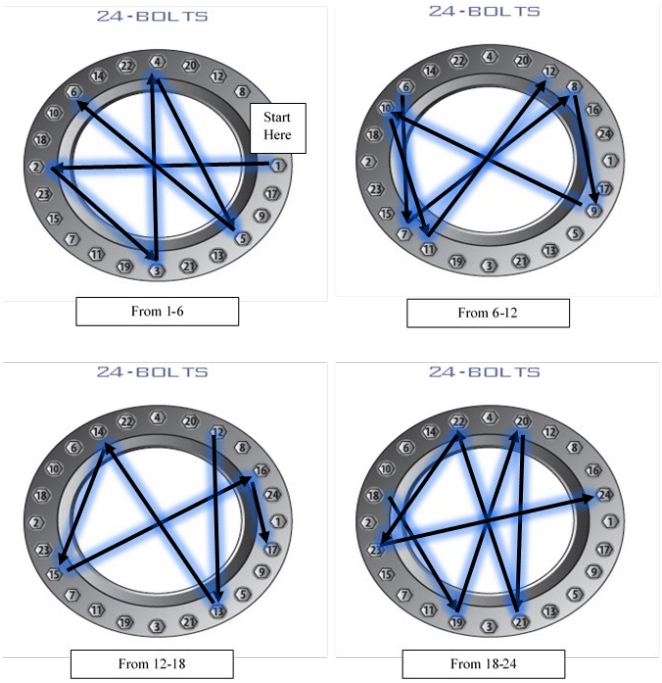

Figure 153 Torque sequence

Main Body & Exhaust

- Main Body is standing up vertically

- Technician 1, on the second floor will put x bolts from the Component Flange
- Bring the Main Body next to the Vertical Test Stand, standing upright
- Place with a Fork Lift, the Main Body into a Platform Lift
- Put the Sealing Gasket at the top of the Main Body, at the Flange
- Slowly lift the Main Body upwards until there's approximately a 4-inch gap, between the Component and the Main Body
- Technician 1 will check if the holes of the Flanges align using lasers
- If required, Re-orient the Main Body to align with the Flange of the powerhead
- Once Technician 1 determines that the Flanges are aligned, the Load Conductor will continue to lift the Main Body.
- Technician 2, lifted from below, from below will place the washers and the nuts and hand tighten them in a star pattern, shown in Figure 18.
- Take the torque wrench and increase the torque the bolts to a third of the total torque; two-thirds and final torque; verify torque on all bolts. Use designated bolt pattern.

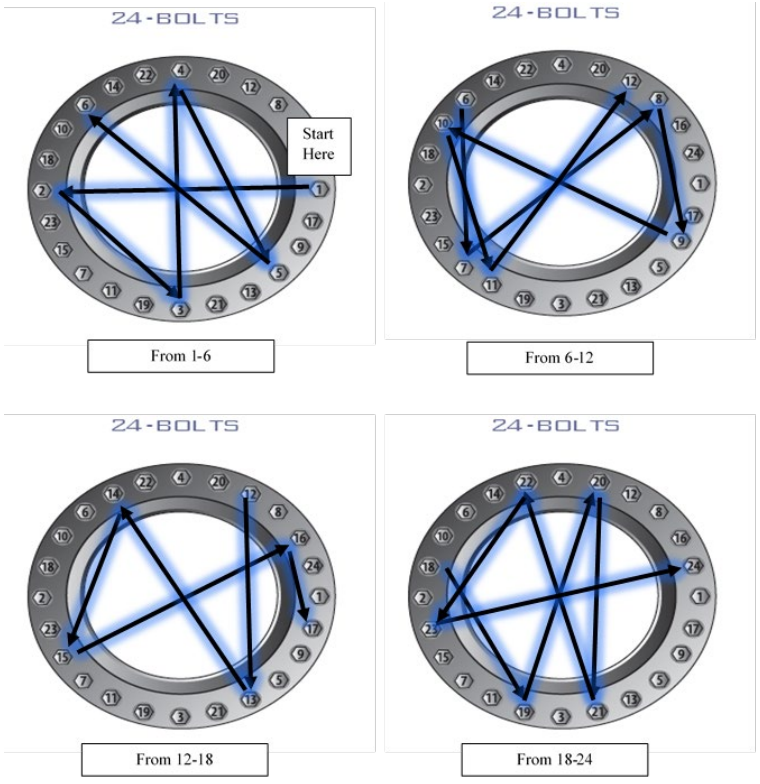

Figure 154 Torque sequence interface A

- Place with a Fork Lift, the Exhaust into a Platform Lift
- Put the Sealing Gasket at the top of the Exhaust, at the Flange

- Slowly lift the Exhaust upwards until there's around a 4-inch gap, between the Exhaust and the Main Body
- Technician 2, lifted to reach interface B, will check that the Flanges are aligned
- Place 1 bolt to ensure alignment
- Place another bolt 180 degrees from the first one.
- Hand tighten the nuts
- Place the rest of the bolts and hand tighten them in the following sequence shown in Figure 22.

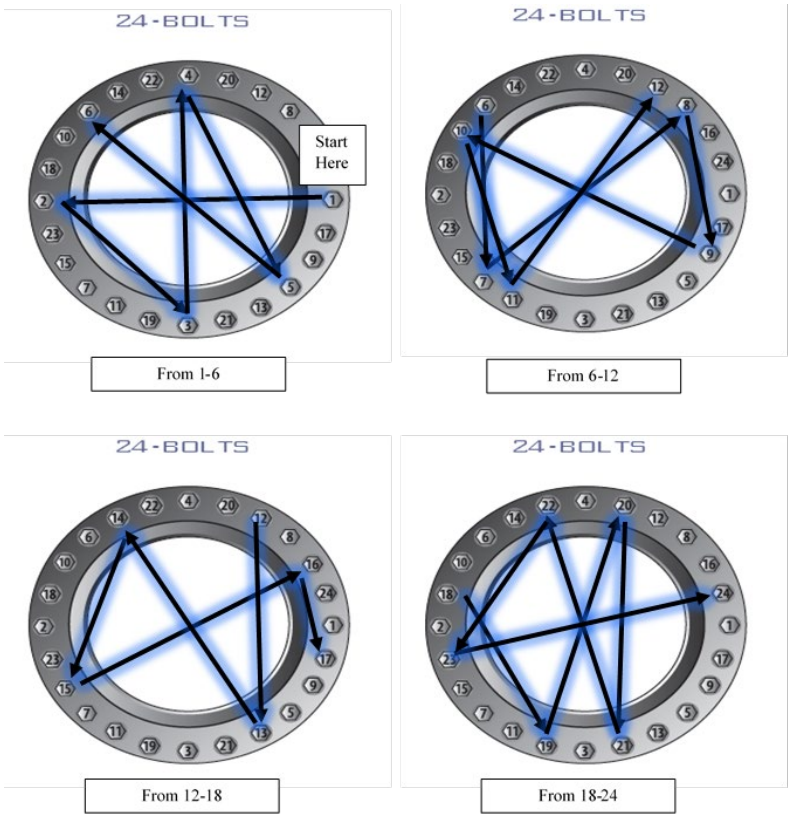

Figure 19 Torque sequence for exhaust flange

- Use the torque wrench to increase the torque of the bolts to a third of the total torque; two-thirds and final torque; verify torque on all bolts.

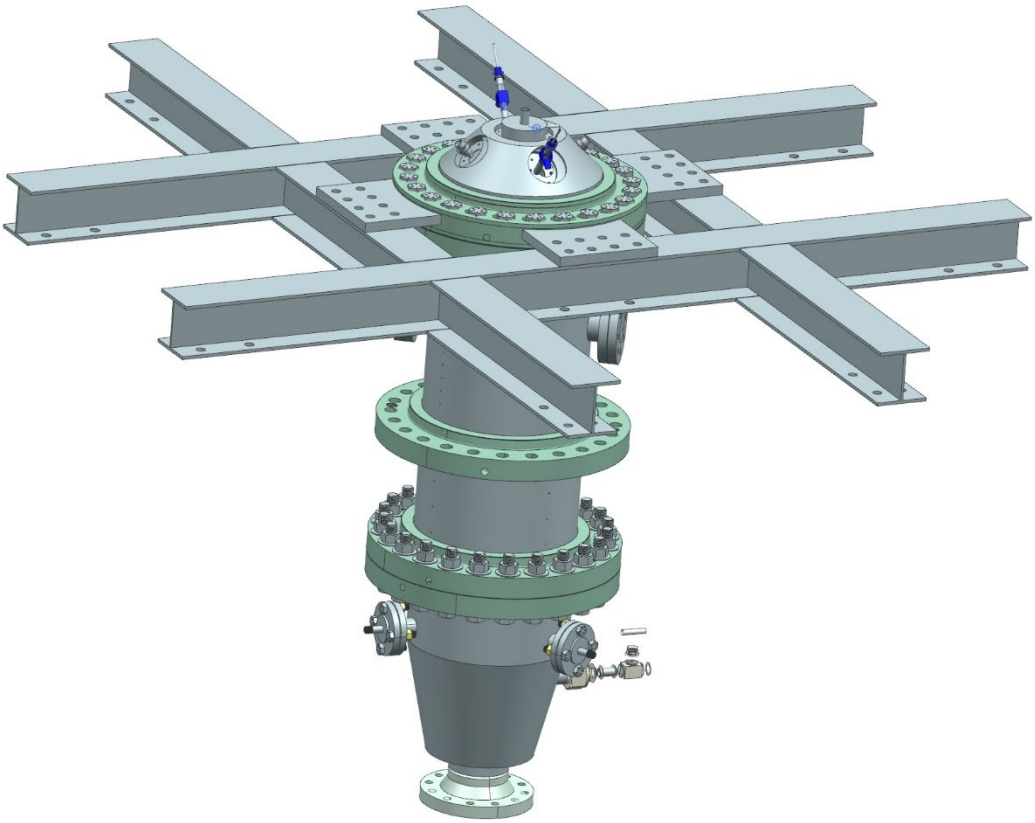

Figure 155 Final Assembly

Publications

Peer Reviewed

1. Khan, M., M, Chowdhury, Chowdhury, A, Aboud, J., and Love, N., "**Effect of Carbon Dioxide Recirculation and Pressure on Efficiency of the TIPS and ENEL Oxy-Coal Power Cycle**", Journal of Energy Resources Technology, Vol. 142, June 2020

Conference Papers

2. Rios, A., Rios, A., Chowdhury, M., Khan, M., and Choudhuri, A., "**Design of a Pintle Injector for Clean, Pressurized Oxy-Coal Combustion**", 2019 International Pittsburgh Coal Conference, Pittsburgh, PA, September 3 - 6, 2019
3. Chowdhury, M., Khan, M., and Choudhuri, A., "Design and Test of a Pintle Injector for Oxy-Coal Combustion", ***2019 AIAA Propulsion and Energy Forum***, Indianapolis, Indiana, 2019
4. Chowdhury, A., Aboud, J., Choudhuri, A., Love, N., Tsiava, R., Dhungel, B., Ma, J., and Kim, H., Paper No. 154, "**Modeling and Testing of a Directly Heated Supercritical CO_2 Combustor**," 6th Supercritical CO_2 Power Cycles Symposium, March 26-28, 2018, Pittsburgh, PA.
5. Chowdhury, M., Khan, M., Chowdhury, A., Choudhuri, A., and Love, N. "**Thermodynamic Analysis of ENEL and TIPS Oxy-coal Power Cycle**", AIAA-2018-2254, 56th AIAA Aerospace Sciences Meeting, Kissimmee, Florida, 2018
6. Chowdhury, A., Cruz, J., Aboud, J., Rios, A., Chodhuri, A., and Love, N. "**Design and Experimental Study of a High Pressure Oxy-Methane Combustor**", AIAA-2018-1476, 56th AIAA Aerospace Sciences Meeting, Kissimmee, Florida, 2018
7. Chowdhury, A., Choudhuri, A., and Love, N., "**Design of a Methane-Oxygen Pilot Burner for High Pressure Oxy-Coal Combustor *Application*",** 2017 International Pittsburgh Coal Conference, Pittsburgh, PA, September 5 - 8, 2017

Poster Presentation

8. Aboud. J, "Oxy-Fuel Combustion Initiatives", ***Presentation to Johnson Space Center***, Houston, Texas, January, 2017

Dissertation and Thesis

9. Chowdhury, A S M Arifur Rahim, **"Design And Experimental Study Of A High Pressure And Supercritical Methane-Oxygen Burner"**, (2018). *PhD Dissertation*. The University of Texas at El Paso. Open Access Theses & Dissertations. 1410. https://digitalcommons.utep.edu/open_etd/1410

Symposium Papers

10. Chowdhury, M., Rios, A., Khan, M., and Choudhuri, A.., "**Design of a Pressurized Oxy-Coal Combustor,**" Southwest Emerging Technology Symposium 2019, El Paso, Texas, April 2019.
11. Khan, M., Chowdhury, M., Chowdhury, Rios, A., and Choudhuri, A., "**Thermal and Structural Analysis of a Cylindrical High Pressure Oxy-Coal Combustor**", Southwest Emerging Technology Symposium 2019, El Paso, Texas, April, 2019.

12. Rios, A., Chowdhury, M, and Choudhuri, A., "**Characterization of A Pintle Injector For Gas-Slurry Combustion**," Southwest Emerging Technology Symposium 2019, El Paso, Texas, April, 2019
13. Rios, A., Chowdhury, A, Aboud, J., and Love, N., "**Design and Experimental Demonstration of a High Pressure Oxy-Methane Combustor**," Southwest Emerging Technology Symposium 2018, El Paso, Texas, April, 2018
14. Khan, M., Chowdhury, M., Chowdhury, A., Choudhuri, A., and Love, N., "**Thermodynamic Analysis of TIPS and ENEL Power Cycles at Varying Recirculation Ratios**," Southwest Emerging Technology Symposium 2018, El Paso, Texas, April, 2018.
15. Aboud, J. G., and Love, N. D., **"Design of a Pintle Injector for an Oxy-Coal Combustor**," Southwest Emerging Technology Symposium 2018, El Paso, Texas, April 2018.
16. Chowdhury. M, Chowdhury, A. A., Choudhuri, A., and Love, N. "**Entropy and Property Analysis of a Supercritical Combustion Process**", Southwest Emerging Technology Symposium 2017, El Paso, Texas, April 2017.

In Progress

17. Khan, M., Chowdhury, M., Chowdhury, Rios, A., and Choudhuri, A., "**Characterization OF Oxy-coal swirl injector**.", 2020 International Pittsburgh Coal Conference, Pittsburgh, PA, September 8 - 11, 2020 (Abstract Approved)
18. Rios Ibañez, Ana C., "**Design And Experimental Study Of A High Pressure And Supercritical Methane-Oxygen Burner**", (2020), PhD Dissertation, The university of Texas at El Paso.

References

[1]. Chen, L., Yong, S. Z., & Ghoniem, A. F. (2012). **Oxy-fuel combustion of pulverized coal: characterization, fundamentals, stabilization and CFD modeling**. Progress in Energy and Combustion Science, 2012, 38(2), pp 156-214.

[2]. Hong, J., Chaudhry, G., Brisson, J. G., Field, R., Gazzino, M., and Ghoniem, A. F. **Analysis of oxy-fuel combustion power cycle utilizing a pressurized coal combustor**. Energy,2009, 34(9), pp 1332-1340

[3]. L. Zheng, R. Pomalis, B. Clements, "**Technical and economic feasibility study of a pressurized oxy-fuel approach to carbon capture: Part 1-Technical feasibility study and comparison of the ThermoEnergy Integrated Power System (TIPS) with a conventional power plant and other carbon capture processes**, CANMET Energy Research Centre, Natural Resources Canada (2007)

[4]. Gazzino M, Benelli G. "**Pressurised oxy-coal combustion Rankine-cycle for future zero emission power plants: process design and energy analysis**".Proceedings of ASME ES2008. Jacksonville, Florida, USA; 2008

[5]. Warzecha, P. and Boguslawski, A. (2014) **Simulations of pulverized coal oxy-combustion in swirl burner using RANS and LES methods,** Fuel Processing Technology, Vol. 119, pp. 130-135

[6]. Burke, M. P., Chaos, M., Dryer, F. L., & Ju, Y. (2010). **Negative pressure dependence of mass burning rates of H 2/CO/O 2/diluent flames at low flame temperatures**. Combustion and Flame, 157(4), 618-631

[7]. Suda T, Masuko K, Ji Sato, Yamamoto A, Okazaki K. (2007**) Effect of Carbon Dioxide on Flame Propagation of Pulverized Coal Clouds in CO2/O2 Combustion**, Fuel, Vol. 86, pp. 2008-2015.

[8]. Nozaki T, S-i Takano, Kiga T, Omata K, Kimura N. (1997) **Analysis of The Flame Formed During Oxidation Of Pulverized Coal By An O2eco2 Mixture**, Energy, Vol. 22, pp.199-205.

[9]. Kimura N, Omata K, Kiga T, Takano S, Shikisima S. (1995) **The Characteristics of Pulverized Coal Combustion in O2/CO2 Mixtures for CO2 Recovery**, Energy Conversion and Management, Vol. 36, pp. 805-808.

[10]. Nikzat, H., Pak, H., Fuse, T., Hu, Y., Ogyu, K., Kobayashi, N., And Hasatani, M. (2004) **Characteristics Of Pulverized Coal Burner Using a High-Oxygen Partial Pressure**, Chemical Engineering Research and Design, Vo. 82, pp. 99–104.

[11]. E. Rossetti, M. Malavasi, "**Method and plant for the treatment of materials in particular waste materials and refuse**", (2004)

[12]. M. Malavasi, E. Rossetti, "**High-efficiency combustors with reduced environmental impact and processes for power generation derivable Therefrom**", (2005)

[13]. M. Malavasi, G. Di Salvia, E. Rossetti, "Combustion process", (2009)

[14]. J. Hong, R. Field, M. Gazzino, A.F. Ghoniem, "**Operating pressure dependence of the pressurized oxy-fuel combustion power cycle**", Energy 35 (2010), pp. 5391–5399

[15]. Fassbender AG. "**Pressurized oxy-fuel combustion for multipollutant capture"**, ThermoEnergy Power Systems, LLC. Patent No. 6,196000, Power System with Enhanced Thermodynamic Efficiency and Pollution Control. www.thermoenergy.com. 1960.

[16]. U.Renz. **Investigation of a High Pressure Oxy-Coal Process**. The 7th International Symposium on Coal Combustion (ISCC)

[17]. Yang T, Hunt P, Lisauskas R, Ballas EN, Vitalis B. **Pressurized Oxycombustion Carbon Capture Power System**. In: The 35th international technical conference on clean coal & fuel systems. Clearwater, FL; 2010

[18]. Hu, Y., & Yan, J. (2012). **Characterization of flue gas in oxy-coal combustion processes for CO 2 capture**. *Applied Energy*, *90*(1), 113-121

[19]. Croiset, E., Thambimuthu, K., & Palmer, A. (2000). **Coal combustion in O2/CO2 mixtures compared with air**. The Canadian Journal of Chemical Engineering, 78(2), 402-407.

[20]. Sanchez, L. E., Chaparro, J., Torres, S. A., Love, N. D., & Choudhuri, A. R. (2016). "**Development and Testing of a O2/CH4 Torch Igniter for Propulsion Systems**," 52nd AIAA/SAE/ASEE Joint Propulsion Conference, Utah, 2016, pp. 4975.

[21]. Lux, J., & Haidn, O., "**Effect of recess in high-pressure liquid oxygen/methane coaxial injection and combustion**," *Journal of Propulsion and Power*, Vol. 25, No. 1, 2009, pp. 24-32

[22]. Kendrick, D., Herding, G., Scouflaire, P., Rolon, C., & Candel, S., "**Effects of a recess on cryogenic flame stabilization**," Combustion and Flame, Vol. 118, No. 3, 1999, pp. 327-339.

[23]. Tripathi, A., Juniper, M., Scouflaire, P., Rolon, J. C., Durox, D., & Candel, S. (1999, June). "**LOx tube recess in cryogenic flames investigated using OH and H2O emission**," 35th Joint Propulsion Conference and Exhibit, California, 1999,p. 2490

[24]. Wheeler, D. B., & Kirby, F. M., "**High-pressure LOX/CH4 injector program**," NASA Report, 1979

[25]. Tangirala, V., R. H. Chen, and James F. Driscoll. "**Effect of heat release and swirl on the recirculation within swirl-stabilized flames**." Combustion Science and Technology 51.1-3 (1987): 75-95

[26]. Grinstein, F. F., and Christer Fureby. "**LES studies of the flow in a swirl gas combustor." Proceedings of the Combustion Institute** 30.2 (2005): 1791-1798

[27]. Durox, Daniel, et al. "**Flame dynamics of a variable swirl number system and instability control**." Combustion and Flame 160.9 (2013): 1729-1742

[28]. Zheng, L. (Ed.). (2011). **Oxy-fuel combustion for power generation and carbon dioxide (CO2)capture**. Elsevier

[29]. Cengel, Y. A. (2010). Fluid mechanics. Tata McGraw-Hill Education.

[30]. Anderson W.E., Long M.R. and Heister S.D., "**Liquid Bipropellant Injectors**", Liquid Rocket Thrust Chambers: Aspects of Modeling, Analysis and Design; AIAA, PP. 141-165, 2004.

[31]. [2] C. Heinzen, A. Berger, I. Marison. "**Use of Vibration Technology for Jet Break-Up for Encapsulation of Cells and Liquids in Monodisperse Microcapsules**". Fundamentals of Cell Immobilisation Biotechnology, Focus on Biotecnolgoy, vol 8A. Springer, Dordrecht. 2004